AGN FEEDBACK AND DELIVERY METHODS FOR SIMULATIONS OF COOL-CORE GALAXY CLUSTERS

By

Gregory Robert Meece Jr.

A DISSERTATION

Submitted to
Michigan State University
in partial fulfillment of the requirements
for the degree of

Astrophysics and Astronomy- Doctor of Philosophy

2016

ABSTRACT

AGN FEEDBACK AND DELIVERY METHODS FOR SIMULATIONS OF COOL-CORE GALAXY CLUSTERS

By

Gregory Robert Meece Jr.

As the largest gravitationally bound structures in the universe, galaxy clusters stand at a crossroad between astrophysics and cosmology. Observations of galaxy clusters can reveal information about the composition and evolution of the universe, but in order to interpret these observations, astrophysicists need to understand the processes shaping the gas in the intracluster medium (ICM). This dissertation explores the role of active galactic nuclei (AGN) in regulating cooling in the ICM and focuses on how condensation triggered by thermal instability may form a feedback cycle that prevents clusters from cooling.

Roughly half of galaxy clusters are observed to have cooling times much shorter than the age of the cluster. However, these clusters do not seem to be cooling down and do not appear to form stars at the predicted rate. AGN feedback can solve this problem by reheating the ICM, but only if the AGN power is linked to the ICM cooling rate. This dissertation explores the 'Precipitation-regulated feedback' hypothesis, in which the cooling ICM becomes thermally unstable, leading to the formation of clumps of cold gas. This cold gas triggers AGN activity, which reheats the cluster. The heating stabilizes the ICM against further condensation, leading to the AGN shutting off and allowing the ICM to cool again. Thus, the balance of radiative cooling and AGN heating serve to regulate the temperature of the ICM and keep galaxy clusters in a roughly stable thermal state.

Dedicated to my friends, family, advisors, cats, and my wonderful fiancé Gabrielle, all of whom have supported me in this endeavor, have nodded their heads at appropriate times, and pretended to understand what I am talking about. Special thanks to my family, who have always believed in me and encouraged me in academic pursuits. Much writing credit goes to my cats Peter and Francis who have helped me keep the text succinct by meowing and standing in front of my monitor. Thanks to Gabrielle for putting up with me through all of this. Finally, thank you to the larger astronomy community. Knowing that others find my work interesting and useful is the highest reward that I can imagine.

ACKNOWLEDGMENTS

This work was completed at Michigan State University from 2011-2016, and I would like to thank the University and the Department of Physics and Astronomy for their support during that time. I and/or my research has been supported through NSF grant OCI-1053575, NASA through grant NNX12AC98G and NNX15AP39G, and Hubble Theory Grant HST-AR-13261.01-A and HST-AR-14315.001-A, and by the National Science Foundation through grant PHY-0941373. Simulations were performed on TeraGrid, XSEDE, and NASA resources through grants TG-AST090040, TG-AST100004, and SMD-15-6514. I have also been supported as a graduate teaching assistant by the department and as a research associate by the Lyman-Briggs College and the College of Natural Sciences through Mark Voit. Additional research funding was provided under a fellowship from the Michigan Institute for Plasma Science and Engineering (MIPSE).

I would also like to acknowledge the researchers that have contributed to this work. In addition to my advisors (Drs. Brian O'Shea and Mark Voit) and my dissertation committee, Dr. Megan Donahue, Dr. Britton Smith, Dr. Devin Silva, and Brian Crosby at Michigan State have contributed frequent wisdom and advice. I am also indebted to Drs. Yuan Li (University of Michigan), Greg Bryan (Columbia University), Prateek Sharma (Indian Institute of Science), and Mateusz Ruszkowski (University of Michigan) for useful discussions.

This work is an extension of work done by earlier researchers and would not have been possible without their efforts and contributions. Meece et al. (2015) extends Mike McCourt's (Harvard) dissertation work, and Meece et al. (2016) extends Yuan Li's. This dissertation is inspired and based on the work of Mark Voit and his collaborators. Finally, the `Enzo` and `yt` codes are developed by a large collaboration of users. Without their efforts, this work would not have been possible.

TABLE OF CONTENTS

LIST OF TABLES

LIST OF FIGURES

1 Introduction

Galaxy clusters stand at the crossroads of astrophysics and cosmology. Through observations, galaxy clusters have been used to investigate the contents, structure, and evolution of the universe. In order to use galaxy clusters in this manner, it is necessary that astronomers understand the physical processes that shape the light emitting, baryonic matter. This dissertation will focus on a particular process – feedback from active galactic nuclei – and its role in regulating the thermal state of the intracluster medium.

Galaxy clusters are filled with a hot plasma, known as the intracluster medium, or ICM. This plasma emits X-rays and should cool on timescales much shorter than the ages of many clusters. However, observations show that most of the plasma does not cool down. **Therefore, some physical mechanism must be heating the plasma at a rate that approximately balances radiative cooling**. This is the crux of the cooling-flow problem. In this dissertation I explore a scenario in which powerful jets, triggered by the accretion of cold gas onto supermassive black holes deep in the cluster cores, provide the necessary heating and keep cool-core clusters in a rough state of thermal equilibrium.

This introduction begins by discussing a selection of astronomical concepts that have bearing on the rest of this dissertation, including galaxy cluster formation, galaxy cluster evolution, and active galactic nuclei (AGN). Those with a strong grasp of these concepts can skim these sections. Section 1.4 outlines the cooling flow problem and the precipitation regulation theory of feedback, which forms the basis for this work. Finally, Section 1.5 presents the outline of the rest of this dissertation.

1.1 Formation of Galaxy Clusters and the Cosmological Context

1.1.1 The ΛCDM Model of Cosmology

In the ΛCDM cosmological model, the universe consists of dark energy (the Λ term) and 'cold' dark matter (CDM), along with baryons, electrons, neutrinos, and radiation all evolving in a general relativistic framework. The universe began in the Big Bang approximately 13.6 billion years ago as a hot, dense, expanding medium. The physics of the universe immediately following the Big Bang is not fully understood, and will require the development of a quantum theory of gravity. The evidence suggests that the universe underwent a period of exponential expansion soon after the Big Bang, termed 'Inflation' (first described in the pioneering works of Guth, 1981; Linde, 1982; Bardeen et al., 1983). As the universe expanded the temperature of the background radiation dropped, resulting in the creation of baryons, leptons, and atomic nuclei (Alpher et al., 1948). Although the primordial universe was nearly homogeneous, small perturbations in the dark matter density grew through hierarchical merging to create a web of structure throughout the universe. For the past several billion years, dark energy has been driving the expansion of the cosmos.

Dark energy is the least well understood component of the ΛCDM model and also the most dynamically important at large scales. **The nature and origin of dark energy are not understood, but for astrophysicists, it is more important to know its distribution and equation of state**. The ΛCDM model assumes that dark energy is a 'cosmological constant' that has a uniform, constant, and low density throughout space. Alternative and extended models have been proposed, but they can not currently be observationally distinguished from the cosmological constant model (e.g., Anderson et al., 2012; Planck Collaboration et al., 2015b). Dark energy has the effect of exerting negative pressure on its surroundings, causing the expansion of the universe to accelerate. Due to its relatively low energy density, dark energy was dynamically unimportant in the early universe but as space expanded, the constant density of dark energy meant that it came to dominate the expansion of the universe. Roughly 10 billion years after the Big Bang, dark energy began to dominate the large scale expansion of the universe and has done so ever since. In gravitationally bound systems (including galaxies and galaxy clusters) however, dynamics are dominated by gravity, and the dynamical effects of dark energy can be safely neglected.

ΛCDM assumes that the bulk of the mass in the universe is in the form of cold dark matter, which is believed to be some sort of particle that only interacts through gravity and possibly the weak nuclear force (see Feng, 2010, for a review). The particles are 'cold' in the sense that their initial thermal energy was negligibly small compared to their rest mass energy, making them non-relativistic. As with dark energy, the nature of these particles and their origins are not known. Several theories have been proposed, including super-symmetric partners of Standard Model particles, sterile neutrinos, and axions. Current experiments such as the Large Hadron Collider may confirm or disprove some of these candidates in the near future. Alternatives to particle formulations of dark matter, chiefly Modified Newtonian Dynamics (MOND), have been proposed (Milgrom, 1983), but have so far failed to gain traction in the astrophysics community. MOND type theories are often formulated to explain one particular aspect of structure formation, but so far no theory has been able to match observations on all scales. **Once again, the composition of dark matter is not as important for astrophysics as its dynamic properties.**

While the ΛCDM model has been successful at explaining structure in the universe at large scales, discrepancies remain on the scale of dwarf galaxies. These discrepancies are not directly relevant for the systems considered in this work, but any complications to the cold dark matter hypothesis are worth noting. Hot dark matter models (e.g. Zel'dovich, 1970; Doroshkevich et al., 1980), in which constituent particles do move relativistically, are ruled out as they would result in structure formation occurring at late times and starting at the largest physical scales ('top down structure formation'), which is not consistent with observations. 'Warm dark matter' models, where the thermal energy of the particles is small but non-negligible, have been proposed (e.g. Bode et al., 2001; Abazajian et al., 2001), but strong constraints have been placed on the contribution of WDM to structure formation (e.g. Viel et al., 2013), at least on the scales of large galaxies and galaxy clusters. Self-interacting dark matter models, in which dark matter particles experience binary interactions with each other, have been proposed (e.g. Spergel & Steinhardt, 2000), but observations place limits on such interactions that are similar to the non-interacting case. Finally, it is possible that dark matter particles could decay, possibly emitting electromagnetic radiation. Searches for this are ongoing but have turned up no conclusive results (Jeltema & Profumo, 2016; Storm et al., 2013). Even if dark matter does differ from the ΛCDM model, observations place limits on how large the deviation in dynamic behavior can be. **Thus, any departure from the CDM model would not be expected to have a large effect on the conclusions of this work.**

1.1.2 Cosmological Structure Formation

Galaxy clusters are important as probes of both astrophysics and cosmology. The latter comes from the fact that galaxy clusters are the largest gravitationally bound structures to form in the ΛCDM universe, and their mass distribution contains important information about the contents and history of the universe. To use clusters in this manner, it is necessary to understand how structures like galaxy clusters formed from the homogeneous early conditions of the post Big Bang universe. The study of structure formation is also necessary to understand the history of baryons in galaxy clusters, giving a context for the use of clusters as tests of astrophysical processes.

The early universe ($z > 1100$) consisted of a nearly homogeneous mixture of dark matter, baryons, leptons, and photons. Inhomogeneities, possibly relics of quantum fluctuations from before the inflationary epoch, took the form of a nearly Gaussian random field (Planck Collaboration et al., 2014b) with very small deviations from smoothness. Although the universe was expanding, overdense regions would have expanded slightly more slowly than underdense regions. As the dominant component of the mass-energy density at that epoch, dark matter would have dominated the gravitational interactions. Baryons and leptons were pulled into the dark matter potential wells and photons, trapped in the opaque pre-recombination plasma, followed. Radiation pressure provided a restoring force as overdensities collapse, leading to oscillation of the matter overdensities. At a redshift of $z \sim 1100$ (Planck Collaboration et al., 2015a), the temperature of the universe decreased to the point that electrons and atomic nuclei could combine, letting photons stream freely out of overdensities. This radiation, today redshifted into the microwave part of the spectrum, is observed as the cosmic microwave background (CMB) (Smoot et al., 1990; Bennett et al., 2003; Planck Collaboration et al., 2015a; Ruhl et al., 2004, and related publications). Following the release of photons, overdensities proceeded to collapse uninhibited. Overdensities that had completed an integer or half integer number of oscillations at the time of recombination formed, respectively, the peaks and troughs in the cosmic density distribution. These peaks and troughs were imprinted on the CMB and form one of the most powerful probes of cosmology known to astronomers. At the time of recombination, the RMS density fluctuations in the universe were only 10^{-5} (Smoot et al., 1992), but without the restoring pressure of the trapped photons overdense regions would collapse into the diversity of cosmological structure observed today.

Overdensities in the early universe were not perfectly spherical, causing collapse to proceed at different rates along different axes. The ΛCDM model predicts that overdensities would have first collapsed into sheets. The intersection of these sheets became the sites of filaments of galaxies, and the intersection of filaments became the sites of galactic superclusters. On a large scale, the universe became structured as a cosmic web, with overdense sheets and filaments surrounding large, under-dense voids. The cosmic web has been seen in observations (Gott et al., 2005), lending further credence to the ΛCDM picture.

Overdense regions of the universe collapsed hierarchically, with the smallest regions collapsing first and later coalescing into larger structures. Baryons followed the dark matter and settled into the cores of gravitationally bound halos. Once the density of the baryons had increased and radiative cooling became efficient, the first stars began to form around $z = 20$. Since primordial gas is a poor coolant (Galli & Palla, 1998), the first star forming clouds were not as susceptible to fragmentation as are star forming regions in the present universe (Meece et al., 2014; Abel et al., 2002; O'Shea & Norman, 2007; Turk et al., 2012, and Appendix D). Thus, it is expected that the first stars were massive and short-lived. Nevertheless, these stars transformed the baryonic universe by reionizing the interstellar gas (Wise et al., 2014; Xu et al., 2014) and producing the first heavy elements Heger & Woosley (2010).

The first stars are thought to have ended their lives in massive explosions (Whalen et al., 2013; Ohkubo et al., 2009) that would have expelled gas from their host halo (Smith et al., 2015). Hierarchical collapse, however, would eventually create halos massive enough to host ongoing star formation. Galaxies have been observed out to a redshift of $z = 11.1$ (Oesch et al., 2016). More galaxies formed in the densest regions, growing the first proto-clusters (Kravtsov & Borgani, 2012). These protoclusters continued to accrete gas and galaxies along cosmic filaments, merged with other protoclusters, and formed the massive galaxy clusters that we observe today.

1.2 Galaxy Clusters

What are galaxy clusters? As the name would imply, a galaxy cluster is a region in which several galaxies are found in close proximity to one another relative to the mean distribution of galaxies in the universe. A galaxy cluster is more properly defined as a large, virialized (dynamically relaxed), gravitationally bound structure containing a mix of baryonic matter [1]and dark matter. In fact, the galaxies that dominate the optical emission from the cluster encompass only a small percentage of the cluster's total mass. Dark matter accounts for the bulk of the gravitational mass in a cluster while most of the baryonic component resides in a diffuse plasma of hot gas spread throughout the cluster. This plasma is called the intracluster medium, or ICM.

While the definition of a galaxy cluster as 'large' is somewhat imprecise, there are various constraints and metrics that may be used to label collections of galaxies as clusters. An upper mass limit is provided by the ΛCDM hierarchical collapse model of structure formation in the universe. In ΛCDM the largest gravitationally bound structures were formed the most recently. Therefore, since galaxy clusters are the largest gravitationally bound objects in the universe, the upper mass limit is set by the rate of structure formation. Analytical models such as the work of Press & Schechter (1974) provide a rough estimate of the cluster mass function, with an upper mass limit that is strongly dependent on the choice of cosmology. Simulations such as the Millennium Run (Springel et al., 2005b) and observations such as those of 'El Gordo'- the most massive galaxy cluster known (Menanteau et al., 2012)- are consistent with analytical results and independent cosmological probes.

While galaxy clusters are the largest gravitationally bound structures in the universe, this does not mean that they are the largest structures that exist. The ΛCDM model predicts that matter in the universe is organized into a web of over-dense filaments and walls surrounding under-dense voids. Additionally, galaxy clusters are not scattered randomly about the sky but instead are found in proximity to each other in over-dense regions known as superclusters, which form where filaments intersect. **Superclusters have not fully collapsed and virialized and in many cases are not gravitationally bound, instead continuing to partake in cosmic expansion.** The formation of the cosmic web has been well studied with simulations such as the Millennium run (Springel et al., 2005b).

Galaxy clusters are often characterized by richness, defined as the number of galaxies above a given magnitude within a given distance of a bright central galaxy. The standard for galaxy cluster classification

[1]Technically, the term 'baryonic matter' only refers to matter composed of baryons, e.g. protons and neutrons. Baryonic matter thus does not include free electrons or neutrinos. Although these species are present in clusters, they do not contribute significantly to the mass. Thus, the term baryonic matter can be reasonably understood in this work to include all 'normal matter'- that is, everything other than dark matter- unless otherwise specified.

is the Abell catalogue (Abell, 1958; Abell et al., 1989), which defined richness classes for clusters containing at least 30 bright members. In practice, clusters with less than 50 members are known as 'galaxy groups'. Indeed, most galaxies (including our own) are found in groups, but few galaxies are found in rich clusters. If gravitation is the only force shaping the properties of galaxy clusters, galaxy groups should act like scaled down versions of clusters. When non-gravitational effects such as radiative cooling and feedback are included, however, differences will emerge between clusters of different masses. Thus, differences in the behavior of galaxy groups and clusters is an active area of research.

When defining a galaxy cluster, it is important to remember that the optical light traces only the stars in galaxies, which make up only a small percentage of a cluster's mass. In order to know what a galaxy cluster is and to understand which physical processes are important to their behavior, it is necessary to have a description of the different components of a cluster and of how those components are distributed.

Galaxy clusters are gravitationally bound, over-dense regions of the universe and are composed of roughly 85% dark matter and 15% baryonic matter. The composition of galaxy clusters is relatively well known– in fact, clusters are the only structures in the universe where we can observe all of the components. The dark matter distribution can be studied through the motion of cluster galaxies or through gravitational lensing of background galaxies. The baryonic component is divided between stars and gas. The stellar component is easily studied through optical light, while the gas phase is studied through X-ray emission or through the Sunyaev-Zel'Dovich effect.

1.2.1 Dark Matter in Clusters

In the ΛCDM model of cosmology, the bulk of the matter in clusters is composed of some type of particle that only allows weak and gravitational interactions. Due to the lack of strong interactions, dark matter particles do not interact with each other, and due to the lack of electromagnetic interactions, do not emit radiation (hence the term 'dark matter') or interact closely with baryonic matter. Dark matter particles are assumed to be 'cold', meaning that they are created with negligible thermal energy. From a cosmological perspective, the coldness of dark matter and the properties of the allowed interactions will have a large effect on structure formation. For the work presented in this dissertation, however, it is adequate to assume that the ΛCDM picture is correct, and that the exact nature of dark matter particles is not important. In fact, for most astrophysical applications it is sufficient to treat dark matter as a continuous medium and ignore the particle nature entirely.

Of greater interest for cluster studies is the form of the dark matter density profile. The dynamics of dark matter in halos are dominated by gravity, which is scale free. Thus, dark matter halos of different masses would be expected to have similar forms. As a self-gravitating medium, the dark matter density will peak near the center of the cluster. Due to the collisionless nature of the particles, it would not be expected to form complex structures. Simulations show that the functional form of dark matter profiles is similar for a wide range of gravitationally dominated systems. The most commonly used form is the Navarro-Frenk-White (NFW) profile (Navarro et al., 1997) given by

$$\rho(r) = \frac{\rho_0}{\frac{r}{R_S}\left(1 + \frac{r}{R_S}\right)^2} \tag{1.1}$$

where ρ_0 is equal to 4 times the density at the scale radius R_S. A second commonly used form for the dark matter profile is the Einasto profile, first described by J. Einasto at a conference (Einasto, 1965) and later found to be a better fit for dark matter haloes (e.g. Navarro et al., 2004, 2010). The Einasto profile is given by

$$\rho(r) = \rho_0 \exp\left[\frac{2}{\alpha}\left(1 - (r/R_S)^{\alpha}\right)\right] \tag{1.2}$$

where ρ_0 is the density at the scale radius and α is generally between 0.2 and 0.3 (Kravtsov & Borgani, 2012, and references therein) for clusters, with some power law dependence on redshift (Gao et al., 2008).

Measurements of velocity dispersions in clusters provided some of the first evidence for the existence of dark matter. In particular, Fritz Zwicky (Zwicky, 1933) realized that in order for the Coma cluster of galaxies to satisfy the Virial theorem, most of the cluster's mass would need to consist of non-luminous matter. According to the baryon census conducted by Gonzalez et al. (2013), dark matter is estimated to make up either 86.4 % (assuming WMAP cosmology) or 85.6 % (assuming Planck cosmology) of the total matter in a cluster within R_{500}, which is close to the universal value of 83.4% (WMAP) or 84.5% (Planck). As discussed in Gonzalez et al. (2013), the partitioning between gas and dark matter is found to be only weakly dependent on cluster mass, with the baryon fraction rising slightly with increasing cluster mass.

1.2.2 Baryons in Clusters

The remainder of a galaxy cluster's mass is composed of baryonic matter either in the form of stars or gas. Baryons emit energy through electromagnetic interactions, making them suitable for observation from Earth. Thus, **it is primarily through observations of the baryonic mass that scientists are able to study galaxy cluster properties, even though baryons only compose a small fraction of the cluster mass.**

The baryonic matter in clusters is divided into a stellar component and a gaseous component. The stellar component is composed of stars within galaxies and a population of extra-galactic stars, termed the intracluster light. Uniquely among astrophysical structures, it is possible for modern observations to reveal all forms of baryonic matter within a cluster, resulting in the possibility of a complete baryon census.

Such a baryon census was conducted by Gonzalez et al. (2013) who concluded that the baryon fraction[2] in clusters is $f_{baryon} = 0.136 \pm 0.005$ using WMAP7 Cosmology or $f_{baryon} = 0.144 \pm 0.005$ using Planck cosmology. There was found to be a weak but statistically significant correlation between cluster mass and baryon fraction, with f_{baryon} rising slightly in more massive clusters. This represents an update to the group's earlier baryon census (Gonzalez et al., 2007), which found results consistent with a universal baryon fraction.

The partition of baryons between stars and gas does vary significantly with cluster mass. Gonzalez et al. (2013) finds a stellar mass fraction of between 1% and 4%, with more massive clusters having a lower stellar mass fraction. Correspondingly, the gas fraction rises from around 7% in clusters with a mass of 10^{14} $M_{\odot}$to around 15% in the most massive clusters. The decrease in the fraction of matter in stars reflects a reduction in the efficiency of star formation in more massive clusters. It is curious that galaxy clusters are so inefficient at turning gas into stars, and the reason is thought to involve stellar and AGN feedback. Thus, the stellar mass fraction can be used as a probe of feedback processes in galaxy clusters.

The gaseous portion of galaxy clusters (the intracluster medium, or ICM) is primarily composed of Hydrogen and Helium with a small fraction of heavy elements, which are termed 'metals'. **Various studies (e.g. Leccardi & Molendi, 2008; Matsushita, 2011) find an average metallicity of around** $Z/Z_{\odot} = 0.3$ **(around 1/3 of the solar metallicity).** However, the metallicity distribution in clusters is not generally flat. Gas in the centers of clusters is enriched to a higher level, up to $Z/Z_{\odot} = 0.45$ within R_{180} in Leccardi & Molendi (2008) or $Z/Z_{\odot} = 0.88$ within R_{180} in Matsushita (2011). The metallicity distribution is generally found to be sharply peaked in the center and to flatten off around the virial radius to a value of $Z/Z_{\odot} = 0.2$. This is in rough agreement with the results of hydrodynamics simulations in Fabjan et al. (2008), although the metallicity distribution in the simulations is higher near the centers of the clusters. It should be noted that Fabjan et al. (2008) studied relaxed clusters, which would be expected to have more sharply peaked central metallicity distributions due to a lack of turbulence and mixing from major mergers.

1.2.3 Observing Galaxy Clusters

Like most astrophysical objects, galaxy clusters emit light across the electromagnetic spectrum. Only a fraction of the total cluster mass can be directly observed, but the radiation that can be detected can say an enormous amount about the contents and dynamics of clusters. This section briefly discusses what features are observed in each wavelength.

[2]The mass of Baryons as a fraction of the total mass (Baryons and Dark matter).

1.2.3.1 Radio

Radio emission from galaxy clusters primarily traces synchrotron radiation from accelerating electrons. These can be produced by several mechanisms (Ferrari et al., 2008; Feretti et al., 2012; Zandanel et al., 2014), including mergers, AGN, turbulence, shocks, and stellar activity. In addition, atomic and molecular transitions can also emit radio waves. Processes observed in the radio include (but are not limited to)

- Radio relics from mergers (e.g., Ensslin et al., 1998; Skillman et al., 2013)
- Radio halos(e.g., Ferrari et al., 2008; Feretti et al., 2012; Zandanel et al., 2014)
- Radio loud AGN (e.g., Best et al., 2007; Sambruna et al., 1999; McNamara & Nulsen, 2007)
- 2.6 mm CO emission(e.g., Edge, 2001; Russell et al., 2016)

1.2.3.2 Microwave

The microwave sky is dominated by the cosmic microwave background (CMB; Smoot et al., 1990; Bennett et al., 2003; Planck Collaboration et al., 2015a; Ruhl et al., 2004, and related publications). In galaxy clusters, the CMB up-scatters (Inverse Compton Scattering) off of the hot ICM, producing a small upward shift in the observed frequency. This effect – the Sunyaev-Zeldovich (SZ) effect (Sunyaev & Zeldovich, 1970) – can be used to infer the masses of galaxy clusters (e.g., Carlstrom et al., 2011; Planck Collaboration et al., 2014a). As the SZ effect depends on the integrated pressure over the cluster, and since high redshift clusters were denser and hotter than clusters today, the SZ effect is essentially independent of redshift and allows mass estimates of distant clusters. Recently, CMB surveys have used the SZ effect to find massive clusters that have later been detected in the optical. The SZ effect can also be used to infer cluster properties via the kinetic SZ effect (e.g. Sievers et al., 2013).

1.2.3.3 Infrared, Optical, and UV

Most of the infrared light emitted by clusters comes from stars – specifically redder, low mass stars. Infrared light is a frequently used to determine the total stellar mass of a cluster and of cluster galaxies since low mass stars are long lived, meaning that their abundance traces integrated star formation history rather than recent. On the other hand, protostellar clouds surrounded by dust glow brightly in the IR, meaning IR can be used to infer ongoing star formation as well (O'Dea et al., 2008). The far-IR can also be used to trace cold gas (Werner et al., 2014).

Like IR emissions, optical light in clusters is emitted by stars. Observations in the optical are therefore important for measuring the stellar mass of clusters, studying stellar populations, and inferring the star formation history of the cluster (e.g., Fogarty et al., 2015; McDonald et al., 2015; Loubser et al., 2016). The amount of intracluster light (ICL) might say something about the merger history of cluster galaxies.

Optical emission can also be affected by gravitational lensing, which can give information about the mass distribution in the cluster (e.g. Postman et al., 2012). Lensing provides an independent constraint on cluster masses. Strong lensing occurs when light from a background source is bent by intervening matter, leading to the formation of rings, arcs, and multiple images (e.g., Broadhurst et al., 2005; Kelly et al., 2015). Weak lensing occurs when gravitational lensing distorts the shapes of background galaxies (e.g., Bartelmann & Schneider, 2001; von der Linden et al., 2014).

The UV light from galaxy clusters, like the UV light from most galaxies, is produced by young, massive stars. Therefore, UV observations can be used to determine the star formation rate of cluster galaxies (e.g. O'Dea et al., 2010).

1.2.3.4 X-ray

X-rays are possibly the most important part of the spectrum for studying the ICM in galaxy clusters. Hot gas in the ICM emits X-rays via Bremmstrahlung, which occurs when charged particles are accelerated through binary interactions (e.g., Cavaliere & Fusco-Femiano, 1976; Sarazin, 1988). This radiation can be used to infer the temperature and density of the gas and, assuming hydrostatic equilibrium (HSE), to derive a mass profile (e.g., Donahue et al., 2014). This mass estimate depends on established scaling relations. The major observatories for studying galaxy clusters in the X-ray are the Chandra X-ray Observatory (Weisskopf et al., 2000) and the XMM-Newton Observatory (Jansen et al., 2001). X-rays can also be used to infer the metallicity distribution (e.g., Mitchell et al., 1976; Matsushita, 2011).

1.2.3.5 Gamma Rays

Galaxy clusters have not been definitively detected in Gamma rays (Ackermann et al., 2014). In theory, some classes of dark matter candidates could produce X-rays through self-annihilation, but this has not been conclusively observed (Jeltema & Profumo, 2016).

1.2.4 Magnetic Fields in Galaxy Clusters

Galaxy clusters are known to contain weak, tangled magnetic fields which extend throughout the cluster (see Carilli & Taylor, 2002, for a review). These fields are typically on the order of a few microGauss (μG), although they may be somewhat stronger in the core region, especially in cooling flow clusters. The fields are too weak to be dynamically important, but are likely to play a role in energy transport through anisotropic conduction. In addition, the Larmor radius of a thermal electron in a cluster magnetic field is significantly shorter than the collisional mean free path, meaning that the dynamics of electrons on large scales will be dominated by effects from the magnetic field. Thus, magnetic fields would be expected to suppress thermal conduction in a tangled magnetic medium, though the extent to which this happens in clusters is debated (Smith et al., 2013; Ruszkowski & Oh, 2011; Wagh et al., 2014). Additionally, the dynamic effects of magnetic fields might be expected to increase the viscosity of the gas, though whether this is appreciable in clusters is unknown. For a general overview of magnetic fields in clusters with additional references, see McNamara & Nulsen (2007).

1.2.4.1 Observation of Magnetic Fields in Clusters

Magnetic fields in clusters can be observed and studied with several methods. The observational probes discussed include synchrotron radiation, polarized radio emission, Faraday rotation of background sources, and inverse Compton scattering. All of these methods are described in more detail in Carilli & Taylor (2002).

If clusters do have magnetic fields and are roughly in equilibrium, there should be some equipartition between the energy in magnetic fields and the kinetic energies of particles. The amount of synchrotron radiation is an indicator of the particle energy, and from this we can infer the magnetic field strength. This method gives values on the order of a few μG, with cool-core clusters having higher fields than non-cool-core clusters.

Synchrotron radiation from galaxies should be polarized, since the magnetic field creates a preferred direction for electrons to move. While some degree of polarization is caused by our own galaxy, radio emission from clusters appears to be more polarized. This is a second indicator that clusters have magnetic fields.

Thirdly, a magnetic field in a cluster would cause Faraday rotation of emission from sources behind the cluster. This is one of the most important probes of field strength, and again gives estimates on the order of a few μG. The simplest estimates of the magnetic fields from polarization assume that the field is uniform, but this is unlikely to be the case. A more detailed method is to assume that the field is tangled and to approximate it as being composed of cells of some characteristic length l, each with a random orientation. Polarization measurements indicate that this length scale is on the order of 5-10 kpc. The polarization that is observed is taken to be the product of a random walk through the cells that compose the field.

Finally, cluster magnetic fields can be measured by deriving a relation between the synchrotron radiation luminosity and Compton up-scattering. In theory both are caused by the same population of relativistic electrons. Compton up-scattering is caused by scattering of background photons, and thus measures the photon field energy, while synchrotron is caused by scattering off of virtual photons, and measures the magnetic field energy. Thus, the ratio of synchrotron to Compton up-scattering scales like the ratio of photon energy to magnetic energy.

By itself, this method gives estimates on the order of 0.1 μG for most clusters, an order of magnitude lower than from other methods. However, some additional factors have been identified that can bring these numbers into agreement with other estimates. For example, collisions would keep the pitch angle of electrons isotropic even though classical theory says they would not remain that way for long. Secondly, the synchrotron radiation measurement assumes an energy spectrum for the electrons that might in fact be steeper. For the inverse Compton case, it is possible that some of the X-rays could come from thermal Bremmstrahlung, although it is hard to make this work energetically without evaporating the cluster. Finally, substructure in the magnetic field could lead to errors. If the characteristic length scale of the region where electrons are relativistic is larger than the scale of the magnetic fields, the X-rays could be coming from further out, where the field is weaker, while the polarization is coming from the strong field in the core, leading to an inaccurate comparison.

1.2.4.2 The Origin of Magnetic Fields in Clusters

Several theories have been proposed to explain where the magnetic fields in galaxy clusters come from and how they are amplified to their current strength. In theory, if a small magnetic field existed in the IGM after recombination, it would have been amplified by gas compression during structure formation. Early stars could have also generated magnetic fields and expelled them in outflows. Finally, AGN generate magnetized jets and could in principle deposit some of their energy in the magnetic field of the cluster.

However they are generated, magnetic fields can be amplified by compression of the field lines, either through compression of the ICM or by turbulence through a dynamo effect. It is likely that both of these factors play a role in generating the field amplitudes that are observed. Cool-core clusters have fields that are higher than non-cool-core clusters, which is expected from the higher density of gas in the core. Mergers and shocks could generate turbulence, amplifying the field further.

AGN feedback has been suggested as a method for amplifying magnetic fields in cool core clusters, and there is evidence (Dubois et al., 2009) that this could in fact be happening. It is not obvious what effect AGN would have on existing magnetic fields – they could either strengthen (through turbulence) or weaken them (by reducing the gas density.) Dubois et al. (2009) finds that magnetic fields in idealized clusters are enhanced either with or without AGN feedback, but for different reasons. Without feedback, a cooling catastrophe occurs that compresses the gas, strengthening the field. With feedback, the cooling catastrophe is prevented but the gas becomes more turbulent. It is worth noting that even if conduction is important, it would not amplify the magnetic field, leaving the observations unexplained.

1.3 Active Galactic Nuclei and Supermassive Black Holes

Many galaxies are seen to have bright emission regions in their cores. Based on the inferred energies needed to power this emission, active galactic nuclei (AGN) are among the most powerful phenomena in the universe. In recent decades, a consensus has emerged that AGN are composed of an accretion disk surrounding a supermassive black hole (SMBH). Magnetic fields become twisted in the differentially rotating accretion disk, funnelling charged particles into powerful jets. These jets, along with winds from the hot accretion disk itself, are in principle energetic enough to balance radiative cooling losses and cause a large scale redistribution of gas in galaxies. Observed scaling relations between SMBH mass and galactic properties have strengthened the idea that SMBHs and AGN play a critical role in galaxy evolution. In particular, **it has been argued that AGN in brightest cluster galaxies (BCGs) are responsible for balancing cooling losses and halting a cooling catastrophe in cool-core galaxy clusters.** This section gives a short introduction to AGN and how they can couple to their environments.

1.3.1 A Short History of AGN

Though AGN have been observed in one way or another for over a century, the nature of these objects has only become clear in recent decades, and there are still many mysteries left to unravel. This section contains a short history of observations of AGN activity.

AGN were first observed serendipitously and at first were not recognized as extragalactic objects. AGN were first noticed in spectral emission by Fath (1909), who described strong emission lines in the nucleus of NGC 1068. Curtis (1918) describes the first optical detection of an AGN – a curious bright feature in the nucleus of M87 with extended emission. Seyfert (1943) made a survey of spiral nebulae with bright nuclear emission and found great variability in their spectral features, with combinations of broad and narrow emission lines. The broad lines, when interpreted as stemming from a Doppler shift, implied gas moving at 1000s of km/s – much higher than galactic escape velocity. Additionally, the rapid variability implied that the emitting region was very small.

Radio surveys in the 1950s and early 1960s (Edge et al., 1959; Bennett, 1962) identified a population of point source radio emissions with no bright optical counterpart. The first of these objects to be matched with an optical source was 3C 273, which appeared as a faint star with a small jet. Optical spectra of 3C 273 (Schmidt, 1963) were consistent with a source at a redshift of 1.58, implying a very bright, very distant object emitting from a small region. Schmidt (1963) hypothesized that the emission could be coming from the nucleus of a distant galaxy.

Spectral observations of AGN revealed point sources that looked like stars (hence the term 'quasar', short for quasi-stellar object) but with large redshifts and luminosities far above typical stellar values. For example, Baade & Minkowski (1954) found optical and radio luminosities of over 10^{42} erg/s for the AGN in Cygnus A – over 10 billion times higher than the solar luminosity. Although the authors erroneously attributed the emission to a pair of merging galaxies, further observations by Schmidt (1963) would show that the AGN emission region must be smaller than 1 kpc – too small to be a galaxy. The observations also showed that jets near the object were on the order of 50 kpc in length, implying that the source had been active for at least 100,000 years and had emitted at least 10^{59} ergs in that time.

At the time of their discovery, there was no physical process known that could explain the high power and small size of AGN. Salpeter (1964) and Zel'dovich & Novikov (1965) independently hypothesized that accretion onto a super-massive black hole could in theory generate the required amounts of energy, presuming that angular momentum could be transported outwards allowing material to fall in. The SMBH powered AGN hypothesis was fleshed out by Lynden-Bell (1969), who also argued that many galaxies should contain quiescent AGN that could in principle be observed. Although the SMBH at the centers of AGN were not (and still have not been) directly observed, the SMBH paradigm continued to gain traction as details were clarified and alternative explanations ruled out.

1.3.2 The Unified model of AGN

Despite the plausibility of the SMBH argument for explaining AGN observations, it was not clear that all AGN behaved the same way or indeed were powered by the same physical process. From the beginning, it was noticed that AGN exhibited a diversity of spectral features. Many AGN exhibited narrow line emission spectra, but some also showed broad emission lines. Further, some AGN were bright radio sources – often among the brightest in the sky – while others were radio quiet. A small percentage of AGN seemed to show a continuous spectra with no emission or absorption lines and apparently exhibited superluminal motion in their jets. These observations led to AGN being grouped into several empirically defined categories (see Lawrence, 1987, for a review). Despite the diversity of AGN observations, it was suspected that many of these differences could be explained in terms of the orientation of the AGN system and its recent activity.

In unification models (see Urry & Padovani (1995) for a review), **all AGN consist of a disk of accreting material surrounding a supermassive black hole.** When clouds of material come near the SMBH, they will settle into rotation within a torus. Closer in, the torus flattens into a differentially rotating accretion disk. The accreting material generally has some (weak) magnetic field, the field lines of which tend to be dragged along with the flow. Through a combination of friction in the disk and electromagnetic effects, angular momentum is transfered outwards and gas can flow towards the SMBH. Differential rotation causes the disk to heat up, causing it to emit UV and X-ray light as well as blasting off a hot wind. Within a radius[3] of

$$R_{ISCO} = 6\frac{GM_{SMBH}}{c^2} \tag{1.3}$$

general relativity predicts that no stable circular orbit exists — hence Equation 1.3 is the radius of the innermost stable circular orbit (ISCO). R_{ISCO} therefore forms the inner boundary of the accretion disk, within which material falls into the SMBH.

During the accretion process, the gravitational energy of the accreting material can be released in several ways. As mentioned above, differential rotation heats the accretion disk, driving a wind and causing the hot material to emit like a black body. Secondly, differential rotation will cause magnetic field lines to become stretched and twisted. This process, analogous to twisting and stretching rubber bands, stores magnetic energy and channels charged particles into the observed relativistic jets. It is estimated that during the in-spiral period, a particle being accreted onto an SMBH can radiate away up to 10% of its rest mass energy – even more efficient than H-He fusion, which only releases 0.7% of the rest mass energy.

Aside from these classical processes, **general relativity predicts that energy can be extracted from the SMBH itself**, further boosting the energy of the relativistic jets. Energy can not be extracted from within the event horizon of a black hole, but the Kerr Metric (Kerr, 1963) predicts[4] that a rotating black hole will drag space-time in a region outside the event horizon. Energy can in principle be extracted from this region, termed the 'Ergosphere', allowing for energy to be extracted from the spin of the SMBH. In the Blandford-Znajec process (Blandford & Znajek, 1977), magnetic field lines pass through the Ergosphere, where they are rotated and twisted, transferring energy outwards at the expense of the SMBH's angular momentum. In the Penrose process (Penrose & Floyd, 1971), a clump of matter falls into the ergosphere and splits in two, with one part falling into the SMBH and the other being ejected with more energy than the original clump. The jet production process is still not fully understood (see Tchekhovskoy et al., 2011; Sądowski & Narayan, 2015; McKinney et al., 2012, for some recent work), but it is clear that SMBH-disk interactions are easily capable of producing the enormous luminosities observed from AGN.

With this model of an AGN in mind, the diversity of observations becomes clearer. The rapidly rotating inner accretion disk will produce broad line emission, while the slower outer torus will have narrower emission lines. Thus, Type 1 AGN, which exhibit broad line emission features, can be understood as AGN where we

[3]For a non-rotating black hole – the leading factor decreases from 6 to 1 for a maximally rotating black hole

[4]As a historical aside, the discovery that a rotating SMBH could power an AGN was one of the first known problems in which general relativity predicted a significant and observable deviation from the classical expectation.

have a view of the inner accretion disk since they are oriented nearly face-on to us. Type 2 AGN, with only narrow line features, are viewed at a larger angle (more edge-on) such that the torus blocks our view of the inner region, so that only narrow lines are seen. BL Lac objects (named for their prototype[5]), which show neither absorption nor emission lines, are seen nearly along the axis of the jet. Differences in radio emission can be differences in the spin of the black hole (Wilson & Colbert, 1995), which would affect the properties of the relativistic jets, in turn affecting the amount of hot, synchrotron emitting plasma produced by the AGN.

1.3.3 Interactions Between AGN and their Environment

On the surface, it would seem unlikely that SMBHs would have a noticeable effect on their surrounding galaxies. The physical size of a black hole is very small (on the order of AU for the event horizon radius) compared to the size of galaxies (tens of kpc) or galaxy clusters (of order Mpc). The mass of a SMBH is also very small compared to typical masses for galaxies and clusters, with galaxies generally outweighing their central SMBH by factors of 10^3 or more. Although the gravitational acceleration produced by an SMBH is large, the magnitude falls off as r^{-2} and should not dominate dynamics beyond a few tens of pc. As outlined in the previous section, however, AGN are capable of releasing enough energy to significantly affect the thermal structure of the gas or to drive significant gas motion (Voit et al., 2015c,a). Therefore, it is correct to think that **through AGN, SMBHs should have a strong influence on their environment.**

Near the SMBH, the energy released from the AGN acts on the accreting material as a type of negative feedback. When the accretion rate increases, so does the power released by the AGN, which will generate radiation pressure and limit further increases in the accretion rate. It is common to measure AGN luminosity in terms of the Eddington luminosity (Eddington, 1916)

$$L_{EDD} = \frac{4\pi G M_{BH} m_p c}{\sigma_T} \tag{1.4}$$

which is the luminosity at which radiation pressure balances gravity. While this would in principle give an upper limit to the black hole accretion rate, the Eddington luminosity calculation assumes spherical accretion, which is almost certainly invalid. Still, while super-Eddington accretion may occur, the Eddington luminosity provides a good reference for the realm where negative feedback begins to stifle accretion, and it is difficult to imagine an AGN exceeding the Eddington luminosity by more than an order of magnitude.

On larger scales, **the masses of SMBHs correlate with various galactic properties**, including galactic luminosity (Magorrian et al., 1998), the central stellar velocity dispersion (the $M - \sigma$ relation;

[5]Ironically, BL Lac is has been observed to have weak emission lines, and thus is not a BL Lac object

Merritt, 2000; Ferrarese & Merritt, 2000; Gebhardt et al., 2000), and the galactic virial mass (Ferrarese et al., 2006). That these quantities are correlated implies some connection between the growth of the SMBH and the host galaxy. This connection could manifest in a number of ways: either the SMBH growth regulates the formation of stars through AGN feedback, star formation drives the growth of AGN through winds and stellar mass loss, or accretion onto the galaxy fuels both star formation and SMBH growth at proportional rates. Although the true causes of the relations have not been firmly established, several theories have been proposed. One widely accepted theory, that of King (2003), holds that outflows from AGN push gas out of the host galaxy, limiting the rate at which stars can form.

AGN feedback is most apparent in observations of massive galaxies and galaxy clusters. In cool-core galaxy clusters, the role of AGN in preventing a cooling catastrophe has been well established through the lack of observed cold gas (e.g., Peterson et al., 2003; Peterson & Fabian, 2006), the availability of energy generated by the AGN to balance cooling, and the lack of viable alternative explanations (Skory et al., 2013). Studying the cooling flow problem forms the basis for this dissertation, and it is summarized in Section 1.4 A more detailed journey through the literature on the cooling flow problem is presented in Chapter 2. In addition to the cooling-flow problem, evidence for AGN feedback at cluster scales is seen in ICM shocks (Fabian et al., 2003), X-ray bubbles (Fanaroff & Riley, 1974), and jet-driven redistribution of metals (Kirkpatrick & McNamara, 2015). For a thorough review of the observational evidence relating to AGN feedback, see Fabian (2012).

1.3.4 The Origin of Supermassive Black Holes

Finally, with the mechanics of AGN feedback in hand, there remains the question of where, when, and how the SMBHs that power AGN form. This remains an active topic of research (see Volonteri (2010) for a review), and no SMBH creation theory has gained the full acceptance of the astrophysics community. It is clear that essentially all nearby large galaxies contain central SMBHs (Ferrarese & Ford, 2005), indicating that their formation is reasonably common. Observations (Momjian et al., 2014; Willott et al., 2015) show that powerful AGN were in place in some galaxies by a redshift of $z = 6 - 7$, indicating that massive SMBHs had already formed at that time. Willott et al. (2003) finds evidence for a 3×10^8 $M_\odot$ SMBH powering a quasar at $z = 6.41$ – less than 1 Gyr after the Big Bang. For such an SMBH to exist, it must have formed early in the universe and grown at the Eddington rate or faster for its entire lifetime.

Several theories have been posited to explain the formation of SMBH seeds. In the single stellar progenitor model, massive Pop III stars ($M > 260$ $M_\odot$) collapsed into the seeds of SMBHs. Proponents of this theory argue that the initial mass function (IMF) of the first stars was likely top heavy, leading to higher mass stars (e.g. Bromm et al., 2002), but large uncertainties in the Pop III IMF still exist (e.g. Glover & Abel, 2008; Turk et al., 2009), and the low mass of Pop III remnants (~ 100 $M_\odot$) would have difficulty growing to larger masses unless they formed very early and were not ejected from their host galaxies (Tanaka & Haiman, 2009).

A second theory (Begelman & Rees, 1978; Gürkan et al., 2006) is that SMBH seeds form through mergers of multiple stellar remnants. The theory holds that a primordial proto-stellar cloud can reach high densities before fragmenting, resulting in several massive stars forming close together. The remnants of these stars then merge hierarchically, creating a SMBH seed of mass $10^3 - 10^4$ $M_\odot$. These seeds are more massive than those in the single stellar progenitor model, and thus would have an easier time growing to high masses. Once again, however, the mass function of the first stars is not well understood enough to predict whether this scenario can explain all SMBHs.

Thirdly, it has been posited (e.g, Begelman et al., 2006; Bromm & Loeb, 2003) that SMBH seeds could form through a 'direct collapse' scenario, in which a primordial cloud with mass $10^4 - 10^5$ $M_\odot$ collapses directly into an SMBH without forming stars. The difficulty in this scenario is that ordinarily such a cloud would form H_2, which would be able to cool the gas, making it unstable to Jeans fragmentation. If some mechanism existed to prevent the formation of H_2, however, a cloud might be stable enough against fragmentation to collapse into a single massive object. Possible suppression mechanisms include a halo with virial temperature $> 10^4$ K or a strong UV background capable of disassociating H_2 (Dijkstra et al., 2008). Alternately, it has been proposed (Shlosman et al., 1989; Begelman et al., 2006) that gravitational instabilities within low angular momentum gas could concentrate enough material in one place to make the direct collapse scenario plausible.

Finally, the seeds of SMBHs could have been primordial black holes produced by a variety of processes in the early universe (reviewed in Carr, 2003). Such primordial black holes could have masses of up to 10^5 $M_\odot$(Khlopov et al., 2005), but there is still much uncertainty in how (or if) such black holes formed and what their initial masses would have been. A large population of primordial black holes would have observable consequence, causing gravitational lensing or disrupting stellar orbits, thereby helping to constrain the contribution of primordial black holes to SMBH formation.

1.4 The Cooling Flow Problem and Precipitation Regulated AGN Feedback

Since the dawn of X-ray observations (e.g. Felten et al., 1966; Bridle & Feldman, 1972), it has been apparent that galaxy clusters are emitting copious amounts of X-rays. For the majority of clusters, this radiation should be sufficient to cool the cluster core on a timescale much shorter than the age of the cluster (e.g. Lea et al., 1973; Mitchell et al., 1976; Edge et al., 1992). In theory, this should lead to hundreds of solar masses of gas cooling per year (Fabian, 1994), which would be expected to accumulate in the core, possibly forming stars, and leading to a slow flow of gas towards the center of the cluster. Instead, galaxy clusters show little evidence of cold gas (Peterson & Fabian, 2006) and have low rates of star formation (O'Dea et al., 2010). It would therefore appear that the gas is radiating strongly but not cooling. This is the crux of the cooling flow problem.

If the gas is not cooling, some additional heat source must exist that is able to maintain the thermal equilibrium of the gas over long periods of time. Several mechanisms have been proposed, but only AGN feedback seems energetic enough to counter cooling losses. AGN feedback is in principle powerful enough to balance cooling (see McNamara & Nulsen, 2007, 2012, for a review) but how the feedback and the cooling couple are not well understood.

Recently, evidence has grown for a 'precipitation-regulated' model of AGN feedback in galaxy clusters (Voit et al., 2015b). The ICM is subject to both heating and cooling processes and therefore may be thermally unstable (Field, 1965, and subsequent papers), meaning that cooler regions may cool faster than they are being heated, causing cold clouds to 'condense' out of the ICM. If these clouds are accreted by the SMBH in the BCG, a feedback loop may be established. Cold clumps will form as the ICM cools, triggering AGN feedback that will reheat the cluster, prohibiting further condensation. This cycle could in theory maintain thermal balance in the cluster core, assuming that the AGN feedback can couple to the ICM.

Simulations of galaxy clusters support this picture of precipitation-regulated feedback. Analysis of the thermal stability of the ICM (McCourt et al., 2012) indicate that condensation is expected to occur under certain conditions, producing the cold gas needed to power the AGN. Simulations of AGN feedback (Li & Bryan, 2014a,b; Li et al., 2015) show that AGN feedback triggered by cold gas accretion can prevent a cooling flow and produce simulated clusters with properties that agree with observations. This dissertation will further explore the susceptibility of the ICM to thermal instability and the coupling of AGN feedback to the ICM, with the aim of applying these results to the cooling flow problem.

1.5 Plan of This Dissertation

In this dissertation, I explore the physical processes that regulate the state of the ICM, with a particular focus on the role of precipitation-triggered AGN feedback. Chapter 2 provides a discussion of the literature related to AGN feedback in galaxy clusters and includes reviews of the cooling flow problem from an observational and theoretical standpoint, simulations of galaxy clusters, the precipitation triggering theory of feedback regulation, and simulations of AGN feedback. Chapter 3 presents original research on the development of thermal instability and the production of multiphase gas in galaxy clusters. Further original research on the topic of modeling AGN feedback in galaxy clusters is presented in chapter 4. Finally, Chapter 5 presents this work within the broader context of astrophysics, discusses unanswered questions in the field, and offers avenues for future research. The simulations in this work were performed using the `Enzo` hydrodynamics code, which is described in Appendix A. Appendicies B and C contain details about the implementation and setup of the simulations discussed in this work. Appendix D contains work on Pop III and low-metallicity star formation. This work was completed while I was a graduate student at Michigan State University, but which does not relate to the main focus of my dissertation work.

2 Literature Review

2.1 Introduction

This section presents an overview of the historical literature relating to the precipitation-regulated theory of AGN feedback in the ICM. This section will attempt to present results in a pedagogical fashion and focuses on historical works. More recent studies and my own research are discussed in subsequent chapters.

Section 2.2 presents evidence from early X-ray observations of galaxy clusters that indicates that the ICM in many clusters should be cooling rapidly. Such cooling should lead to an accumulation of cold gas and other observable consequences — however, high resolution X-ray data presented in Section 2.3 differ from the predictions of the cooling flow model. Theories that explain the observations by allowing for cooling gas to remain undetected are discussed in Section 2.3.1 but are ultimately unconvincing, indicating that some heat source must balance radiative cooling. Section 2.2 presents several proposed heating mechanisms. The most plausible candidate is AGN heating, but this can only explain the observations if the heating is 1.) strongly tied to the cooling rate of the ICM and 2.) distributed throughout the cluster core. The first condition can be satisfied with triggering by the accretion of cold gas produced via thermal instability, and the second through a variety of coupling mechanisms. Section 2.5 argues that thermal instability leading to a multiphase medium is plausible in the ICM, and Section 2.8 describes how AGN feedback can be dispersed. All of these processes can be wrapped into a full theory of precipitation-regulated AGN feedback, which is presented and advocated in Section 2.9.

2.2 The Cooling Flow Problem

As discussed in Section 1.2, galaxy clusters are filled with a hot (10^7-10^8 K, diffuse ($n_{\mathrm{e}} \sim 10^{-4}-10^{-2}$ cm $^{-3}$) plasma called the intracluster medium (ICM; Fabian, 1994). Roughly half of galaxy clusters are classified as 'cool-core' clusters, in which the ICM is generally spherical and undisturbed, the density distribution centrally peaked, and the temperature centrally decreasing. Theory suggests that although the ages of these clusters are large (several Gyr), the time for the ICM in their cores to radiate away its thermal energy is comparatively short (tens or hundreds of Myr). This should lead to an accumulation of cold gas in the core, fuelling star formation and resulting in peaked X-ray emission. Since this cooling should lead to an inward flow of gas, this phenomenon is known as a 'cooling flow'.

At temperatures above 10^7 K, the plasma is fully ionized, meaning that the dominant radiative emission mechanism is Bremsstrahlung, or free-free, emission. For a plasma with electron and ion number densities n_e and n_i and temperature T, the emissivity per unit volume is

$$
\begin{aligned}
Ł_{\rm ff} &= \left(\frac{2\pi \mathrm{k_B} T}{3m}\right) \frac{2^5 \pi e^6}{3 h m_e c^3} Z^2 n_e n_i \bar{g}_B &(2.1)\\
&= (1.4 \times 10^{-27} \mathrm{erg\,cm^3\,s^{-1}\,K^{-1/2}}) \mathrm{Z^2 n_e n_i \bar{g}_B} &(2.2)
\end{aligned}
$$

where m is the average particle mass, Z is the average nuclear number, and $\bar{g}_B$ is the Gaunt factor, which is of order unity and accounts for quantum effects.

The cooling timescale is defined as the time that it would take the plasma to radiate away its thermal energy at its current cooling rate, and is given by

$$t_{\rm cool} = \frac{3n\mathrm{k_B}T}{2L} \quad . \tag{2.3}$$

where L is the volumetric cooling rate. While obviously inexact (since the cooling rate is temperature dependent), the cooling time can be used to estimate the timescale over which cooling is important, or how long it would take for cooling to alter the temperature of the plasma by a significant amount.

Fabian (1994) summarizes the expected evolution of a cooling flow in a cool-core cluster with an idealized, spherical profile. The gas in such a cluster would be expected to be in hydrostatic equilibrium. One can define a cooling radius $R_{\rm cool}$ in which the cooling time is less than the age of the universe, or

$$t_{\rm cool}(R_{\rm cool}) < H_0^{-1} \tag{2.4}$$

where H_0 is the Hubble constant. Although the gas within this radius will be cooling, it must still support the weight of the gas outside of $R_{\rm cool}$, implying that the pressure must rise. If the gas is cooling, this means that the density must be increasing, which can only be achieved through a compressive flow of cooling gas towards the center. Even if adiabatic heating prevents the inflowing gas from decreasing in temperature at first, gas in the center of the flow will radiate away its energy and cool catastrophically.

Assuming that all of the radiated energy escapes the cluster (valid for the optically thin ICM plasma), the cluster luminosity is related to the mass cooling rate (the mass of gas cooling in a given time) by

$$L_{\rm cool} = \frac{5}{2} \frac{\dot{M}}{\mu m_\mu} \mathrm{k_B} T \tag{2.5}$$

where L_{cool} is the total luminosity and $\dot{M}$ is the mass cooling rate. The factor of $5/2$ is due to the thermal energy of the gas (3/2 k_BT) and the decrease in gas volume (k_BT). For typical cluster properties and luminosities (discussed in the next section), the value of $\dot{M}$ may be greater than 100 $M_\odot yr^{-1}$. This gas could either accumulate as cold clumps in the central region or fuel star formation. Whatever the fate of the gas, the cooling flow theory predicts that a large volume of cold mass should accumulate in the centers of cool-core clusters. Observations, however, do not find this to be the case.

2.3 Observational Evidence (or lack thereof) for Cooling Flows

The first X-ray observations (for example, the Geiger-counter-in-a-rocket observations of Byram et al., 1966) revealed strong extragalactic X-ray sources that were later identified (Cavaliere et al., 1971) as galaxy clusters with X-ray luminosities of $10^{43} - 10^{45} \mathrm{erg\,s^{-1}}$. More detailed observations by X-ray observational satellites like Uhuru (Giacconi et al., 1972, 1974; Forman et al., 1978) and HEAO-1 (Forman et al., 1978) found more X-ray clusters and provided further constraints on their luminosity. For a more detailed review of the history of X-ray observations of clusters, see the review by Sarazin (1988).

At first, the emission mechanism for cluster X-rays was not known, though several theories were proposed. Some (e.g., Katz, 1976; Fabian et al., 1976) favored models in which a large number of X-ray point sources produced the emission. Others (e.g., Brecher & Burbidge, 1972; Bridle & Feldman, 1972) proposed models wherein cosmic rays were responsible for the X-rays. Finally, it was theorized that the emission might be coming from Bremsstrahlung in a hot plasma (Felten et al., 1966; Lea et al., 1973). Bremsstrahlung emission became the most convincing explanation following the detection of 7 KeV X-rays from heavily ionized Fe (Mitchell et al., 1976). The Fe emission could only have been produced in a hot gas ($> 10^7$K), which set a lower limit on the ICM temperature and made the Bremsstahlung emission model more compelling.

Given the large X-ray luminosities observed, Equation 2.5 suggests mass cooling rates of several hundred Solar masses per year. Lea et al. (1973) and Fabian (1994) found that this is the case for many of the X-ray brightest clusters. Edge et al. (1992) found that between 70% and 90% of observed clusters had central cooling times $< H_0^{-1}$. Even if the cooling time threshold was reduced to $t_{\mathrm{cool}} < H_0^{-1}/2$, the majority of galaxy clusters were still observed to host cooling flows. That the fraction was so high implied that this strong cooling was probably not a recent or transient phenomena, but was instead a persistent and common feature.

The launch of new X-ray observatories like the Chandra X-ray Observatory (Weisskopf et al., 2000) and the XMM-Newton Observatory (Jansen et al., 2001) allowed for deeper spectroscopic investigation. Peterson et al. (2001) was the first study to use XMM-Newton for studying galaxy clusters (specifically Abell 1835), but found much less emission from gas at cold temperatures than was expected. At the very least this hinted that the cooling flow process was more complicated than originally thought, and offered the possibility that some unknown heat source was preventing the gas from cooling as theorized. Similar studies in the same year (Tamura et al., 2001a,b; Kaastra et al., 2001) found no evidence of gas colder than around 1/3 of the maximum temperature in the cores of X-ray bright clusters. Peterson et al. (2003), using a sample of 14 galaxy clusters observed with XMM-Newton, confirmed that cooling flow clusters do not seem to accumulate much cold gas. By the time of the Peterson & Fabian (2006) review, it was established that the predictions of the standard cooling flow model did not match observations.

2.3.1 Proposed Solutions to the Cooling Flow Problem

With the high resolution spectra, it became clear that the behavior of gas in cooling flow clusters was significantly different than originally thought. Several mechanisms were proposed to explain the lack of soft X-ray emission from gas at less than 1/3 of the maximum temperature. These mechanisms included 1.) absorption of soft X-rays by intervening material, 2.) non-radiative cooling of gas below the observed cutoff, 3.) reduction of the cold gas by star formation, and 4.) distributed heating that prevented gas from cooling completely.

Early models (Johnstone et al., 1992) attempted to explain the absence of soft X-rays via absorption by material in the cluster cores. If this were the case, however, the absorption should have been seen in other light sources from the centers of clusters. Observations of the jet in M87 and the Perseus cluster (Böhringer et al., 2002; Churazov et al., 2003) did not see much evidence for absorption of soft X-rays.

A second possibility for the lack of X-rays was that gas below the cutoff was cooling without radiating in X-rays. In this scenario, cooling gas was mixed with cold gas, which then radiated the energy away in the optical or UV. Alternatively, the cooling gas could have transferred its energy to the cold gas via conduction. Fabian et al. (2002) examined such a scenario and found it plausible, but it does not explain the ultimate fate of the cold gas and is still difficult to reconcile with the high resolution X-ray spectra.

A third possibility offered was that the cooling gas was turning into stars. This would be the expected fate of cold gas trapped in a potential well such as a cluster core. However, the cooling gas should still emit soft X-rays. More importantly, the star formation rate in clusters was estimated to be at least an order of magnitude below the mass cooling rate (Crawford et al., 1999; Donahue et al., 2000). Indeed, most BCGs host low rates of star formation, implying that the predicted cooling flow gas was not being turned into stars. Models including modified stellar initial mass functions (IMFs) were also proposed (Prestwich et al., 1997), but would have required no stars to form above 0.2 $M_\odot$, inconsistent with theory and observation (e.g. Salpeter, 1955).

2.3.2 Proposed Heating Sources

Finally, it was proposed that the reason for a lack of observations of gas cooling below 1/3 of the maximum temperature might be that some heating source existed that prevented the gas from cooling below that temperature. While physically plausible, such a heat source would need to fulfill a number of important requirements. First, the heating needed to be distributed over the entire cluster core. This is difficult to do since the cooling rate is strongly density-dependent while heating rates generally are not. Second, heating would need to be more or less constant over several Gyr, at least when averaged over periods of 10^8 years (the minimum observed cooling time). Third, the heating rate would need to be closely coupled to the cooling rate in order to prevent the cluster from over or under heating. Various studies have proposed thermal conduction, turbulent decay, mergers, supernova, and AGN as heat sources in cool-core clusters. The evidence for and against each of these is summarized below.

2.3.2.1 Conduction

Because as the cooling cores of galaxy clusters are surrounded by the hot gas of the ICM, thermal conduction has been invoked as a possible solution or at least a contributing factor to the cooling flow problem (e.g. Zakamska & Narayan, 2003; Voit et al., 2008). The ionized plasma of the ICM is expected to conduct heat via Spitzer conduction (Spitzer, 1962), given by Fourier's Law

$$\vec{j} = -\kappa_S \vec{\nabla} T \tag{2.6}$$

where $\vec{j}$ is the heat flux, κ is the conductivity coefficient, and $\vec{\nabla} T$ is the temperature gradient. Making the assumptions described in Smith et al. (2013), the conductivity coefficient is given by

$$\kappa_S = 4.9 \times 10^{-7}\, T^{5/2}\, \mathrm{ergs^{-1}cm^{-1}K^{-1}} \tag{2.7}$$

Observations reveal that while conduction may well have an effect on cooling flows (Voigt et al., 2002; Voit, 2011), it is not powerful enough to prevent cooling in all cases (Voigt & Fabian, 2004). More importantly, conductive balance is a finely tuned and unstable equilibrium (Bregman & David, 1988; Voit et al., 2015b). If a cluster is hotter than the profile specified by conductive balance, conduction will heat the core faster than it can cool, driving the cluster to isothermality. If the core is cooling faster than conduction can stabilize it, the core will cool catastrophically, leading to the classic cooling flow. Simulations such as Smith et al. (2013) have found that conduction may be important in hotter clusters but is not sufficient to affect the thermal structure of cool-core clusters.

2.3.2.2 Turbulence and Mergers

Several observations (e.g., Inogamov & Sunyaev, 2003; Zhuravleva et al., 2014, 2015) have noted some level of turbulence in the ICM. This turbulent motion would be expected to decay into thermal energy, heating the gas in the cluster core. As analyzed in Zhuravleva et al. (2014), turbulent heating could be of the same order of magnitude as heat losses throughout the cluster core and could thus form a solution to the cooling flow problem.

Currently, the statistics of turbulence in the broader cluster population is not known and the driving force is not well understood. Mergers could in principle drive turbulence (Valdarnini, 2006; Markevitch & Vikhlinin, 2007; Burns et al., 2008; ZuHone et al., 2010), but most cool-core clusters do not appear to have undergone major mergers in the last several Gyr. Furthermore, it is difficult to see how momentum from a merger could penetrate down into the cluster core. Other methods for driving turbulence include supernova, AGN, and convection. In short, while turbulence may well be important for transferring energy to the ICM, some additional process is needed to produce the energy in the first place.

2.3.2.3 Supernovae

Supernovae are another phenomena that could in theory deposit heat into the centers of cool-core clusters (Voit & Bryan, 2001), but observational constraints limit their contribution to the cooling flow problem. BCGs tend to have star formation rates of 10s of solar masses per year, only a small fraction of which goes into massive supernova progenitors. Simulations such as Dubois et al. (2010) and Skory et al. (2013) have included or modelled supernova heating but find it to be more than an order of magnitude weaker than needed to prevent a cooling catastrophe. In fact, Skory et al. (2013) finds that even when the supernova efficiency is turned up to 10x the expected power, it is still not enough to prevent the gas from cooling. Although supernova feedback may be more important on the galaxy scale (Voit et al., 2015a), it can not by itself prevent a cooling flow. Additionally, supernova deposit metals (which increase the cooling rate) in the same place that they deposit energy, further decreasing their effectiveness).

2.3.2.4 AGN

As mentioned earlier, AGN are currently considered to be the most likely solution to the cooling flow problem. AGN are observed to exist in the vast majority of cool-core clusters, as evidenced by emission from jets and large radio bubbles. Estimates of the energy needed to inflate the bubbles (e.g. Churazov et al., 2003) indicate that AGN are easily powerful enough to balance cooling, provided their energy can be efficiently transferred to the ICM and that the rate of AGN feedback can be coupled to the ICM cooling. A full description of AGN feedback would require general relativity, magnetohydrodynamics, and radiative transfer. Due to this complexity, the physics of AGN feedback remain uncertain.

In order for AGN feedback to regulate the thermal structure of the ICM and prevent (or greatly reduce) a cooling flow, two processes must be understood: 1) how the cooling of the ICM can trigger AGN feedback and 2) how energy from the AGN is distributed throughout the cluster core. A number of triggering methods have been proposed, including accretion of hot gas from the ambient medium ("Bondi Accretion"; Bondi & Hoyle, 1944) and accretion of cold gas (Pizzolato & Soker, 2005). The AGN may transfer energy to the surrounding medium through a number of processes such as inflating cavities (Churazov et al., 2001), cosmic rays, driving turbulence (Ruszkowski & Oh, 2010), and dredging cold gas from the core (Meece et al., 2016).

The next section will discuss possible AGN triggering methods, with an emphasis on the precipitation theory. The following section will discuss how the AGN can return energy to its surroundings.

2.4 AGN Triggering: Hot vs. Cold Gas

As outlined in Chapter 1, AGN are powered by the accretion of material onto an SMBH. If the SMBH is accreting material at a rate $\dot{M}$, the power of the outflow is expected to scale with the rest mass energy of the accretion as

$$\dot{E} = \epsilon \dot{M} c^2 \tag{2.8}$$

where ϵ is an efficiency factor that includes the fraction of accreting material that ultimately reaches the SMBH (rather than being ejected by outflows), the efficiency of converting rest mass into energy, and the fraction of feedback energy that couples to the ICM.

Two principal scenarios have been proposed for triggering AGN feedback in galaxy clusters: 1.) accretion of hot gas from the ambient medium or 2.) accretion of clouds of cold, dense gas. Each scenario results in gas being channeled towards the SMBH and producing outflows, but they differ in how they couple the accretion rate to the bulk properties of the ICM, which may have important consequences for the effects of AGN heating and cycling. Understanding what sets the AGN accretion rate (and therefore jet power) is critical to deciding whether AGN can solve the cooling flow problem.

2.4.1 Hot Mode (Bondi-like) Accretion

As the SMBH is moving through (or just sitting in) the ICM, it would be expected to accrete material that comes within its gravitational radius. In the Bondi-Hoyle-Lyttleton accretion scheme (Hoyle & Lyttleton, 1939; Bondi & Hoyle, 1944) [1], the accreting object is taken to move through an infinite gas cloud and accrete matter as it goes. In Bondi accretion, the accreting object is taken to be stationary within the cloud, leading to a steady accretion flow.

[1] Hoyle & Lyttleton (1939) is an interesting read from a historical perspective. The focus of the article is to suggest that changes in the Solar accretion rate could in theory lead to changes in the Solar luminosity and cause ice ages or warm periods. Basically, the article suggests that if the accretion rate scales as ρ/v^3, small changes in the density of the ISM or in the relatives velocity of the sun with the ISM could potentially lead to large changes in the accretion rate. If the kinetic energy of the accreted material were converted into radiation, the changes in the Earth's temperature could be explained. The paper does not go so far to argue that this is actually the case, but does suggest that Solar accretion should be taken into account in future climate studies. Although this theory does not seem to have gained any traction (and I would assume has been invalidated by the discovery of the heliosphere and Solar winds), the paper lived on to serve a different purpose and now forms as part of the foundation of accretion theory.

Bondi accretion gives an accretion rate

$$\dot{M} = \frac{2\pi G^2 M_{\rm BH}^2 \rho_\infty}{c_{s,\infty}^3} \tag{2.9}$$

where ρ_∞ and $c_{s,\infty}$ are the density and sound speed of the ambient medium far from the SMBH. The assumption of Bondi accretion is that the accretion flow is steady and has a characteristic radius

$$R_{\rm B} = \frac{G M_{\rm BH}}{c_{s,\infty}^2} \tag{2.10}$$

which is around 50 pc for typical SMBHs in galaxy clusters. The Bondi accretion rate couples linearly to the ICM density (and therefore temperature for a subsonic flow), meaning that a colder gas will have a higher accretion rate.

Bondi accretion is simple, and it is unlikely that many of the assumptions backing the theory will be satisfied in practice. Accretion is almost certainly not a steady-state flow, and the ICM is likely to be mixed and turbulent, rather than homogeneous and static. Further, outflows mean that accretion is unlikely to be spherical within the Bondi radius. Due to the weak dependence on gas temperature, Bondi accretion would likely lead to a more-or-less steady accretion rate, rather than the highly variable rates that are observed.

2.4.2 Cold Mode Accretion

In 'cold mode' accretion theory (e.g. Pizzolato & Soker, 2005), the SMBH primarily accretes gas through the stochastic accretion of cold clouds from the ICM. This theory presupposes that the ICM has a multiphase temperature structure, with cold, dense clumps embedded within a hot, low density plasma. Stochastic accretion could naturally explain the rapid variability of observed AGN and may better couple the accretion rate to the temperature of the ICM. Intuitively, the amount of cold gas will be linked to the average temperature of the ICM, with a colder, denser ICM hosting more cold gas. For a deeper understanding of how conditions in the ICM can generate a multiphase medium with cold gas, and to estimate whether the cold mode accretion rate provides a plausible accretion rate to the cooling flow problem, we must delve into the exciting realm of thermal instability theory.

2.5 Thermal Instability

The density and temperature structures of the ICM are shaped by the underlying gravitational potential, hydrostatic pressure, magnetic fields, turbulence, and heat transport processes. In particular, the last of these may drive changes in the thermodynamic structure of the ICM and can strongly induce or inhibit the growth of substructure. If the balance between heating and cooling is such that density and temperature perturbations are isobarically amplified, the gas is said to be thermally unstable, and may develop a multiphase structure in which regions of hot and cold gas coexist at constant pressure. The question addressed in this section is whether thermal instability is likely to affect the ICM and, if so, in what manner. This section discusses the history of thermal instability theory as applied to the ICM.

Thermal instability in the ICM has been studied using several techniques, each with its own strengths and weaknesses. Theoretical arguments deliver a deep understanding of the processes underlying thermal instability and may be applicable over a wide range of environments, but the results obtained strongly depend on the underlying assumptions and simplifications employed. Simulations are able to follow the evolution of gas under conditions not amenable to analytic study, but are still limited by the initial conditions and included physics. Additionally, the results of a simulation are dependent on the interpretation of the researcher, who must interpret the data through the lens of their own knowledge and prejudice. Observations can in theory provide the ultimate truth about the state of clusters, but do not always reveal what physical processes are important or how the ICM reaches the observed state. Further, current observations are only capable of revealing select components of galaxy clusters, meaning that further knowledge is necessary to complete the picture and fill in the gaps.

This section summarizes the historic and current theoretical understanding of thermal instability in the ICM. Theoreticians tend to treat thermal instability by running a perturbation analysis on an initially static (or at least steady-state) setup. The growth of perturbations is followed in the linear regime. While the media studied by theory are very approximate to the true state of the ICM, they reveal important truths about the criteria for thermal instability. Additionally, they show how these criteria may be modified by other physical processes such as thermal conduction, magnetic fields, rotation, expansion, and density stratification.

2.5.1 Field 1965

George Field's 1965 treatise on thermal instability (Field, 1965) is often taken as a starting point in the study of astrophysical multiphase media. While previous authors (Field cites Parker, 1953; Zanstra, 1955a,b) had studied thermal instability in astrophysical media, these authors had incorrectly derived the criterion for thermal instability, leading to erroneous results. The correct criterion was derived by Weymann (1960), although the significance was not realized at the time. For a medium in thermal equilibrium where a perturbation is added, such that some thermodynamic variable A is kept constant, Field (1965) gives the criterion as

$$\left(\frac{\partial \Psi}{\partial S}\right)_A > 0 \tag{2.11}$$

where S is the entropy and Ψ is the net heat loss function (heat lost per unit mass per unit time) given by

$$\Psi(\rho, T) = \Lambda(\rho, T) - \Gamma(\rho, T) \tag{2.12}$$

where Λ is the cooling rate (thermal energy per unit mass per unit time) and Γ is the heating contribution. Therefore, in the equilibrium state

$$\Psi(\rho_0, T_0) = 0 \tag{2.13}$$

where ρ_0 and T_0 represent the density and temperature of the unperturbed states, respectively. Depending on which thermodynamic variable is held constant, the resulting instability criteria become

$$\left(\frac{\partial \Psi}{\partial T}\right)_\rho < 0 \qquad \text{(Isochoric)}$$

$$\left(\frac{\partial \Psi}{\partial T}\right)_P = \left(\frac{\partial \Psi}{\partial T}\right)_\rho - \frac{\rho_0}{T_0}\left(\frac{\partial \Psi}{\partial \rho}\right)_T < 0 \qquad \text{(Isobaric)}$$

$$\left(\frac{\partial \Psi}{\partial T}\right)_S = \left(\frac{\partial \Psi}{\partial T}\right)_\rho + \frac{1}{\gamma - 1}\frac{\rho_0}{T_0}\left(\frac{\partial \Psi}{\partial \rho}\right)_T < 0 \qquad \text{(Isentropic)}$$

The isochoric case is not very interesting, as constant-density perturbations lead to pressure differences which would cause the state to be out of equilibrium. It is the isobaric case which is most interesting when studying condensation modes. Isentropic perturbations may lead to or result from sound waves. As sound waves may be amplified or damped in a gaseous medium, the study of isentropic perturbations may also be of interest.

Field (1965) goes on to discuss the growth rate of a perturbation of form

$$a(\vec{r}, t) = a_1 \exp(nt + i\vec{k} \cdot \vec{r}) \tag{2.14}$$

to a medium in thermal equilibrium where a is density, velocity, temperature, or some other property of the gas. Here, it is assumed that $a_1 \ll a_0$, the equilibrium value of a, meaning that the perturbation may be treated in the linear regime. The growth rate n of the perturbation is controlled by the thermal properties of the medium.

By substituting the perturbations into the Euler equations, Field (1965) arrives at a cubic equation for n. Positive roots (real or imaginary roots with positive real components) will correspond to growing perturbations, while negative roots will correspond to damped perturbations. The cubic equation allows three roots. Two of the roots correspond to sound waves, in which temperature and density vary. If n is positive, the medium is unstable to isentropic disturbances, and the sound waves will be amplified. For the third root, temperature and density vary out of phase with one another, leading to no overall change in pressure as the perturbation evolves. This is the condensation mode which may lead to the formation of a multiphase medium.

If thermal conduction is important in the medium, perturbations below some critical wavelength will be stabilized by conduction before they can grow. For low conductivity, the growth rate of the condensation mode rises with wave-number and plateaus towards smaller wavelengths. As conductivity rises, the growth rate will fall for wave-numbers above the critical value, meaning that perturbation growth will be a stronger function of wave-number and will peak somewhere around the wavelength of waves corresponding to isothermal perturbations. For high conductivity, the growth rate function will be more strongly peaked as a function of wave-number, since conduction will be better able to stabilize the medium at small scales.

Adding a magnetic field to the medium (Field, 1965, specifically considers a uniform field) has a number of effects on the condensation process. First, the field introduces two additional wave roots in the growth rate equation, corresponding to Alfvén waves. One of the new roots corresponds to a wave moving perpendicular to the field, which is stable. The other root corresponds to a wave moving along the field and can grow. Secondly, the magnetic field inhibits condensation perpendicular to the field, as compression of the gas must overcome the pressure of the magnetic field. Condensation along the direction of the field is unaffected. Lastly, conduction perpendicular to the direction of the field will be reduced. This anisotropic conduction means that a magnetic field can stabilize the medium perpendicular to the field but will not affect condensation parallel to the field.

In the case of a rotating medium where the centrifugal force is comparable to gravity, radial condensation will be inhibited for perturbations above a critical wavelength. For smaller perturbations and for azimuthal condensation, the growth rate is unaffected.

The situations mentioned above are all worked out for the case of a uniform, static medium. For a gravitationally stratified medium, the growth of perturbations might be expected to vary when the scale of the perturbations is similar to that of the scale height, such that the effects of density and/or temperature stratification would be non-negligible. One major change is that small scale perturbations may grow even when thermal conductivity is large. In the uniform case, temperature variations are necessary to balance density perturbations (keeping pressure constant). If conduction was large, the temperature variations would be wiped out and the perturbations would not grow. In the stratified case, pressure variations can be balanced by gravity, allowing perturbations to grow even if temperature variations are erased.

The paper also considers the case of condensation in an expanding medium. This is relevant for novae and other explosions but not for the present work[2]. Finally, the paper concludes with applications of the thermal instability theory to the Chromosphere, the solar corona, the galactic halo, planetary nebula, and the formation of galaxy clusters. While many of these topics have since been revised by others, this paper is interesting as a historical treatment of these topics.

2.5.2 Defouw 1970

Defouw (1970) explores the connection between thermal instability and convective instability and reaches the conclusion that any thermally unstable atmosphere will also be convectivly unstable. Though Field (1965) studies the case of a gravitationally stratified atmosphere, only vertical motion of the gas is considered, leading to overall expansion or contraction of the atmosphere. In addition, the acceleration term is not considered in the motion of the gas. Therefore, convection does not occur in that work. However, Defouw (1970) argues that in a realistic medium, thermal instability is more likely to lead to convection than to expansion or contraction.

The manner of the onset of convection in a thermally unstable medium depends on the temperature gradient of the gas. As an aside from this paper, consider the case without external heating or radiative cooling. The temperature gradient can be either superadiabatic, adiabatic, or subadiabatic. Consider a medium in gravitational equilibrium where temperature and density increase with depth. Now, imagine that a small parcel of fluid is given a slight upward nudge. Since the pressure decreases as the parcel ascends, the parcel expands, cools, and decreases in density.

- Adiabatic: When the parcel expands to equilibrate with the reduced pressure, the density of material in the parcel is the same as the density of the surrounding medium. The parcel experiences no force. The medium is **stable** to convection.

- Superadiabatic: The parcel expands to equilibrate, but when the pressure is equal to the surrounding pressure, the density is now lower than the surrounding density. In fact, the density contrast is even greater than it was at the lower height, meaning that the parcel continues to rise upwards. The gas is now **unstable** to convection.

- Subadiabatic: The parcel expands until the pressure matches the new surrounding pressure, but the density ends up being greater than the surrounding pressure. The parcel experiences a restoring force and must descend. It then proceeds to oscillate around its original position. The medium is **overstable** to convection.

[2] Also, this section references Stephen Hawking when he was still a graduate student at Cambridge. His name is spelled wrong (Stephan)

Therefore, the superadiabatic case is unconditionally unstable, while the subadiabatic case is overly stable. Now, consider the case where the heat loss function is non-zero and the gas is thermally unstable. In the subadiabatic case, the parcel will rise as described above. As it rises, however, it will remain denser than its surroundings. This means that the parcel will cool faster than its surroundings, since the medium is unstable. Therefore, the density contrast will increase as the particle rises and falls, meaning that when it returns to its original height, the parcel will be denser than its surroundings and will descend further than it ascended. The parcel will then descend to a level where it is under-dense, at which point the thermal instability will lead to it rising to a higher height than on its previous ascent. Thus, the oscillation about the original point will grow with time, leading to convection.

Of course, the parcel approach is a very idealized method which ignores some important factors such as viscosity, conduction, and magnetic fields. Repeating the analysis using the Boussinesq framework and including viscosity and conduction confirms the result that there is always some sort of thermal-convective instability, unless the perturbations are small enough that conduction or viscosity can stabilize them. Thus, the result is basically the same as in Field (1965). Adding in rotation and magnetic fields allows the possibility of monotonic instability[3][4][5] instead of oscillatory instability. The author points out that while the oscillatory motion may in fact result in some energy transfer between fluid layers, dampening the oscillations and weakening the validity of the results derived in this work, monotonic instability would be harder to damp.

2.5.3 Nulsen 1986

Nulsen (1986) takes the ideas of thermal instability theory and applies them to the context of cooling flows in galaxy clusters.

This paper cites the work of Cowie et al. (1980), which as part of a case study of the Perseus cluster describes how convection could potentially stabilize the gas in a cooling flow against thermal instability. Nulsen (1986) however argues that convective blobs would be disrupted, making this effect unimportant. The conclusion of this work is that all but the most overdense perturbations will be disrupted long before they reach their equilibrium position. As the blob is disrupted, its velocity relative to its surroundings will decrease, and the flow will become effectively co-moving.

The paper goes on to study the dynamics of the cooling flow allowing for mass drop out and convection. The conclusion seems to be that cold mass would be deposited over a large range of radii, not only near

[3] I assume that this means exponential growth, rather than a complex growth rate.

[4] Searching for this term online shows that it nearly always occurs in the context of fluid dynamics, most of the time in reference to this paper.

[5] Mark Voit confirms that this means exponential growth.

the center where the flow is steady. Convection would not stabilize the flow, since parcels of gas would be disrupted before reaching equilibrium. However, this analysis does not seem to include a central heating term and thus predicts more condensation than is observed by more recent studies.

Balbus & Soker (1989) point out that this paper deals more with the fate of nonlinear perturbations within a cooling flow, rather than with the thermal stability of the flow in the first place. Nevertheless, this paper is important for considering the evolution of perturbations in a dynamic rather than in a static medium.

2.5.4 Malagoli 1987

Malagoli et al. (1987) reconsiders the analysis of Defouw (1970), Cowie et al. (1980), and Nulsen (1986) and applies their analysis to a numerical model of M87. They conclude that it is incorrect to treat overdensities as free-floating blobs, and instead agree with the results of Defouw (1970) in that the buoyancy will push the medium to over-stability. They note that conduction will make the gas stable on scales of a few kpc, but at larger scales the gas should be over-stable, leading to condensation.

2.5.5 Balbus 1988

Balbus (1988) re-analyses the conditions under which gas in cooling flows can be thermally unstable using a Lagrangian approach rather than an Eulerian approach. In doing this, they arrive at a number of surprising conclusions:

1. Radial thermal instability does not occur in spherical systems in hydrostatic equilibrium (contrasting with many earlier works.)

2. Local isobaric instability (e.g. condensation) can only occur if perturbations are growing on something similar to the thermal timescale.

3. Building off of Defouw (1970), gas which is stable against convection according to the Schwartzchild criteria may in fact be convectively unstable if the gas is cooling radiatively.

The main results of this work are that radial thermal instability does not occur and that the growth rate of non-radial modes would be weak – thus, we should not expect the gas in cooling flows to be unstable. In analysing the radial instability, Balbus (1988) finds that the only growth of radial modes occurs on the same scale as the growth of the cooling flow, and is thus indistinguishable.

An important caveat to this study is that the analysis does not include the effects of the background motion of the medium. This is taken into account in Balbus & Soker (1989), which modifies these results.

2.5.6 Balbus & Soker 1989

Balbus & Soker (1989) presents a re-analysis of Balbus (1988) as well as a more general study of thermal instability in cooling flows using Lagrangian dynamics.

In the introduction, Balbus & Soker (1989) points out an error in the analysis of Defouw (1970). While that study took into account azimuthal structure (the lack of which was cited as a deficit of Field (1965), it did not allow for azimuthal dynamics. Movement in the azimuthal direction could in fact be important, since having small δP small does not necessarily mean that $\nabla(\delta P)$ is small. These azimuthal displacements could contribute to thermal instability much more than the oscillating radial modes.

This paper makes a point of differentiating between local and global instabilities. Past analysis using Eulerian plane waves studied the global instability of the gas to condensation or oscillation. This type of analysis does not necessarily capture a local instability that might exist even when the medium is globally stable. Using a Lagrangian framework rather than an Eulerian one could therefore give a more accurate picture of the conditions for thermal instability.

In examining Defouw (1970), Balbus & Soker (1989) contends that in a static medium where the heat-loss rate per gram is constant throughout, thermal and convective instability must be linked; that is, if a medium is thermally unstable it will necessarily be convectively unstable, and if it is thermally stable it will also be stable to convection. Thus, over-stability will not be a factor since the two instability conditions do not occur independently. If, on the other hand, the background is dynamic, thermal equilibrium is not enforced, or the heat-loss function explicitly depends on position (as in the case of an AGN), the two criterion can occur independently, and over-stability may be important.

2.6 Observations of Multiphase Gas

As the preceeding section makes clear, thermal instability is difficult to study from a purely theoretical standpoint, and significant uncertainty remains in determining the susceptability of the ICM to the formation of a multiphase medium. With the advent of space-based observatories, it has become feasible to conduct multi-wavelength searches for multiphase gas in clusters. Although the amounts of cold gas observed are much lower than what is predicted by the cooling flow model, it is clear that in some clusters at least, cold gas is forming. It has been hypothesized that this gas may originate from thermal instability and could be driving AGN feedback. This section discusses some of the observational evidence for multiphase gas in galaxy clusters.

2.6.1 Cavagnolo 2008

Cavagnolo et al. (2008) examines the entropy profiles, Hα emission, and radio emission from a large number of galaxy clusters. The cluster data is taken from the Chandra archives, and is named the ACCEPT (Archive of Chandra Cluster Entropy Profile Tables) sample. For each cluster, the author fits the entropy profile to the form

$$K(r) = K_0 + K_{100}(r/100\text{kpc})^\alpha \tag{2.15}$$

Where $K(r)$ is the entropy as a function of radius, K_0 is the central entropy, and K_{100} and α describe the power law behavior of the entropy profile at large radii.

Hα is used in the study as a tracer of star formation and cold gas. While they assume that star formation is the principle producer of Hα, they allow that this is not necessarily the case. Although the Hα values are taken from different observations, the study does make an effort to make them consistent. More importantly, their results only depend on whether Hα was detected, rather than the exact amount.

In the ACCEPT sample, 64/110 clusters have only upper limits on Hα detection. The clusters that do have detections almost all have central entropies below 30 keV cm^2, corresponding to a cooling time $<$ 1 billion years, while those clusters with upper limits lie almost entirely above 30 keV cm^2. Thus, the presence of Hα is strongly correlated with the central entropy value, producing a bimodality of cluster core properties. Voit et al. (2015b) explains this as a divide between feedback-regulated cores (low entropy, Hα) and conduction-regulated cores (high entropy, no Hα). This study does not propose an explanation for the dichotomy.

The radio observations were used to deduce whether or not the BCG hosted an AGN. On the reasoning that BCGs are more likely to show radio loud AGN than other galaxies in a cluster, radio emission was taken as evidence of AGN activity.

The radio data also yields a split in cluster properties, though the distinction is not as clear as in the Hα case. It is seen that all clusters with radio luminosities above 10^{40} erg/s have central entropies below 30 keV, and that all clusters with central entropy above 30 keV have radio luminosities below 10^{40} erg/s. There does not appear to be a correlation between radio power and entropy, however. Some clusters with Hα do not have radio detections, and several with radio detections do not have Hα. This could simply be due to episodic or variable AGN activity.

2.6.2 Werner 2010

Werner et al. (2010) describes observations of multiphase gas in M87[6], one of the brightest central galaxies in the Virgo Cluster. M87 is a giant elliptical galaxy with a visible AGN jet. The observations show that while some of the gas uplifted by the jets is radiatively cooling, the bulk of the material remains hot, indicating that some sort of heating mechanism is preventing most of the gas from cooling. M87 is well studied. In different observations, it shows multiphase gas in some sort of filamentary structure, radio emission, and X-ray cavities. This paper uses Chandra data to probe the structure of the multiphase gas at higher resolutions.

The X-ray observations show that there is cold gas (0.5 keV) in M87 in filaments near the jet. The 1 keV gas is spatially coincident with radio emission and is thought to fill the cavities, which are more or less isothermal. 2 keV emission is fairly smooth and forms a sphere. This gas is surrounded by 3 keV emission outside of the inner core.

The 0.5 keV gas is spatially coincident with Hα emission near the core. Both have a filamentary nature. There is also a horseshoe-shaped feature a few kpc from the center. Using the Chandra data, the group plots a pressure profile for the core, which shows a discontinuity outside of a high pressure sphere, indicating some form of shock. All of the Hα is found inside of the high pressure region. X-ray spectra indicate that very little of the gas is cold, with a maximum cooling rate of 0.06 $M_{\odot}$per year.

The X-ray arms observed in M87 are relatively smooth and straight, indicating that the gas is not being disrupted by turbulent motion. The filaments of Hα do not show polarization, indicating that if magnetic fields are present, they are tangled on scales below 0.1 kpc.

While X-ray emitting gas is seen at 0.5 keV, no X-ray gas is seen below 0.5 keV. If the gas were in a steady state and were being heated by a volume averaged term, heating strong enough to keep the 0.5 keV gas from cooling would overheat the surrounding gas. Thus, they authors conclude that the heating is not due to a volume averaged mechanism. Instead, they suggest that the cooler gas is heated by mixing with warmer gas.

[6]The introduction to this paper contains some good information on M87 as well as possible AGN heating mechanisms.

2.7 Simulations of Multiphase Gas Formation

Analytical studies of thermal instability are limited in that they can only describe the linear regime where perturbations are small, and generally only apply to contrived setups that may not approximate reality. Simulations offer an alternative approach, allowing researchers to follow the evolution of gas behavior over long periods of time into the non-linear regime. This section discusses several milestone studies of multiphase gas in simulations.

A variety of types of simulations have been developed to study thermal instability. 2D simulations are quick to run, but do not necessarily capture phenomena like convection or magnetic fields, which are inherently 3D processes. Further, thermal instability requires a heating and a cooling term, the forms of which must be assumed. The simulations discussed in these works (and in Chapter 3) generally assume heating functions that are able to balance cooling in the unperturbed case. Most of the simulations follow the outline of Field (1965) and add small perturbations to an idealized, equilibrium setup, though some deal with larger overdensities.

2.7.1 Malagoli 1990

Malagoli et al. (1990) is an early paper that uses 2D simulations to study the growth and evolution of perturbations in ionized gas. This work is a follow up to an earlier paper (Malagoli et al., 1987) in which the authors analytically studied the growth of isobaric perturbations in the linear regime. In this paper, the authors simulate the evolution of a spherical overdensity in order to determine the set of conditions for which the blob condenses and under which it is shredded by the Kelvin-Helmholtz (Thomson, 1871) or the Raleigh-Taylor (Rayleigh, 1882) instabilities.

This work considers an isothermal setup with gas in hydrostatic equilibrium with the strength of the cooling rate as an independent parameter in order to study the effect of cooling rate on the growth of instabilities. A constant heating term equal to the (negative) cooling in the unperturbed state was imposed. The simulations were performed on a Cartesian mesh with the perturbation on the z axis and symmetry imposed across that axis. The perturbation was fixed at an initial overdensity of $\delta\rho = 0.0067$. Thermal conduction was neglected, though they mentioned that its inclusion does not significantly affect their results.

For this study, different values for the cooling rate were considered. In the first case, the buoyancy time scale is much shorter than the cooling time, while in the second case the two are similar. For both cases, the blob is shredded by instabilities as it oscillates. The run with more cooling stays together longer, but both are ultimately torn apart.

2.7.2 McCourt 2012

McCourt et al. (2012) (which forms the precursor for the work in Chapter 3) studied the possibility of forming a multiphase medium in a 2D simulation of the ICM. These simulations approximated the ICM as a stratified medium, constructed in a planar fashion with gravity pulling towards the mid-plane. In this simulation, gas was initialized in hydrostatic equilibrium with a cooling rate that scaled as $n^2T^{1/2}$. The heating rate was then constructed such that the instantaneous heating rate at a given height was equal to the average cooling rate at that height. Although somewhat artificial, observations show that heating in real clusters roughly balances cooling at all heights, meaning that this heating method is not a terrible approximation.

The study starts out with an analytic stability analysis for the plasma and concludes that perturbations should develop when the cooling time (t_{cool}) is less than the free fall time (t_{ff}) at a given height. When the ratio is less than one, overdense clumps can cool faster than they fall, resulting in cold blobs occurring in place. When the ratio is greater than one, blobs of gas are able to fall a significant distance before cooling, leading to convection rather than condensation.

The simulations in this paper largely confirm the results of the analytic study. They find that the key parameter controlling the development of multiphase gas is the timescale ratio $t_{\text{cool}}/t_{\text{ff}}$. The paper also considers additional physics like magnetic fields and conduction, though these are not found to have significant effects unless the strength of conduction is very high.

Notably, this study does not treat heating or cooling in the vicinity of the mid-plane, as they say that their heating routine is not an accurate measure of feedback near the center of clusters. This is addressed in Meece et al. (2015), which includes heating and cooling near the mid-plane and finds that it makes an important difference in the results.

2.7.3 Sharma 2012

Sharma et al. (2012b) explores the formation of multiphase gas in a 3D spherical environment where heating balances cooling at all radii. They then test a second heating method in which heating is proportional to the mass flux through some inner region. This paper finds that multiphase gas is able to form when the ratio of cooling time to free-fall time is less than 10.

The simulations in Sharma et al. (2012b) are carried out in spherical coordinates, with logarithmic bins in radius and equally spaced bins in the azimuthal (ϕ) and polar (θ) directions. In most cases, they use 1 ϕ bin, but they do a test with 32 bins. The gas is initialized to have a power law entropy profile and reside in an NFW halo. The concentration parameter of the halo is fixed at 3.3, but the mass of the halo is varied between runs. Gas is initially smooth and in hydrostatic equilibrium with density perturbations up to $\delta\rho/\rho = 0.3$ added on. Gas cools according to the curve given in Sutherland & Dopita (1993) and is heated such that heating isotropically balances cooling at all radii. A few runs experiment with variations in the heating function. They also try a heating function which is proportional to the flux of gas through the inner shell and heats as a power law function of radius.

First, the authors study the effects of heating on the mass accretion rate by carrying out simulations of cluster mass halos with and without an idealized heating term. Without heating, all simulations (except for one with very high initial entropy) show strong, steady mass accretion rates of between 100 and 1000 $M_\odot$/year as in the classic cooling flow model. With heating, the accretion rate is much lower in all simulations. The two runs with low initial entropy do show strong accretion at first, but it soon settles down to between 1 and 10 $M_\odot$/year. The run with middle entropy never develops a strong cooling flow. Later on, they show that the accretion rate and the portion of time that a cluster spends with a given accretion rate is not sensitive to the type of heating or details of the implementation.

They also carry out a series of runs with different halo masses but similar entropy profiles. The lower mass halos have lower temperatures (and thus lower $t_{\rm cool}$) but similar freefall times since the NFW profile is self-similar. Therefore, they are more likely to form multiphase gas. The simulations show that hot mode accretion is lower for the lower mass runs, but that the rate of cold mode accretion is similar. This leads to similar amounts of feedback in lower mass halos, which means that the gas gets heated more. This causes the $t_{\rm cool}/t_{\rm ff}$ ratio to rise above 10. Halos with different masses tended to end up with the same core entropy. Since lower mass halos had lower core temperatures, the density was higher, meaning that the cool core in lower mass halos was larger. Very little emission is seen from gas with temperatures below about 1/3 of the virial temperature. For larger halos, feedback needs to be fairly efficient, but at low masses it does not, since the cold gas accretion rate is similar but less feedback is needed to heat the gas. Thus, AGN are more necessary for heating large groups and clusters than for galactic-scale halos.

2.7.4 Joung 2012

Joung et al. (2012) looks at the possibility of condensation in the galactic halo and whether the resulting cold gas could provide fuel for star formation in galaxies. Simulations and galaxy evolution models reveal that most star forming galaxies seem to be running out of fuel to form stars (see for example Sommer-Larsen et al., 2003). As star formation appears to be happening at a roughly steady rate, it is hypothesized that the supply of cold gas needed for star formation is being constantly replenished. One theory is that cold gas condenses out of the hot galactic corona and rains down on the galaxy, providing the necessary fuel to form stars. This paper investigates whether such a condensation/accretion process is feasible by simulating the growth of thermal instabilities in the galactic corona.

This work uses `Enzo` to study the evolution of an isolated overdensity in a stratified, isothermal column of gas. Initially, the gas in in hydrostatic equilibrium (HSE) with gravity pulling towards the center. Gravity is treated as a static potential appropriate for a Milky Way like galaxy. A spherical overdensity is added at a given height above the center. The size of the overdensity is varied from $\delta\rho/\rho = 1.01$ to 100.0. Gas is allowed to cool radiatively, with some simulations using a metal-free cooling function and others using a metallicity of 0.3 Solar. The gas is radiatively heated with using a photoelectric model which is said to depend weakly on density.

Without cooling, the blob essentially bobs up and down, in good agreement with theory. When cooling is turned on, they find that clouds are able to cool if the t_{cool}/t_{accel} ratio is less than 1. Otherwise, the cloud gets shredded by the Kelvin-Helmholtz instability before it can radiate its energy. The key result is that small perturbations in the galactic corona should be essentially stable, but large overdensities could conceivably cool and fall, providing fuel for star formation.

2.7.5 Scannapieco 2012

Scannapieco et al. (2012) describes the formation of multiphase gas in a simulation with driven turbulence. While this work focuses on the ISM in star forming galaxies, the results are relevant to clusters. In a nutshell, star-forming galaxies are observed to host large outflows that are not accurately modeled by simulations. One reason for this could be that turbulent motion on scales below the resolution of most simulations is important for separating the gas into a multiphase medium. This process is explored in this work.

The simulations described in this paper were run using FLASH. Gas was initialized in a $128 \times 128 \times 512$ box covering 4 gravitational scale heights in the $\pm z$ directions. Gravity is the same as in McCourt et al. (2012). The gas initially has an exponential density profile and is in hydrostatic equilibrium. They use a tabulated cooling rate for Solar metallicity gas and include primordial chemistry. Turbulent forcing is added to exactly balance radiative cooling at each time-step.

In the fiducial run, the gas remains stable for approximately 3 dynamical times before separating into a hot and a cold phase. Since the hot gas is unable to cool yet is being volumetrically heated by decaying turbulence, there is a runaway push to higher temperatures, in theory driving an outflow. In this case, the turbulent velocity reaches roughly $\sigma = 45$ km/s before the formation of a multiphase medium.

Another run is conducted with a lower initial density and gravitational scale. Here, the turbulent velocity only reaches $\sigma = 20$ km/s, and the medium remains stable for over 40 dynamical times. When the density is increased so that $\sigma = 29$ km/s, the fraction of cold gas increases, but the medium still remains stable. In a run with stronger turbulence than in the fiducial run, a multiphase medium again develops. Thus, they infer that somewhere around $\sigma = 35$ km/s there is a transition from stability to instability. Finally, they find that increasing the resolution leads to the same behavior with regards to forming a multiphase medium, but that the outflow rate is increased a bit.

The discussion section of this work argues that the results could well be applicable to the ISM. While these simulations do not include rotation, self gravity, magnetic fields, or conduction, it is argued that these would be unlikely to have a large impact under ISM conditions. Star formation and feedback could provide an additional heat source, but the author argues that observations of outflows could indicate that the driving mechanism is more spread out. It is also possible that massive stars are driving turbulence, which is in turn creating the outflows observed.

2.7.6 Banerjee 2014

Banerjee & Sharma (2014a) studies how turbulent mixing can couple AGN feedback to the intracluster medium. They note that this work is similar to Sharma et al. (2010), except that instead of adding the jet energy to the energy part of the hydro equations, they add it to the momentum part as turbulence. Thus, energy is injected as turbulence which later decays and heats the gas. The simulations are performed with MHD using the ATHENA MHD code including anisotropic thermal conduction.

The study uses two initial setups. One uses a cube of gas with uniform initial conditions appropriate for a cluster core. The second setup (the 'mixing setup' as they refer to it) uses two regions with different densities in pressure balance. Small density perturbations and turbulent forcing are then added to the box. Cooling is carried out using the same cooling function from Sharma et al. (2010). Rather than putting in explicit heating, they add forced turbulence which is calibrated to balance losses from cooling.

As the gas evolves, it goes through two phases. First, the gas evolves a steady turbulent state. Second, the gas develops multiphase structure due to cooling.

Other results:

- Changing the box size changes the driving scale of the turbulence. This in turn affects how much multiphase gas is formed.

- Magnetic fields make the condensed gas more filamentary.

- In the mixing runs, the heating mechanism is mixing between the hot and cool gas rather than turbulent decay.

2.8 AGN and Energy Transfer

AGN can provide a solution to the cooling flow problem if the energy generation rate can be coupled to the ICM cooling rate and the feedback energy can be coupled to the ICM in a manner that offsets cooling. The last section showed that cold gas condensing out of the ICM due to thermal instability can provide a fuel source for the AGN. The next question therefore is whether the AGN feedback energy can be returned to the ICM.

For a heating source to be effective in offsetting cooling, it must satisfy a number of criterion. First, the feedback energy must be of the right magnitude to balance cooling in the gas. Second, the heat must be distributed throughout the ICM rather than being deposited very close to the AGN. Third, the feedback rate must be able to adjust on timescales shorter than the cooling time. Fourth, the feedback can not generate very strong shocks, as these are ruled out by observations.

AGN are powerful, but how they transfer energy to the ICM is still unclear (see McNamara & Nulsen, 2007, 2012; Fabian, 2012, for reviews). In theory, there are many ways in which AGN heating can satisfy these criterion. These methods include 1.) Inflating buoyant bubbles, 2.) Shocks or sound waves, 3.) Turbulence, and 4.) Cosmic rays. Each of these methods, along with the observational evidence, is discussed below.

2.8.1 Buoyant Bubbles

The jets from AGN are known to inflate massive bubbles (e.g. Churazov et al., 2001) of hot gas that proceed to rise buoyantly through the ICM. These bubbles can heat the ICM in a number of ways. First, expanding the bubbles does $P\,\mathrm{d}V$ work on the surrounding gas, heating it through compression. These rising bubbles can therefore be used as calorimeters (Churazov et al., 2002) of the AGN power, by assuming that the cumulative output from the AGN over the bubble inflation time is equal to the energy needed to inflate the bubble. The bubble inflation timescale can be measured from the rise of the bubble due to buoyancy.

Rising bubbles will eventually be disrupted by fluid instabilities, which completes the process of transferring their energy into the ICM. Thus, the ability of bubbles to heat gas throughout the ICM will be in part determined by the processes that disrupt or prevent disruption of bubbles. Pure hydrodynamic calculations suggest that Kelvin-Helmholtz (KH) and Rayleigh-Taylor (RT) instabilities should shred bubbles rapidly, but observations (Fabian et al., 2011) find that many bubbles are longer lived than expected, indicating that additional physical processes are preventing bubble disruption. Viscosity (Reynolds et al., 2005) and magnetic draping (where magnetic fields wrap around a rising bubble; see Ruszkowski et al., 2007) could in theory stabilize the bubbles and allow them to propagate to larger radii.

In addition to $P\,\mathrm{d}V$ work and dissipation, buoyant bubbles could also provide distributed heating through cosmic ray injection and by stirring turbulence, both of which are discussed in more detail below. Rising bubbles may also stabilize the cooling flow by dredging up low entropy gas in their wake (Churazov et al., 2001), which is then replaced with higher entropy gas from further out.

2.8.2 Cosmic Rays

AGN can also heat the ICM in a distributed manner through diffusion of cosmic rays from hot bubbles. Cosmic rays can easily be generated in the relativistic plasma within the bubbles (Sijacki et al., 2008) and can diffuse out into the surrounding medium. Studies like Sijacki et al. (2008) indicate that cosmic rays can provide significant heating. Unfortunately, the creation and diffusion of cosmic rays requires complex plasma physics and is difficult to study.

2.8.3 Turbulence

Rising bubbles can stir turbulence in their wake that can heat the ICM either through dissipation or by mixing cold gas with hot. Simulations find that rising bubbles can indeed create a significant amount of turbulence (Walg et al., 2013). Observations such as Zhuravleva et al. (2014) show significant density fluctuations in the ICM of clusters with AGN that, if due to turbulence, hold enough energy to largely offset cooling. The true driver of these density fluctuations remain unknown and will require more detailed investigation using next generation X-ray telescopes like Athena (Nandra et al., 2013).

2.8.4 Shocks and Sound Waves

Hot and fast AGN outflows are expected to interact with the ICM, producing shocks that can distribute energy more isotropically than the jet itself. While most clusters do not exhibit strong shocks (McNamara & Nulsen, 2007), weak shocks linked to the AGN are common (McNamara et al., 2005). These shocks are roughly spherical, may extend for 100s of kpc, have Mach numbers between 1.2 and 1.7, and can have energies of up to 10^{61} ergs. Many clusters (such as the Perseus cluster – see Fabian et al., 2006) show several weak shocks emanating from the core region.

Weaker outbursts could also produce sound waves that could travel through the ICM and deposit heat through dissipation. This process has been explored in Ruszkowski et al. (2004), which tentatively finds that sound waves may carry enough energy to offset radiative cooling.

In reality, it is likely that some combination of all of these methods is necessary for distributing AGN heating throughout the ICM. Figures 2.1 and 2.2 show how these processes can be observed using data from

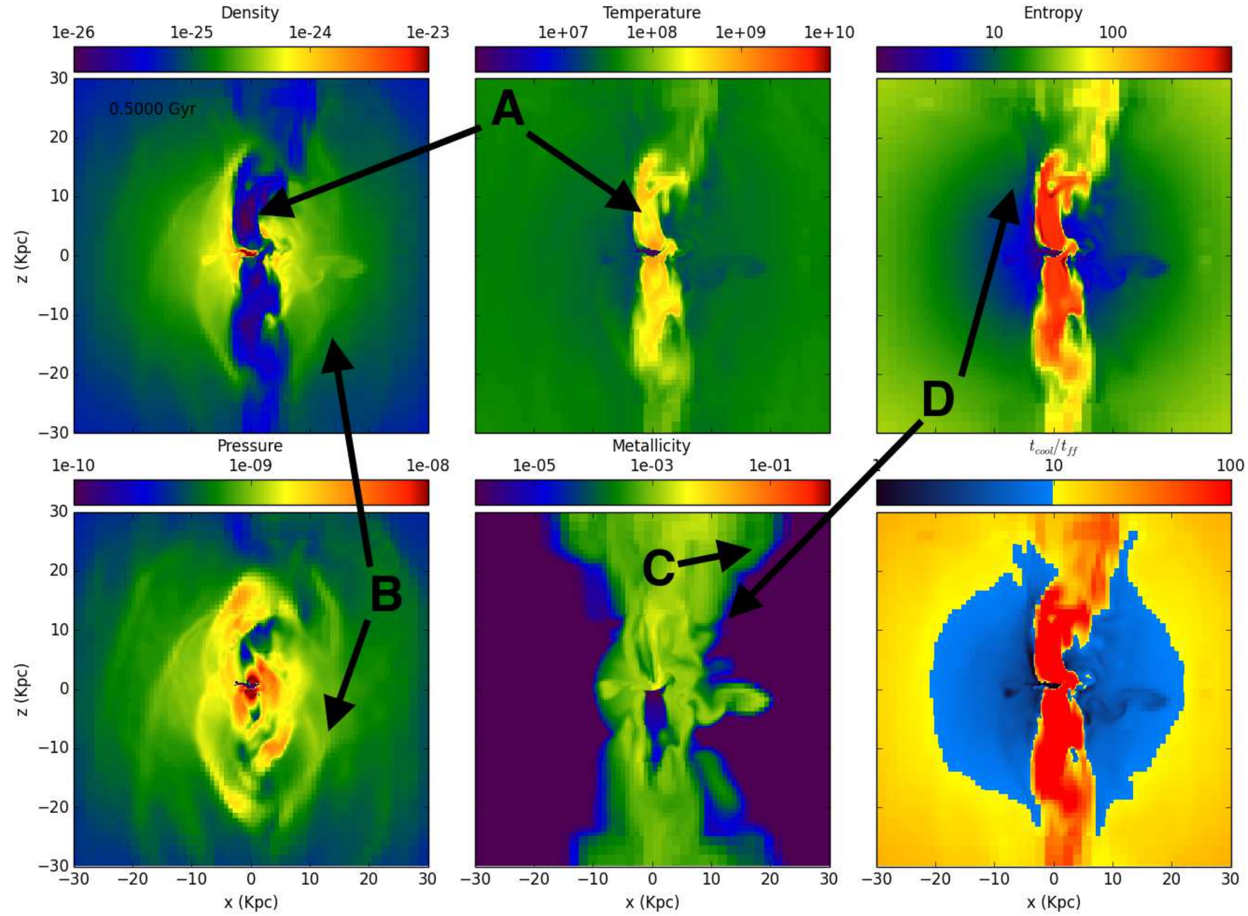

Figure 2.1 **How AGN Feedback Affects Cluster Cores:** The AGN feedback process as seen in simulations performed by Meece et al. (2016). Each frame shows different physical quantities for the same slice of the simulation. The AGN itself is located at the center of the slice. For more details on the simulations, see Chapter 4. Different feedback processes and effects are highlighted. A: AGN outflows inflate hot, low density cavities within the ICM. B: Cavity inflation produces weak, roughly spherical shocks. C: Interactions between the outflow and the ICM produce turbulence that can dissipate or transport hot gas away from the jet axis. D: Rising bubbles dredge up metals and low entropy gas in their wake.

Meece et al. (2016). In particular, the use of difference imaging (Figure 2.2; inspired by Zhuravleva et al., 2016) can disentangle different heating processes and can be used to quantify their importance.

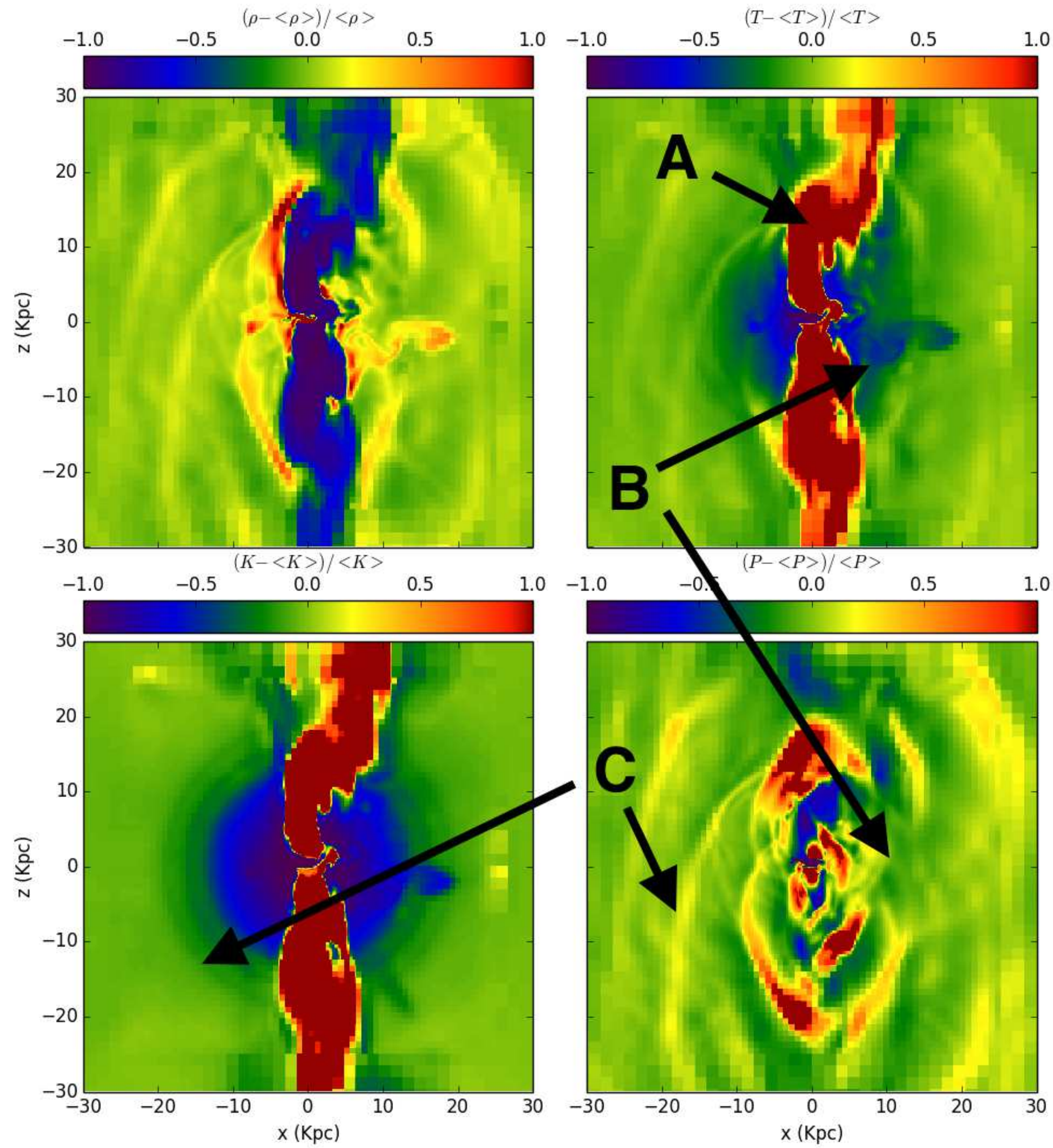

Figure 2.2 **AGN Feedback Energy Transfer Illustreated with Perturbed Quantities:** Perturbations in different quantities for the slice depicted in Figure 2.1 are shown. The average quantities $\langle q \rangle$ are the volume averaged values of q at each radius. This type of perturbation analysis is useful for disentangling the effects of different energy transport processes. A: Direct injection of hot gas is most clearly visible in temperature perturbations, as the outflows are largely isothermal and much hotter than their surroundings. B: Subsonic mixing is isobaric. The churning gas is prominent in the temperature map but invisible in the pressure map. C: Weak shock are largely isentropic. Shocks are most visible in the density and pressure maps but invisible in the perturbed entropy.

2.9 Precipitation-Regulated Feedback

As the preceding sections make clear, AGN feedback is energetic enough to balance radiative cooling, can become strongly coupled to the cooling properties of the ICM through thermal instability, and can distribute energy throughout the ICM. These facts motivate the precipitation-regulation theory of feedback described by Voit et al. (2015b).

As discussed in Section 2.5, a cooler ICM is more susceptible to thermal instability, which can lead to the condensation of cold clumps of gas. In the precipitation-regulation model, these cold clumps then 'precipitate' down towards the SMBH, triggering the AGN. The AGN then produces feedback that heats the ICM, stabilizing it against further precipitation by reducing the amount of cold gas available for fuel. The power of the AGN then drops until the ICM cools down, and the cycle repeats. Thus, precipitation and AGN feedback couple and maintain the ICM in a state of thermal equilibrium.

The ACCEPT sample of Cavagnolo et al. (2009) finds that clusters seem to have an 'entropy floor' of around 30 KeV cm^2 in their cores. When converted to a $t_{\rm cool}/t_{\rm ff}$ ratio, as done in Voit & Donahue (2015), this corresponds to a floor of around $t_{\rm cool}/t_{\rm ff} = 10$. This is in agreement with the results of Sharma et al. (2012b) and Meece et al. (2015), which find that a ratio of $t_{\rm cool}/t_{\rm ff} = 10$ is a threshold for the rapid formation of multiphase gas.

The ratio of cooling time and free-fall time is seen as a strong trigger for the formation of multiphase gas in observations of galaxy clusters, as discussed in Voit & Donahue (2015) and Voit et al. (2015b). Cluster with high central entropy and large ratios of $t_{\rm cool}/t_{\rm ff}$ do not have detected Hα emission, indicating that little, if any, multiphase gas is present. As the timescale ratio drops, however, a strong ramp up in the amount of multiphase gas present is seen.

From this evidence, Voit et al. (2015b) offers the assertion that $t_{\rm cool}/t_{\rm ff} = 10$ is a floor below which clusters and galaxies can not fall. Whenever the ratio drops below 10, precipitation will drive strong feedback that heats the cluster, increasing the cooling time and restoring balance. The nature of the feedback is taken to be AGN feedback in clusters, but may include supernova and star formation in lower mass systems (Voit et al., 2015a,c).

Precipitation driven feedback and conduction work to constrain cluster entropy and cooling time profiles to a narrow band, as seen in Figures 1 and 2 of Voit et al. (2015b). This constraint naturally explains the observed bimodality of clusters into cool-core and non-cool-core clusters. Conductive equilibrium (Voit et al., 2008) is an unstable equilibrium. Clusters below the conduction balance line will cool faster than conduction can heat them, pushing them down to the precipitation line, where they will become cool-core clusters with

$t_{\rm cool}/t_{\rm ff}$ slightly above 10. Clusters above the conduction line will be heated by conduction until they are isothermal, making them non-cool-core clusters. Clusters may transition from cool-core to non-cool-core if and only if they can be pushed above the conductive balance line, either by strong AGN outbursts or major mergers that disrupt the cool-core.

The rest of this dissertation contains original research examining different facets of the precipitation-regulation model. Chapter 3 presents a detailed analysis of multiphase gas formation in the ICM, and Chapter 4 discusses the creation of sub-grid models of AGN feedback that are driven by precipitation and can largely solve the cool-core problem. Chapter 5 concludes by discussing unanswered questions and complications with the model.

3 Growth and Evolution of Thermal Instabilities in Idealized Galaxy Cluster Cores

3.1 Introduction

[1]X-ray observations of galaxy clusters have revealed that the radiative cooling time of gas in many cluster cores is much shorter than the Hubble time. If radiative cooling were uncompensated by heating, the gas would radiate away its thermal energy, causing cooling gas to flow toward the center of the cluster. This would be a classical cooling flow, in which the accumulating cold gas would be observable and would lead to star formation rates of $\gtrsim 100\,\mathrm{M}_\odot\,\mathrm{yr}^{-1}$ (see Fabian (1994) for a review). Instead, X-ray observations reveal little gas cooling below X-ray emitting temperatures (e.g. Peterson et al., 2003; Peterson & Fabian, 2006) and observed star-formation rates that are one or two orders of magnitude lower than predicted by the classic cooling-flow model (O'Dea et al., 2010; McDonald et al., 2011). Thus, an additional process or processes must be heating the ICM to maintain approximate thermal equilibrium. Several mechanisms have been proposed and tested through simulations, including energy injection from supernovae (Nagai et al., 2007; Burns et al., 2008; Skory et al., 2013), conduction of heat from outside of the core (Voigt et al., 2002; Zakamska & Narayan, 2003; Smith et al., 2013), heating through mergers (Valdarnini, 2006; Markevitch & Vikhlinin, 2007; ZuHone et al., 2010), dynamical friction from galaxy cluster motion (Ruszkowski & Oh, 2011; Kim et al., 2005), **turbulent dissipation (Zhuravleva et al., 2014),** and feedback from AGN outbursts (reviewed by McNamara & Nulsen, 2007), which is the mechanism we explore in this work.

AGN feedback is attractive because a simple estimate shows that an accreting supermassive black hole (SMBH) can provide enough energy to offset cooling. For example, a 10^9 $\mathrm{M}_\odot$SMBH accreting over the lifetime of the universe and radiating with a mass-energy conversion efficiency of around 10% would release a total of $\sim 10^{62}$ ergs, corresponding to an average power output of around 10^{44} ergs per second—easily enough to offset radiative cooling if a large fraction of that power is injected into the ICM (see Churazov et al. (2002) for further discussion). Theoretical and observational studies support the conclusion that many cool-core clusters host AGN with enough power to balance cooling (e.g., McNamara & Nulsen, 2007; Dunn & Fabian, 2006; Bîrzan et al., 2004) if a significant fraction of the AGN energy is transfered to the ICM. Nevertheless,

[1]This chapter was originally published in The Astrophysical Journal (Meece et al., 2015). It has been reformatted for inclusion here. For information about copyright and reuse, see Appendix E.

the details of the AGN fueling process and feedback mode are not fully understood.

If SMBH accretion is to explain thermal regulation of the core, then the accretion rate must be linked to the thermal properties of the ICM. As pointed out by McNamara & Nulsen (2007), if the time-averaged heating rate exceeds the cooling rate, the core will heat beyond what is observed, and if it is lower it will fail to prevent gas from cooling. More importantly, the short cooling times observed in many cluster cores require the heating mechanism to respond on short timescales. It is therefore desirable that heating be coupled to the cooling rate, to ensure that feedback is able to balance cooling both on short timescales and over the lifetime of the cluster. Two qualitatively different accretion modes have been described in the literature and implemented in numerical simulations of AGN feedback. Most implementations base the black hole accretion rate on the properties of the ambient hot gas using modifications of the classic Bondi (1952) analysis of smooth, adiabatic accretion, while others rely on condensation and infall of cold clouds to fuel the black hole (e.g., Pizzolato & Soker, 2005; Gaspari et al., 2012b,a). The analysis of Voit et al. (2014) strongly suggests that the latter "cold feedback" mode is more important, because of a universal floor observed in the radial cooling-time profiles of galaxy clusters that corresponds to the predicted threshold for condensation of cold clouds (Sharma et al., 2012a).

"Cold mode" accretion could be fueled by cold gas condensing out of the ICM in response to thermal instability. The transition of the ICM from a homogeneous to a hetrogeneous, multiphase structure has a long history of investigation using theoretical arguments and simulations. From a theoretical standpoint, Field (1965) studied the evolution of small perturbations in cooling plasmas and described an isobaric condensation mode, in which variations in temperature and density may be amplified. Defouw (1970) extended this analysis, finding that thermal and convective stability are tightly coupled, a connection further explored in Balbus & Soker (1989). The problem of thermal instability in the context of cooling flows in clusters was subsequently considered by numerous authors (e.g. Cowie et al., 1980; Nulsen, 1986; Malagoli et al., 1987; Loewenstein, 1990) who concluded that the cooling ICM should indeed be subject to thermal instability. However, further analysis by Balbus (1988) and Balbus & Soker (1989) using a Lagrangian framework (in contrast to the Eulerian approach of the earlier works) indicated that the ICM might be less susceptible to thermal instability than previously thought, especially without the inclusion of a heating term. These studies generally take as their starting point an equilibrium or steady-state configuration of gas that may not accurately capture the behavior of the dynamic ICM. Further, theoretical studies are often incapable of dealing with spatially dependent heating terms, such as would be expected from star formation and AGN feedback.

There is growing evidence suggesting that the dominant parameter controlling the transition to a multiphase state and the amount of cold gas that condenses is the ratio of gas cooling time, $t_{\rm cool}$, to freefall time, $t_{\rm ff}$. Both numerical simulations of thermal instability (McCourt et al., 2012) and observations of galaxy-cluster cores (Cavagnolo et al., 2008; Rafferty et al., 2008; Voit et al., 2014) support this conclusion. Without gravity to restore equilibrium, multiphase structure can develop within a few cooling times, because collisional cooling processes scale with the square of the gas density, allowing denser regions to cool faster than their surroundings. If the medium is in overall thermal balance, gas clumps that are denser than average cool and condense, while underdense regions heat and expand faster than they can cool. In a gravitational potential, however, buoyancy complicates the development of thermal instability and can inhibit condensation (Malagoli et al., 1987; Balbus & Soker, 1989). If the freefall time is **shorter** than the radiative cooling time, an overdense clump can sink to a denser layer before it can significantly cool.

While theoretical studies provide insight into the general physics behind condensation in the ICM, they are necessarily limited by model assumptions and can say little about the fate of instabilities that enter the nonlinear regime. In recent decades, hydrodynamic simulations such as those of Malagoli et al. (1990), McCourt et al. (2012), and Li & Bryan (2014b) have explored the development of thermal instability in astrophysical environments. These works demonstrated that condensation can indeed be expected to occur in environments comparable to the ICM, at a level exceeding the predictions of Balbus & Soker (1989).

Condensation has been explored in the idealized simulations of McCourt et al. (2012), which show that the growth of thermal instabilities is significantly inhibited if $t_{\rm cool}/t_{\rm ff} \gtrsim 1$. However, further studies by Sharma et al. (2012b) have found that in a spherical geometry, multiphase gas can still condense whenever $t_{\rm cool}/t_{\rm ff} \lesssim 10$ due to geometric compression (see Singh & Sharma (2015) for further discussion.) Gaspari et al. (2012b) also finds that a ratio of around 10 is required for the formation of cold clumps. Alternately, recent work by Li & Bryan (2014b) finds that condensation occurs when $t_{\rm cool}/t_{\rm ff}$ is between 3 and 10. There, condensation is stimulated by interactions between the ICM and an AGN jet. The jet entrains cold gas from near the SMBH, pushing it to less dense regions. The clump's positive radial velocity prevents it from returning to an equilibrium position, and the gas rapidly cools. Finally, observations by Voit & Donahue (2015) find that the minimum value of $t_{\rm cool}/t_{\rm ff}$ in clusters with multiphase gas in the form of Hα nebulae generally lies between 5 and 30.

In this paper, we use idealized 2D and 3D hydrodynamic simulations to study how the onset of condensation depends on the ratio of cooling time to freefall time and why there appears to be a change in cluster core properties around a ratio of 10. Section D.2 presents simulations based on McCourt et al. (2012) in which we explore a wider range of initial conditions. Section 4.3 analyzes how thermal instabilities grow in these simulations and investigate how that growth depends on the initial conditions. Section D.6 relates this work to previous theoretical work and discusses the validity of these results in the context of real galaxy clusters. Section 4.5 concludes by discussing future work along these lines.

3.2 Method

In this study, we consider simulations of idealized cluster cores with planar, cylindrical, and spherical geometries in 2 and 3 dimensions. The simulations were carried out using the AMR Hydrodynamics code `Enzo`[2] (Bryan et al., 2014). Unless otherwise noted, 2D runs were conducted on a 300x300 cell grid with no adaptive mesh, and 3D runs employed a 128^3 cell root grid with 2 layers of adaptive mesh, with refinement based on overdensity, density gradient, and cooling time. We do not include magnetic fields, conduction, or the self gravity of the gas. The simulations were analyzed using the `yt`[3] analysis toolkit (Turk et al., 2011).

3.2.1 Problem Setup

We set up the gas in our simulations subject to the constraint of hydrostatic equilibrium (HSE) and an 'iso-cooling' initial condition, under which the $t_{\rm cool}/t_{\rm ff}$ ratio is uniform throughout the volume. Additionally, we run a number of simulations using an isothermal initial condition instead of the iso-cooling one.

The setup described in this section applies to all geometries, as long as the definition of the height coordinate z changes accordingly. In planar geometries, z is the distance from the midplane, in cylindrical geometries it is the distance from the axis of symmetry, and in spherical geometries it is the distance from the origin. We choose a scale height of $z_{\rm S} = 100$ kpc (roughly corresponding to a large cluster), a box size of $R_{\rm S} = 2z_S$, a scale temperature of $T_{\rm S} = 10^8$ K, and a gravitational acceleration scale

$$g_{\rm S} = \frac{{\rm k_B} T_{\rm S}}{\mu m_p z_{\rm S}} \tag{3.1}$$

so that the gravitational potential energy and thermal energy are of similar magnitude at the scale height $z_{\rm S}$. The cooling time is given by

$$t_{\rm cool}(n, T) \equiv \frac{E}{|\dot{E}|} = \frac{3}{2} \frac{n\, {\rm k_B} T}{n_{\rm e} n_{\rm H} \Lambda(T)} \tag{3.2}$$

where E is the thermal energy per unit volume and the form of the cooling function $\Lambda(T)$ is taken from Sarazin & White (1987) for gas of half-solar metallicity.

The standard normalization of $\Lambda(T)$ is used for gas with an iso-cooling initial condition of $t_{\rm cool}/t_{\rm ff} = 1$, and we obtain initial conditions corresponding to other initial values of $t_{\rm cool}/t_{\rm ff}$ by adjusting the normalization of Λ while keeping the gas density and temperature profiles fixed. Two time scales characterizing the initial conditions will be useful in our analysis of the onset of thermal instability. One is the cooling time $t_{\rm cool,S}$ at one scale height ($z = z_{\rm S}$) at the beginning of the simulation. The other is the freefall time at one scale

[2]http://enzo-project.org/
[3]http://yt-project.org/

height, $t_{\rm ff,S}$, which stays constant throughout the simulation.

In general, the freefall time of the gas at height z is

$$t_{\rm ff}(z) = \sqrt{\frac{2z}{g(z)}} \tag{3.3}$$

where the gravitational acceleration defining the potential well is

$$g(z) = -g_{\rm S} \tanh(\alpha z/z_{\rm S}) \tag{3.4}$$

for $-R_{\rm S} \leq z \leq R_{\rm S}$ and is directed toward either the midplane, the symmetry axis, or the origin, depending on the geometry of the potential. The relative constancy of $g(z)$ away from the origin is meant to mimic the inner region of a spherical gravitational potential in which the mass density is proportional to $1/z$. For $|z| \ll z_{\rm S}$, the tanh function ensures continuity of the potential, while the parameter α allows adjustment of its cuspiness. **To mitigate boundary effects, we add a small buffer region of $0.3z_S$ around the outside of our simulation volume and have $g(z)$ decrease rapidly in that region. We restrict our analysis to the region $z \leq R_{\rm s}$.** The simulations we present here use $\alpha = 1.0$, which results in a relatively smooth potential with a gradual softening near the midplane.

Following the work of McCourt et al. (2012), we implement a heating rate that exactly balances the average cooling rate at each height. To do this, we sum the total amount of cooling in each bin of z, divide by the total volume of the bin, and change the sign to get the volumetric heating rate at height z. While clearly idealized, this heating prescription ensures that the gas remains in overall thermal balance, in agreement with the observed thermal behavior of clusters. The validity of this prescription is discussed in Section 3.4.3.

For iso-cooling initial conditions, the initial temperature at $z_{\rm S}$ is $T_{\rm S}$. Equations 3.2 and 3.3 relate density to temperature via

$$\frac{t_{\rm cool}}{t_{\rm ff}} = \frac{3}{2} \frac{n\, {\rm k_B} T}{\Lambda(T) n_{\rm e} n_{\rm p}} \sqrt{\frac{g(z)}{2\, z}} \ , \tag{3.5}$$

and the HSE condition for an ideal gas is

$$\frac{\rm k_B}{\mu m_{\rm p}} \left[T(z) \frac{{\rm d}\rho}{{\rm d}z} + \rho(z) \frac{{\rm d}T}{{\rm d}z} \right] = -\rho(z)\, g(z) \tag{3.6}$$

Combining these two expressions gives the temperature derivative for iso-cooling initial conditions in the form of an ODE:

$$\frac{{\rm d}\ln T}{{\rm d}\ln z} = \left[\frac{\mu m_{\rm p} g(z) z}{{\rm k_B} T(z)} + \frac{1}{2} \left(\frac{{\rm d}\ln g}{{\rm d}\ln z} - 1 \right) \right] \left(\frac{{\rm d}\ln \Lambda}{{\rm d}\ln T} - 2 \right)^{-1} \tag{3.7}$$

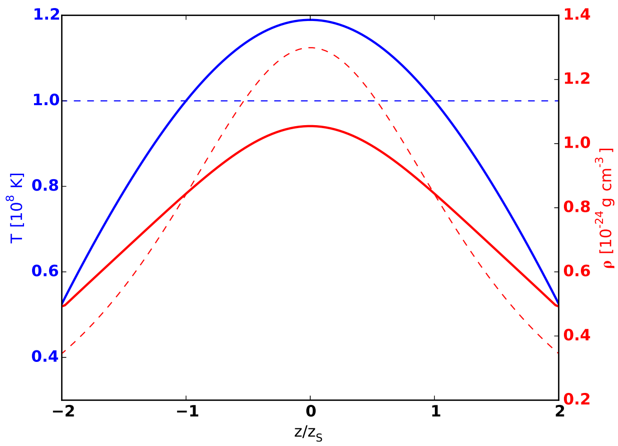

Figure 3.1 **Multiphase Gas Density and Temperature Configurations:** The initial temperature (blue) and density (red) profiles used in this work is shown for planar geometry. In simulations with cylindrical and spherical geometries, the gas is isothermal beyond $z = 2$. The iso-cooling setup, with a constant value of $t_{\rm cool}/t_{\rm ff}$, is shown with a solid line. The isothermal setup is shown with a dashed line. Both setups are in hydrostatic equilibrium and have a ratio of $t_{\rm cool}/t_{\rm ff} = 1.0$ at 1 scale height. These profiles are used for all simulations; runs with different initial values of $t_{\rm cool}/t_{\rm ff}$ are achieved by scaling $\Lambda(T)$ after initialization.

We integrate this equation to find $T(z)$ and determine the density from the iso-cooling condition. For cylindrical and planar simulations, gas outside of $R_{\rm S}$ is taken to be isothermal and in HSE, with $T(z) = T(R_{\rm S})$.

The resulting density and temperature profiles are shown in Figure D.1. We impose a temperature floor at $T_{\rm floor} = 5.0 \times 10^6$ K, as we assume that gas below that temperature inevitably cools rapidly to much lower temperature. The details of the gas flow below that temperature occur at finer resolutions than are employed in our models, and do not affect the overall condensation rate. Finally, we add randomly generated isobaric perturbations to the gas with an RMS overdensity of 0.01 and a flat spectrum with wave numbers between 2 and 20 (with k=1 corresponding to the box size). The same realization of perturbations is used across all simulations to ensure consistency. As the gas quickly settles into a convective state, the details of the initial perturbations are soon forgotten.

Figure D.1 also shows a comparison between the iso-cooling and isothermal setups. In both setups, the initial density and temperature profiles do not vary by more than a factor of 4 throughout the volume. The density is more sharply peaked in the isothermal case, leading to a shorter cooling time in the center. Consequently, the growth of thermal instabilities in the isothermal case is more dependent on height and the initial conditions than in the iso-cooling setup.

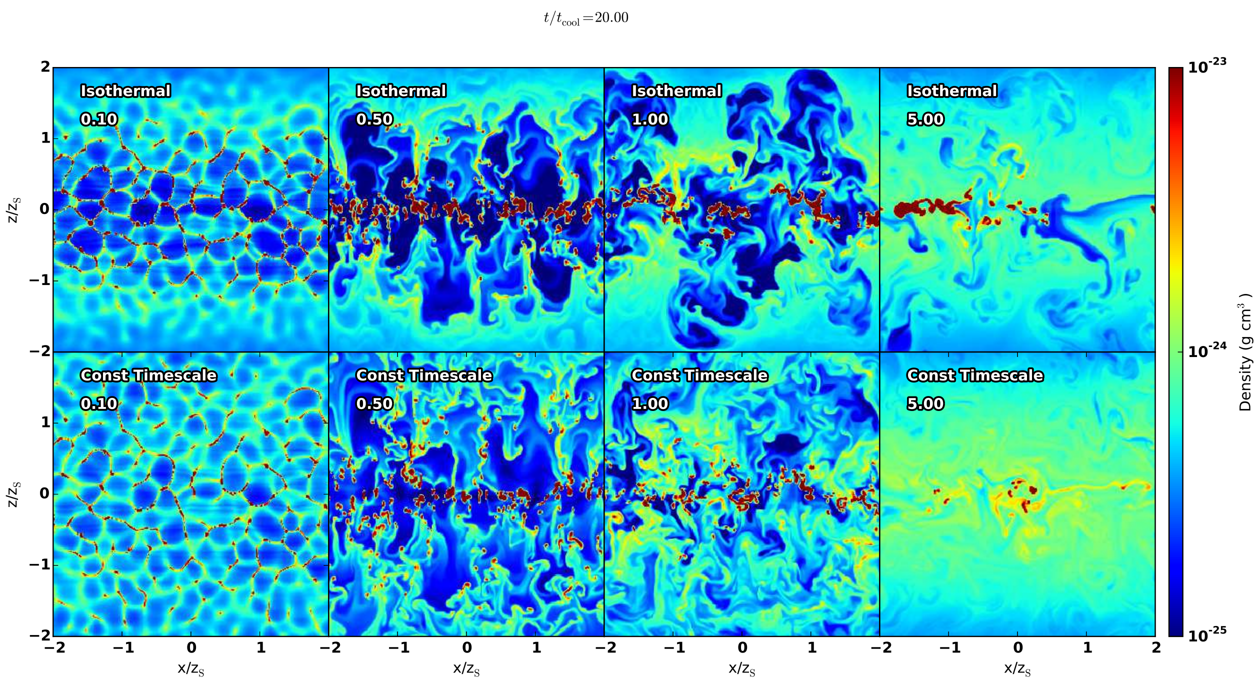

Figure 3.2 **Comparison of Meece (2015) with McCourt (2012):** Slices of gas density are shown for 2D planar simulations with initial values of $t_{\rm cool}/t_{\rm ff}$ at one scale height of 0.1, 0.5, 1.0, and 5.0 after the simulation has evolved for a time $t = 20\ t_{\rm cool,S}$. In the top row, the gas is initially isothermal. In the bottom row, the initial timescale ratio is identical throughout the entire region. Both models produce qualitatively similar results. In the isothermal case, gas near the midplane has a shorter cooling time than gas above a scale height, leading to earlier condensation near the midplane and the creation of hot bubbles that rise up through layers that have not yet begun to condense. In both cases, condensation occurs near the midplane in simulations with an an initial value of $t_{\rm cool}/t_{\rm ff} = 5$ at one sale height.

3.3 Results: The Growth of Thermal Instabilities

3.3.1 Validation of Method

We begin by conducting simulations with initial conditions similar to those in McCourt et al. (2012) to check if our model produces qualitatively similar results. Our setup differs from theirs in a number of minor details, including the shape of the gravitational profile (ours is less cuspy near the midplane) and the form of the cooling function $\Lambda(T)$. More importantly, the region near the midplane does not receive special treatment in our simulations, whereas McCourt et al. (2012) shut off heating and cooling in this region and exclude the midplane region from analysis. In spite of these differences, we obtain qualitatively similar results in the regime $t_{\rm cool}/t_{\rm ff} \lesssim 1.0$. We see close agreement for the isothermal setup for higher ratios, and somewhat more condensation is seen for the iso-cooling case for $t_{\rm cool}/t_{\rm ff} \gtrsim 1.0$.

Figure 3.2 shows slices of density in 2D Cartesian simulations with similar initial conditions to those explored by McCourt et al. (2012). The top row of Figure 3.2 uses isothermal initial conditions determined by the initial value of $t_{\rm cool}/t_{\rm ff}$ at one scale height. In comparison, the simulations in the bottom row use the iso-cooling initial conditions described in Section D.2 for which $t_{\rm cool}/t_{\rm ff}$ is initially constant throughout the simulation volume. The overall behavior is qualitatively similar in both cases and resembles the results obtained by McCourt et al. (2012) outside of the midplane region. When the ratio of timescales is below unity, the gas cools in place and forms droplets of condensate that rain down towards the midplane. In these cases, convection does not hinder thermal instability because the gas is able to adjust its thermal state faster than it is able to convect. As the ratio of timescales is increased, the dynamics of the gas become increasingly dominated by convection, although gas continues to condense around the midplane.

While each vertical pair of models illustrated in Figure 3.2 behaves similarly, a number of minor differences can be observed. Principally, condensation occurs more uniformly for iso-cooling initial conditions than for isothermal ones. This result arises from the differing density profiles needed to satisfy the HSE constraint—isothermal initial conditions have a steeper gas-density gradient and consequently a larger range in cooling time across the simulation domain. Shorter cooling times near the midplane lead to a 'cross talk' effect that is more pronounced for isothermal initial conditions. Condensation of gas near the midplane causes hot, low-density bubbles to form there and to rise to greater altitudes, creating inhomogeneity at those altitudes on a freefall time scale instead of a cooling time scale. This cross talk between lower and upper layers complicates the task of interpreting how thermal instability and condensation depend on the choice of initial timescale ratio at one scale height. The 'iso-cooling' condition, while not necessarily more physically valid, reduces this cross talk and allows for clearer interpretation of the relationship between the initial timescale ratio and

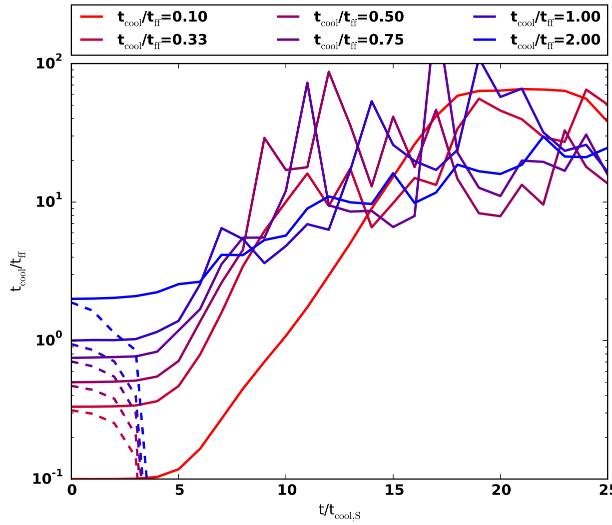

Figure 3.3 **Cooling time over freefall time for Multiphase Gas Simulations:** The average ratio of cooling time to freefall time in the ambient gas is shown as a function of time for simulations with low initial values of $t_{\rm cool}/t_{\rm ff}$. The x axis is in units of the initial cooling time at one scale height, $t_{\rm cool,S}$, rather than absolute time. Values are shown for the 2D planar geometry case. Solid lines indicate the volume-averaged value of $t_{\rm cool}/t_{\rm ff}$ within a zone $0.8\ z_{\rm S} < z < 1.2\ z_{\rm S}$. Dashed lines show the minimum value of $t_{\rm cool}/t_{\rm ff}$ within the entire box. At low values of the initial timescale ratio, the gas is able to cool in place within a few cooling times, driving the rest of the gas to $t_{\rm cool}/t_{\rm ff} > 10$. As the gas cools largely in place, instabilities grow purely on the cooling time, leading to similar behavior for all runs.

the onset of condensation. In contrast, dense midplane gas in models with isothermal initial conditions is able to condense quickly even when the initial ratio of timescales at one scale height is large. This happens because the gas near the midplane will have a lower ratio of $t_{\rm cool}/t_{\rm ff}$, leading to localized condensation.

3.3.2 Instability Growth in the Strong Cooling Regime

Using the iso-cooling simulations presented in the previous section, we have examined the evolution of perturbations for the case in which rapid cooling dominates the dynamics of the gas. If perturbations are able to cool and collapse more rapidly than they can sink, condensation proceeds on a time scale $\sim\ t_{\rm cool}$. When global thermal balance is maintained, the average $t_{\rm cool}/t_{\rm ff}$ of the ambient gas quickly increases as condensation lowers the gas mass and density of the ambient medium. Within a few cooling times, $t_{\rm cool}/t_{\rm ff}$ rises to $\gtrsim 10$, as shown in Figure 3.3. In this strong-cooling regime, the onset of condensation is determined by the growth of the initial perturbations and does not depend strongly on the initial ratio of $t_{\rm cool}/t_{\rm ff}$. Condensation continues unabated until the timescale ratio is above 10, at which point the cooling is weak enough that the condensation rate slows.

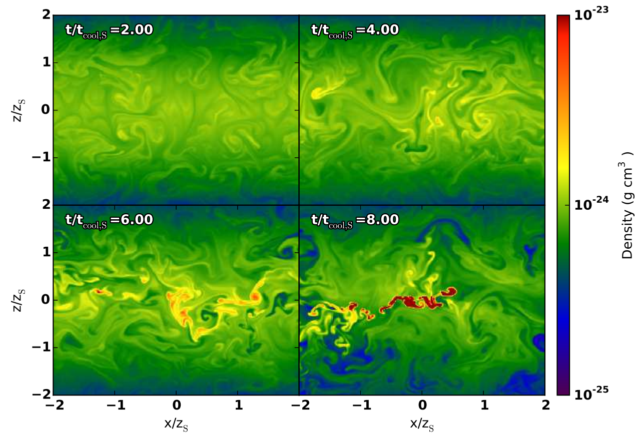

Figure 3.4 **Gas Density Evolution Over Time in Multiphase Simulations** Evolution of gas density in a 2D planar simulation with an iso-cooling initial condition of $t_{\rm cool}/t_{\rm ff} = 5.0$. After two cooling times, the gas is clearly convecting. At four cooling times no cold gas has condensed, but the amplitude of the perturbations has increased. The perturbations have been further amplified after six cooling times, and the first condensate has formed. After eight cooling times, the densest gas near the center has entered into runaway cooling, leading to continuous condensation.

3.3.3 Instability Growth in the Convective Regime

When the initial ratio of $t_{\rm cool}/t_{\rm ff}$ is large, incipient condensing regions sink into the gravitational potential faster than they can cool, leading to a roiling, convective state. The convection is subsonic, and although the pressure remains nearly constant at a given height, convection does not prevent the temperature and density perturbations generated by cooling from growing. Figure 3.4 illustrates the growth of perturbations in a medium with an initial timescale ratio of $t_{\rm cool}/t_{\rm ff} = 5.0$. After 2 cooling times (1 cooling time = 585 Myr), the gas is convecting. After 4 cooling times, the gas continues to convect, but the density perturbations have increased. After 6 cooling times, convection can no longer suppress condensation of gas near the midplane, and it cools catastrophically. After 8 cooling times, a significant amount of the dense gas has condensed.

It is thus clear that the condensation does not simply switch on when the average ratio of cooling time to the dynamical time drops below some special value. To quantify the transition of the gas from a relatively smooth, convective state to a multiphase medium, we plot in Figure 3.5 the probability distribution function of the thermal state of the gas as the run with initial $t_{\rm cool}/t_{\rm ff} = 5.0$ evolves. After several cooling times the distribution of gas in the z–$(t_{\rm cool}/t_{\rm ff})$ plane has widened considerably. After 4 cooling times, gas in the tail of the distribution has reached a ratio of around 3. At this point, further perturbation growth is inevitable and condensation begins.

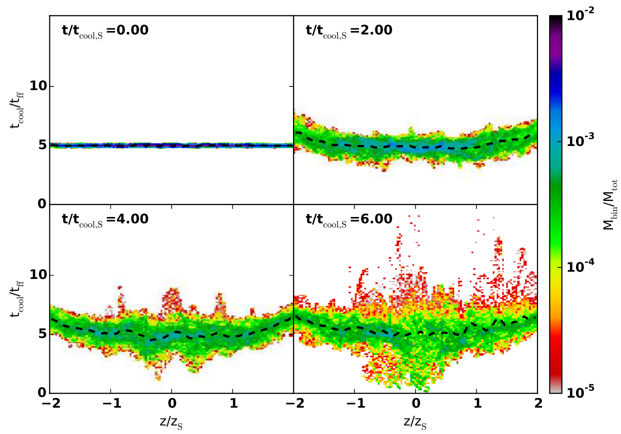

Figure 3.5 **Evolution of the Timescale Ratio in Multiphase Simulations:** Evolution of the mass-weighted probability distribution for the ratio of cooling time to freefall time for a 2D planar geometry with initial $t_{\rm cool}/t_{\rm ff} = 5.0$. The dashed black line shows the volume-weighted average ratio as a function of height. Note that when gas condenses, most of the volume is occupied by the hot gas, meaning that the volume-averaged ratio will tend to lie above the mass-weighted mean. The first panel shows the initial state of the gas where the timescale ratio is held constant throughout (with some spread due to the initial perturbation spectrum). At $t = 2.0\ t_{\rm cool,S}$, the gas has entered into a convective state and although condensation has not yet commenced, a spread in gas properties is evident. By $t = 6.0\ t_{\rm cool,S}$, a portion of the gas has reached a state with $t_{\rm cool}/t_{\rm ff} \approx 2 - 3$, and the condensation process has begun. Although some gas is entering into the cold phase, the volume averaged ratio of $t_{\rm cool}/t_{\rm ff}$ remains near its initial value as the cold gas occupies negligible volume.

Increasing the initial timescale ratio to $t_{\rm cool}/t_{\rm ff} = 20.0$ slows the condensation process and further restricts it to the midplane region, as shown in Figure 3.6. Condensation follows the same general pattern as in Figure 3.5, except that it is delayed for more than 10 times the initial cooling time and is much more pronounced near the midplane. The concentration toward the midplane occurs because cooling gas blobs can settle over a larger number of freefall times and preferentially accumulate in the midplane before condensing.

In all of our simulations, which have iso-cooling initial conditions up to $t_{\rm cool}/t_{\rm ff} = 30$, condensation eventually occurs as long as it is given enough time to develop. Figure 3.7 shows how both the average and minimum values of $t_{\rm cool}/t_{\rm ff}$ evolve during each run. Condensation in the runs with large values of $t_{\rm cool}/t_{\rm ff}$ may be surprising in light of recent theoretical studies predicting that the medium should become multiphase only if $t_{\rm cool}/t_{\rm ff} \lesssim 10$ (Sharma et al., 2012b; Gaspari et al., 2012b; Singh & Sharma, 2015), and we will discuss possible explanations for this difference in Section D.6.

Figure 3.8 shows the same simulations as Figure 3.7 plotted with time in units of the freefall time at one scale height rather than the initial cooling time. As all simulations use the same gravitational potential, the freefall time is a standard clock and corresponds to the same time interval in physical units (approximately 117 million years). When the initial ratio of cooling time to freefall time exceeds ~ 10, condensation occurs after ~ 100 freefall times, corresponding to a timescale comparable to the Hubble time.

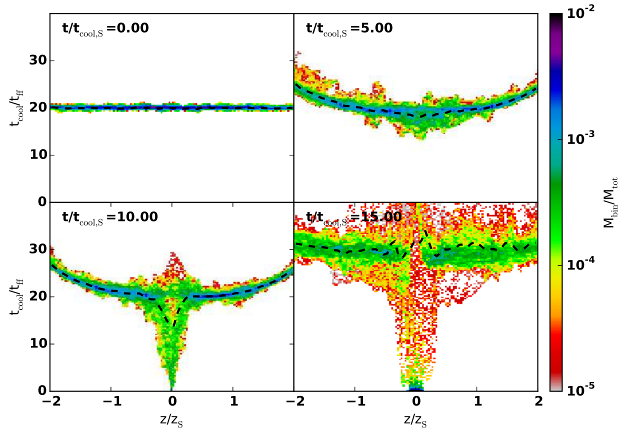

Figure 3.6 **Evolution of the Timescale for More Stable Initial Conditions:** Same as Figure 3.5 except for an initial timescale ratio of $t_{\rm cool}/t_{\rm ff} = 20.0$. By $t = 5.0$ $\rm t_{cool}$, perturbations have started to grow but have not yet led to condensation. As the gas is able to undergo more freefall times per cooling time than in the case of $t_{\rm cool}/t_{\rm ff} = 5.0$, cooler gas is able to effectively settle towards the midplane. Nevertheless, condensation is still able to occur near the midplane even though the volume averaged value of $t_{\rm cool}/t_{\rm ff}$ remains near 10.

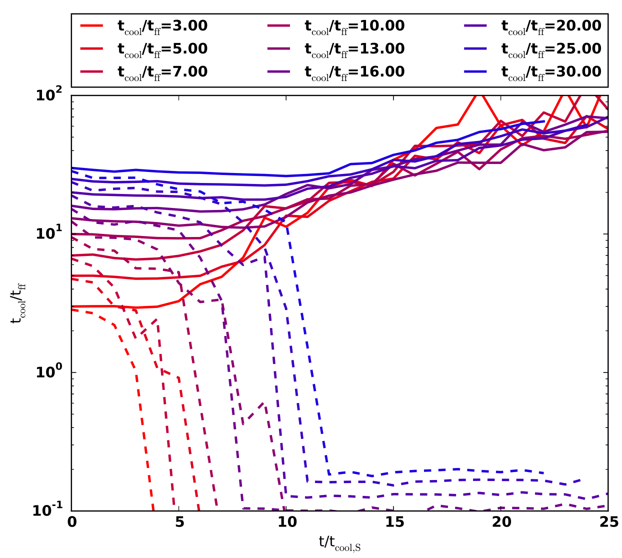

Figure 3.7 **Evolution of the TimeScale Ratio for More Stable ICs:** Same as Figure 3.3, except for runs with larger initial values of $t_{\rm cool}/t_{\rm ff}$. In each simulation, the minimum value of $t_{\rm cool}/t_{\rm ff}$ decreases on a timescale roughly proportional to the cooling time. When the initial ratio is higher, it takes several cooling times for gas to develop regions with a minimum timescale ratio near unity; therefore, condensation is delayed in these runs. Note that runs with larger values of $t_{\rm cool}/t_{\rm ff}$ have a low overall cooling rate which, combined with the temperature floor of $\rm T_{floor} = 5 \times 10^6$ K, produces the floor in the timescale ratio.

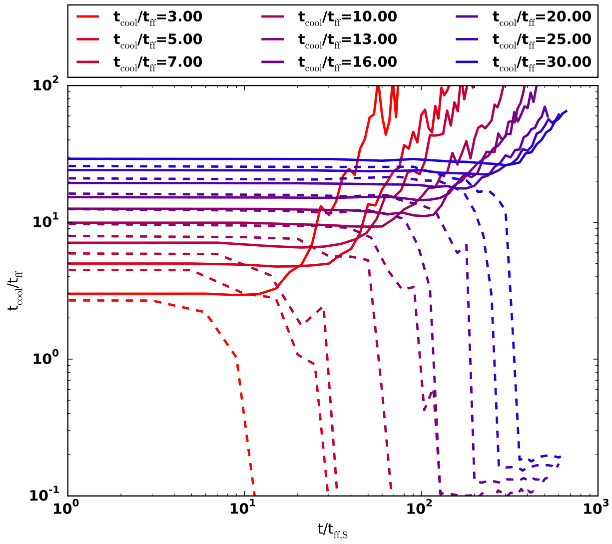

Figure 3.8 **Evolution of the TimeScale Ration in Freefall Times:** Same as Figure 3.7 except with time plotted in units of the freefall time at one scale height rather than the initial cooling time at one scale height.

3.3.4 Transition to the Condensed State

While studying the growth of thermal instabilities gives insight into the conditions under which gas will condense, it does not necessarily explain how the gas reaches a condensed state or how an individual parcel of gas behaves. Figure 3.9 depicts the gas distribution in the $\rho - T$ plane integrated over 30 cooling times. To compute this distribution, we bin gas mass in $\rho - T$ space in each data output (which are evenly spaced in time), sum over all of the outputs, and normalize so that the integral over the distribution is equal to 1. This probability distribution corresponds to the probability of a parcel of gas being found in a given thermodynamic state at some point during the simulation. The gas is for the most part constrained to a line of constant pressure with spread due to gravitational stratification. The distribution has two peaks; a low density, high temperature node in which the gas is convecting, and a cool, low temperature node representing the condensed state of the gas. The probability of finding gas in the connecting region is low, indicating that condensation from the hot phase into the cold phase proceeds rapidly once it begins.

Figure 3.10 illustrates the dynamics of the gas during the convective stage and the condensation process using the motion of a Lagrangian tracer particle in phase space. The figure shows the path of a representative particle which condenses early in the simulation. For several cooling times, the gas simply convects within a narrow portion of phase space. As the thermal perturbations are amplified, the gas is driven to a colder, denser state which is where condensation occurs. When the gas does condense, the condensation process is very rapid, and the gas stays in the condensed phase afterwards.

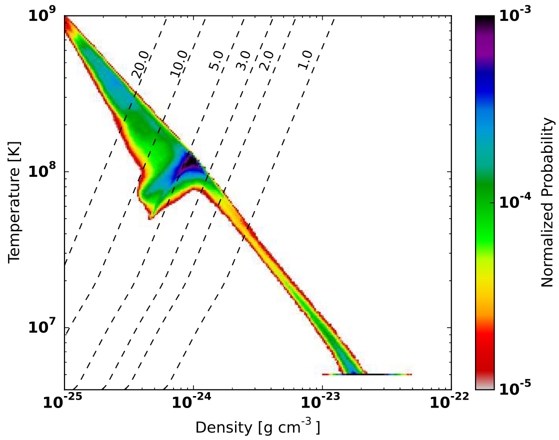

Figure 3.9 **PDF of Gas Density and Temperature:** The probability distribution function of the gas in the $\rho - T$ plane, averaged over 30 cooling times in the 2D planar simulation with an initial timescale ratio of $t_{\rm cool}/t_{\rm ff} = 5$. Note that a large fraction of the gas is located at the temperature floor, near the x-axis at a density slightly above 10^{-23} g cm^{-3}. As the convection and condensation processes proceed subsonically, the process is largely isobaric, with a modest spread due to gravitational stratification. Lines of constant cooling time are shown as dashed lines, labeled with the ratio of cooling time to freefall time at 1 scale height. Note that the gas spends very little time between the line $t_{\rm cool}/t_{\rm ff} = 2$ and the temperature floor, indicating that once the threshold is reached, condensation proceeds rapidly.

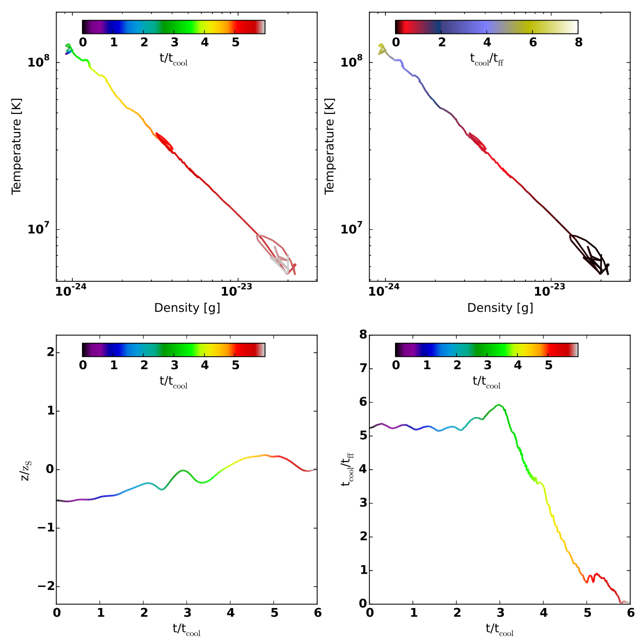

Figure 3.10 **Tracer Particle Evolution:** The dynamics of fluid during the condensation process are shown in the dynamics of a Lagrangian tracer particle through phase space. The particles are inserted during initialization in the 2D planar simulation with an initial timescale ratio of 5. The upper left panel shows the particle's path through $\rho - T$ space, with the color of the line showing elapsed time in cooling times. The upper right panel also shows the path through $\rho - T$ space, but is colored by the ratio of cooling to freefall time. The bottom left panel shows particle height vs. time, and the bottom **right** shows the timescale ratio as a function of time.

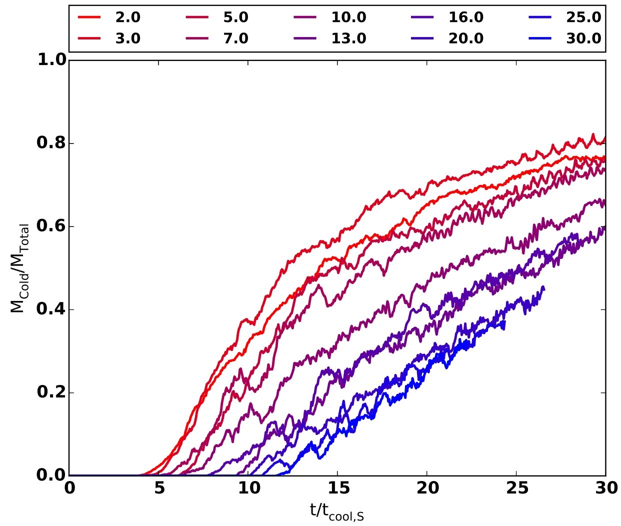

Figure 3.11 **Cold Gas Fraction in the Multiphase Simulations:** The fraction of mass in the condensed state is shown as a function of time for 2D planar runs with large initial values of $t_{\rm cool}/t_{\rm ff}$. The condensed fraction is measured over the entire domain.

3.3.5 Condensation Rate

In our simulations, condensed gas remains in the condensed state and settles towards the center. After the onset of condensation the gas segregates into two phases - the cool condensed material in the center and the hot, convective gas that remains uncondensed. This departure from the expectation of self-regulation is a consequence of our feedback implementation and is discussed further in Section 3.4.4. Still, it is instructive to examine the rate of condensation in our simulations, as is shown in Figure 3.11. Following the onset of condensation, instabilities continue to grow on the cooling timescale. Each simulation behaves similarly on a thermal timescale, with a roughly linear growth in the total condensed fraction.

3.3.6 Effect of Geometry

Simulations with different geometries are shown in Figure 3.12. All simulations use the same initial conditions ($t_{\rm cool}/t_{\rm ff} = 5.0$). In the spherical case, gravity pulls towards the origin, while in the cylindrical setup gravity pulls towards the symmetry axis. All simulations exhibit similar thermal behavior. After 10 cooling times, the gas has entered into a convective state and condensation has begun near the center of the potential. In the non-planar runs, less gas condenses as the region near the center occupies less volume. Nevertheless, we do not observe a significant change in the condensation process among simulations with different geometries.

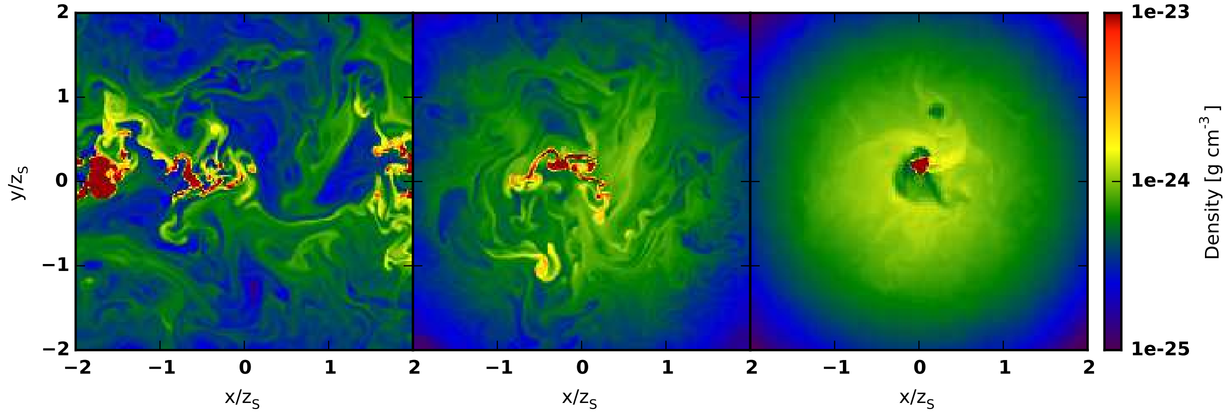

Figure 3.12 **Effect of Geometry in Multiphase Gas Simulations:** The evolution of runs with an initial $t_{\mathrm{cool}}/t_{\mathrm{ff}}$ of 5.0 are shown for different geometries at $t = 10\ t_{\mathrm{cool}}$. All runs use an identical setup with respect to the radial coordinate, though the definition or the radial coordinate is changed based on the geometry of the simulation. The 2D runs use a static grid of 300×300 cells, while the 3D runs use a root grid of 128^3 cells with 2 layers of adaptive mesh.

3.4 Discussion and Relationship to Related Work

Our simulations would seem to indicate that any medium subject to a heating/cooling balance as we have described in our model will eventually succumb to thermal instability and produce condensation. Nevertheless, observations seem to indicate that clusters with time scale ratios above roughly 10 do not produce much multiphase gas. To explain this discrepancy, we note that at a radius of around 30 kpc, a time scale ratio of 10 in a large galaxy cluster corresponds to a cooling time on the order of a Gyr. Physical processes such as mergers, star formation, and AGN feedback occur on shorter timescales, rendering the condensation process sub-dominant in these cases. Therefore, in a realistic cluster environment only clusters with a cooling time to freefall time ratio of $\lesssim 10$ are likely to develop condensation. An important caveat to this observation is that while the growth of thermal instabilities from initially small perturbations may be unimportant on cluster timescales, if the gas is inhomogeneous due to other physical processes (such as an AGN jet) condensation may occur in the tail of the thermal distributions shown in Figure 3.5 and 3.6. Thus, predicting the onset of condensation is not as simple as measuring the value of $t_{\mathrm{cool}}/t_{\mathrm{ff}}$; the level of inhomogeneity must also be taken into account.

Our simulations examine the formation of multiphase gas in an idealized setting wherein global balance between heating and cooling is strictly enforced. While this model gives rise to results that are qualitatively consistent with observations, it clearly neglects the complex physics of AGN feedback and heat transport which occur in real clusters. In this section, we discuss our results in light of current observations of multiphase gas and previous simulations of condensation and consider the complications that inclusion of additional physical processes would cause.

3.4.1 Observations of Multiphase Gas

Owing to the timescales involved and the limits of current telescopes, astronomers can not directly observe the condensation process in the ICM. Nevertheless, the past decade has deepened the field's appreciation of a fascinating dichotomy in cluster properties when cluster cores are probed for cold gas and signatures of AGN feedback. While cooling is generally suppressed in cool-core galaxy clusters (Peterson et al., 2003; Peterson & Fabian, 2006), at least some cold gas is observed in galaxies with low central temperatures, as seen in the works of McDonald et al. (2010) and Werner et al. (2010). Cavagnolo et al. (2008) considers the entropy profiles, radio emissions, and presence of Hα in the ACCEPT sample of 222 galaxy clusters. As Hα emission requires the presence of cold (relative to the ICM) gas, the presence or absence of Hα in a cluster may be taken as an indicator of multiphase gas. In the clusters with Hα observations, Hα is conclusively detected in slightly over half of the sample. A strong correlation is seen between the presence of Hα and the core entropy; clusters with Hα have central entropies below 30 keV cm^2, while those without Hα detections tend to lie above the 30 KeV line. When the entropy profile is used to infer a cooling time, (as in Voit & Donahue, 2015; Voit et al., 2014) a central entropy of 30 KeV corresponds to a cooling time of around 1 billion years, consistent with a cooling time to freefall time ratio of around 10. In clusters in the ACCEPT sample, those with detected Hα emission consistently have $t_{\rm cool}/t_{\rm ff}$ values below $\simeq 20$, while those without Hα detections lie entirely above that value.

3.4.2 Simulations of Multiphase Gas

McCourt et al. (2012), upon which this study is based, finds that precipitation will occur rapidly if the gas is able to cool in place, which occurs when $t_{\rm cool}/t_{\rm ff} \lesssim 1$. The authors also conclude that the condensation process is relatively insensitive to variations in the heating rate and mechanism. Employing a similar method, Sharma et al. (2012b) finds that condensation may occur in gas with a timescale ratio of $\lesssim 10$ in a spherical simulation, an enhancement they attribute to the compression of overdense blobs descending in a spherical geometry. Additionally, Sharma et al. (2012b) concludes that condensation does not occur when the timescale ratio rises above 10.

Analytic work has lent further credence to the idea that $t_{\rm cool}/t_{\rm ff} \lesssim 10$ represents a critical threshold for condensation. Singh & Sharma (2015), extending the analysis of Pizzolato & Soker (2005), finds that small instabilities may grow when $t_{\rm cool}/t_{\rm ff} \lesssim 1$ for planar geometries and, when the effects of geometric compression are included, may grow for $t_{\rm cool}/t_{\rm ff} \lesssim 10$ for spherical geometries. While the results presented in Section 4.3 of this paper suggest a moderately higher threshold for the planar case, we believe that these results are largely consistent with Singh & Sharma (2015) in the context of individual overdensities cooling and condensing in place. In our simulations, however, we see that overdensities in a medium above the critical threshold oscillate, leading to a roiling state that develops further perturbations. This cross talk effect between layers generates non-linear perturbations and causes the temperature dispersion in the medium to grow on the cooling timescale. When the cold tail of the distribution has dropped to $t_{\rm cool}/t_{\rm ff} \lesssim 2-3$ the condensation process begins. Thus we find that the mechanism responsible for condensation above the critical threshold is not geometric compression but the continued growth of perturbations following the onset of convection in the gas.

Simulations that employ more realistic heating mechanisms also find that condensation occurs in galaxy clusters, albeit under somewhat different circumstances than in simulations with idealized heating. Li & Bryan (2014b) employ an AGN feedback algorithm in which heating is triggered by cold gas accretion. The study finds that condensation occurs when $3 \lesssim t_{\rm cool}/t_{\rm ff} \lesssim 10$. This condensation occurs along the axis of the jet, where dense gas is dragged up and is able to cool as it falls. This is consistent with our findings, in which the thermal instability can grow when $t_{\rm cool}/t_{\rm ff} \lesssim 10$, but only when gas is sufficiently hetrogeneous. Similarly, Gaspari et al. (2012b) employs jet heating in response to accretion and finds that multiphase gas can form when $t_{\rm cool}/t_{\rm ff} \lesssim 10$.

3.4.3 Caveats and Limitations

In this study, we have used an idealized model to simulate the onset of condensation in galaxy clusters. While the simplicity makes this model easy to analyze, we have left out physics that may have significant impact on the development of a multiphase medium. In particular, conduction and the presence of magnetic fields may inhibit or shape the growth of condensation. Conduction works to smooth out temperature perturbations, while magnetic fields will lead to conduction being anisotropic.

Magnetic fields in clusters are poorly understood. While weak, they are known to be present and may be dynamically important in cluster cores (Carilli & Taylor (2002) and references therein). More important for this work, magnetic fields in a plasma will lead to anisotropic conduction, channeling heat along the direction of magnetic field lines as explored in Ruszkowski et al. (2011). Similarly, Wagh et al. (2014) studies the growth of thermal instabilities in a spherical setup and includes both conduction and magnetic fields. Anisotropic conduction is not found to inhibit condensation, but does lead to the formation of filaments rather than globules of dense gas. Conduction is found to inhibit condensation if the efficiency is above 0.3 of the Spitzer value.

In addition to these omissions, our assumed heating function does not capture the true physical process responsible for transferring energy from the AGN to the ICM. While the details of AGN heat transfer are not currently understood, several mechanisms have been proposed, including shocks (McNamara & Nulsen, 2012; Ruszkowski et al., 2004), cosmic rays (Sharma et al., 2010; Fujita et al., 2013; Fujita & Ohira, 2011, 2012), turbulent mixing (Sharma et al., 2009; Banerjee & Sharma, 2014b), PdV work from the inflation of hot bubbles (McNamara & Nulsen, 2007; Bîrzan et al., 2004), and the uplifting of cool gas by rising bubbles (Million et al., 2010). The actual heating function is unlikely to maintain perfect thermal balance, and presumably does not act in a strictly volumetric sense as assumed in this work. Still, the lack of cold gas and star formation in cool-core clusters implies that the heating function must broadly maintain thermal equilibrium, making the model considered in this work physically relevant.

3.4.4 Self-Regulation

The gas does not reach a steady state, as might be expected for an ideal self-regulating system. Instead, condensation continues in the convective gas after the condensation process has begun, increasing the separation between the hot and cold phases. In real clusters, feedback is expected to operate in a thermostat-like manner, which should produce a rough thermal equilibrium. The lack of self-regulation in our simulations is purely an effect of the heating model that we employ, and does not accurately capture the response of feedback to condensation. However, if we imagine feedback to be powered by condensation, we can use the calculated heating rate to determine what feedback efficiency would be necessary for the system to balance radiative losses.

During accretion, AGN are expected to convert a significant fraction of the infalling mass into energy that is then returned to the surrounding medium. The feedback rate can be related to the mass accretion via

$$\dot{E} \approx \epsilon \dot{M} c^2 \tag{3.8}$$

where $\dot{E}$ is the total energy output, ϵ is an efficiency parameter, and $\dot{M}$ is the mass accretion rate. Under the assumptions that all of the condensing gas is used to power feedback and that all of the feedback energy is transferred to the ICM, we have estimated the conversion efficiency necessary to maintain thermal balance. The estimate is shown in Figure 3.13 for several initial values of $t_{\rm cool}/t_{\rm ff}$. Once condensation has begun, the required efficiency in all runs reaches a value of around 10^{-3}, in line with the values found in Sharma et al. (2012b). As the accumulation of cold gas near the midplane is an artifact of our setup and would not be expected in a real cluster, we calculate the cooling rate over the ambient gas, which is that gas that is above the temperature floor of 5.0×10^6 K. Although we do not explore the mechanism for releasing mass-energy

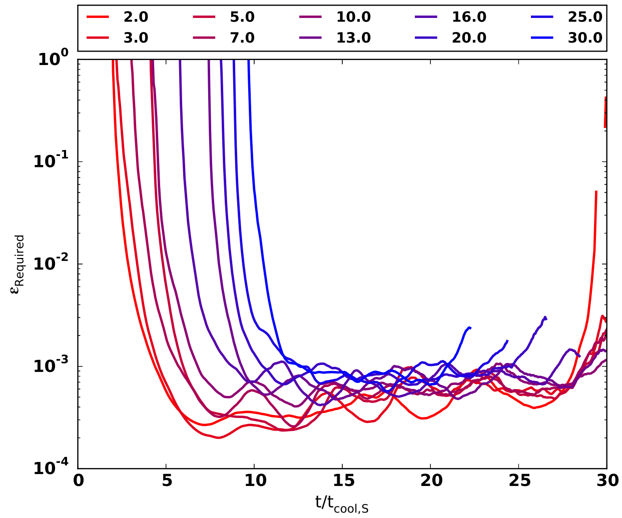

Figure 3.13 **Necessary AGN Efficiency to Balance Cooling in Multiphase Gas Simulations:** The feedback efficiency necessary to maintain thermal balance in the hot gas is shown for 2D planar runs starting with different values of $t_{\rm cool}/t_{\rm ff}$. The required efficiency is calculated as $\epsilon = \dot{E}/\dot{M}_{Cold}c^2$, where $\dot{E}$ is the cooling rate of all gas above the temperature floor. Both the cooling rate and the condensation rate have been smoothed over a cooling time.

from condensed gas in this work, if condensation resulting from the growth of thermal perturbations is in principle capable of balancing radiative cooling in the ICM, thermal instability must be taken seriously as a feature of a self-regulating energy cycle in cool-core clusters.

3.5 Conclusions and Future Work

In this study, we have investigated the onset of convection in a thermally unstable medium using an idealized model, including a heating scheme that strictly enforces a global heating-cooling balance. Although a simplification, this model gives insight into the conditions necessary for the onset of condensation in a gravitationally stratified medium such as that in a cool-core galaxy cluster. This study indicates that condensation proceeds as follows:

- If heating is able to balance cooling at all radii, thermal instabilities will grow in amplitude, regardless of the initial conditions.
- If the ratio of the cooling to the freefall time is $\lesssim 2$, (the strong cooling regime) the gas will condense in place, driving the volume-averaged $t_{\rm cool}/t_{\rm ff}$ value above 10.
- Above a ratio of $t_{\rm cool}/t_{\rm ff} \approx 10$, perturbations will grow on a timescale proportional to the cooling time.
- Once the perturbation distribution has broadened, gas with $t_{\rm cool}/t_{\rm ff} \approx 2 - 4$ will condense, even if the volume-averaged ratio of $t_{\rm cool}/t_{\rm ff}$ is above 10.
- If the timescale ratio is $\gtrsim 10$, the timescale for condensation to occur in gas with $t_{\rm cool} \sim 1$ Gyr is comparable to the Hubble Time and greatly exceeds other relevant cluster timescales.

A fundamental limitation of this work is that the model assumes a heating function that is idealized and does not mimic a specific physical process. In preparation for future work, it will be necessary to examine a greater variety of heating modes, including models more analogous to jet feedback and quasar winds from accreting supermassive black holes. The physical processes underlying black hole accretion, feedback, and heat transfer to the ICM are still poorly understood, and elucidating them will form the focus of future studies.

3.6 Acknowledgments

The authors would like to thank Gus Evrard, Devin Silvia, Greg Bryan, and Yuan Li for helpful discussions during the preparation of this paper. This work was supported by NASA through grant NNX12AC98G and Hubble Theory Grant HST-AR-13261.01-A, and by the National Science Foundation through grant PHY-0941373. The simulations presented in this paper were performed and analyzed on the TACC Stampede supercomputer under XSEDE allocations TG-AST090040 and TG-AST100004. This work was supported in part by Michigan State University through computational resources provided by the Institute for Cyber-Enabled Research. BWO was supported in part by the sabbatical visitor program at the Michigan Institute for Research in Astrophysics (MIRA) at the University of Michigan in Ann Arbor, and gratefully acknowledges their hospitality. `Enzo` and `yt` are developed by a large number of independent researchers from numerous institutions around the world. Their commitment to open science has helped make this work possible.

4 Triggering and Delivery Algorithms for AGN Feedback

4.1 Introduction

[1]An active galactic nucleus (AGN) is thought to be present in the core of nearly every massive galaxy and galaxy cluster. Based on estimates of jet power from AGN-inflated cavities, it has become clear that an AGN can strongly influence cooling and condensation of gas in its host galaxy (e.g., McNamara & Nulsen, 2012), potentially explaining the relationships observed between the mass of a galaxy's central black hole and the velocity dispersion of its stars (e.g., Merritt, 2000; Ferrarese & Merritt, 2000), as well as the star-formation properties of galaxies with AGNs (e.g., Kauffmann et al., 2003). Directly simulating the co-evolution of AGNs together with their host galaxies is not computationally feasible due to the large differences in mass and size between an AGN and its host galaxy. Also, the diverse set of complex physical processes that govern AGN accretion and outflow production remain poorly understood. To circumvent these difficulties in studies of galaxy evolution, simulators have developed a number of "subgrid" implementations of AGN feedback that are intended to capture the interplay between the AGN and its environment without representing the details of AGN accretion on smaller scales (see, for example Omma et al., 2004; Springel et al., 2005a; Puchwein et al., 2008; Booth & Schaye, 2009; Gaspari et al., 2011b; Dubois et al., 2012; Li & Bryan, 2014a; Steinborn et al., 2015). However, subgrid implementations of AGN feedback vary widely, and there has been little systematic comparison (but see Wurster & Thacker, 2013; Yang et al., 2012). From the explorations of parameter space carried out in these studies, it has become evident that varying certain AGN feedback parameters can lead to strong differences in feedback power and energy propogation. In this paper, we compare several of the popular methods for implementing AGN feedback.

An AGN consists of a supermassive black hole (SMBH) surrounded by a disk of accreting material. Twisted magnetic fields in the disk are thought to channel charged particles into jets, which can draw additional power from the spin of the SMBH via the Blandford-Znajek effect (Blandford & Znajek, 1977; Blandford & Payne, 1982). These relativistic jets produce synchrotron emission, which is observed in the radio band. Hence, this mode of AGN energy output is termed "radio-mode" feedback (e.g., Churazov et al., 2001; Springel et al., 2005b). Additionally, differential rotation in the accretion disk will heat the accreting

[1]This chapter consists of material submitted to The Astrophysical Journal (Meece et al., 2016). It has been reformatted for inclusion here. For information about copyright and reuse, see Appendix E.

material, producing a strong UV flux. If the SMBH is accreting near the Eddington Limit, radiation pressure may also drive large outflows. This "quasar-mode" feedback (e.g., Churazov et al., 2005) is composed of non-relativistic material and is more isotropic than radio-mode feedback.

The length and mass scales that are important for AGN are much smaller than the range covered by galaxies and galaxy clusters. For example, a black hole with a mass similar to the one dwelling at the center of the Perseus Cluster ($\sim 3.4 \times 10^8 \, M_\odot$; see Wilman et al., 2005) has a Schwarzchild radius of only a few AU, whereas the virial radius of a galaxy cluster is $\gtrsim 1$ Mpc. Cosmological simulations capable of modeling entire galaxy clusters typically have a maximum resolution of ~ 1 kpc, meaning that the AGN's behavior must be approximated with a subgrid model. Furthermore, AGN are known to be variable on timescales much shorter than the dynamical time of a galaxy. Cosmological simulations that model structure formation over a Hubble Time must therefore rely on an AGN model that smooths out this short-term variability while preserving the large-scale behavior of the resulting feedback.

In order for a self-regulated feedback loop to arise, a subgrid AGN model must capture the coupling between an AGN and its fuel supply. A triggering algorithm must somehow estimate the mass accretion rate onto the SMBH, which translates into a proportional release of feedback energy. Then a delivery algorithm must prescribe how that feedback energy interacts with the local environment. In cosmological simulations, the subgrid AGN model must also include prescriptions for following the creation, advection, and merger of SMBHs, although these are not discussed in this work (see Sijacki et al., 2007; Di Matteo et al., 2008; Wurster & Thacker, 2013; Vogelsberger et al., 2013, for more discussion on these topics). Instead, we are focusing on just the triggering and delivery algorithms.

There are a number of reasons to believe that AGN feedback in massive galaxies is self-regulated. First, as stated earlier, strong relationships have been found between the masses of SMBHs and the properties of their host galaxies. Second, AGNs are considered the best candidates for solving the "Cooling Flow" problem in galaxy clusters and elliptical galaxies (Binney & Tabor, 1995; McNamara & Nulsen, 2007; Nulsen & McNamara, 2013). Many galaxy clusters have central cooling times that are far shorter than the age of the clusters, but the observed star-formation rates are an order of magnitude or more below what would be expected from uninhibited cooling (O'Dea et al., 2008, 2010; McDonald et al., 2011). Also, the amounts of cold gas that seem to be accumulating are much less than one would naively expect (Peterson et al., 2003; Peterson & Fabian, 2006). This tension implies the existence of a heat source that roughly balances cooling losses. Non-AGN heat sources, such as supernovae, mergers, conduction, and preheating have been proposed, but are either not powerful enough to balance cooling (e.g., Skory et al., 2013) or are inconsistent with observations. AGNs, however, are known to be present in the central galaxies of galaxy clusters and produce feedback energy comparable to the cooling rate. Binney & Tabor (1995) showed that when cooling-triggered jets are added to models of cool-core clusters, alternating periods cooling and jet heating can lead to a quasi-steady state for the ICM in the cluster core. As discussed in McNamara & Nulsen (2012), the jet power must be closely coupled to the cooling rate if AGN are balancing cooling in clusters. Otherwise, the AGN would either overheat or underheat the intracluster medium (ICM).

One simple algorithm for estimating the AGN accretion rate bases the scaling properties on the Bondi-Hoyle accretion model, set out in Bondi (1952), which implicitly assumes that the SMBH is accreting hot ambient gas directly from the ICM. Strictly speaking, such a Bondi accretion flow should be steady-state, spherically symmetric, and isentropic. Accretion then becomes supersonic within the Bondi radius given by $R_{\rm Bondi} \approx 2GM_{\rm BH}/c_s^2$ where $M_{\rm BH}$ is the black hole mass and c_s is the sound speed of the gas near $R_{\rm Bondi}$, and proceeds at a rate $\dot{M}_{\rm Bondi}$ that depends on $M_{\rm BH}$ and c_s. However, the Bondi radius is unresolved in many numerical simulations of AGN feedback, as is its impact on galaxy evolution. Springel et al. (2005a) therefore proposed a parameterized Bondi accretion rate with an artificial boost factor α such that $\dot{M}_{\rm BH} = \alpha \dot{M}_{\rm Bondi}$. The boost factor α is typically chosen to be large because the actual gas properties at the Bondi radius are likely to permit a greater accretion rate than would arise in under-resolved simulations. Springel et al. (2005a) and subsequent studies following up on that work use $\alpha = 100$, while Khalatyan et al. (2008) use $\alpha = 300$. Hopkins & Hernquist (2006), in contrast, use a factor that is near unity, albeit for studies of galaxy-scale phenomena.

In reality, the assumptions of Bondi accretion — steady homogeneous flow, spherical symmetry, and adiabaticity — are unlikely to be valid near the Bondi radius around a massive galaxy's SMBH (see, for example, the discussion in Mathews & Guo, 2012). Furthermore, models relying on standard Bondi accretion have problems generating sufficiently powerful outflows without a large boosting factor (see BS09 for discussion) and with reproducing the properties of observed cool-core clusters absent fine tuning. An alternative model for self-regulated accretion, described by Pizzolato & Soker (2005), posits that the AGN is primarily fueled by accretion of cold, dense gas that rains down in a stochastic manner. Aside from the prior assumption that the AGN heating rate is linked to cooling in the ICM, this model is supported by observations of cold gas and star formation which indicate that at least some gas is able to cool (e.g., Edge, 2001; Cavagnolo et al., 2008; O'Dea et al., 2008). In this "moderate cooling flow" or "cold feedback" model, radial mixing resulting from strong AGN outbursts creates large inhomogeneities that cool and condense at radii between 5 and 30 kpc from the AGN. The condensates then rain down on the SMBH, powering subsequent outbursts. This model couples the AGN to the cooling properties of the entire cluster core rather than only to the region directly surrounding the SMBH. Importantly, the coupling also occurs over timescales longer than the freefall in the core, leaving time for gas to cool and condense. Cold mode feedback has been implemented in recent simulations, notably those of Gaspari et al. (2011a,b, 2012b); Li & Bryan (2014a,b); Li et al. (2015), which attain self-regulated states similar to those observed in galaxy-cluster cores.

To mimic the effects of both cold and hot accretion modes, Booth & Schaye (2009, hereafter referred to as BS09) proposed a model that invokes Bondi accretion with a density-dependent boost factor. This boost factor equals unity at low densities, giving the classical Bondi accretion rate, but ramps up quickly above a pre-chosen density threshold in order to account, rather crudely, for cooling, condensation, and accretion of condensed gas.

In the simplest models for delivery of AGN feedback, all of the feedback energy is assumed to thermalize at scales below the resolution of the grid and is deposited as thermal energy in a small central region. This approach is used in Springel et al. (2005a) and subsequent works, including recent simulations such as the Illustris simulation (Vogelsberger et al., 2014), Rhapsody-G (Hahn et al., 2015) and the simulations of Rasia et al. (2015). In reality, AGN outflows are likely asymmetric on scales of several kpc with a significant proportion of their energy in kinetic form. Such bipolar outflows may be important for transporting feedback energy to large distances from the AGN and for mixing metals out to distances of ~ 100 kpc from the central galaxy (Kirkpatrick et al., 2011; Kirkpatrick & McNamara, 2015). Although much work has been done studying highly collimated outflows on small scales over short time periods (Vernaleo & Reynolds, 2006; Omma et al., 2004), it is not straightforward to implement them in large-scale simulations with coarser resolution.

Given the increasing awareness that a proper treatment of AGN feedback is essential for accurate modeling of the evolution of large galaxies, it is important that the consequences of different AGN feedback implementations be understood. The rest of this paper compares several commonly used algorithms for triggering and delivery of AGN feedback in the context of an idealized galaxy-cluster core, in order to explore how they differ in representing the coupling of an AGN to its environment, the total AGN feedback energy produced, and the resulting thermodynamic profiles of the ambient medium. Section D.2 discusses our simulation setup and outlines the triggering and delivery methods we study. Section 4.3 describes the results of changing the triggering and delivery algorithms. Section D.6 discusses our results in the context of thermal-instability analyses of cold gas accumulation and self regulation, along with a discussion of how physical processes that were not included might have affected our results if they had been included. Finally, Section 4.5 summarizes the key results and points out avenues and opportunities for further study.

4.2 Method

In this work, we consider the interplay between ICM cooling and AGN feedback using a simplified AGN model in an idealized galaxy cluster environment. The simulations are performed using the adaptive mesh hydrodynamics code `Enzo`[2] (Bryan et al., 2014) and analyzed using the `yt`[3] analysis toolkit (Turk et al., 2011).

4.2.1 Simulation Environment

Our simulations include hydrodynamics, gravity, radiative cooling, and AGN feedback. We use a static gravitational potential representing both the cluster and its BCG but do not account for the self-gravity of the gas, which we assume to be negligible. We use a tabulated cooling function taken from Schure et al. (2009), assuming a uniform metallicity of half the Solar value. This cooling function does not allow gas to cool below 10^4 K, which does not affect the qualitative behavior of our simulations, since any processes occurring at lower temperatures would take place below our spatial resolution limit. For analysis purposes, we define any gas below 3×10^4 K as "cold." Section 4.4.2 discusses the potential effects of including additional physical processes such as magnetic fields, conduction, and star formation, which may affect AGN feedback but are not included in our simulations.

Unless otherwise noted, the simulation setup encompassed a box of length 3.2 Mpc per side with a 64^3 cell root grid and 8 levels of AMR refinement, giving a maximum spatial resolution of 196 pc. A set of 8 nested grids, centered on the cluster core, with twice the resolution and half the width of the previous level, were created during initialization and were never de-refined. Additional refinement was allowed to occur based on strong density or energy gradients, baryon overdensity, and cooling. All cells containing material that was ejected from the central 10 kpc, as indicated by a passive tracer field added to material within that region, were covered by at least 4 levels of refinement. Finally, the zone around the AGN where accretion was measured and feedback was applied was always refined to the maximum level. We do not take cosmological expansion into account.

4.2.2 Cluster Setup

Following the work of Li & Bryan (2012), we initialize the ICM as a hydrostatic sphere of gas within a static spherical gravitational potential. The gravitational potential comprises two components: an NFW halo and the stellar mass profile of the BCG. The virial mass M_{200} and concentration parameter c of the NFW halo

[2]http://enzo-project.org/
[3]http://yt-project.org/

are defined with respect to the radius within which the mean mass density is 200 times the critical density. For the BCG we assume a mass profile of the form

$$M_*(r) = M_4 \left[\frac{2^{\alpha_* - \beta_*}}{(r/4\,\mathrm{kpc})^{-\alpha_*} (1 + r/4\,\mathrm{kpc})^{\alpha_* - \beta_*}} \right] \ , \tag{4.1}$$

where M_4 is the stellar mass within 4 kpc and α_* and β_* are constants. As in Li & Bryan (2012) and Mathews et al. (2006), we used the Perseus cluster as a template, choosing $M_{200} = 8.5 \times 10^{14}$ $\mathrm{M}_\odot$, $c = 6.81$ for the NFW halo, $M_4 = 7.5 \times 10^{10}$ $\mathrm{M}_\odot$, $\alpha_* = 0.1$, and $\beta_* = 1.43$ for the BCG. With these mass profiles, the BCG is gravitationally dominant $\lesssim 10$ kpc from the center, while outside of this radius the NFW halo dominates the potential.

Although we do not take cosmological expansion into account in our simulations, we do use a vanilla ΛCDM model in order to specify the virial mass of the NFW halo and to set its gas temperature. For initialization, we assume a cluster at redshift $z = 0$ and a cosmology with $\Omega_M = 0.3$, $\Omega_\Lambda = 0.7$, and $H_0 = 70$ km/s/Mpc. We do not expect our results to be sensitive to small changes in these parameter values.

The hydrostatic gas in the halo is initialized with an entropy profile of the form

$$K(r) = K_0 + K_{100}(r/100\mathrm{kpc})^{\alpha_\mathrm{K}} \tag{4.2}$$

where we use the definition of specific entropy used in the ACCEPT database (Cavagnolo et al., 2009):

$$K \equiv \frac{k_B T}{n_e^{2/3}} \ . \tag{4.3}$$

For the Perseus cluster, ACCEPT gives values of $K_0 = 19.38$ keV cm^2, $K_{100} = 119.87$ keV cm^2, and $\alpha_K = 1.74$, and we use them for our initial configuration. The condition for hydrostatic equilibrium is

$$\frac{\mathrm{d}P}{\mathrm{d}r} = -\rho g \ . \tag{4.4}$$

Together, the the specified entropy profile and the hydrostatic condition (equations 4.2, 4.3, and 4.4) give a differential equation relating temperature and entropy. It remains to specify a boundary condition so that this equation can be integrated. Following Voit (2005), the temperature of a hydrostatic ICM can be approximated as

$$k_B T_{200} = \frac{\mu m_p}{2} \left[10 G M_{200} H(z)\right]^{2/3} \tag{4.5}$$

We take this as a characteristic temperature for the ICM near the virial radius and integrate inwards and outwards to find the temperature and density profiles for the rest of the cluster.

4.2.2.1 Tracer Fluid

In order to track the gas directly affected by AGN feedback, we continuously inject a (passive) tracer fluid into the central 10 kpc. This passive tracer also allows us to measure the radial extent of feedback heating and also indicates the amount of metal transport facilitated by AGN jets and rising cavities, which are thought to play an important role in shaping the metallicity profiles of clusters. The amount of tracer injected per unit mass $\Delta\rho_T$ is given by

$$\Delta\rho_T = \mathrm{SSFR} * Y \tag{4.6}$$

where we assume a specific star-formation rate $\mathrm{SSFR} = 10^{-11}\ \mathrm{yr}^{-1}$ and a yield $Y = 0.02$. These assumptions are meant to be a crude approximation for metal injection by the old stellar population of the BCG. We emphasize that all we are doing is injecting passive tracer fluid. No actual star formation takes place, and the tracer fluid does not affect the radiative cooling rate. Our primary interest is radial transport and distribution of the tracer fluid. We do not expect its concentration to match metallicity values in the ICM of observed clusters.

4.2.3 Feedback and Jet Modeling

AGN are complicated systems governed by physical processes that are poorly constrained and span many orders of magnitude in space and time. Our goal here is not to understand all the details of AGN physics but rather to study the interplay between accretion, jet outflows, and the thermal state of the ICM. To this end, we implement a simplified "AGN Particle" model, wherein accretion onto the AGN launches outflows that are insensitive to the details of gas accretion on scales < 200 pc. We implement several triggering mechanisms, each with a different algorithm for determining the accretion rate $\dot{M}$ into the region surrounding the central supermassive black hole, which sets the scale of the AGN feedback response. In each case, the resulting output of feedback power is taken to be $\dot{E} = \epsilon \dot{M} c^2$, where ϵ is a feedback efficiency factor and c is the speed of light. The accretion rate $\dot{M}$ is not necessarily the actual accretion rate onto the central black hole, and in our idealized implementations no gas is removed from the simulation volume. Instead, it is assumed to be reheated and expelled from the vicinity of the black hole by feedback. Regardless of the triggering mechanism, precessing jets are launched from disk-shaped regions on either side of the AGN as described in the following subsections. Please refer to Table 4.1 for fiducial values of the AGN feedback parameters.

4.2.3.1 Triggering Mechanisms

Each of the following triggering methods calculates $\dot{M}$ and removes gas mass from the grid within a specified radius given by the parameter R_{acc}.

Cold-Gas Triggered Feedback: Meant to replicate the triggering mechanism used in Li & Bryan (2014a), feedback is triggered by the presence of gas within R_{acc} and at or below a threshold temperature T_{floor}. The accretion rate corresponding to a single cell is

$$\dot{M}_{\mathrm{cell}} = \frac{M_{\mathrm{cell}}}{t_{\mathrm{acc}}} \tag{4.7}$$

where t_{acc} is a constant timescale. Following Li & Bryan (2014a), we choose $t_{acc} = 5\mathrm{Myr}$, which is close to the average freefall time near the accretion radius.

Boosted Bondi-like Triggering: The accretion rate is set to the Bondi accretion rate derived from conditions within R_{acc} and multiplied by a constant boost factor α so that

$$\dot{M} = \alpha \frac{2\pi G^2 M_{\mathrm{BH}}^2 \hat{\rho}}{(\hat{v}^2 + \hat{c_s}^2)^{3/2}} \tag{4.8}$$

where G is the gravitational constant, M_{BH} is the mass of the black hole, and $\hat{\rho}$, $\hat{v}$, and $\hat{c_s}$ are the mass-averaged density, velocity magnitude, and sound speed within R_{acc}. In this work we adopt $\alpha = 100$. Mass is removed from each cell within R_{acc} in a mass-averaged sense, such that

$$\Delta M_{\mathrm{cell}} = \frac{M_{\mathrm{cell}}}{M(< R_{\mathrm{acc}})} \dot{M}\, \Delta t \tag{4.9}$$

Booth and Schaye Accretion: As described in BS09, the accretion rate follows the Bondi formula but with a boost that depends on the gas density as

$$\alpha = \begin{cases} 1 & n \leq n_0 \\ (n/n_0)^{\beta} & n > n_0 \end{cases} \tag{4.10}$$

Following Booth & Schaye (2009), we take $n_0 = 0.1\ \mathrm{cm}^{-3}$ and $\beta = 2$.

Parameter	Value	Description
ϵ	10^{-3}	Jet efficiency
$R_{\rm acc}$	0.5 kpc	Accretion radius
$T_{\rm Floor}$	3×10^4 K	Temperature floor
$M_{\rm BH}$	1.0×10^8 $M_\odot$	SMBH mass
$\phi_{\rm Jet}$	0.15 radians	Jet precession angle
$\tau_{\rm Jet}$	10 myr	Jet precession period
R_J	0.5 kpc	Radius at which jets are launched
R_D	0.5 kpc	Initial radial thickness of jets

Table 4.1 **Parameters for AGN Simulations:** These parameter values are used for all simulations unless otherwise noted in the text.

4.2.3.2 Jet Implementation

After the total accretion rate $\dot{M}$ during a timestep Δt is calculated with one of these triggering methods, a corresponding amount of feedback energy $\epsilon \dot{M} c^2 \, \Delta t$ is added to the ejected gas. We assume the ejected mass to be equal to $\dot{M}\Delta t$, which is an idealization. In reality, the mass-loading factor of the jets will depend on subgrid physics that is not yet well understood. However, Dubois et al. (2012) find that the choice of mass-loading factor does not strongly affect their results.

A fraction $f_{\rm k}$ of the feedback energy is added to the ejected mass as kinetic energy, while the rest is added as thermal energy. This naturally results in a jet velocity of

$$v_{\rm Jet} = c\sqrt{2\epsilon f_{\rm kinetic}} \tag{4.11}$$

or around $v \approx 0.045c$ for our fiducial parameter choices. Kinetic energy and the associated mass are put into the grid through two disks each of radius R_D located on either side of the AGN at a distance R_J from the center. The jets are oriented at a fixed angle $\phi_{\rm Jet}$ with respect to the z axis and precess around it with a period $\tau_{\rm jet}$.

For simulations with pure thermal feedback ($f_{\rm k} = 0$), we again follow the method of BS09 in order to prevent the injected thermal energy from immediately being radiated away. Feedback energy is stored up until enough accumulates to heat the gas in the injection zone to at least $T_{min} = 10^7$ K. Exploratory simulations with $T_{min} = 10^8$ did not show a noticeable difference in behavior, in agreement with BS09. We observe that this algorithm results in a series of thermal pulses as AGN feedback is ramping up, but comes close to steady injection when the AGN power is high. We performed tests using this injection threshold with some kinetic feedback ($f_K > 0.0$) but did not observe a noticeable difference when compared to simulations with continuous energy injection.

Unless otherwise noted we use the parameters given in Table 4.1 for all simulations.

4.2.4 Hydro Method

The simulations in this work use a 3D version of the ZEUS hydrodynamics method (Stone & Norman, 1992) because of its robustness and speed. ZEUS is known to be a relatively diffusive method and requires an artificial viscosity term that may affect the accuracy of our hydrodynamics calculations. We have experimented with using a piecewise-parabolic method (PPM) (Colella & Woodward, 1984), but encountered numerical difficulties relating to the strong discontinuities occurring at the injection site.

4.3 Results

The most striking differences within our suite of simulations are between AGN feedback algorithms that deliver all of the feedback in thermal form ($f_{\rm k} = 0$) and those that deliver at least some kinetic feedback ($f_{\rm k} > 0$). Changes in the triggering method produce smaller differences in qualitative behavior, probably because all three triggering methods implemented here end up strongly boosting the feedback response when significant amounts of cold gas accumulate near the central black hole. We will therefore present our results on delivery mechanisms first and triggering mechanisms second.

4.3.1 Delivery of Feedback: Thermal vs. Kinetic

Injection of AGN feedback energy heats the surrounding gas through several processes. First, if $f_{\rm k} < 1.0$, then the AGN directly injects thermal energy into the ICM. Second, interactions between the AGN outflow and the ICM produce shocks that propagate outward and heat the ambient gas in a quasi-isotropic manner. Third, outflows drive turbulence that can heat the ICM as the turbulence decays. Finally, momentum from the AGN outflow—either directly injected in the form of a kinetic jet or driven by thermal expansion of hot bubbles—can dredge low-entropy gas out of the core and mix it with higher entropy gas at larger radii.

4.3.1.1 Feedback Power

All of our simulations with $f_{\rm k} > 0.0$ follow similar patterns of evolution. Initially, the cluster core is smooth, spherically symmetric, and contains no cold gas. The core gas then cools, contracts, and grows denser for ~ 0.3 Gyr until cold clouds begin to condense at the center and strongly boost the jet power. Figure 4.1 shows both the jet power and cooling luminosity within different radii during the first 2 Gyr of a cold-gas triggered feedback simulation that delivers 50% of the feedback power as kinetic energy. Notice that the core achieves approximate long-term balance when the jet power rises to match the cooling luminosity from within the central ~ 100 kpc. This is typical of our simulations that have a significant fraction of the feedback

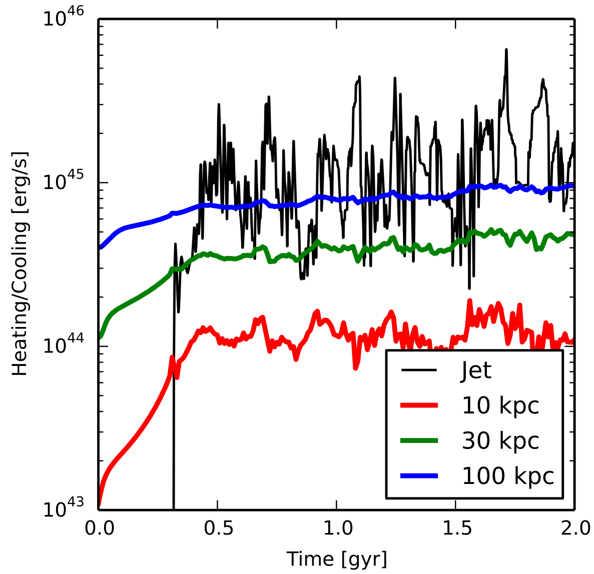

Figure 4.1 **AGN Power vs. Cooling Rate in Idealized AGn Simulations:** Total AGN power (thermal + kinetic) and cooling luminosity for a simulation with cold gas triggered feedback and $f_{\mathrm{k}} = 0.5$. The jagged black line shows instantaneous jet power sampled every 5 Myr. Red, green, and blue lines show the total cooling luminosity of gas within 10, 30, and 100 kpc respectively, sampled at the same cadence.

power in kinetic form. However, the total feedback power becomes much greater in simulations with purely thermal feedback.

Figure 4.2 illustrates the vast difference in feedback power between our simulations with $f_{\mathrm{k}} = 0$ and those with $f_{\mathrm{k}} > 0$. Pure thermal feedback eventually saturates at a power level more than two orders of magnitude greater than in the simulations with some kinetic feedback, even when compared to the case with $f_{\mathrm{k}} = 0.25$. Furthermore, it can be seen that the average feedback power in the self-regulated systems with at least some kinetic power is not monotonically dependent on f_{k}. As long as some of the feedback power is kinetic, self-regulation happens at a power level of $\sim 10^{45}\,\mathrm{erg\,s^{-1}}$, which is similar to the time-averaged AGN power inferred from observations of X-ray cavities in galaxy cluster cores (e.g., McNamara & Nulsen, 2012).

4.3.1.2 Cold Gas Accumulation

Feedback power becomes excessively large in the $f_{\mathrm{k}} = 0$ case because pure thermal feedback is ineffective at preventing large amounts of cold gas from accumulating. Figure 4.3 shows that $\sim 10^{12}$ $\mathrm{M_{\odot}}$of cold gas accumulates in less than 1 Gyr when $f_{\mathrm{k}} = 0$, whereas $\lesssim 10^{10}$ $\mathrm{M_{\odot}}$accumulates during the same time period in simulations with at least some kinetic power. The large cold-gas reservoir in the $f_{\mathrm{k}} = 0$ case is not sufficiently disrupted by thermal feedback and therefore provides enough cold fuel for the AGN to maintain a feedback

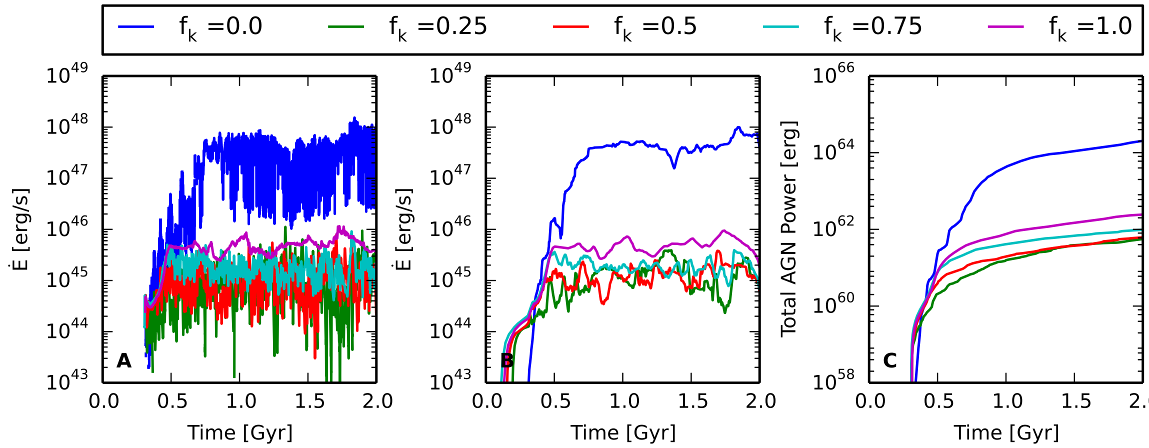

Figure 4.2 **Effect of Kinetic Fraction on Jet Power:** Feedback power ($\dot{E}$) (thermal + kinetic) as a function of time for simulations with cold gas triggering and varying values of $f_{\rm k}$, the fraction of feedback power in kinetic form. Panel A shows the instantaneous value of $\dot{E}$. In Panel B, $\dot{E}$ has been smoothed over a 50 Myr uniform smoothing kernel. Panel C shows the cumulative energy released by the AGN.

power exceeding $10^{47}\,{\rm erg\,s^{-1}}$. Even at this power level, the AGN fails to eject or eliminate much of the cold gas because the cold gas is very efficient at radiating away feedback energy owing to the n^2 dependence of the cooling rate. The result is that the feedback energy that does go into the cold gas is almost immediately radiated away. Further, feedback energy tends to propagate more readily through the hot ambient medium along the paths of least resistance, and ends up increasing the thermal energy of the diffuse, volume-filling gas without diminishing the mass of cold gas embedded within it.

If star formation had been allowed to proceed in our simulations, much of the cold gas that accumulates near the center would eventually have formed stars. The results shown in Figure 4.3 therefore indicate that that pure thermal feedback would permit a time-averaged star-formation rate $\sim 10^{2-3}\,{\rm M_\odot\,yr^{-1}}$ during the first $\sim$ 1 Gyr, which is much larger than observed in all but the most actively star-forming galaxy cluster cores (O'Dea et al., 2008). In order to understand why kinetic feedback is so much more successful than thermal feedback in suppressing cold gas accumulation and the star formation that would result, we need to look at how the choice of $f_{\rm k}$ affects the radial distribution of density, temperature, and entropy in the hot ambient medium.

4.3.1.3 Radial Profiles

Figure 4.4 shows how the average values of density, temperature, entropy, and concentration of tracer fluid change over time at each radius in simulations with mixed kinetic and thermal feedback ($f_{\rm k}$ = 0.5, left panels) and pure thermal feedback ($f_{\rm k}$ = 0, right panels). Gas outside of $\sim$ 100 kpc is not shown because it does not evolve appreciably over 2 Gyr, as the cooling time at large radii is long and little of the AGN

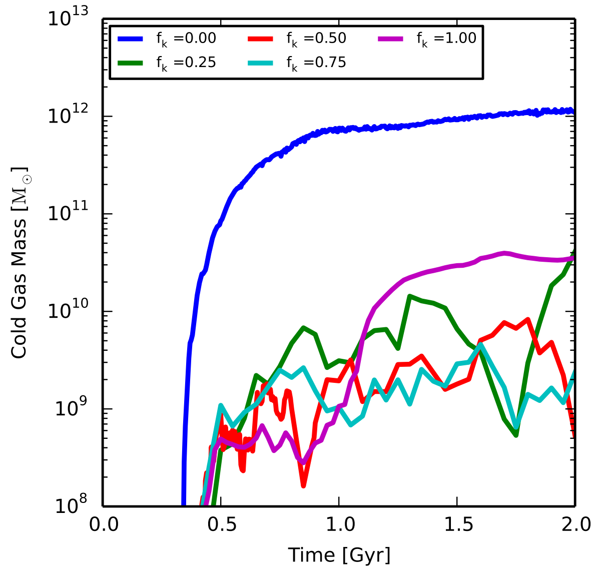

Figure 4.3 **Cold gas Mass for Different AGN Triggering Algorithms:** Total mass of cold gas as function of time for simulations with cold gas triggering and differing values of $f_{\rm k}$. The amount of cold gas that accumulates in the simulation with $f_{\rm k} = 0$ is two orders of magnitude greater than in any of the simulations with some of the feedback energy in kinetic form.

feedback energy propagates to those radii. Inside of 100 kpc, the $f_{\rm k} = 0.5$ simulation reaches a nearly steady state in ~ 0.5 Gyr, with density, temperature, and entropy continuing to fluctuate within narrow ranges after that time. The profiles of the tracer fluid concentration do not reach a steady state, as the tracer is continuously injected over time and distributed outward by the jet. However, those profiles do show that tracer fluid is quickly mixed with the ambient gas out to $\gtrsim 50$ kpc from the center.

In contrast, the simulation with $f_{\rm k} = 0$ does not reach a steady state. In particular, the azimuthally averaged specific entropy of gas outside of the central few kpc steadily rises with time, causing a steady drop in ambient density and a steady rise in ambient temperature. Initially, some of the increase in mean entropy comes from the removal of low-entropy gas through condensation (Voit & Bryan, 2001; Voit et al., 2002; Nagai et al., 2007). However, the mean entropy at $\gtrsim 10$ kpc continues to rise during the second Gyr of the simulation, after condensation of cold gas has leveled off. This rise is due to continual input of thermal energy by AGN feedback, a small fraction of which escapes the inner few kpc and propagates into the ICM, causing pressure-driven expansion of the ambient medium. The right-hand panel of Figure 4.2 shows that AGN feedback in the $f_{\rm k} = 0$ simulation has injected $\sim 10^{64}$ erg after 2 Gyr, which is comparable to the binding energy of the entire intracluster medium, although most of this is radiated away by the cold gas. The fraction that does escape the central clump of cold gas slows the condensation process by inflating the cluster core and driving the cooling time of the ambient medium at ~ 10 kpc to ~ 5 Gyr but fails to establish

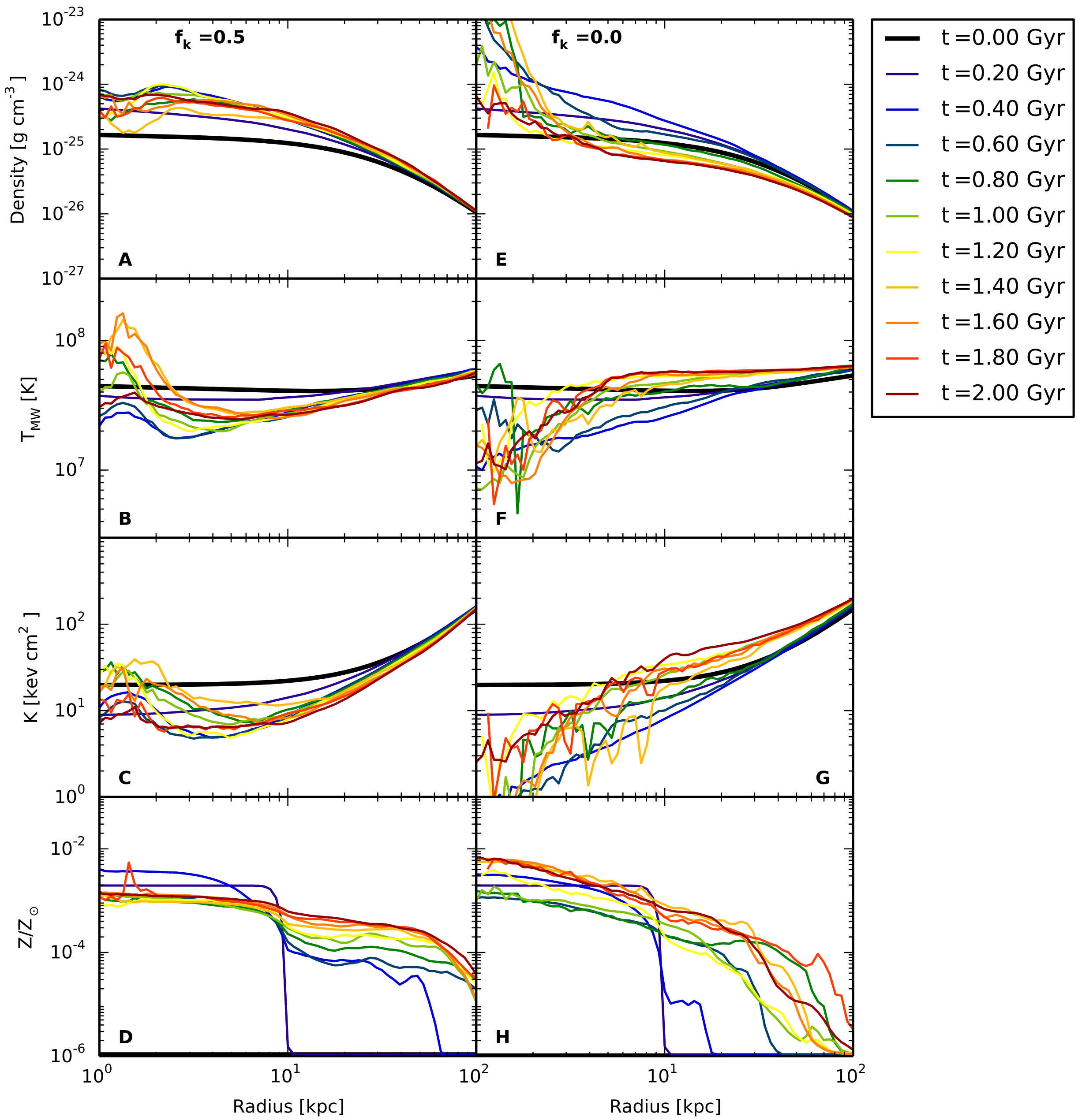

Figure 4.4 **Evolution of Gas Quantities for Different Kinetic Fractions:** Profiles of various quantities as the simulation evolves for simulations with $f_\mathrm{k} = 0.5$ (left) and $f_\mathrm{k} = 0.0$ (right) with cold gas triggering. Thick black lines denote the initial conditions, while other line colors indicate values at later times. Density is weighted by volume, temperature by mass, and metallicity my mass. Entropy is computed using the volume weighted temperature and the mass weighted density, as discussed in Section 3.2.3 of Skory et al. (2013).

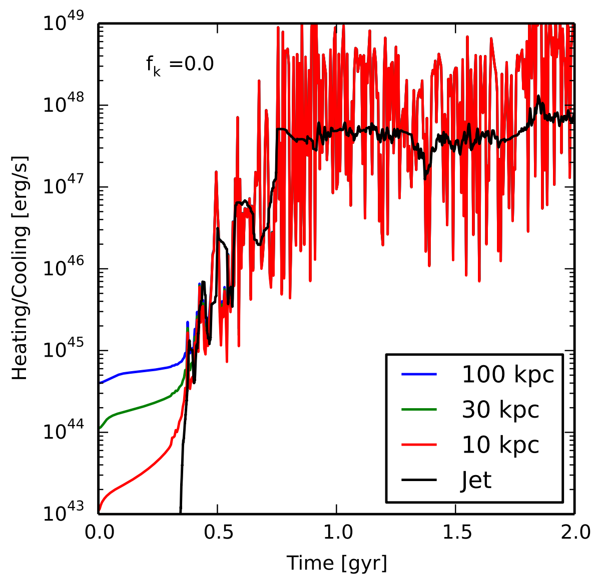

Figure 4.5 **Jet Power vs. Cooling Rate for Different Triggering Methods:** The radiative cooling rate of the gas within different radii is compared to the total jet power (thermal + kinetic) for the simulation with $f_k = 0.0$. At times greater than 0.5 Gyr, all of the cooling is occuring within 10 kpc, and the three lines overlap.

a self-regulated feedback loop.

Despite the high AGN power, this simulation is not able to prevent a buildup of cold gas for two reasons: (1) feedback energy does not propagate far enough from the center, and (2) thermal feedback cannot destroy a large cold-gas reservoir, once it develops. As illustrated in Figure 4.5, almost all of the cooling comes from the central 10 kpc where there is a concentration of cold gas with a very short cooling time. Although gas at the temperature floor does not cool, a small rise in temperature greatly increases its cooling rate and prevents the cold gas from heating to the ambient temperature.

The development of a large cold-gas reservoir is closely related to the failure of thermal feedback to propagate feedback energy beyond the central ~ 30 kpc. Figure 4.6 shows the rms gas velocity as a function of radius in simulations with different proportions of kinetic feedback ($f_k = 0.0$, 0.5, and 1.0, respectively). In the pure thermal case, there is a sharp drop in rms velocity beyond ~ 30 kpc which is not seen in the simulations having some kinetic feedback. Apparently, kinetic feedback is more effective at transporting feedback energy to large radii.

This discrepancy arises because outward propagation of centrally injected thermal feedback is limited by the amount of entropy it can generate. It creates central bubbles of hot gas which can buoyantly rise only until they reach a layer of equivalent entropy. Then the bubbles blend with their surroundings. In this set of simulations, centrally injected hot bubbles stop rising and blend with the ambient medium at ~ 30 kpc,

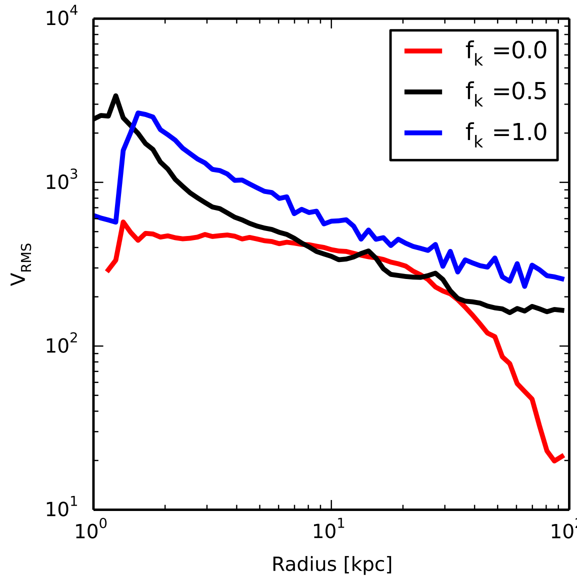

Figure 4.6 **Effect of Triggering Method on Velocity Profiles:** Mass weighted profile of RMS velocity in the hot ambient medium for simulations with cold gas triggering and different kinetic fractions. All profiles are computed 1.75 Gyr after the beginning of the simulation.

as indicated by the rms velocity curves in Figure 4.6, as well as the propagation of tracer fluid in panel H of Figure 4.4. We therefore conclude that our implementation of pure thermal feedback does not add much heat to gas in the 30–100 kpc range of radii but instead steadily raises the entropy of ambient gas at 10–30 kpc, which flattens its entropy gradient. Kinetic feedback, on the other hand does propagate beyond 30 kpc and consequently allows gas in the entire 10–100 kpc range to settle into a quasi-steady, self-regulated state.

4.3.1.4 Jet Precession

In addition to the breakdown between kinetic and thermal feedback, we have also investigated the role of jet precession. Jets from AGN can reorient themselves on timescales of a few tens of Myr (Dunn et al., 2006; Babul et al., 2013), but the details of this process are still uncertain, and our subgrid model and idealized setup are not capable of self-consistently modeling jet precession. Instead, we follow Li & Bryan (2014a) and force the jets to precess around a fixed axis. Previous studies have found that some precession is necessary for self-regulation if the jets are highly collimated. Otherwise, they drill long, narrow channels through the ICM and deposit the bulk of their energy far from the zone in which self-regulation can happen Vernaleo & Reynolds (2006).

Figure 4.7 shows slices of four simulations performed with different jet precession angles. When the jets do not precess ($\theta_{jet} = 0$), they carve channels through the ICM that extend well beyond ~ 40 kpc. However, due to Kelvin-Helmholz instabilities and artificial viscosity in the ZEUS code, they still produce some heating

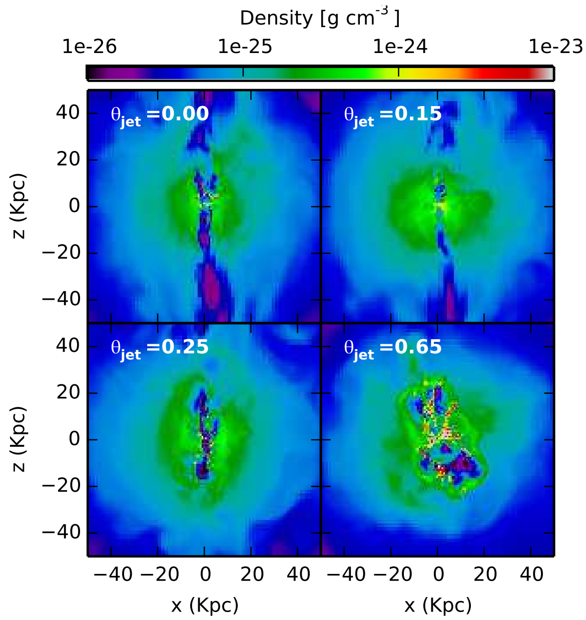

Figure 4.7 **Effect of Jet Precession:** Density slices for simulations with different values of θ_{jet}. In our model, the AGN jet precesses around the z axis with a period of 10 Myr at a constant angle θ_{jet} with the z axis. All simulations use cold gas triggering and have $f_{\mathrm{k}} = 0.5$.

close to the AGN but do not drive strong shocks. With a small precession angle ($\theta_{jet} = 0.15, 0.25$), each jet continually encounters cold clouds of condensing material that block its path. These jet-cloud interactions randomly divert the jets, depositing their energy in a wider range of directions, which causes more of their kinetic energy to thermalize at smaller radii. Precession also produces more turbulence and creates shocks that propagate outward over a large range of solid angles. As the precession angle increases, the jet energy spreads over a larger range of solid angles at ever smaller radii, and jet-cloud collisions become more frequent. As seen in the last panel of Figure 4.7, this leads to a more disturbed morphology at $\lesssim 20$ kpc and a larger mass of accumulated cold gas. In that respect, kinetic feedback with a very large precession angle becomes more like thermal feedback, in that feedback energy does not propagate as far from the center before it becomes thermalized.

4.3.2 AGN Triggering Mechanisms

We do not see strong differences between our simulations with different AGN triggering mechanisms, as long as we are using a maximum spatial resolution of 196 pc (see Figure 4.8). This is likely a consequence of being able to resolve the multiphase medium in the region surrounding the AGN. Since all of the triggering mechanisms considered are dependent on gas density, a cold, dense clump of gas accreting will trigger a large outburst regardless of the details of the triggering algorithm. The outburst will continue until the cold gas is gone, ensuring that roughly the same amount of energy is released in all cases. The cold gas would not

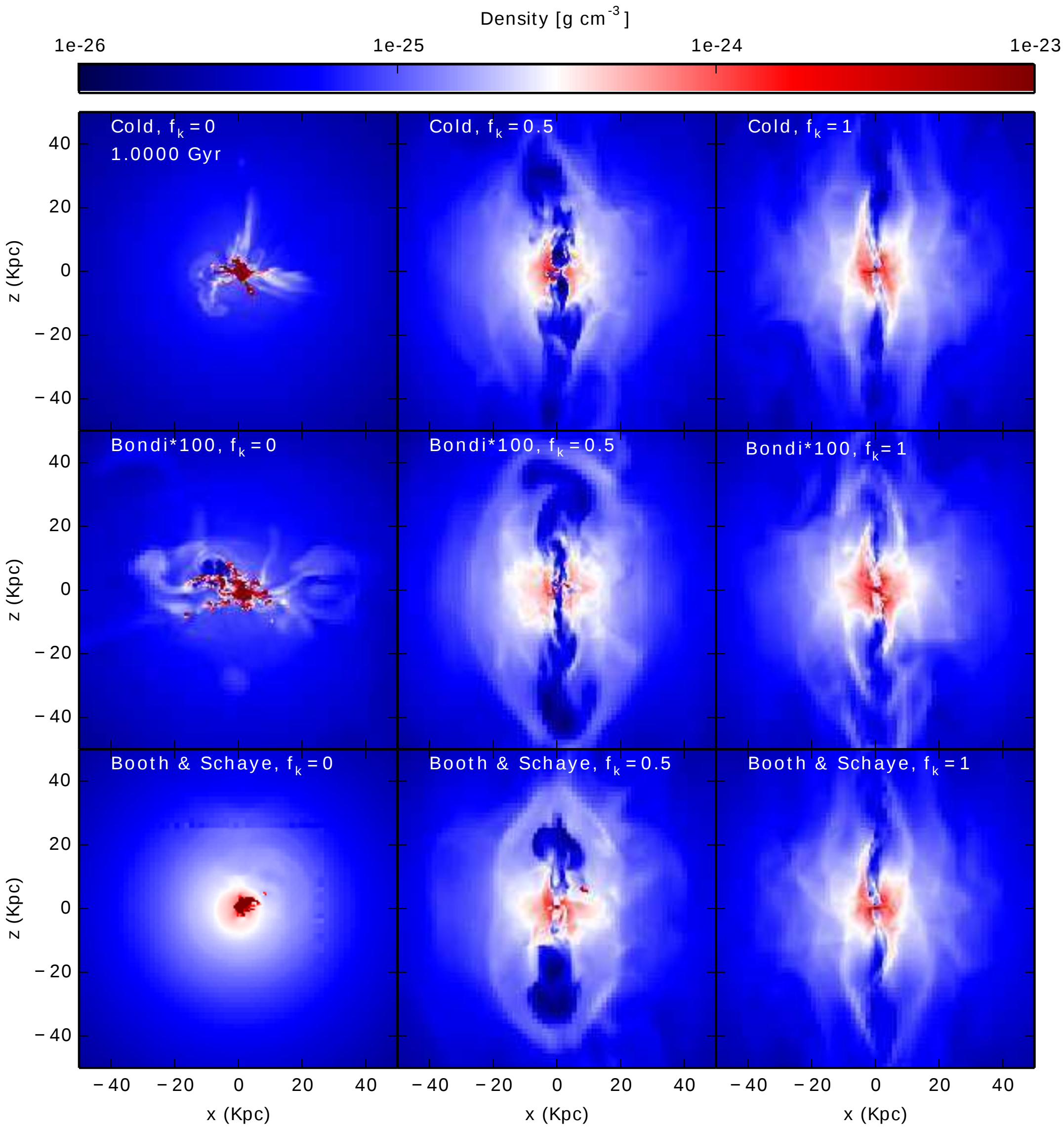

Figure 4.8 **Comparison of Simulations with Different Triggering Algorithms and Kinetic Fractions:** Slices of density through 9 simulations with different triggering mechanisms and kinetic feedback levels. All simulations are shown 1 Gyr after the beginning of the run. Simulations in the top row are triggered by cold gas accretion, the middle row by Bondi accretion with a constant boost factor, and the bottom row using the method of BS09. f_k gives the fraction of the feedback that is returned as kinetic energy.

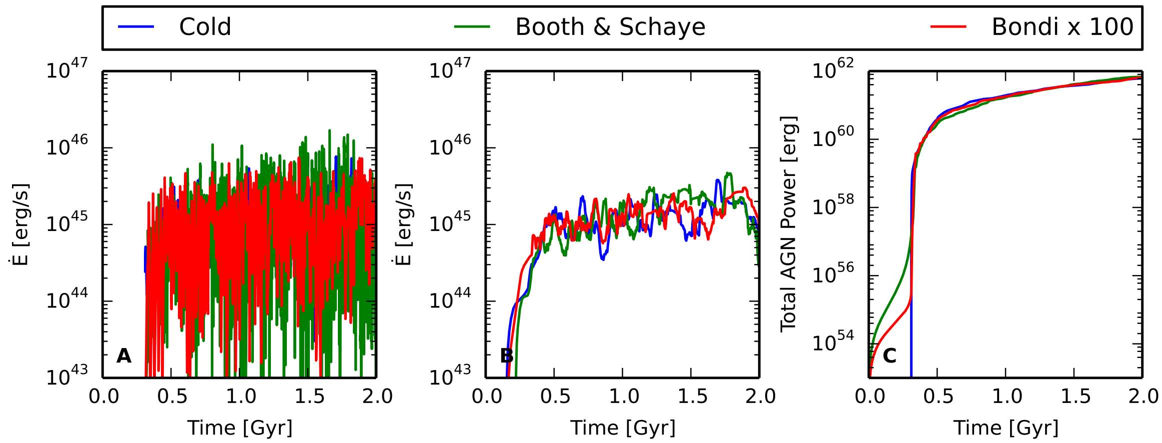

Figure 4.9 **Effect of Triggering Mechanism on Jet Power:** Like Figure 4.2, but for simulations with different triggering mechanisms. All simulations have $f_{\mathrm{k}} = 0.5$. As in Figure 4.2, Panel A shows the instantaneous value of $\dot{E}$, Panel B shows $\dot{E}$ smoothed over 50 Myr, and Panel C shows the cumulative jet power.

necessary be resolved by simulations with coarser resolution, implying that those simulations might be more sensitive to the choice of triggering algorithm.

Each triggering mechanism depends on gas density either directly (BS and Boosted Bondi-like accretion) or indirectly (cold gas triggering), and in the BS and Boosted Bondi-like cases the boost parameters have been chosen to provide the "right" amount of feedback. Due to the density-dependent accretion rate, a cold clump falling into the accretion zone then always produces a surge in jet power that continues until the clump is either completely heated or completely accreted.

Figure 4.9 shows total jet power (thermal + kinetic) versus time for simulations with different triggering mechanisms. In the Bondi-like and BS runs, feedback is always active, but the power level is relatively low before cold gas starts to condense and drives up the AGN accretion rate. After condensation begins, all three triggering mechanisms lead to self-regulated jet power levels that are nearly identical. Figure 4.10 shows the radial profiles of various quantities in the ambient hot ICM after 2 Gyr for each triggering mechanism. There are some differences in the inner 10 kpc, but this zone is strongly affected by the quickly varying jet, producing profiles that are variable with time (see Figure 4.4). Between 10 and 30 kpc, the run with cold-gas triggering is slightly colder and more susceptible to thermal instability than the other runs, based on the lower $t_{\mathrm{cool}}/t_{\mathrm{ff}}$ ratio. Beyond 30 kpc, there are no significant differences between runs with different triggering mechanisms.

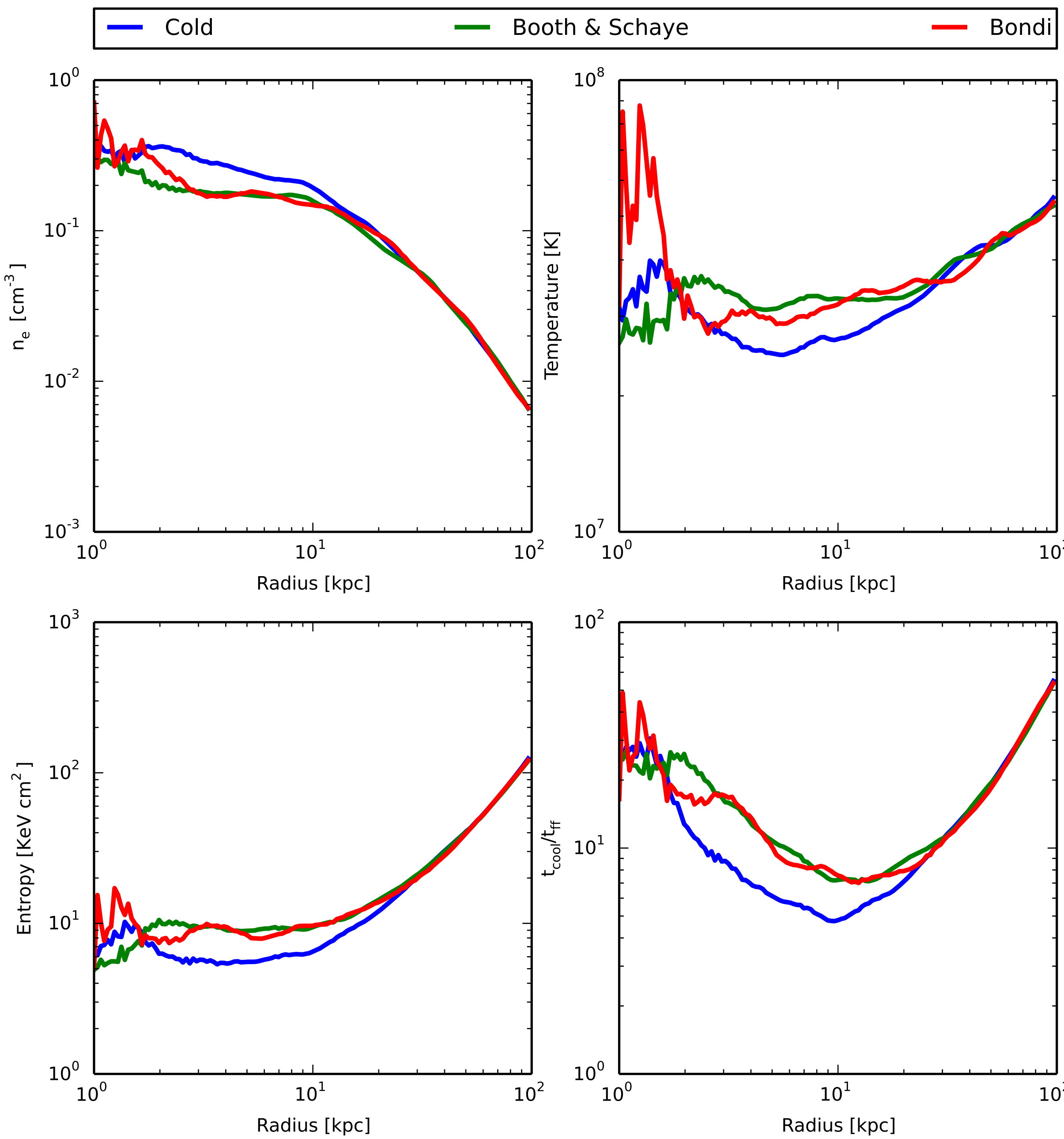

Figure 4.10 **Effect of Triggering Mechanism on Gas Quantities:** Profiles of different quantities for simulations with different triggering mechanisms after 2 Gyr. All simulations use $f_{\rm k} = 0.5$. n_e is weighted by volume, while the other profiles are weighted by mass. All profiles excise gas below 3×10^4 K.

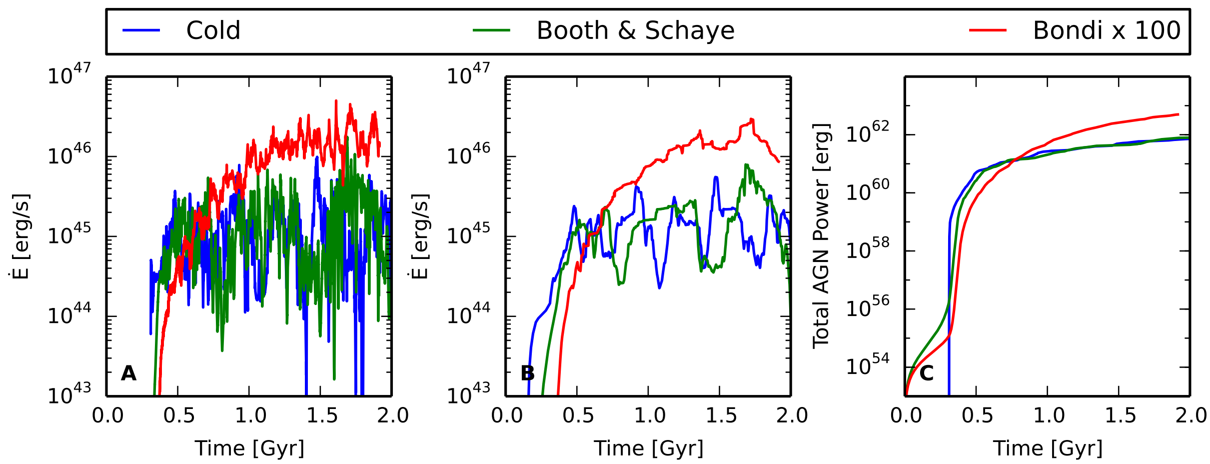

Figure 4.11 **Effect of Accretion Radius on Jet Power:** Jet power vs. time for simulations with $r_{acc} = r_{disk} = 2$ kpc. All simulations have $f_{\rm k} = 0.5$. Like in Figure 4.2, Panel A shows the instantaneous value of $\dot{E}$, Panel B shows $\dot{E}$ smoothed over 50 Myr, and Panel C shows the cumulative jet power.

4.3.3 Accretion Radius

In cosmological simulations of galaxy cluster evolution, one would like a subgrid model for AGN feedback that gives reliable results for the SMBH accretion rate even when the Bondi radius (let alone the Schwarzschild radius) is not resolved. At spatial resolutions coarser than ~ 0.5 kpc, the size of the "accretion zone" that determines AGN feedback power will necessarily be larger than that used in our fiducial simulations. With this increase in $R_{\rm acc}$, the responses of AGN triggering algorithms will depend on conditions at larger radii, which can couple AGN feedback to ICM properties at greater distances but may also permit larger amounts of gas to condense before the AGN feedback response becomes strong enough to oppose cooling.

To understand how the size of the accretion zone affects AGN triggering, we have carried out simulations in which $R_{\rm acc}$ is increased to 2 kpc. The maximum spatial resolution remains the same, with a smallest cell width of 196 pc, meaning that the accretion radius is always resolved by multiple cells. In carrying out these simulations we set the distance $R_{\rm J}$ of the disk-shaped jet injection region equal to $R_{\rm acc}$, so that the jet emanates from the edge of the accretion sphere, not from within it.

Figure 4.11 shows jet power as a function of time for the simulations with a larger accretion radius. In all three simulations, fluctuations in jet power are noticeably smaller than in the fiducial case. With the exception of the Boosted Bondi-like run the cumulative jet power is comparable to the earlier runs, and we did not observe quantitative differences in the ICM properties. However, the Boosted Bondi-like simulation, in which AGN feedback power now depends on average gas properties within a larger volume, takes longer to ramp up, resulting in a large ($> 10^{12}$) mass of cold gas and a higher cumulative jet power.

4.4 Discussion

Our simulations have shown that different triggering and delivery methods for subgrid models of AGN feedback can have profoundly different effects on the resulting properties of the ICM. We are not attempting to determine which method is the most accurate model of an AGN but rather to analyze the reasons for those differences. In each case, tracking the accumulation of cold-gas fuel is critical, meaning that we must consider what allows gas to transition from the hot ambient medium into the cold-gas fuel reservoir. In this section, we discuss that transition and consider the potential effects of physical processes not included in our models.

4.4.1 Precipitation and AGN Fueling

Clearly, our simulations with pure thermal feedback behave markedly differently than simulations with kinetic feedback, even when f_{k} is small. The pure thermal feedback runs experience a large buildup of cold gas that essentially smothers the AGN, causing it to fight back with increasingly powerful bursts. The ICM in the vicinity of the AGN is subject to both radiative cooling and heating from mixing, dissipation, and shocks. Thus, analyzing the thermal stability of the ICM may give insight into the accumulation of cold gas and help to explain the differences that arise from among these feedback algorithms.

Voit et al. (2015b) presented evidence for a “precipitation triggered” model for coupling the AGN power to the cooling rate of the ICM. In the precipitation model, the cooling ICM becomes thermally unstable, leading to the condensation of cold gas. This cold gas is then accreted by the AGN, triggering feedback. The feedback heats the ICM, restoring thermal stability and reducing further accretion. As cosmological simulations typically lack the resolution to model the condensation process itself, the thermal instability criterion can be used to predict the amount of cold gas available for accretion. For a gravitationally stratified medium, one would expect that thermal stability would be related to two natural timescales — the cooling timescale t_{cool} and the dynamical timescale t_{ff}. Simulations (McCourt et al., 2012; Sharma et al., 2012b) find that the formation of cold gas from a thermally unstable medium can occur whenever $t_{\mathrm{cool}}/t_{\mathrm{ff}} \lesssim 10$ (But see Meece et al. (2015), which finds that condensation can occur for larger values in some circumstances.) Similarly, the observations of Voit & Donahue (2015) and Cavagnolo et al. (2008) show that clusters with $t_{\mathrm{cool}}/t_{\mathrm{ff}} \lesssim 10$ are likely to exhibit multiphase gas, while clusters above that ratio do not.

Figure 4.12 shows the distributions of $t_{\mathrm{cool}}/t_{\mathrm{ff}}$ and specific entropy (K) for simulations with pure thermal ($f_{\mathrm{k}} = 0.0$) and part kinetic ($f_{\mathrm{k}} = 0.5$) feedback. Panel A of Figure 4.12 shows that the ICM in the thermal feedback simulation is divided into two phases. First, there is a hot phase with $t_{\mathrm{cool}}/t_{\mathrm{ff}} \gg 10$ that occupies

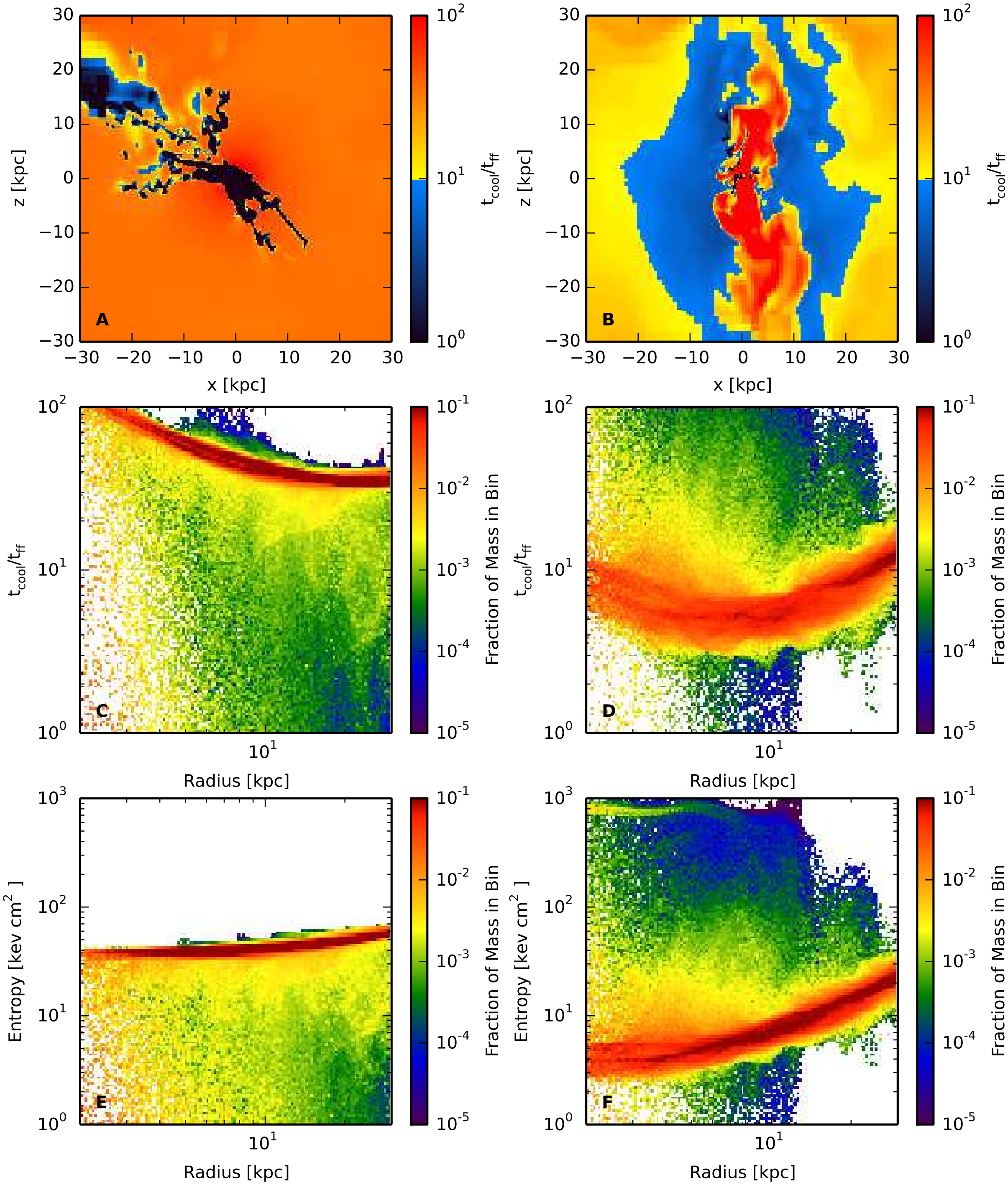

Figure 4.12 **PDF of Timescale Ratio for Thermal and Kinetic Feedback:** Distribution of the t_{cool}/t_{ff} ratio for simulations with cold triggering and either $f_{\rm k} = 0.0$ (left column) or $f_{\rm k} = 0.5$ (right column), shown at 1.46 Gyr after the beginning of the simulation. Panels A and B show slices of the local $t_{\rm cool}/t_{\rm ff}$ for each simulation. The color-break in the scale at $t_{\rm cool}/t_{\rm ff} = 10$ indicates the precipitation threshold identified by earlier studies. Panels C and D show the distribution of $t_{\rm cool}/t_{\rm ff}$ values normalized by the total mass at each radius. The colors show the mass in each bin divided by the total mass in that radial shell. Similarly, Panels E and F show the Entropy distribution. Cold gas ($< 3 \times 10^4$ K) is excluded from the analysis.

the bulk of the volume outside of 10 kpc. Second, there is a large accumulation of cold gas that nearly smothers the AGN. The cold gas mass builds up quickly and then stops growing when the cooling time in the hot ICM rises to several Gyr. Outbursts of thermal feedback sporadically propel streamers and blobs of cool gas radially outwards from the AGN. These cold streamers travel out several tens of kpc before turning around and raining back down onto the core. Panel C shows that there is a large spread in $t_{\rm cool}/t_{\rm ff}$ and K in the 10–30 kpc range. Most of the gas at intermediate values of $t_{\rm cool}/t_{\rm ff}$ does not represent condensation in the usual sense. Instead, it is gas in the boundary layers of the streamers that is either cooling onto them or being heated by interactions with the hot ICM.

As Panels B, D, and F of Figure 4.12 illustrate, the gas properties of the ICM for the simulation with $f_{\rm k} = 0.5$ are very different. The ICM has much lower mean values of $t_{\rm cool}/t_{\rm ff}$ and K at each radius out to 30 kpc. Panel B is typical of the state of the cluster after the jet has formed, with the volume in which $t_{\rm cool}/t_{\rm ff} \lesssim 10$ occupying a roughly spherical region of radius ~ 20 kpc, excluding a hot channel near the jet axis. Overall radiative losses are nearly balanced by gentle shock heating over several cooling times. However, at radii of ~ 10 kpc, where $t_{\rm cool}/t_{\rm ff}$ reaches a minimum value $\lesssim 10$, we observe relatively small amounts of condensing gas. Consistent with Li & Bryan (2014b), this condensation occurs at the jet/ICM interface where the jet generates non-linear entropy fluctuations by uplifting low-entropy gas close to the AGN to greater heights, where it then condenses and falls back toward the center. These condensates are then accreted by the AGN, powering the jets and maintaining thermal balance in the cluster.

The dramatic differences in the behavior of the cold gas and the jet in these simulations has to do with how the AGN distributes energy to the surrounding gas. In the pure thermal feedback case, the gas heated by the AGN at first tends to follow the path of least resistance, bypassing the denser gas near the core. This leads to an accumulation of cold gas with a very short cooling time, which is able to absorb and reradiate the AGN feedback at later times. The AGN injects energy very close to the center of the cluster, where it is immediately radiated away by cold gas. In the ($f_{\rm k}$ simulation, the outflow creates a hot cocoon around itself that rapidly rises. This outflow lifts the central gas outward, which helps disrupt the cooling flow and pulls some low-entropy gas upward along with the jets. The kinetic outflow also allows the feedback energy to penetrate to larger radii (> 10 kpc) and heat the ICM at greater radii. This helps to maintain the balance of heating and cooling globally and prevents the ICM from dividing into a hot and a cold phase. The jet is able to heat gas further out, through mixing, turbulent decay and weak shocks, which prevents the cooling time of a large fraction of the ICM from going below $10 t_{\rm ff}$. Thus, a cluster with a warmer, less dense core will require less energy input to regulate than a cluster with a cold, dense core.

In addition to depositing feedback further out, the kinetic outflows allow cooling gas to mix with the hot gas in the jet. This increases the cooling time of the ICM and strongly inhibits the formation of more cold gas. The cold or cooling gas that is not accreted is soon swept up in the jet, where it is disrupted or heated. The jet thus prevents the cold gas from smothering the AGN, allowing the feedback to heat the ICM rather than quickly radiating away. This explains why a weaker AGN is able to regulate the ICM in the kinetic jet case than in the more powerful pure thermal feedback case.

4.4.2 Caveats and Additional Physics

In this study, both our setup and our implementation of AGN feedback have been simplified in order to focus on the essential features of coupling between the AGN and the ICM. Of course, the situation in real clusters is more complicated than our model. In addition to these simplifications, there are a number of possibly relevant physical processes that we have not included in our model, both to simplify the problem and to reduce the computational resources required. These processes and their potential effects are discussed in this section.

4.4.2.1 Conduction

Our simulations do not include thermal conduction, either isotropic or along magnetic fields. From a theoretical point of view (Voit et al., 2015b, 2008), while conduction may well be important for regulating the thermal state of warm-core clusters, cool-core clusters lie below the t_{cool} profile at which conductive transport can balance radiative losses. Smith et al. (2013) has simulated cool-core clusters with thermal conduction but without AGN feedback, and concludes that thermal conduction is not able to prevent the cooling catastrophe on its own and does not have a large impact on global cluster properties. However, conduction could well be important for the precipitation theory, as strong conduction could smooth out the perturbations that evolve into non-linear overdensities. Wagh et al. (2014) have investigated the effects of conduction on thermal stability and found that conduction would need to be quite strong to prevent condensation.

4.4.2.2 Magnetic Fields

The intracluster medium is known to be weakly magnetized (Carilli & Taylor, 2002). Overall, the magnetic field is believed to be tangled and dynamically unimportant. However, magnetic fields may affect heat transport in the core by making conduction anisotropic, as the electrons that mediate conduction will travel more easily along field lines than perpendicular to them. The importance of anisotropic conduction will depend on the magnetic field configuration, the development of plasma instabilities, and stirring of the plasma by galaxy motions or AGN outflows. A tangled magnetic field would be expected to supress conduction to roughly 1/3 of the Spitzer value. However, a weakly magnetized, conducting ICM with a temperature gradient might be susceptable to either the magnetothermal instability (MTI; Balbus, 2000, 2001; Quataert, 2008) or the heat-flux-driven buoyancy instability (HBI; Quataert, 2008; Parrish et al., 2009). In cool-core clusters, the HBI would align the magnetic field perpendicular to an outward temperature gradient, limiting the inward heat flux. However, simulations such as Ruszkowski et al. (2011) have found that anisotropic thermal conduction is not strong enough to reorient the magnetic fields, and Yang & Reynolds (2015) find that stirring by the AGN would overcome the HBI, leading to conduction with an effectiveness of > 0.2 times the Spitzer value.

While not dynamically important on large scales, magnetic fields may affect the precipitation and AGN feedback processes. Wagh et al. (2014) found that anisotropic conduction will not prevent condensation unless the field is very strong. Magnetic fields may be stronger and dynamically important close to the AGN, where jet induced turbulence and field injection from the jet may amplify the magnetic field (Dubois et al., 2009; Sutter et al., 2012; Ruszkowski et al., 2011). Along the AGN jets, magnetic draping is thought to play an important role in preserving cavities and cold fronts against disruption from Kelvin-Helmholz instabilities (Ruszkowski et al., 2007; Dursi & Pfrommer, 2008). The preservation of cavities would change the mode of heat transport in the cluster, because inflating cavities and rising bubbles would be better able to stir turbulence, transport hot gas to larger radii, and dredge up cold gas in their wake.

4.4.2.3 Star Formation

BCGs in many cool core clusters are observed to be forming stars (O'Dea et al., 2008, 2010; Loubser et al., 2015; McDonald et al., 2015), but stellar feedback alone can not prevent the cooling catastrophe in cool-core clusters (e.g. Skory et al., 2013). Although we do not include star formation in our model, Li et al. (2015) use a setup very similar to our fiducial model to perform an extensive investigation of the role of star formation in regulating AGN feedback. One expects the star formation rate (SFR) of a BCG to be related to the amount of multiphase gas present. Li et al. (2015) do see a correlation between AGN feedback and the SFR. In those simulations, stellar feedback is less effective than the AGN at heating the ICM but more effective at consuming cold gas. If the AGN is in a low-power state, a central reservoir of cold gas builds up and boosts the AGN power on a ~ 100 Myr timescale. AGN feedback then heats the ICM and slows the rate of gas condensation. However, the AGN remains powerful until star formation consumes the cold gas in the central reservoir on a ~ 2 Gyr timescale. Without cold clouds to fuel it, the AGN feedback power subsides, and another cycle soon begins as the ambient medium once again cools and becomes thermally unstable. Thus, the primary effect of star formation is to regulate the cycling behavior of the AGN on Gyr timescales.

4.4.3 Comparison With Similar Studies

As the importance of AGN feedback has gained greater appreciation in recent years, several studies have been carried out to investigate the best way to implement AGN feedback in simulations. It is difficult to do a comprehensive comparison between our results and those of previous studies as those works have generally sampled a limited fraction of the AGN feedback parameter space or assume vastly different initial conditions than we do here.

The chief aim of this paper is to better understand which aspects of AGN feedback implementations are most decisive in determining the qualitative consequences of sub-grid models for AGN feedback. With this in mind, we discuss the major differences between our implementation and some AGN implementations used in related studies of AGN feedback. Where possible, we compare our results to those obtained using these other algorithms. Note that in addition to the major differences discussed here, there are many other small differences in the details of how AGN feedback is implemented and in the choices of physical models considered. As demonstrated by Section 4.3, the results of an AGN feedback simulation may be sensitive to seemingly small differences in implementation, and caution should be taken when comparing one set of results to another.

4.4.3.1 Li & Bryan 2012-2015

The cluster and AGN model employed in our paper are largely an extension of the Li & Bryan simulations of AGN feedback (Li & Bryan, 2012, 2014a,b; Li et al., 2015), with only small changes to the cluster and jet model (although we extend the range of triggering and feedback parameters). Both our study and theirs use `Enzo`.

Given the similarities of our setups, it is not surprising that our simulations give similar results. Our maximum spatial resolution is slightly coarser (196 pc vs. 60 pc), but we obtain similar behavior for similar choices of feedback parameters. Our findings indicate that the Li & Bryan results should be relatively insensitive to variations in the triggering mechanism, the amount of AGN precession, and the details of the accretion process. Both studies find that the behavior of the AGN is relatively insensitive to the kinetic fraction of the outflow as long as the kinetic fraction is non-zero. Our study does find that the mass of cold gas formed depends strongly on the AGN implementation, but does not affect the long term behavior of the simulation. We generally see a mass of cold gas that is an order of magnitude less than what Li & Bryan found in their fiducial model but obtain a similar mass when we use the same set of parameters. This variability in the cold gas mass is consistent with the parameter variation studies in Li & Bryan (2014a).

4.4.3.2 Gaspari et al. 2011

Gaspari et al. (2011b) simulate AGN feedback using the `FLASH` code (Fryxell et al., 2000). They model an idealized version of the cluster Abell 1795 within a static and spherically symmetric gravitational potential using a set of physical processes similar to those used here. The minimum resolution in their study is 2.7 kpc. AGN feedback is modeled as a purely mechanical jet with either cold or hot (Bondi-like) triggering and different jet efficiencies. They also consider both steady and intermittent jets. For Bondi-like triggering, the accretion rate is calculated from the properties of gas within 5 or 10 kpc. Gaspari et al. (2011a) uses a similar AGN model but a gravitational potential appropriate for a galaxy group.

Gaspari et al. (2011b) finds that both a cold gas triggered and a Bondi triggered AGN implementation are able to balance radiative cooling and preserve a cool-core state. The most successful cold gas model (model A3 in that paper) is significantly more bursty than our simulations, with a duty cycle of only 6%, resulting in only around 50 outbursts each with power on the order of 10^{48} erg/s. The total injected energy after 2 Gyr is on the order of 10^{61} erg, consistent with our results. We attribute the observed difference in outburst power and duty cycle to the choice of accretion radius, where we use 0.5 kpc and they use 10 kpc. As seen in Figure 4.11 in our paper, increasing the size of the accretion radius results in a larger variation in AGN power. This follows from more cold gas being able to fit inside the larger accretion zone and from the difficulty of expelling cold gas from a larger gravitational well.

In agreement with our results, Gaspari et al. (2011b) finds that Bondi feedback with a large averaging zone (10 kpc in their simulations) is not able to halt the cooling catastrophe. Their model with an averaging zone of 5 kpc is able to balance cooling over a long period of time. Unlike the cold gas triggered case, the Bondi implementation results in a low power (order 10^{44} erg/s) jet with little variation in intensity. In our simulations, the Bondi and cold-triggered implementations act similarly when using an accretion radius/averaging zone of 0.5 kpc. We ascribe this to the higher resolution of our simulations, which are able to resolve the cold gas directly.

4.4.3.3 Yang et al. 2012

Yang et al. (2012) examines the effect of different AGN subgrid models on observable properties of simulated galaxy clusters. They model an idealized cluster with virial mass 1.5×10^{14} $M_\odot$and a polytropic equation of state, also using `FLASH`. The minimum resolution of these simulations is 1.0 kpc. The physical processes considered are again similar to ours, while the AGN feedback model is somewhat different, consisting of either large (tens of kpc) thermal bubbles offset from the core or jets with widths of a few kpc. The accretion rate was determined from the Bondi rate, with a constant boost factor ranging from 1 to 100 in different runs.

Although Yang et al. (2012) do consider jets with pure thermal feedback (as well as thermal bubbles originating near the AGN), they do not see the same smothering behavior that we do. In fact, the gas in their simulations does not become very dense, rarely exceeding densities of $n_e = 10^{-1}$ cm^{-3}. We attribute these differences to the finer resolution of our simulations, which allow us to resolve the condensation process and the formation of cold gas near the AGN.

4.4.3.4 Dubois et al. 2012

Dubois et al. (2012) compare thermal and mechanical feedback in cosmological simulations using the code `RAMSES`. The simulations generally have a minimum resolution of 1.52 kpc, but some runs have higher resolution. The AGN power is determined using the BS09 method. Thermal energy is released in a sphere of a a few cells near the AGN, while kinetic feedback is released in a jet. Similar to Yang et al. (2012), they do not observe AGN smothering, but again employ a coarser resolution than we use in our simulations.

4.5 Conclusions

We have carried out a controlled comparison of several commonly used sub-grid implementations of AGN feedback. Our model treats the AGN as a particle sitting in the core of an idealized cool-core cluster. The AGN is triggered based on local conditions (either the amount of cold gas or the Bondi rate, with either a fixed or a density dependent boost) and returns energy to the ICM as either centralized thermal blasts, a kinetic jet, or a mix of thermal and kinetic energy. Our main conclusions are:

1. Purely thermal feedback produces very different results than feedback with even a small kinetic component. In the pure thermal case, the AGN is initially unable to inhibit cooling immediately outside of the core, leading to a buildup of cold gas. This gas smothers the AGN and immediately radiates away the feedback energy, even if the feedback zone itself is heated to a high temperature. This also results in heating of the ICM outside of the core through a combination of shock heating and preferential condensation of low entropy gas. Adding a kinetic component allows the AGN to propagate energy outside of the core and prevents smothering of the AGN.

2. When some fraction of the feedback is returned as a kinetic jet, the AGN is able to prevent the large accumulation of cold gas that results from a cooling catastrophe. Instead, AGN feedback self-regulates the ICM in a quasi-steady state with $t_{\rm cool}/t_{\rm ff} \sim 10$ at $\lesssim 20$ kpc. The cluster core is cooler overall than the case with pure thermal feedback, but contains much less cold gas around the AGN.

3. We do observe large differences between cold-gas triggered feedback, boosted Bondi-like triggering or Booth and Schaye accretion, as long as the "accretion zone" used to determine the AGN fueling rate is sufficiently small (~ 200 pc). This is probably because all three methods, by design, end up triggering strong AGN feedback when cold clouds begin to accumulate in the accretion zone.

4. Increasing the size of the accretion zone (to 2 kpc) reduces short-term variation in jet power but does not significantly alter the total amount of AGN feedback or the global ICM properties in the cold-gas triggered or Booth and Schaye cases. However, the boosted Bondi-like simulation does not achieve self-regulation, because AGN feedback does not ramp up fast enough to prevent a cooling catastrophe, resulting in a large central accumulation of cold gas.

5. Very large jet precession angles distribute the AGN feedback energy, making simulations with significant kinetic output behave more like simulations having pure thermal feedback. This happens because the kinetic energy does not escape to large radii and thermalizes closer to the AGN when it is spread over too large a solid angle.

Further improvements to sub-grid feedback models and a better understanding of the AGN feedback process are necessary for the next generation of galaxy and galaxy cluster simulations. On a theoretical level, much work is currently being done on the link between thermal instability, cold gas formation, and its role in triggering feedback. Ongoing observations with Chandra and XMM-Newton as well as future observations with the Smart-X and Athena missions will give a better understanding how the AGN feedback process operates in real clusters. Finally, new implementations must be developed for capturing the connection between AGN and their environments. While the simulations in this work have a maximum resolution of ~ 200 pc, cosmological simulations and simulations with more complicated physics generally have $\gtrsim$ kpc resolution due to computational resource limits. In future work, we will aim at translating the results from this project into a sub-grid implementation that can be used at these coarser resolutions.

4.6 Acknowledgments

The authors would like to thank Gus Evrard, Mateusz Ruszkowski, Greg Bryan, and Yuan Li for helpful discussions during the preparation of this paper. This work was supported in part by Michigan State University through computational resources provided by the Institute for Cyber-Enabled Research. BWO was supported in part by the sabbatical visitor program at the Michigan Institute for Research in Astrophysics (MIRA) at the University of Michigan in Ann Arbor, and gratefully acknowledges their hospitality. This work was supported in part by NASA through grants NNX12AC98G, NNX15AP39G, and Hubble Theory

Grants HST-AR-13261.01-A and HST-AR-14315.001-A. The simulations were run on the NASA Pleiades supercomputer under allocation SMD-15-6514. The active particle framework, upon which our AGN implementation is based, was developed by Nathan Goldbaum at NCSA, and we thank him for his support. `Enzo` and `yt` are developed by a large number of independent researchers from numerous institutions around the world. Their commitment to open science has helped make this work possible.

5 Conclusions

The work discussed in this dissertation has focused on the role of AGN in regulating the thermal state of cool-core galaxy clusters. Chapters 1 and 2 laid out the physical background of the cooling flow problem, the evidence for some form of feedback gained from observations, and motivated the precipitation-regulated feedback scenario in which cold gas condenses out of a thermally unstable medium, accretes onto the SMBH, and powers an AGN that restores thermal balance to the cluster. Chapter 3 demonstrated how thermal instability can lead to the condensation of cold gas clumps, and led to the conclusion that cold gas can rapidly condense out of the ICM when $t_{\rm cool}/t_{\rm ff} < 10$. Chapter 4 discussed the implementation and robustness of subgrid models of AGN feedback, finding that models with some degree of kinetic feedback can do a good job of solving the cooling flow problem. Here, I conclude with a discussion of open questions relating to AGN feedback in clusters and present some avenues for future work.

5.1 The 'Last Kpc' Problem

The subgrid models discussed in Meece et al. (2016) and references therein base the accretion rate on the gas within some fixed radius, and thus make the implicit assumption that gas within that radius makes its way to the SMBH, where it is accreted and powers the AGN. This assumption is necessary, as the size of the SMBH is typically well below the resolution of the simulations — the SMBH event horizon is on the order of AU and the Bondi radius and gravitational influence radius on the order of 10s of pc, while simulations generally have resolution on the order of 100s of pc or more. However, it is not at all obvious how and whether a cold gas cloud at several 100s of pc would reach the SMBH.

Clumps of gas condensing out of the turbulent ICM would be expected to have some amount of angular momentum relative to the SMBH, but need to somehow shed almost all of it in order to reach the SMBH. Otherwise, the clouds would move ballistically and would have little chance of hitting the relatively small SMBH. It is possible that some clouds are created with virtually no angular momentum, but then the rest of the gas would remain. That gas would likely settle into a large, rotating disk around the SMBH, which is not observed (Li & Bryan, 2014a). An alternative explanation is that clumps of gas moving in opposite directions would collide and fall in[1].

A full explanation of how gas reaches the SMBH will require modelling additional physics in high resolution simulations. Magnetic fields and radiative transfer are likely to be dynamically important close to

[1]Termed the 'Three Stooges' model by Brian O'Shea.

the AGN, even if they are not further out. The physics of accretion disks are not well understood (see Tchekhovskoy et al., 2011), and it is likely that disk interactions/instabilities are important for funnelling gas towards the SMBH.

5.2 Galaxy/AGN Interactions

This dissertation has almost entirely ignored the most obvious component of galaxy clusters, namely the galaxies. While the stellar mass of galaxies is only a small fraction of the total cluster mass, feedback from stellar processes have an important impact on gas dynamics, chemical evolution, and observable properties of clusters. A full understanding of galaxy clusters will need to take galaxies into account.

Star formation is generally modeled in simulations using a sub-grid model, similar to what I have done with AGN. Unfortunately, the current generation of subgrid models is tuned for simulations of galaxies and do not produce realistic results when applied to the scale of clusters (see Arieli et al., 2008). Specifically, classic star formation algorithms applied to clusters fail to reproduce the observed number, distribution, and colors of galaxies. This in turn leads to problems in the chemical evolution of galaxy clusters.

New algorithms for generating galaxies in simulations of clusters have been developed by Arieli et al. (2008), Arieli et al. (2010), and Crosby (2016, in prep.). These models use the underlying dark matter distribution to generate galaxies and model the interaction of galactic winds, star formation, and ram pressure stripping from the ICM. Initial results show that these models provide a better match to observations than previous studies. Future simulations will need to combine galaxy and AGN subgrid models in order to provide a full description of the evolution of baryons in clusters.

5.3 Additional Physics and Jet/ICM Interactions

Both theory and simulations must necessarily adopt a range of assumptions and a limited set of physics due to the complexity of the underlying system. There remain a number of physical processes that might be important to the dynamics and thermal evolution of galaxy clusters but that are not widely incorporated in simulations (including those presented in this dissertation). Here I discuss some of these processes and consider their likely effect on the work in this dissertation.

5.3.1 Cooling

In principle, the cooling rate Λ depends on the abundance and distribution of each ionization state of each atomic species as well as the free electron density and the background radiation field. This is obviously impractical to compute at runtime while following the non-equilibrium abundances of each species, as each type of atom will have several ionization states, each with different atomic levels. In addition, many reaction coefficients are poorly constrained. Finally, chemical abundances in clusters are only known with accuracy for a few easily observed elements (and these for only select ionization states), and these are still uncertain due to observational and modeling limits. Therefore, simulations must make approximations when it comes to cooling.

The cooling routines in this work use a tabulated cooling rate (see Appendix A) based on a constant and uniform chemical composition and assuming equilibrium abundances of ionization states. In reality, cooling is metallicity-dependent. The assumption of ionization equilibrium is usually, but not always, valid. Skory et al. (2013) varied the cooling rate model used for studying galaxy clusters and found that using metallicity dependent cooling had a noticeable effect, but did not change the outcome of the cooling flow. Similarly, I do not expect uncertainties in the cooling rate to change the ultimate conclusions of Meece et al. (2015) or Meece et al. (2016), though the results are somewhat dependent on the cooling model that is assumed. For the former, variations in the cooling rate might change the location of the $t_{\rm cool}/t_{\rm ff}$ threshold for precipitation, but would not eliminate it. Therefore, precipitation would still be likely to occur in the latter study, and the AGN would be expected to respond accordingly.

Cooling routines more advanced than those used in this dissertation exist, and using them would provide a fuller understanding of the behavior of gas in galaxy clusters. Grackle (created by Britton Smith, described in Kim et al., 2014) implements metallicity-dependent cooling and can compute non-equilibrium abundances for several primordial species (H, D, He and associated molecules) at low temperature. Dengo (Silvia, 2013), created by Devin Silvia, is able to track non-equilibrium abundances for a larger range of elements and molecules.

5.3.2 Plasma Physics

Most simulations treat the ICM as a purely hydrodynamical problem and neglect the role of magnetic fields or plasma effects. Magnetic fields in clusters are generally weak (Carilli & Taylor, 2002), so this assumption is generally appropriate. In addition, plasma physics is complicated (Schekochihin et al., 2009) and difficult to implement. The state of the plasma in the ICM is also uncertain (Egan et al., 2016).

Magnetic fields and conduction may be important for determining thermal stability, but only if these effects are strong. Field (1965) treats magnetic fields in his study of thermal instability, but finds that magnetic effects are only able to suppress instability if the field is strong. Similarly, McCourt et al. (2012) considers magnetic fields in their simulations but finds that they do not prevent the instability. Conduction can stabilize the medium, but only if conduction is very strong.

Plasma effects are most likely to affect the details of heat transport via conduction and interactions between the AGN jet and the ICM. Conduction in magnetically-threaded plasma is anisotropic since electrons can move along magnetic field lines more easily than perpendicular to them. This can lead to various plasma effects such as the heat-flux driven buoyancy instability or magneto-thermal instabilities (Yang & Reynolds, 2015). Magnetic fields may become dynamically important closer to the SMBH, and are almost certainly important in the dynamics of the disk and the jet.

Finally, plasma effects will alter the interaction of the AGN jet with the ICM. As discussed in Chapter 2, purely hydrodynamic cavities would be shredded by instabilities as they rise, but magnetic fields and viscosity could act to keep them together. This could in turn affect the ability of jets to dredge up gas and metals from the core of the cluster and deliver them further out.

5.4 Cosmological Simulations

The simulations discussed in Chapters 3 and 4 use idealized initial conditions specified in terms of analytical formulae. Idealized setups are useful for performing controlled experiments, but do not capture the effects of inhomogeneity or cosmological structure formation. For a true test of the precipitation-regulated feedback hypothesis, the algorithms and additional physics discussed in this dissertation must be tested in simulations that use cosmological initial conditions.

Cosmological simulations are more difficult to run than idealized simulations due to their increased computational complexity. The dark matter must be followed using n-body dynamics rather than approximated with a static formula. The effects of cosmological expansion must also be taken into account. Finally, an adaptive mesh code like Enzo may end up refining more cells in a cosmological simulation than in an idealized one, as the 'interesting' cells might be spread over a larger volume.

This increased complexity also limits the resolution of cosmological simulations. The idealized setup of Meece et al. (2016) attains a spatial resolution of 200 pc in the smallest cell, but cosmological simulations of galaxy clusters generally have resolutions on the order of a few kpc. As the outflows from AGN are also of order kpc in width, the algorithms discussed here will need to be adapted for use in cosmological simulations. Similarly, the coarser resolution will limit the ability to resolve cold gas directly, meaning that alternate criteria (perhaps the $t_{\rm cool}/t_{\rm ff}$ ratio) will need to be used to approximate the accretion rate.

Galaxy clusters are the most massive structures in the universe and host some of the most energetic processes to ever occur. The dynamics and evolution of the baryonic components involve scales ranging from the microphysics of the atoms to structure formation in the cosmic web. The observable components of clusters encompass only a tiny fraction of their total mass and energy, and much of what is not observable is not well understood. Nevertheless, modern theories and algorithms coupled with powerful supercomputers have achieved results that, considering the breadth and complexity of the problem to be solved, are astonishing. By incorporating better models of feedback and physics in simulations of galaxy clusters, it is promising that we will attain a better understanding of galaxy clusters and the history and evolution of the universe.

APPENDICES

Appendix A Enzo: An Adaptive Mesh Hydrodynamics Code for Astrophysics

In the past two decades, simulation has joined theory and observation as the third pillar of astrophysics. Hydrodynamic simulations, which attempt to follow the dynamics of gas, are often the most informative type of astrophysics simulation. The simulations in this paper make use of the astrophysics hydrodynamics simulation code `Enzo` . A full description of `Enzo` is given in the `Enzo` Method Paper (Bryan et al., 2014). In this chapter, I give a brief overview of hydrodynamics simulations in general and the `Enzo` code in particular.

A.1 Eulerian Hydrodynamics

Enzo is a hydrodynamics code that uses an adaptively refined mesh to solve the Euler equations. For an ideal fluid with a known equation of state and negligible viscosity, the dynamics of the fluid can be described with a set of conservation laws:

Symbol	Description
t	Time
ρ	Density
$\mathbf{v}$	Velocity vector
e	Specific energy
P	Pressure
ϕ	Gravitational Potential
Ł	Volumetric Cooling rate
Γ	Volumetric Heating rate

Table A.1 **Symbols used in the Euler equations** (A.1, A.2, and A.3)

$$\frac{\partial \rho}{\partial t} + \nabla \cdot (\rho \mathbf{v}) = 0 \tag{A.1}$$

$$\frac{\partial \rho \mathbf{v}}{\partial t} + \nabla \cdot (\rho \mathbf{v} \otimes \mathbf{v} + \mathbf{I}P) = -\rho \nabla \phi \tag{A.2}$$

$$\frac{\partial e}{\partial t} + \nabla \cdot [(e + P)\mathbf{v}] = -\rho \mathbf{v} \cdot \nabla \phi - L + \Gamma \tag{A.3}$$

which describe the conservation of mass, momentum, and energy respectively. The meaning of the symbols in Equations A.1, A.2, and A.3 are given in Table A.1.

The Euler equations yield a set of 5 hyperbolic partial differential equations (mass, energy, and three momentum components) that describe the motion of the fluid. Hyperbolic differential equations do not in general yield analytical solutions and must be solved numerically. In practice, this involves discretizing the equations in either mass (the Lagrangian approach) or space (the Eulerian approach.) `Enzo` is an Eulerian code that discretizes space by solving the hydrodynamics equations on a Cartesian mesh.

Typical problems in astrophysics, including the situations discussed in this work, often involve spatial scales that can vary by several orders of magnitude. However, only a small volume of a simulation may be 'interesting' enough to warrant high resolution, and the extra computational resources needed to model the 'non-interesting' volume of the simulation may not be justified. Enzo circumvents this problem by using an adaptive meshing algorithm to overlay grids with higher resolution over low resolution grids. With a smart choice of refinement criterion, Enzo is thus able to achieve a high effective spatial resolution without significant computational overhead. Common refinement strategies in Enzo are refining regions based on over-density, density or temperature slope, high cooling rates, or the Jeans criterion.

Although adaptive refinement allows Enzo to efficiently simulate large volumes with high resolution where needed, issues relating to the time-step and load balancing may limit the advantages of refinement in certain situations. The time-step in Enzo (and all explicit hydrodynamics codes) is limited by the Courant-

Freidrichs-Levy (CFL) condition

$$\Delta t_{\mathrm{hydro}} \leq \min\left(\frac{\Delta \mathrm{x_i}}{\mathrm{c_s} + \mid \mathrm{v_i} \mid}\right)_{\mathrm{i}} \tag{A.4}$$

for each dimension i. Conceptually, Equation A.4 means that the time-step must be shorter than the time that it takes information (in the form of translational motion or sound waves) to cross a cell. The CFL condition means that the most highly refined regions generally require the smallest time-step. For simulations with a wide range of refinement levels, this can result in load balancing issues, where most of the processing work in a simulation is dedicated to updating a small, highly refined region while the rest of the simulation waits. In a parallel computing environment, this means that only the processors updating the finest grid cells are in use, limiting opportunities for parallelization.

`Enzo` implements two main numerical methods for solving the Euler equations. The ZEUS method (Stone & Norman, 1992) uses a finite difference algorithm to compute fluxes. The method is second order in space and first order in time. ZEUS is more diffusive than other methods but is robust. The second method, the Piecewise Parabolic Method (PPM; Colella & Woodward, 1984), uses parabolic interpolation to calculate fluxes. The PPM method is formally third order accurate in space and second order in time, although the use of adaptive meshing can impair this somewhat. Although PPM is formally more accurate than ZEUS, PPM can fail in regions of strong gradients or in the presence of strong cooling. This lack of robustness can make ZEUS an attractive choice for simulations with strong feedback, such as those discussed in chapter 4. Enzo also contains solvers for Magneto-Hydrodynamics (MHD) and fluids cosmological comoving coordinates, but these are not used in the current work.

A.2 Dark Matter and Gravitation

The grid based approach used for computing fluid dynamics cannot be applied to the dark matter in galaxies and clusters. Unlike the collisional particles in the plasma, dark matter is assumed to be collisionless (see Section 1.1.1). Dark matter particles that are close to one another in space will not generally have the same velocity, meaning that the particles will occupy a 6D phase space of position and velocity. This would quickly become intractable for even a coarsely resolved grid.

`Enzo` models the potential due to dark matter by using tracer 'Dark Matter Particles' that are assumed to represent random samplings of phase space. The particles evolve according to N-body dynamics, computed using an adaptive particle-mesh algorithm. The same particle-mesh algorithm is used to compute the self gravity of the gas by assigning gas to nearby grid points.

In idealized simulations such as those discussed in this work, directly modeling the dark matter can introduce an unnecessary degree of complexity into the simulation. For this reason, idealized simulations often use an analytic form for the gravitational potential. Furthermore, the self gravity of the gas is often sub-dominant on the length scales of interest (for example in the ICM away from dense stellar structures such as galaxies), and this too may be neglected in the interest of computational efficiency.

A.3 Radiative Cooling

The gas and plasma that fills space between the stars cools via radiation originating from atomic and molecular transitions or free-free emission. These cooling processes are captured by the L term in Equation A.3. The simplest form of cooling currently implemented in `Enzo` uses a tabulated form of the analytic cooling function $\Lambda(T)$ from Sarazin & White (1987). A graph of $\Lambda(T)$ is shown in Figure A.1. The cooling rate is defined such that the cooling rate per unit volume $L(T, n_e, n_p)$ is given by

$$L(T, n_e, n_p) = \Lambda(T) n_e n_p \ . \tag{A.5}$$

The energy of the photons released by each transition depends on the structure of the atoms and molecules, while the rates of each transition depend on the densities of each atomic or molecular species, the temperature, and microphysics. Ideally, the simulation would track the abundances of each species and calculate Λ directly, but this would be impractical do to the large number of possible states and transitions as well as uncertainties in many of the rate coefficients. However, simulators can often make assumptions about equilibrium or the nature of the dominant transitions to approximate Λ in a tractable amount of time.

Below 10^4 K the gas is partially molecular. Cooling is dominated by molecular transitions, the rates of which depend on density, abundance, and temperature. The rate calculation is complicated, and equilibrium can not be assumed. Fortunately, the gas in this work does not cool below 10^4 K, and so these processes are not discussed here (see Smith et al., 2008, for more information). Between 10^4 and 10^5 K, cooling is dominated by recombination lines from H and He. C and O recombination dominates near 10^5 K, with Ne and Fe recombination dominating near 10^6 K. The importance of heavy elements at higher temperatures is a natural consequence of the increased binding energy that leads to higher ionization temperatures. Above $\sim 10^6$ K the plasma is fully ionized, and emission is dominated by Bremsstrahlung radiation, which goes as $T^{1/2}$.

Seeing as high Z elements dominate the cooling rate (despite their low abundance relative to H and He) outside of the free-free regime, Λ is clearly metallicity dependent, with more metal rich gas having a higher cooling rate (see Sutherland & Dopita, 1993, for more information). For simplicity, the simulations

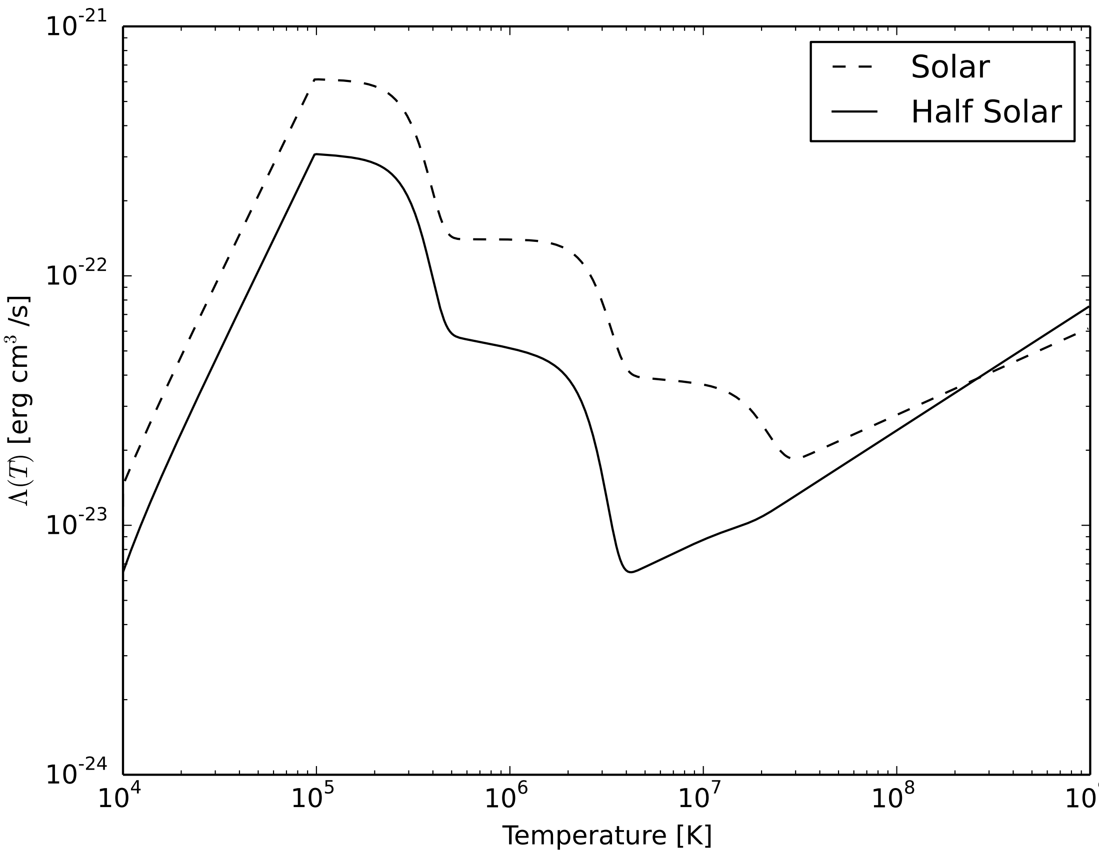

Figure A.1 **Cooling Rates in Enzo:** The cooling rates given by the analytic expression in Sarazin & White (1987) and stored in the Enzo file cool_rates.in. The solid line gives the cooling rate for gas of half solar metallicity while the dashed line shows the rate for a solar abundance. The former is generally used in Enzo simulations.

in this work (and many others) assume a constant metallicity of $Z = 0.5\ \mathrm{Z}_{\odot}$. Methods for metal dependent cooling and non-equilibrium cooling (Abel et al., 1997; Silvia et al., 2015) are available for simulations where detailed cooling is important. In our work, however, we are interested in the interplay of feedback and the ICM, and we do not expect our results to depend strongly on the details of the cooling curve.

A.4 Structure and Development of `Enzo`

The `Enzo` code[1] was originally developed by Greg Bryan and Mike Norman at the University of Illinois in Urban-Champagne in the mid 1990s and further developed at the University of California in San Diego (see Greg Bryan's thesis, Bryan, 1996) with the explicit goal of being useful to researchers beyond the initial authors. `Enzo` was utilized and expanded by subsequent members of the Norman group at UCSD, and was eventually made available to a wider audience through version control systems such as Subversion and Mercurial[2]. Today, `Enzo` is used by hundreds of researchers world wide and is actively developed by dozens of users. `Enzo` is open source, and users are encouraged to contribute their work to the codebase.

`Enzo` is primarily written in C++, with Fortran used for certain numerical routines. The code uses MPI parallelization with adaptive load balancing and has demonstrated the ability to scale to several thousand CPUs. Data is written out in the HDF5 format.

A.5 The `yt` Analysis Code

The `yt` analysis code[3] was created by Matt Turk (Turk et al., 2011) at Columbia University as a tool for analysing Enzo simulation data. `yt` is capable of automatically parsing the output of `Enzo` simulations, abstracting the details of the simulation structure, and returning physically relevant quantities. `yt` can also be used to generate profiles, slices, projections, or volume renderings of different quantities. Although initially developed for use with `Enzo` data, `yt` has been extended for use with a variety of astrophysical codes (Kim et al., 2014).

`yt` is primarily coded in Python. Like `Enzo` , the codebase is open source[4] and is developed by a wide community of researchers.

[1] `http://enzo-project.org`
[2] `https://bitbucket.org/enzo/enzo-dev`
[3] `http://yt-project.org`
[4] `https://bitbucket.org/yt_analysis/yt`

Appendix B The Iso-cooling Setup

This section gives the derivation for the initial conditions used in Chapter 3 and Meece et al. (2015). The end result is included in the paper, but the full derivation is presented here.

The iso-cooling setup is governed by three conditions:

- The gas is in hydrostatic equilibrium
- The ratio of cooling time to freefall time is the same at all heights.
- Pressure, density, and temperature are related by the ideal gas law.

B.1 Definitions

The gas density is given by ρ, which is mass per unit volume (g/cc or appropriate code units.)

The number density- the number of particles per unit volume, is given by

$$n \equiv \frac{\rho}{\mu\,\mathrm{m}_\mu} \tag{B.1}$$

where μ is the mean molecular weight and m_μ is the atomic mass unit.

The Hydrogen number density is the number density of protons.

$$n_\mathrm{H} \equiv \frac{\mathrm{f_H}\rho}{\mathrm{m_H}} \tag{B.2}$$

where $\mathrm{f_H}$ is the mass fraction of Hydrogen (0.76 for primordial gas).

The cooling rate in terms of change in energy per unit volume per unit time is given by

$$\dot{E} \equiv \Lambda(T)\, n_\mathrm{e}\, n_\mathrm{H} \quad . \tag{B.3}$$

Following the derivation used in Enzo, this becomes

$$\dot{E} \equiv \Lambda(T)\, n_\mathrm{e}\, n_\mathrm{H} \tag{B.4}$$

$$= 0.5\mu^2(\,\mathrm{f_H}+1)\,\mathrm{f_H}\Lambda n^2 \quad . \tag{B.5}$$

The cooling time is defined as the thermal energy over the energy loss rate

$$t_{\mathrm{cool}} \equiv \frac{3}{2} \frac{n \mathrm{k_B} T}{\Lambda(T)\, n_{\mathrm{e}}\, n_{\mathrm{H}}} \tag{B.6}$$

$$= \frac{3}{\mu^2\, \mathrm{f_H}(\, \mathrm{f_H}+1)} \frac{\mathrm{k_B} T}{\Lambda n} \quad . \tag{B.7}$$

The free fall time is defined as

$$t_{\mathrm{ff}} \equiv \sqrt{\frac{2z}{g}} \tag{B.8}$$

where the gravitational aceleration is

$$g(z) \equiv \mathrm{g_s} \tanh\left(\pi z / \mathrm{zs}\right) \quad . \tag{B.9}$$

Here, $\mathrm{g_s}$ and zs are scale factors chosen to match the desired properties at the scale heights.

For this setup, $t_{\mathrm{cool}}/t_{\mathrm{ff}}$ is assumed to be constant within a certain range of heights. For brevity, this ratio will be written

$$\beta \equiv t_{\mathrm{cool}}/t_{\mathrm{ff}} \quad . \tag{B.10}$$

B.2 Derivation

The equation for hydrostatic equilibrium involves both temperature and density. The time scale ratio gives a relation between temperature and density, which can be used to turn this into an ordinary differential equation.

Combining equations B.7 and B.8 gives the relation between density and temperature.

$$\beta = \frac{3}{\mu^2\, \mathrm{f_H}(\, \mathrm{f_H}+1)} \frac{\mathrm{k_B} T}{\Lambda n} \sqrt{\frac{g}{2z}} \quad . \tag{B.11}$$

Rearranging this gives the density in terms of the temperature and height,

$$n = \frac{3}{\mu^2\, \mathrm{f_H}(\, \mathrm{f_H}+1)} \frac{\mathrm{k_B} T}{\Lambda \beta} \sqrt{\frac{g}{2z}} \tag{B.12}$$

Grouping the constants gives

$$n = \frac{3 \mathrm{k_B}}{\sqrt{2} \beta \mu^2\, \mathrm{f_H}(\, \mathrm{f_H}+1)} T g^{1/2} \Lambda^{-1} z^{-1/2} \tag{B.13}$$

or

$$\rho = \frac{3\, \mathrm{m}_\mu \mathrm{k_B}}{\sqrt{2} \beta \mu\, \mathrm{f_H}(\, \mathrm{f_H}+1)} T g^{1/2} \Lambda^{-1} z^{-1/2} \quad . \tag{B.14}$$

Next, the condition for HSE is

$$\frac{\mathrm{d}P}{\mathrm{d}z} = -\rho g \ . \tag{B.15}$$

For an ideal gas,

$$P = \frac{\rho \mathrm{k_B} T}{\mu\, \mathrm{m}_\mu} \ . \tag{B.16}$$

Substituting this into the HSE equation gives

$$\frac{\mathrm{k_B}}{\mu\, \mathrm{m}_\mu}\left(T\frac{\mathrm{d}\rho}{\mathrm{d}z} + \rho\frac{\mathrm{d}T}{\mathrm{d}z}\right) = -\rho g \ . \tag{B.17}$$

Rearranging and dividing through by ρ gives

$$\frac{\mathrm{d}T}{\mathrm{d}z} = -\frac{\mu\, \mathrm{m}_\mu g}{\mathrm{k_B}} - \frac{T}{\rho}\frac{\mathrm{d}\rho}{\mathrm{d}z} \ . \tag{B.18}$$

Calculating the density derivative is not as complicated as it might appear. First, write the density as

$$\rho = \alpha T g^{1/2} \Lambda^{-1} z^{-1/2} \tag{B.19}$$

where α is the group of constants above. The derivative is then

$$\frac{\mathrm{d}\rho}{\mathrm{d}z} = \alpha\left(\frac{\mathrm{d}T}{\mathrm{d}z} g^{1/2}\Lambda^{-1}z^{-1/2} + \frac{1}{2}T\frac{\mathrm{d}g}{\mathrm{d}z}g^{-1/2}\Lambda{-1}z^{-1/2} - Tg^{1/2}\frac{\mathrm{d}\Lambda}{\mathrm{d}z}\Lambda^{-2}z^{-1/2} - \frac{1}{2}Tg^{-1/2}\Lambda^{-1}z^{-3/2}\right) \tag{B.20}$$

which is admittedly long, but pulling out $Tg^{1/2}\Lambda^{-1}z^{-1/2}$ gives

$$\frac{\mathrm{d}\rho}{\mathrm{d}z} = \alpha T g^{1/2}\Lambda^{-1}z^{-1/2}\left(\frac{\mathrm{d}T}{\mathrm{d}z}T^{-1} + \frac{1}{2}\frac{\mathrm{d}g}{\mathrm{d}z}g^{-1} - \frac{\mathrm{d}\Lambda}{\mathrm{d}z}\Lambda^{-1} - \frac{1}{2}z^{-1}\right) \tag{B.21}$$

which is just

$$\frac{\mathrm{d}\rho}{\mathrm{d}z} = \rho\left(\frac{\mathrm{d}T}{\mathrm{d}z}T^{-1} + \frac{1}{2}\frac{\mathrm{d}g}{\mathrm{d}z}g^{-1} - \frac{\mathrm{d}\Lambda}{\mathrm{d}z}\Lambda^{-1} - \frac{1}{2}z^{-1}\right) \ . \tag{B.22}$$

Note that you could also do this with logs and get the same result. Anyway, plugging this into the HSE equation gives

$$\frac{\mathrm{d}T}{\mathrm{d}z} = -\frac{\mu\, \mathrm{m}_\mu g}{\mathrm{k_B}} - T\left(\frac{\mathrm{d}T}{\mathrm{d}z}T^{-1} + \frac{1}{2}\frac{\mathrm{d}g}{\mathrm{d}z}g^{-1} - \frac{\mathrm{d}\Lambda}{\mathrm{d}z}\Lambda^{-1} - \frac{1}{2}z^{-1}\right) \ . \tag{B.23}$$

One important note is that the cooling rate is a function of T, not z. The cooling rate derivative really only makes sense at the beginning of the simulation, when T is a function of z. Therefore,

$$\frac{\mathrm{d}T}{\mathrm{d}z} = -\frac{\mu\,\mathrm{m}_\mu g}{\mathrm{k_B}} - T\left(\frac{\mathrm{d}T}{\mathrm{d}z}T^{-1} + \frac{1}{2}\frac{\mathrm{d}g}{\mathrm{d}z}g^{-1} - \frac{\mathrm{d}\Lambda}{\mathrm{d}T}\frac{\mathrm{d}T}{\mathrm{d}z}\Lambda^{-1} - \frac{1}{2}z^{-1}\right) \quad . \tag{B.24}$$

Rearranging again gives

$$\frac{\mathrm{d}T}{\mathrm{d}z} + \left(\frac{\mathrm{d}T}{\mathrm{d}z} - \frac{\mathrm{d}\Lambda}{\mathrm{d}T}\frac{\mathrm{d}T}{\mathrm{d}z}\frac{T}{\Lambda}\right) = -\frac{\mu\,\mathrm{m}_\mu g}{\mathrm{k_B}} - T\left(\frac{1}{2}\frac{\mathrm{d}g}{\mathrm{d}z}g^{-1} - \frac{1}{2}z^{-1}\right) \tag{B.25}$$

or

$$\frac{\mathrm{d}T}{\mathrm{d}z}\left(2 - \frac{\mathrm{d}\Lambda}{\mathrm{d}T}\frac{T}{\Lambda}\right) = -\frac{\mu\,\mathrm{m}_\mu g}{\mathrm{k_B}} - T\left(\frac{1}{2}\frac{\mathrm{d}g}{\mathrm{d}z}g^{-1} - \frac{1}{2}z^{-1}\right) \tag{B.26}$$

and finally,

$$\frac{\mathrm{d}T}{\mathrm{d}z} = \frac{\frac{\mu\,\mathrm{m}_\mu g}{\mathrm{k_B}} + T\left(\frac{1}{2}\frac{\mathrm{d}g}{\mathrm{d}z}g^{-1} - \frac{1}{2}z^{-1}\right)}{\left(\frac{\mathrm{d}\Lambda}{\mathrm{d}T}\frac{T}{\Lambda} - 2\right)} \quad . \tag{B.27}$$

Appendix C Idealized Cluster Setup

This section discusses the problem setup used in Meece et al. (2016).

C.1 Motivation

Galaxy clusters can roughly be described as spheres of gas and dark matter. The gas component (the ICM) is made up of a hot plasma that is roughly in hydrostatic equilibrium (HSE). Theory (Voit, 2005) and observation Cavagnolo et al. (2008, 2009) predicts that the entropy profiles of most cool-core clusters are described by a common profile that decreases towards the center of the cluster and then levels off towards an entropy floor.

C.2 Definitions

The entropy (see Voit, 2005, for a thorough discussion) is defined using the definition of Cavagnolo et al. (2008) as

$$K \equiv \frac{\mathrm{k_B} T}{n_\mathrm{e}^{\gamma-1}} \tag{C.1}$$

where K is the entropy, $\mathrm{k_B}$ is the Boltzmann constant, T the temperature in Kelvin, n_e is the electron density, and $\gamma = 5/3$ is the gas constant. The electron density is related to the particle density by

$$n_\mathrm{e} = \mu(\mathrm{f_H} + (1 - \mathrm{f_H})/2) \tag{C.2}$$

$$= \alpha n \tag{C.3}$$

where μ is the mean molecular weight (around 0.6 for ionized plasma) and $\mathrm{f_H} = 0.76$ is the Hydrogen mass fraction. The symbol α has been introduced here for brevity.

For an ideal gas, the pressure P is given by

$$P = n\mathrm{k_B}T \tag{C.4}$$

which, using the definition of entropy, becomes

$$P = \alpha^{\gamma-1} K n^{\gamma} \ . \tag{C.5}$$

Assume that all quantities are in cgs units. Note that entropy is usually given in keV cm^2 which will need to be converted.

C.3 The Gravitational Profile

The gravitational acceleration of the simulation is dominated by the dark matter halo and by the BCG at small radii. Thus, the acceleration profile can be written

$$g(r) = g_{NFW}(r) + g_{BCG}(r) \ . \tag{C.6}$$

Since the BCG and the cluster are both centered on the origin, this becomes

$$g(r) = -\frac{G(M_{NFW}(r) + M_{BCG}(r)}{r^2} \tag{C.7}$$

The NFW halo has the density profile

$$\rho = \frac{\rho_S}{(r/R_S)(1 + r/R_S)^2} \tag{C.8}$$

where ρ_S and R_S are the characteristic density and radius respectively. However, dark matter halos are usually described in terms of the virial mass (M_{200}, the mass enclosed within R_{200}, withing which the density is 200 times the critical density) and the concentration parameter

$$R_{200} = cR_S \tag{C.9}$$

From the definitions of c and M_{200},

$$\frac{4}{3}\pi c^3 R_S^3 (200\rho_c) = M_{200} \tag{C.10}$$

which can be rearranged to get the scale radius

$$R_S = \left(\frac{3M_{200}}{4\pi c^3 (200\rho_c)}\right)^{1/3} \ . \tag{C.11}$$

The mass enclosed within a given radius r in an NFW halo is

$$M(r) = 4\pi\rho_S R_S^3 \left[\ln\left(\frac{r + R_S}{R_S}\right) - \frac{r}{r + R_S}\right] \tag{C.12}$$

taking the mass at the virial radius gives the scale density

$$\rho_S = \frac{M_{200}}{4\pi R_S^3}\left[\ln(1+c) - \frac{c}{1+c}\right]^{-1} \quad . \tag{C.13}$$

We assume a mass profile for the BCG of the form

$$M_*(r) = M_4 \left[\frac{2^{\alpha_* - \beta_*}}{(r/4\,\mathrm{kpc})^{-\alpha_*}\,(1 + r/4\,\mathrm{kpc})^{\alpha_* - \beta_*}}\right] \quad , \tag{C.14}$$

where M_4 is the stellar mass within 4 kpc and α_* and β_* are constants. This form gives a good match to the empirically derived form used in Li & Bryan (2012) when using the constants given in Meece et al. (2016) and can easily be adapted for other galaxies.

C.4 Density Profile

We assume that the cluster is in HSE and has a static gravitational potential $g(r)$ (based on the NFW halo and BCG). The entropy profile is given by

$$K(r) = K_0 + K_S (r/R_S)^{\beta} \tag{C.15}$$

where K_0, K_S, R_S and β are constants. The ACCEPT sample (Cavagnolo et al., 2009) uses a scale radius $R_S = 100$kpc.

The condition for HSE is

$$\frac{\mathrm{d}P}{\mathrm{d}r} = \mu\,\mathrm{m}_{\mu} g \quad . \tag{C.16}$$

Substituting the expression for P, taking the derivatives, and solving gives the final equation for the density profile

$$\frac{\mathrm{d}n}{\mathrm{d}r} = \left(\frac{\mu\,\mathrm{m}_{\mu} n g}{\alpha^{\gamma-1}} - n^{\gamma}\frac{\mathrm{d}K}{\mathrm{d}r}\right)\left(K\gamma n^{\gamma-1}\right)^{-1} \quad . \tag{C.17}$$

C.5 Temperature Profile

The entropy definition and profile relate the density and temperature at a given radius

$$T = \frac{K(\alpha n)^{2/3}}{\mathrm{k_B}} \tag{C.18}$$

This is used to find the temperature profile once the density profile has been integrated.

C.6 Integrating the Density Profile

The density profile is a non-linear differential equation and can be integrated numerically using an RK4 integrator. First, we need a boundary condition. Following Voit (2005), the temperature of a hydrostatic ICM can be approximated as

$$k_B T = \frac{\mu m_p}{2} \left[10 G M_{200} H(z)\right]^{2/3} \tag{C.19}$$

where m_p is the proton mass, G is the gravitational constant, M_{200} is the mass within R_{200}, and $H(z)$ is the Hubble constant at redshift z. I use this as the temperature at R_{200}, use that to find n at R_{200}, and integrate inwards(towards the center) and outwards to find the entire density profile. Finally, I use Equation C.18 and the entropy profile to find the temperature, and the setup is complete.

Appendix D Fragmentation in dusty low-metallicity star forming halos

Abstract

The first stars in the universe, termed Population III, are thought to have been very massive compared to the stars that form in the present epoch. As feedback from the first generation of stars altered the contents of the interstellar medium, the universe switched to a low-mass mode of star formation, which continues in the high metallicity stars formed in the present era. Several studies have investigated the transition between metal-free and metal-enriched star formation, with tentative evidence being found for a metallicity threshold near $10^{-3.5}\,Z_\odot$due to atomic and molecular transitions and another threshold near $10^{-5.5}\,Z_\odot$due to dust. In this work, we simulate the fragmentation of cooling gas in idealized, low-metallicity halos using the AMR code Enzo. We conduct several simulations of $10^6\,M_\odot$and $10^7\,M_\odot$halos **at** $z = 20$ in which the metal content, initial rotation, and degree of turbulence are varied in order to study the effect of these properties on gas fragmentation over a range of densities. We find tentative support for the idea of a critical metallicity, but the effect of varying metallicity on the gas we observe is not as dramatic as what has been reported in earlier studies. **It is theorized that at lower redshifts with a lower CMB temperature, variations in metallicity might have a larger effect on cooling and fragmentation.** We find no clear relation between the initial spin or the initial level of turbulence in the halo and the final properties of the gas contained therein. Additionally, we find that the degree to which the Jeans length is refined, the initial density profile of the gas, and the inclusion of deuterium chemistry each have a significant effect on the evolution and fragmentation of the gas in the halo – in particular, we find that at least 64 grid cells are needed to cover the Jeans length in order to properly resolve the fragmentation.

D.1 Introduction

[1]It is well established that the very early universe contained only trace amounts lithium and essentially no other elements heavier than hydrogen and helium (Steigman, 2007; Wagoner, 1973). After Big Bang nucleosynthesis, virtually all heavy elements are synthesized in stars. It follows that the first stars, termed Population III stars, must have been free of heavy elements. However, observations have yet to identify any of these metal free stars (Ryan et al., 1996; Beers & Christlieb, 2005; Caffau et al., 2012; Yong et al., 2013) ob-

[1]This chapter was originally published in The Astrophysical Journal (Meece et al., 2014). It has been reformatted for inclusion here. For information about copyright and reuse, see Appendix E.

servations of Lyman-α systems reveal that even low density gas at high redshifts is contaminated by heavy elements, indicating significant enrichment by earlier generations of stars (Cowie & Songaila, 1998). This leads to the conclusion that the first stars were massive and short-lived (Barkana & Loeb, 2001; Ripamonti & Abel, 2004; Bromm & Larson, 2004; Glover, 2005; Norman, 2010).

To produce a stellar initial mass function (IMF) consisting of mostly high mass stars, the process of star formation in the primordial universe must have differed substantially from modern day star formation. Stars form when over-dense clouds of gas radiate energy and collapse due to self gravity. Density perturbations larger than the Jeans length will tend to collapse faster than the surrounding gas. If the gas is able to efficiently radiate energy as it collapses, such that the Jeans Mass decreases with increasing temperature, the gas will continuously fragment. Thus, the final mass of the protostellar cloud will be set by the Jeans mass at the point where the gas can no longer cool efficiently. The initial stellar mass will be set by the size of the protostellar cloud and accretion, although the details of this process are quite complicated, and the Population III IMF is highly uncertain as a result (e.g., Tan & McKee, 2004; McKee & Tan, 2008; Norman, 2010; Clark et al., 2011; Greif et al., 2011). In particular, Clark et al. (2011) and Greif et al. (2011) find that fragmentation in the protostellar disk can result in a cluster of low mass stars, rather than the isolated massive star described by Abel et al. (2002). Radiative feedback from the protostar or protostars will eventually halt accretion, setting the final masses of the stars (Hosokawa et al., 2011; Stacy et al., 2012). While many results for Population III stellar masses have been given, a full understanding of the primordial IMF will not be possible without the use of detailed simulations using a full radiative transfer model. Nevertheless, it is also necessary to understand the growth and large scale structure of the pre-stellar halo.

The ability of the gas cloud to cool will be set by the micro-physics of the gas. In the local universe, rotational lines in CO and line cooling from CI and OI are primarily responsible for cooling (Omukai, 2000), and are able to lower the temperatures of star forming clouds to around 10 K. In the early universe, however, the only significant sources of cooling were H_2 and HD molecules. Due to the lack of a permanent dipole in H_2, the rotational energy levels are relatively widely spaced, and rotational transitions are not able to cool the gas below a temperature of around 200K (Galli & Palla, 1998). While HD is a more effective coolant owing to a permanent dipole moment, the low initial fraction of deuterium prevents a high HD fraction from forming, typically preventing HD from contributing to the total cooling as much as H_2 (Galli & Palla, 2002; Ripamonti, 2007). If heavy elements are present, the gas will be able to cool faster and to lower temperatures than is possible in primordial gas. Metals in the form of dust will be able to cool the gas through thermal radiation (Omukai et al., 2005; Schneider & Omukai, 2010). Dust can also serve as a catalyst for H_2 formation, providing an additional source of cooling.

Many authors have studied the transition from metal-free to metal-enriched star formation using idealized models. While the initial conditions of these models are necessarily less accurate than those of cosmological simulations, their fully specified nature allows one parameter to be varied at a time, facilitating our ability to isolate and understand the effects of individual physical processes. Over the past decade, idealized simulations have explored more of the relevant physical and chemical processes underlying star formation in the early universe, resulting in tunable models that more accurately capture the conditions of primordial and low metallicity star formation. Bromm et al. (2001) modeled a $2.0 \times 10^6\,\mathrm{M}_\odot$top-hat overdensity collapsing at $z = 30$ and found the first evidence of a 'critical metallicity' of approximately $5 \times 10^{-4}\,\mathrm{Z}_\odot$. Omukai et al. (2005) has studied the thermodynamics of collapsing primordial and low metallicity gas using one-zone models. More recently, a series of works (Glover & Jappsen, 2007,?; Jappsen et al., 2009a,b) modelled the collapse of a hot, ionized gas which had been allowed to relax to hydrostatic equilibrium within an NFW potential (Navarro et al., 1997) before cooling was turned on. This group concluded that there is no clear critical metallicity, and that fragmentation is more dependent on the choice of initial conditions.

Several works (Omukai, 2000; Omukai et al., 2005; Schneider et al., 2006; Schneider & Omukai, 2010; Schneider et al., 2012) have focused on the effects of dust cooling on fragmentation in low metallicity clouds. Dust cooling is typically effective at densities above $n_H = 10^{10}$ cm $^{-3}$, where the gas and dust temperatures are coupled. These studies have found evidence of a lower metallicity threshold around $10^{-5.5}\,\mathrm{Z}_\odot$due to dust cooling when dust is included in simulations. In addition, the star SDSS J1029151+172927 (Caffau et al., 2011, 2012) has been found to have $[X/H] < 10^{-4}$ for all elements measured, indicating that some cooling process other than molecular cooling is operating. Klessen et al. (2012) has attributed the formation of SDSS J1029151+172927 to dust cooling induced fragmentation, indicating that dust can produce low-mass stars below the metal cooling threshold.

In this work, we extend the study of the transition from metal-free to metal-enriched star formation by using an idealized model based on the results of cosmological simulations. Our model uses several parameters to set the metallicity, chemistry, and the shape of the initial density, temperature, and rotational profiles, as well as allowing for different levels of turbulence and different halo masses. In Section D.2, we discuss our simulation code and the initial setup of our star-forming halos in detail. In Section D.3, we provide an overview of the evolution of our fiducial model. Section D.4 discusses the effects of varying our refinement criteria and establishes the criteria necessary to adequately resolve the collapse. In Section D.5, we discuss the evolution of our model for different points in the parameter space of metallicity, rotation, turbulence, and dust. In Section D.6, we discuss the assumptions in our simulations that may influence our results, including the effects of deuterium chemistry, the shape of the initial density profile, and the validity of our chemical model. We summarize and conclude in Section D.7.

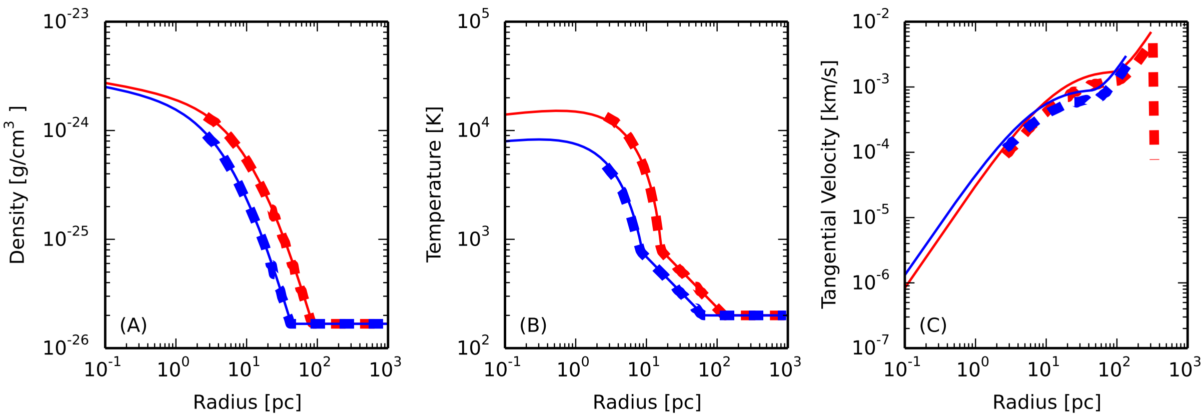

Figure D.1 **Initial Conditions for Low Metallicity Star Formation Simulations:** The initial conditions of our model are shown for our high and mass fiducial models. Solid lines represent the theoretical values, while the dashed lines are the values realized in our simulation. Panel A shows density as a function of radius. The initial temperature profile is derived by assuming hydrostatic equilibrium in the core and a power law fall off in the envelope, and is shown in Panel B. The rotational velocity, shown in Panel C, is derived by assuming that average angular momentum follows a power law relationship as a function of mass enclosed.

D.2 Method

D.2.1 The Simulation Code and Included Physics

We model the collapse of the halo using the Eulerian adaptive mesh refinement code Enzo (O'Shea et al., 2004; Norman et al., 2007; Bryan et al., 2014). The hydrodynamics are calculated using the piecewise parabolic method of Colella & Woodward (1984). In order to ensure conservation of mass within our simulation, we employ periodic boundary conditions for the gas. To calculate the gravitational potential, we assume isolated boundary conditions. In addition to the self gravity of the baryons, we calculate the gravitational potential of a static NFW halo. Each simulation is initialized with a top level grid resolution of 128^3 cells and is refined during setup. Although we do not use comoving coordinates in this work, we assume a redshift of $z = 20$ where necessary during initialization, and all distances in this paper in are in proper parsecs at that redshift. Each halo is placed in the center of a box with a proper size of 2000 pc per side. During initialization, we require that the inner 100 pc be covered by four levels of grid refinement, giving a maximum spatial resolution of 0.977 pc at the beginning of the simulation. As the virial radius of the dark matter halo (taken to be the edge of the sphere) is an order of magnitude smaller than the box size, the effects of boundary conditions on the evolution of the halo should be negligible.

D.2.1.1 Refinement Conditions

We employ four criteria for determining when to refine grid cells. In all simulations, refinement is carried out by subdividing a grid cell by a factor of 2 along each dimension, thus into 8 equal-sized cells. Lagrangian refinement would therefore require that we refine a grid cell whenever the enclosed mass exceeds the average mass in one top level grid cell by a factor of eight. To better understand the evolution of the densest regions, we impose super-Lagrangian refinement by refining whenever cell mass exceeds

$$M_{cell} > M_{top} \times 8^{-0.3 \cdot l} \tag{D.1}$$

Where l is the current refinement level.

Our second refinement condition splits a cell whenever the local cooling time, t_{cool}, is shorter than the sound crossing time of the cell, $\Delta x/c_s$. This requirement is necessary to justify our assumption that the gas is thermodynamically stable at scales smaller than the grid resolution. Thirdly, we refine when the size of a cell is larger than some fraction of the local Jeans length, when $\lambda_J < N_J \Delta x$, where λ_J is the Jeans length (calculated in that cell) and N_J is the number of cells over which the Jeans length must be refined. Unless otherwise noted, we require that the Jeans length be resolved by at least 64 cells at all times, e.g. $N_J = 64$. In Section D.4, we discuss a series of tests to determine the minimum value of N_J necessary in order to accurately model the fragmentation of the collapsing halo. Finally, we require that the region within a cube with side length 100 pc centered on the center of the sphere is always covered by a spatial resolution of less than 1 pc. This criterion ensures that the conditions in the inner region of the halo, as defined by our initial setup, are accurately captured by the mesh. We allow the simulation to dynamically refine using up to 25 levels of grids, for a maximum spatial resolution of 0.0962 AU.

D.2.1.2 Chemistry Model

Our chemistry model follows the non-equilibrium reactions for 12 primordial chemical species (H, H^+, He, He^+, He^{++}, e^-, H_2, H_2^+, H^-, D, D^+, and HD) (Annninos et al., 1997; Abel et al., 1997) and includes H_2 chemistry with three body H_2 formation (Abel et al., 2002) and H_2 formation heating (Turk et al., 2009). In addition, we use the cooling model of Smith et al. (2008) to track cooling from metals in simulations where metals are present. Unlike the chemical model used for primordial species, the metal cooling model does not explicitly track the abundance of individual metal ions. Instead, we use data generated by the photoionization code CLOUDY (see Ferland et al. (1998)) to calculate metal cooling rates for a wide range of densities. Throughout this paper, we assume a scaled solar abundance pattern. The validity of this choice is discussed in Section D.6.5. In Section D.6.1, we discuss the effects of using a reduced chemical model that does not include deuterium chemistry.

D.2.1.3 Dust Model

The presence of dust grains alters the thermal state of the gas by providing a very efficient channel for H_2 formation and through heat transfer via elastic collisions with the gas. Dust grains cool via continuum thermal emission and are heated by incident radiation. Currently, we only consider incident radiation from the CMB, but in principle an additional heating term can be easily added. The rates of H_2 formation on grain surfaces and heat exchange with the gas are dependent on the grain temperature, T_{gr}, which we assume to be in instantaneous equilibrium. The implementation employed here closely follows that of Omukai (2000) and Omukai et al. (2005). We calculate the grain temperature by solving the heat balance equation given by

$$4\sigma T_{gr}^4 \kappa_{gr} = \Lambda_{gas/grain} + 4\sigma T_{rad}^4 \kappa_{gr}, \tag{D.2}$$

where σ is the Stefan-Boltzmann constant and T_{rad} is the radiation temperature, specifically the CMB temperature here. The rate of heat exchange between the gas and dust per unit dust mass, $\Lambda_{gas/grain}$, is given by

$$\Lambda_{gas/grain} = 1.2 \times 10^{-31} \, \frac{n_H^2}{\rho_{gr}} \left(\frac{T}{1000K}\right)^{1/2} (1 - 0.8e^{-75/T})(T - T_{gr}) \quad \mathrm{erg\ s^{-1}\ g^{-1}} \tag{D.3}$$

(Hollenbach & McKee, 1989), where n_H is the H number density and ρ_{gr} is the dust mass density. We assume that as metallicity increases, dust remains a constant fraction of the metallicity. We adopt the piecewise polynomial approximation of the grain opacity of Dopcke et al. (2011), given by

$$\kappa(T_{gr}) \propto \begin{cases} T_{gr}^2 & , T_{gr} < 200 \text{ K}, \\ constant & , 200 \text{ K} < T_{gr} < 1500 \text{ K}, \\ T_{gr}^{-12} & , T_{gr} > 1500 \text{ K}, \end{cases} \tag{D.4}$$

with a normalization of $\kappa_{gr}(T_{gr} = 200\ K) = 16$ cm^2 g^{-1} (Pollack et al., 1994; Omukai, 2000). The steep power law index for $T > 1500$ K mimics the effect of grains melting. We take the exact form of the rate for H_2

formation on grains given in Omukai (2000), which is derived from the work of Tielens & Hollenbach (1985). We include the heating/cooling from H_2 formation/destruction following Omukai (2000) and Hollenbach & McKee (1979).

D.2.2 Initial Conditions

We model the star forming regions as a spherically symmetric baryonic halo with a turbulent velocity field within a static NFW potential. Our models are empirically motivated by the results of cosmological simulations (O'Shea & Norman, 2007; Smith et al., 2009) and informed by the one-zone models of Omukai et al. (2005). Although our simulations are non-cosmological, we assume that the calculation proceeds at a fixed redshift of $z = 20$ for the purposes of calculating heating and cooling rates due to the cosmic microwave background. We assume an ΛCDM universe with $\Omega_\Lambda = 0.7$, $\Omega_M = 0.3$, and $H_0 = 70$ km s^{-1} Mpc^{-1} where relevant during the initialization. These parameters are used when calculating the virial radius of the halo, and small variations in cosmological parameters would not have a large effect on our simulations. We assume that the halo is decoupled from the Hubble flow, and do not take cosmological expansion into account during the simulation (which is reasonable, as the halo is overdense enough to be decoupled from the expansion of the universe.) Thus, all distances quoted in this work are in physical (i.e., proper) units.

D.2.2.1 Dark Matter Halo

The dark matter component of the halo is assumed to reside in an NFW halo (Navarro et al., 1997),

$$\rho_{DM}(r) = \frac{\rho_c}{(r/R_S)\,(1 + r/R_S)^2} \tag{D.5}$$

where ρ_c is equal to four times the density at the virial radius and R_S is the scale radius.

The concentration parameter of the halo, defined as

$$c = \frac{R_{178}}{R_S} \tag{D.6}$$

is set to $c = 2$ for our simulations. Here, R_{178} is the virial radius, calculated as the radius at which the average enclosed density is 178 times the critical density of the universe (see Bryan & Norman (1998) for more discussion). Our value of c is within the expected range for the halos we are studying, as predicted by Davis & Natarajan (2010). In this work, the mass of the halo is taken to mean the mass of dark matter within the viral radius of the halo. Due to the low initial baryon density, the total mass of the halo is not substantially higher. We study models with dark matter masses of 10^6 M$_\odot$and 10^7 M$_\odot$, with corresponding virial radii of 153 and 329 pc. These halos are hereafter referred to as the "low mass" and "high mass" halos, respectively.

D.2.2.2 Baryon Density and Temperature

The baryonic component of the halo is modeled by a core in roughly hydrostatic equilibrium with a diffuse envelope. The envelope drops off rapidly until it reaches the background density of $n_H = 10^{-2}$ cm $^{-3}$. The density profile is described by

$$\rho_B(r) = \frac{\rho_B}{(r/R_{core})^{\alpha}\,(1 + r/R_{core})^{\beta-\alpha}} \tag{D.7}$$

and is shown in the Panel A of Figure D.1. For our simulations, we use $\alpha = 0.1$ and $\beta = 2.5$. These values were chosen by fitting the results of the cosmological simulations performed in O'Shea & Norman (2007) and additional unpublished simulations performed by our group for this study.

For the initial density profile, we use a central baryon number density of $n_H = 1$ cm $^{-3}$for both the high and low mass fiducial cases. For the low mass halo, we choose a core radius of $R_{core} = 8$ pc and for the high mass case $R_{core} = 16$ pc. Our choice of a low initial central density (compared to the dark matter density) is motivated by the desire that the simulation have time to 'forget' the details of the initial conditions and reach a stable configuration before collapse sets in. In Section D.6.3, we discuss the results of starting a simulation with a higher initial central density.

The temperature profile is calculated by assuming that the gas is in hydrostatic equilibrium within the core and is being adiabatically heated in the envelope. The initial temperature profiles is shown in Panel B of Figure D.1.

D.2.2.3 Chemistry and Metallicity

We initialize the gas in our model to a composition consistent with conditions in the $z = 20$ universe for gas that has not been affected by recent star formation. At initialization, all simulations have a uniform electron fraction of $\chi_e = 1.69 \times 10^{-4}$, based on calculations performed with the code RECFAST (Seager et al., 1999, 2000), and a corresponding HI fraction of $f_{\mathrm{HI}} = 0.999831$. The H^- fraction is $f_{\mathrm{H}^-} = 10^{-10}$. The initial molecular hydrogen fraction is $f_{\mathrm{H_2I}} = 10^{-4}$. Initial values for D and HD are scaled to the H and $\mathrm{H_2}$ values using a D/H mass ratio of 6.8×10^{-5}.

In models where metals are present, we assume a scaled solar abundance of heavy elements. Metallicity is kept uniform throughout the simulation. In simulations where dust is present, it is assumed that the mass fraction of heavy elements in dust is 9.23×10^{-3}. The effects of our choice of initial chemistry is discussed in Section D.6.

D.2.2.4 Velocity Profile

The halo is given an initial angular momentum distribution characterized by the dimensionless baryonic spin parameter, defined in Peebles (1971) as

$$\lambda = \frac{J|E|^{1/2}}{GM^{5/2}} \tag{D.8}$$

where J is the total angular momentum of the baryons, E is the binding energy of the baryons, G is the gravitational constant, and M is the mass of the baryons. Based on the results of O'Shea & Norman (2007), the angular momentum is distributed so that the specific angular momentum as a function of mass enclosed is given by

$$|l|(M < r) \propto \left(\frac{M(< r)}{M_{Total}}\right)^{0.9} \tag{D.9}$$

which is scaled by the spin parameter.

Gas outside of the virial radius has no initial velocity, and none of the gas has an initial radial velocity before turbulence is added. The dark matter component of the halo is treated as a static potential, and thus has no velocity. The initial rotation profile for our fiducial models is shown in Panel C of Figure D.1.

D.2.2.5 Turbulence

The rotational velocity is modified by adding a turbulent velocity field with a power spectrum $P(k) \propto k^{-4}$, suitable for compressible gas (Clark et al., 2011). The turbulent field is generated using the method described in Rogallo (1981). The turbulent field is applied only within the virial radius of the halo, and is normalized such that the RMS velocity is a specified fraction of the sound speed of the halo, as defined in Barkana & Loeb (2001). For consistency, the same turbulence field was used for all simulations.

D.2.3 Varying the Initial Conditions

In order to study the importance of different model parameters to the evolution and fragmentation of the gas, we conduct several runs wherein one parameter is systematically varied. For each parameter, we conduct simulations for both the high and low mass halos, as described above. The full list of simulations performed in this work is given in Tables 1-5.

We run our simulations until the central density has reached a hydrogen number density of at least

$n_H = 10^{10}$ cm $^{-3}$, which is near the limits of the validity of our cooling model and is approaching the point where our assumption that the gas is optically thin begins to fail. Thus, we do not model the actual formation of stars, which occurs at higher densities and requires a full radiative transfer model. The final mass of the star will be set by additional physics, including additional cooling processes (such as collisional ionization), radiative feedback, and disk formation. Additionally, while dust cooling had been theorized to be important at high densities (see Section D.6.2 for discussion), we do not fully explore this regime.

D.2.4 Clump Finding

To quantify the degree of fragmentation, we run a clump finder on the central 20 pc of the final output from each simulation. The clump finding algorithm, described in detail in Smith et al. (2009) and implemented in the `yt`[2] simulation analysis toolkit (Turk et al., 2011), works by identifying topologically disconnected structures in density space. Following Smith et al. (2009), we define a clump or fragment as "the mass contained between a local density maximum and the lowest isodensity surface surrounding only that maximum." Smith et al. (2009) only consider clumps that are strictly gravitationally bound, but here we use a modified criterion to include clumps that are marginally unbound but rapidly cooling, since these objects will likely become bound in the future. Clumps are considered valid if they satisfy the following requirement:

$$KE + TE - \sum_i (\Lambda_i \; t_{dyn,i}) < PE, \tag{D.10}$$

where KE, TE, and PE are the total kinetic, thermal, and potential energy of the clump and Λ_i and $t_{dyn,i}$ are the cooling rate and dynamical time for reach grid cell that is a member of the clump. Single cell clumps are not considered valid under any circumstance.

In order to quantify the degree of fragmentation as density increases, we count the number of clumps meeting the above criteria which form in a given density interval. To begin, we search for clumps in half dex density intervals running from $\rho_{\min}$ to $\rho_{\max}$ (in this work, $n_H = 1$ and $n_H = 10^{10}$ respectively). For each clump, we record the density of the surrounding isodensity contour. Secondly, in each density interval we count the number of clumps for which the surrounding contour falls within the interval. In theory, density regimes in which the gas undergoes fragmentation should be marked by an increase in the number of clumps forming at those densities. The degree of fragmentation in different simulations may be compared visually, as in the style of Figure D.8.

Additional tests have shown that the trend produced by our fragmentation quantification procedure are moderately insensitive to the manner in which we define a clump. Specifically, counting clumps in which

[2] http://yt-project.org/

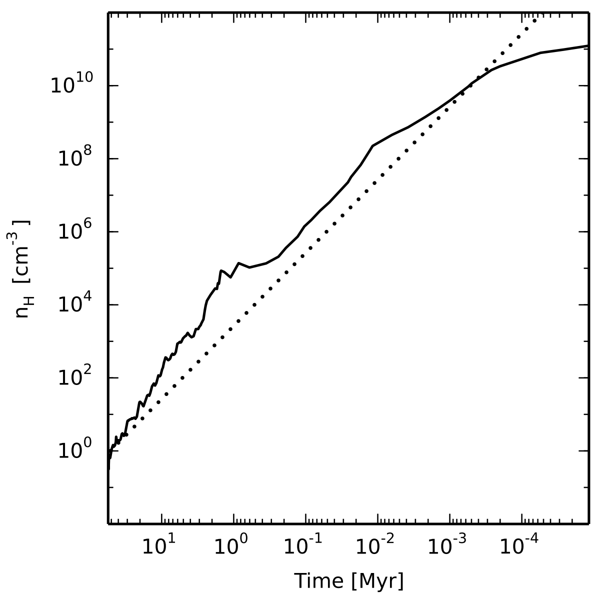

Figure D.2 **Density Evolution of the Fiducial Run:** The central density of the gas is shown as a function of time. The x axis shows time in millions of years before the last data output. The time from the beginning of the simulation to the last data output is 55.36 million years. The dotted line shows the free fall time of a sphere of gas with a given density. On the left hand side of the plot, the central density is increasing faster than the free fall time scale (as indicated by the slopes of the lines), indicating that the dark matter rather than self gravity is controlling the dynamics of the gas. During the last million years of the simulation, the self gravity of the gas dominates in the center. The gas evolves in free fall until roughly 10,000 years before the end of the simulation, in which pressure support delays further collapse.

$KE < 0.1 \times PE$ and counting all clumps containing > 40 cells reproduces the trends seen in section D.5.1.

D.3 Evolution of the Fiducial Model

For our fiducial model, we choose high and low mass halos with a metallicity of $Z = 10^{-3}\,\mathrm{Z}_{\odot}$, a spin parameter of $\lambda = 0.05$, turbulence normalized to 0.4 times the halo sound speed, and with dust present. This model is chosen to simulate a typical star forming halo at $z = 20$, which has not hosted recent star formation (e.g., O'Shea & Norman (2007); Smith et al. (2009)). We choose a metallicity which is in the middle of our range of values, and is near the theoretical "critical metallicity." We mandate that the Jeans length be covered by at least 64 cells at all times by setting $N_J = 64$.

The high mass fiducial halo collapses 55.36 million years after the beginning of our simulation. The evolution of the central density as a function of time is shown in Figure D.2. The collapse begins slowly and accelerates as density increases. While the dark matter dominates during the early stages of the collapse, the baryons come to dominate the potential during the last million years, making our results relatively insensitive to the halo profile at densities above $n_H = 10^5$ cm $^{-3}$, roughly corresponding to the inner 1 pc.

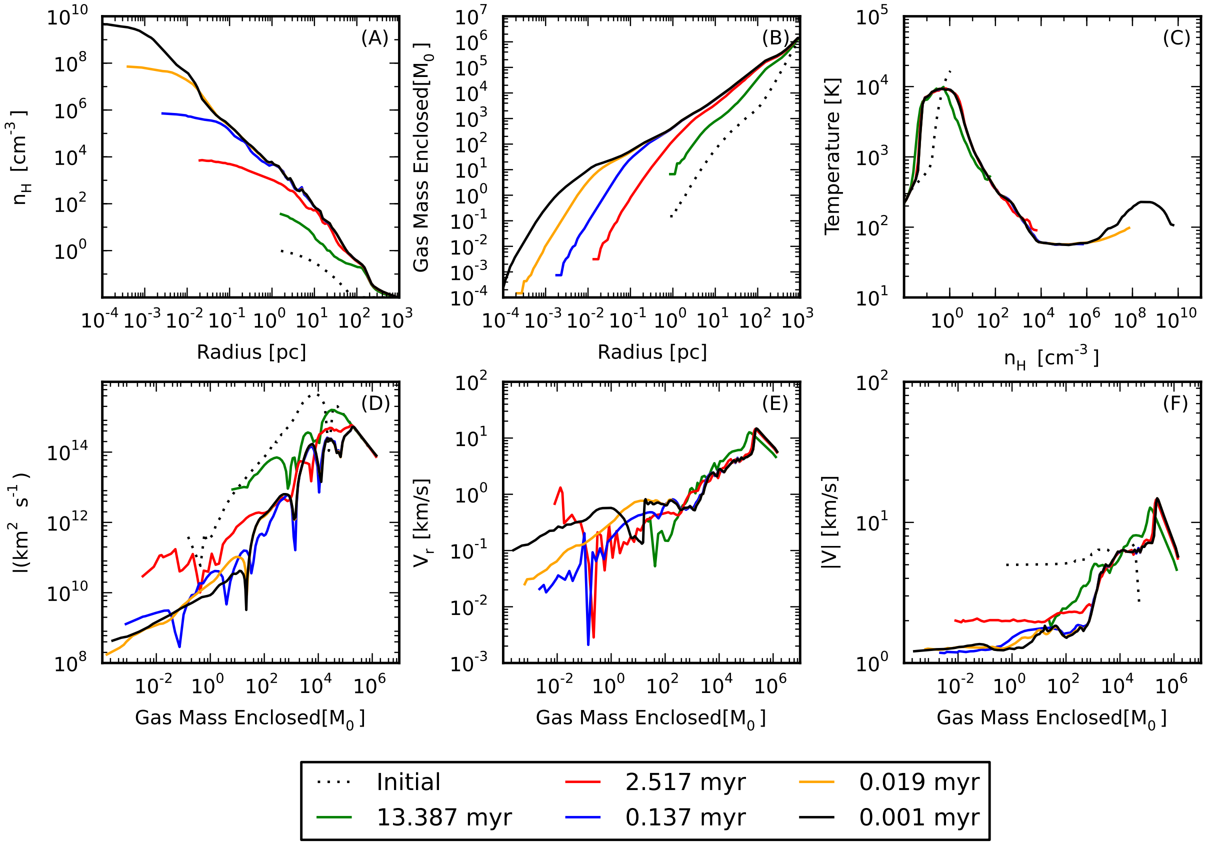

Figure D.3 **Gas Properties for the Fiducial Run:** The physical state of the gas in our high mass fiducial model is shown for a series of outputs. The green, yellow, blue, red, and black lines show the first outputs in which the central density reaches 10^2, 10^4, 10^6, 10^8, and 10^{10} cm $^{-3}$, respectively. For each output, the legend shows the time remaining until the end of the simulation. Panel A shows spherically averaged gas density as a function of radius, centered on the densest point in the simulation. Panel B shows the total gas mass enclosed as a function of radius. Panel C shows the mass weighted spherically averaged temperature of the gas as a function of density. Panel D shows the mass averaged angular momentum as a function of enclosed mass. For a spherically symmetric collapse with not angular momentum transport, the angular momentum profile would not change with time. The fact that it does indicates that angular momentum is being transported out of the core by turbulence. Panels E and F show the mass weighted spherically averaged radial velocity and velocity magnitude of the gas as a function of mass enclosed. In each panel except Panel E, the initial conditions are represented by a dotted black line. The gas has no initial net radial velocity.

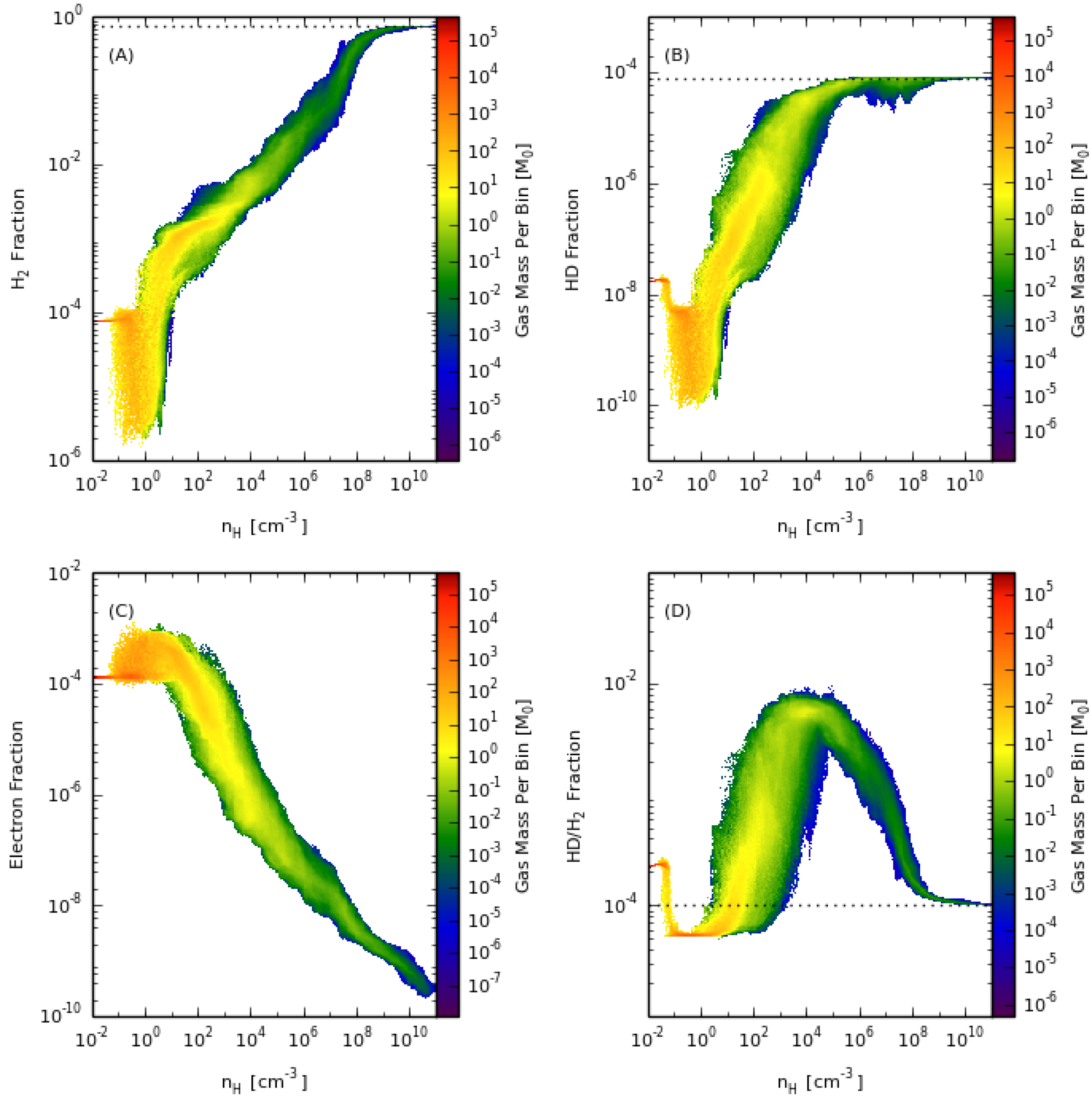

Figure D.4 **Chemical State of the Gas for the Fiducial Run:** The chemical state of the gas for the high mass fiducial model is shown. Panels A and B show the mass fractions of H_2 and HD respectively. Panel C shows the ionization fraction. Panel D shows the ratio of the HD to H_2 mass fractions. The dotted lines in Panels A and B show the mass fractions when H and D respectively are fully molecular, and the dotted line in Panel D shows the mass fraction ratio when both species are fully molecular.

When the simulation is initialized, there is a period lasting around 10 million years during which the velocity profile evolves into a steady state. During this time, the details of the initial conditions are wiped out. At this point, the gas in the envelope is collapsing in free fall and is being heated through adiabatic compression, while the gas in the core is pressure supported. An accretion shock forms at the edge of the sphere, near the virial radius. As the gas is decelerated, it is heated to the virial temperature of the halo. As shown in Panel A of Figure D.3, the collapse evolves self similarly, with the size of the core shrinking as the gas collapses to higher central densities. The velocity profile of the gas as a function of enclosed mass, shown in Panels E and F of Figure D.3, remains roughly constant, with the gas in the envelope in free fall and the gas in the core collapsing slowly. The gas in the core evolves quasi-statically until near the end of the simulation, at which point the gas is able to efficiently cool and collapses on a free fall timescale.

Panel D of Figure D.3 shows the mass averaged angular momentum of the gas as a function of enclosed gas mass, defined as

$$l(M) = \frac{\Delta J(M)}{\Delta M} \tag{D.11}$$

where ΔM is the mass of gas enclosed within a spherical shell and $\Delta J(M)$ is the total angular momentum of the gas within the shell. With no angular momentum transfer and no external torque, $l(M)$ would stay constant throughout the collapse. In our simulations, $l(M)$ decreases, indicating that angular momentum is being transported outward (relative to the Lagrangian mass coordinate) in the central regions.

The physical evolution of the model may be understood by looking at the thermodynamic evolution of the gas, shown in Panel C of Figure D.3, and the chemical evolution, shown in Figure D.4. In low density regions, the gas is in free fall, and is heated by adiabatic compression. The relevant reaction rates are too slow to change the initial molecular chemistry, and radiative cooling is negligible compared to compressive heating.

At the accretion shock, the gas is rapidly heated to the virial temperature of the halo. In the high mass halo, the virial temperature is high enough that the gas enters the regime in which a small fraction of the H_2 and HD molecules are dissociated and some of the gas is ionized. As the gas becomes denser, the gas cools and the molecular fraction begins to increase.

The main coolants in the gas at are H_2, HD, and metals. At temperatures below 10,000 K, atomic hydrogen line cooling becomes negligible. H_2 is the most abundant species that is capable of radiative cooling, but is inefficient owing to the lack of a permanent dipole. Instead, the H_2 molecule must rely on rare quadrupole transitions between widely spaced energy levels, and by itself is unable to cool the gas below a temperature of around 200 K (Galli & Palla, 1998). HD, though rarer, has a permanent dipole moment and thus is able to cool more efficiently. Together, rotational transitions in HD and fine structure transitions in metals can effectively cool the gas to the CMB temperature floor. The ratio of HD and H_2 is set by the equilibrium rate of the reactions

$$H_2 + D^+ \Rightarrow HD + H^+ \tag{D.12}$$

$$HD + H^+ \Rightarrow H_2 + D^+ \tag{D.13}$$

as described in Omukai et al. (2005). Because of the differences in the energy levels of H_2 and HD, Equation D.12 is preferred over Equation D.13, resulting in an HD/H_2 fraction that is higher than the overall D/H fraction by roughly 2 orders of magnitude (Galli & Palla, 1998). This fractionation is observed in Panel D of Figure D.4, which shows the HD/H_2 ratio. As the gas cools, the equilibrium abundance rapidly begins to favor HD production, which further increases cooling and in turn leads to more HD formation. For densities higher than $n_H \sim 10^5$ cm $^{-3}$, the deuterium is fully molecular.

The gas continues to collapse until either the temperature is too low to populate excited states in the coolants or the gas reaches the CMB temperature. For halos at $z = 20$, we impose a CMB with temperature

$$T_{\rm CMB} = 2.725\ (1 + z) = 57.225\ \rm K \tag{D.14}$$

which enters into the heating equation for the gas and dust. The gas remains at the CMB temperature floor until a density of $n_H \sim 10^7$ cm $^{-3}$is reached, at which point rapid formation of H_2 on dust grains briefly reheats the gas. At the highest densities, cooling via dust emission is able to efficiently lower the temperature of the gas, resulting in cooling in the higher-metallicity simulations.

The formation of structure in the halo is governed by the thermodynamics of the gas during collapse. If the collapsing gas is able to cool with increasing density or if the temperature increases with density at a slower rate than $T \propto \rho^{1/2}$, the local Jeans mass will decrease. As the local Jeans mass sets the scale for fragmentation, the gas will be expected to fragment whenever the Jeans length is decreasing. Figure D.5 shows projections of density through the gas as the central density increases. At low densities, the mass of gas in the center region is below the local Jeans mass. As indicated in Panel C of Figure D.3, the gas is able to cool with increasing density for densities between $n_H \sim 10^1$ cm $^{-3}$and $n_H \sim 10^5$ cm $^{-3}$. As the gas cools and density increases, the local Jeans mass is lowered below the central gas mass, causing perturbations to grow in the regime where the density is above $n_H \sim 10^2$ cm $^{-3}$.

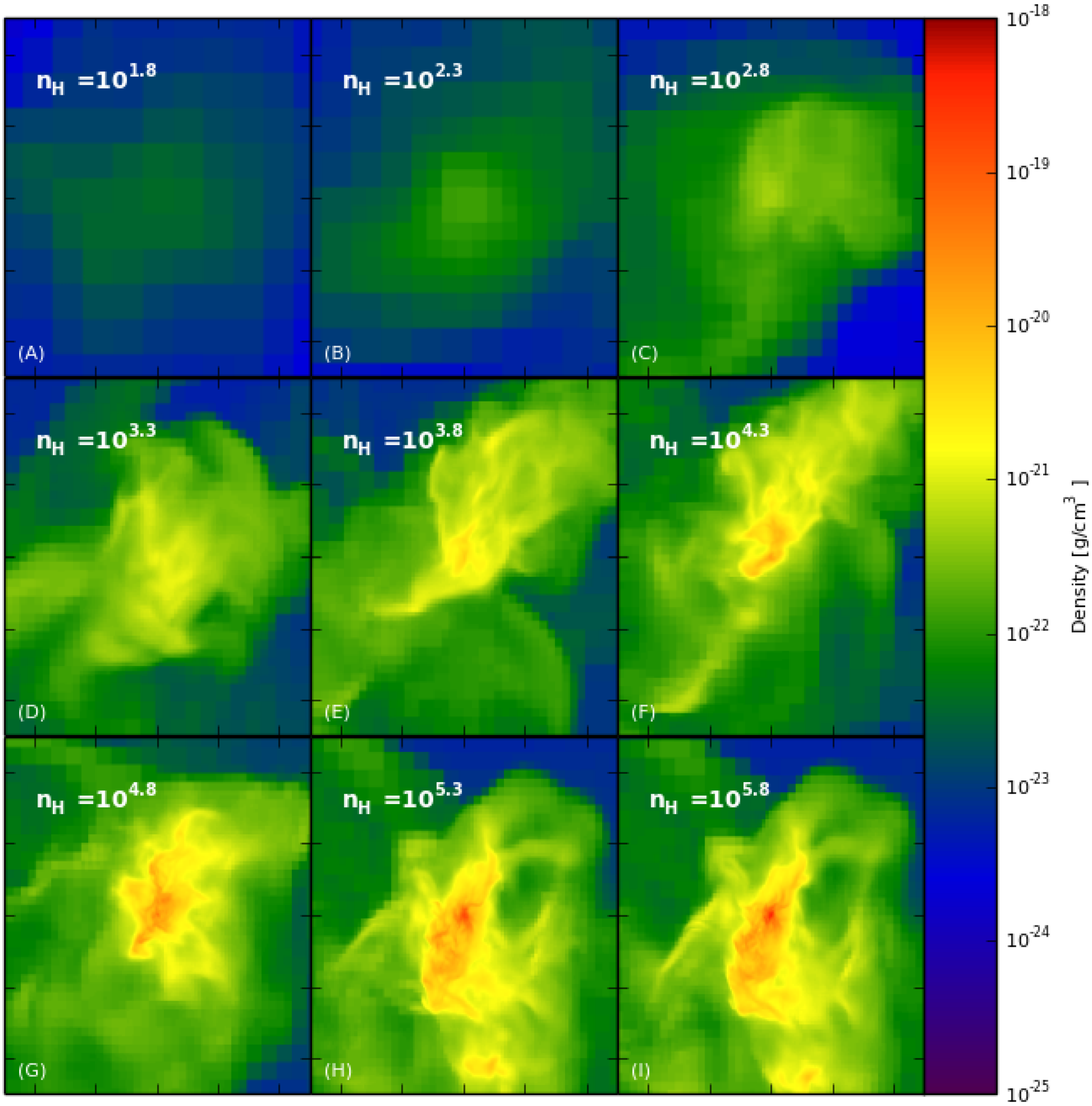

Figure D.5 **Projections of Density for the Fiducial Run:** Projections of average density through the densest point are shown as the central density increases. Each projection has a scale of 10pc. The gas is unstable to fragmentation whenever the Jeans mass decreases with increasing density, which occurs for densities between $n_H \sim 10^1$ and $n_H \sim 10^4$ cm $^{-3}$, but structure will only form when the central gas mass exceeds the local Jeans mass, which only occurs once the central density has increased above $n_H \sim 10^3$ cm $^{-3}$.

D.4 Refinement Criteria

To achieve the large dynamic range studied in our simulations, we selectively refine grid cells based on density, cooling time, and Jeans length, as described in Section D.2.1.1. As part of this work, we have carried out a number of simulations wherein we vary the number of cells required to cover the Jeans length, N_J, in order to determine the minimum set of criteria needed to resolve the collapse.

As described in Truelove et al. (1998), under-resolving the Jeans length in grid based codes can lead to artificial super-Jeans perturbations that may lead to spurious fragmentation. In tests of the collapse of a cloud with a Gaussian density profile, Truelove et al. (1998) concludes that the Jeans length should be covered by at least 4 cells at all times. However, this does not necessarily imply that the simulation is resolved enough to reveal pertinent details of fragmentation in the collapsing gas. Indeed, several studies (Federrath et al. (2011); Turk et al. (2012); Latif et al. (2013) and references therein) have found that at least 32-64 cells per Jeans length are necessary for resolving vorticity when modeling magnetic fields in Population III star formation.

To understand the effects of varying the strictness of the Jeans criterion on the physical phenomenon we are interested in, it is important to understand which refinement criteria dominate at different densities. In Figure D.6, we show the minimum level to which a cell must be resolved as a function of density for each refinement criterion in our fiducial model. From Equation D.1, it is easy to calculate the minimum grid level for which the mass refinement criteria is satisfied for a given density. To calculate the refinement level necessary to satisfy the Jeans and cooling criteria, which rely on the temperature and the cooling time in addition to the density, we use the average values of these quantities at each density from our fiducial model. Since a cell will be refined until all refinement criteria are met, the criterion with the largest minimum value will be the dominant criterion at a given density. In fact, if the required Jeans length coverage is set to $N_J = 64$ or higher, the only place where the Jeans length will not be the dominant criterion is at the lowest densities, where fragmentation has not yet begun. From Figure D.6, it can be seen that the Jeans refinement criterion is the dominant criterion at almost all densities. In addition, it is seen that for a range of densities, the Jeans criterion will be the dominant criterion even when the minimum number of cells covering the Jeans length is lowered. Thus, increasing the mandated Jeans length coverage will change the resolution over a wide range of densities and in general will increase the resolution of the simulation over a large range of spatial and mass scales as compared to the standard density-based criteria.

The lines shown in Figure D.6 are calculated using the mass-weighted average of the temperature and cooling time at a given density. While this approach is useful for finding the regimes when each criterion is

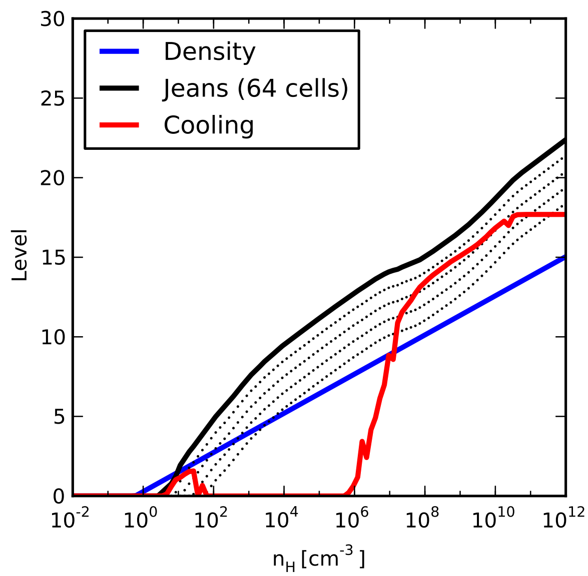

Figure D.6 **Maximum Refinement vs. Density:** The minimum refinement level for each refinement criterion is shown as a function of density for our high mass fiducial halo. In other words, each line represents the level to which the simulation would refine if only that criteria were applied. A cell will be refined until it is at the highest necessary refinement level, meaning that the actual level of refinement at a given density is indicated by the highest level in the plot above. The Jeans criterion and cooling time criterion are evaluated using the mass weighted average temperature and cooling time for each density. The solid black line shows the Jeans refinement level with 64 cells covering the Jeans length. From top to bottom, the dotted black lines show the level with 32, 16, 8, and 4 cells covering the Jeans length.

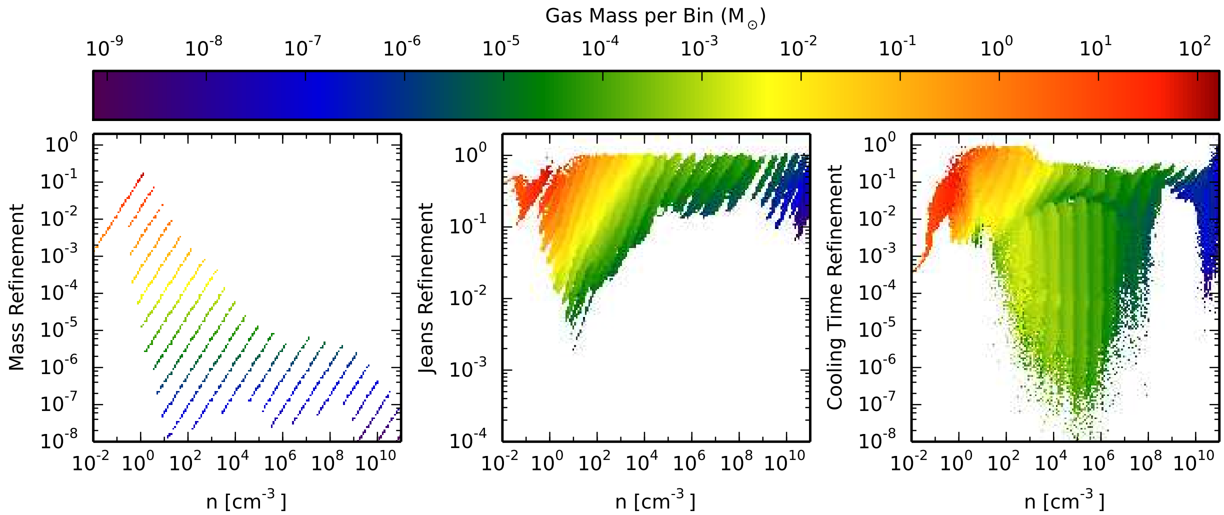

Figure D.7 **Importance of Refinement Criterion:** The importance of different refinement criteria are shown for our $10^7\,\mathrm{M}_\odot$fiducial model. For each criteria, a cell is refined if one quantity (e.g. cell mass) is greater than a second quantity (e.g a minimum mass for refinement). The ratio of the two quantities are denoted by ξ, where ξ_{Mass} is the ratio for mass refinement, ξ_{Jeans} is the ratio for Jeans refinement, and ξ_{Cooling} is the ratio for cooling based refinement. A cell should be flagged for refinement if ξ for any criteria is greater than 1.0. At most densities, the Jeans criterion is the most dominant refinement criterion, with cooling time being important at low densities. Density based refinement is never important.

dominant, it does not take into account variations in the temperature or cooling time of the gas at a given density, which may cause the minimum refinement level to vary. In particular, an average cooling time for gas near the CMB floor is not representative. Gas in that density regime with a temperature above the floor will cool, while gas with a temperature below the floor will heat, giving an average cooling time that is very long but ignoring that the actual cooling or heating time of the gas may be significantly shorter. In order to assess the importance of the different criteria on a cell-by-cell basis, we look at how close each cell in the simulation is to being refined. To do this, we evaluate the ratios

$$\xi_{\mathrm{Mass}} = \frac{M_{cell}}{M_{top} \times 8^{-0.3 \cdot l}} \tag{D.15}$$

$$\xi_{\mathrm{Jeans}} = \frac{N_J \Delta x}{\lambda_J} \tag{D.16}$$

$$\xi_{\mathrm{Cooling}} = \frac{t_{cool}}{t_{sound}} \tag{D.17}$$

where M_{cell} is the mass of the cell, M_{top} is the mass of a top level grid cell, N_J is the number of cells that must cover the local Jeans length, Δx is the cell width, λ_J is the local Jeans length, t_{cool} is the cooling time, and t_{sound} is the sound crossing time of a cell, $t_{sound} = \Delta x / c_s$. If any of these ratios are greater than 1, a cell will be refined. For our fiducial model, the distributions of $\xi_{\rm Mass}$, $\xi_{\rm Jeans}$, and $\xi_{\rm Cooling}$ are shown in Figure D.7. As expected, the density refinement criterion is not important for cells with densities greater than $n_H \sim 10^1$ cm $^{-3}$. At low densities, both the Jeans and cooling time criteria are close to being met in a large number of cells. At higher densities, only the Jeans criterion is close to being met, indicating that it is indeed the only important refinement criterion. Panel C of Figure D.7, however, does indicate that the cooling time refinement is likely to be dominant at low densities for some cells.

Further tests of our fiducial model in which only the Jeans criterion is used show similar overall evolution to the runs with all three refinement criteria, but for the high mass run there are a small number of cells that are not refined, but ordinarily would meet the cooling criterion for refinement. Thus, the cooling time criterion is necessary in some circumstances to fully resolve the collapse of the gas. For our low mass model, we find that the Jeans criteria is always dominant because temperatures are lower and thus the cooling time is longer than in the high mass case.

Having established that the Jeans criteria is nearly always the dominant factor in setting grid resolution, the question becomes how strict our refinement criteria needs to be in order to properly resolve the collapse and fragmentation of the cloud. To understand the effects of resolution criteria, we have carried out a series of runs (described in Table D.2) where we vary the number of cells that must cover the Jeans length from the Truelove criterion of $N_J = 4$ to a maximum of $N_J = 64$, the limit of what is computationally feasible for our study. The final state of this suite of simulations is shown at a scale of 10 pc in Figure D.9 for our high mass halo.

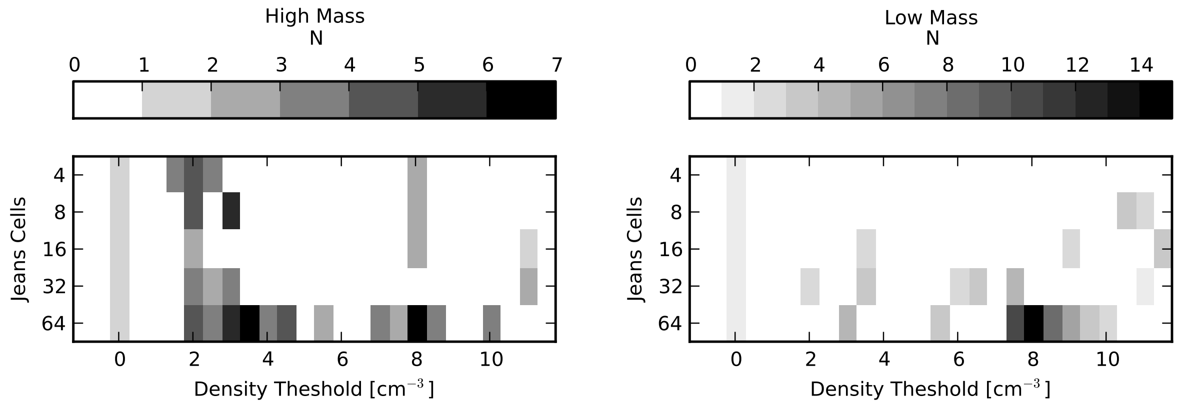

Figure D.8 **Effect of Refinement Criterion on Fragmentation:** The number of gravitationally bound or nearly bound clumps is shown for runs with different levels of Jeans refinement. The y-axis shows the number of cells that must cover the local Jeans length at all times. We identify clumps using a contouring algorithm, and keep only those clumps that are close to being gravitationally bound and which will become bound if cooling continues. The number of clumps in each half dex contour interval is shown above. Clump finding is performed when each run reaches a central density of 10^{10} cm $^{-3}$. For a full description of the clump finding routine, see Section D.2.4.

From these projections, it is clear that the evolution of the gas is affected by the level of resolution, even when the Truelove criterion is substantially exceeded. The runs with $N_J = 32$ and $N_J = 64$ show fragmentation on small scales that is not present in the other runs. The differences stem from increased resolution of the gas at the densities where fragmentation occurs, which leads to an increase in the strength of perturbations with large wave number. From the projections, it is clear that a "phase transition" of sorts occurs between $N_J = 16$ and $N_J = 32$ cells, but there are also hints of additional fragmentation at $N_J = 64$ cells. We note that using $N_J = 128$ when simulating the high mass halo caused a sharp increase in the number of grid cells in the simulation, and the run was terminated when it was determined to be computationally infeasible. For the rest of the runs in this study, we choose to use 64 cells to cover the Jeans length in order to resolve small scale perturbations while maintaining computational feasibility, but caution the reader that further increasing the resolution may have non-negligible effects.

In order to quantify the effect of Jeans resolution on fragmentation, we use the clump finding algorithm described in Section D.2.4 to find the number of potentially bound clumps in each simulation, which is shown in Figure D.8. We observe a trend of increasing fragmentation (inferred from the increase in the number of identified clumps) with higher resolution of the Jeans length. The increase in fragmentation is seen at all densities, and is particularly evident at higher densities ($n_H > 10^3$ cm $^{-3}$). The low mass halo shows less fragmentation overall, but the trend of increasing fragmentation with increasing strictness of the Jeans resolution criteria holds.

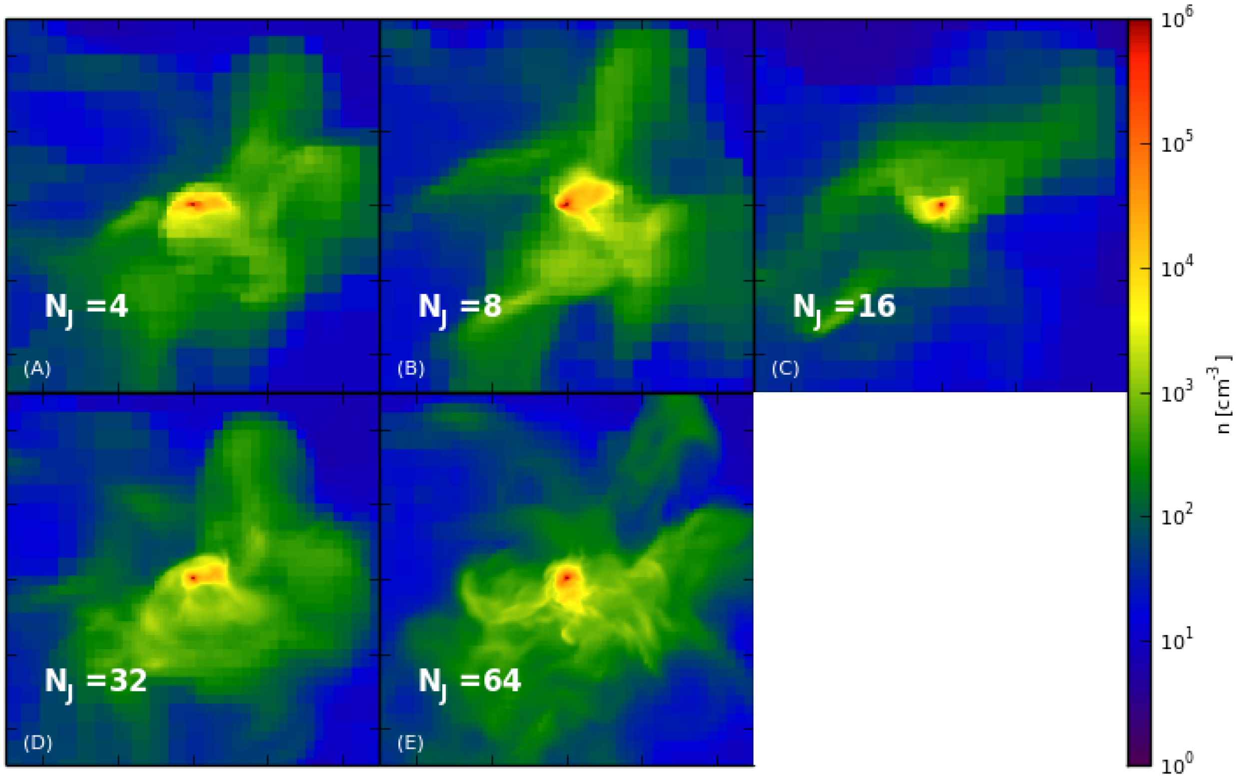

Figure D.9 **Effect of Refinement Criterion on Gas Density:** Projections of average density through the densest point in the simulation for runs with different Jeans refinement criteria for our 10^7 $M_{\odot}$fiducial halo. Each projection has a width of 10 pc, and is taken when the central density has reached $n_H = 10^{10}$ cm $^{-3}$.

D.5 Effects of Physical Parameter Variation on Gas Fragmentation

D.5.1 Metallicity

Several studies have found that the introduction of metals has a strong effect on the cooling properties of star forming gas. As the fraction of metals increases, the gas is able to cool more efficiently. This in turn may lead to increased fragmentation, and is the reason that increasing metallicity has been proposed as the driving factor behind the purported transition between a high characteristic mass Population III IMF and a lower characteristic mass metal-enriched IMF. To understand the effects of metallicity in our model, we perform a series of runs (see Table D.1) where the metal content of the gas is varied from a uniform metallicity of $Z = 0$ (metal free, primordial gas) to $Z = 10^{-2}\,\mathrm{Z}_{\odot}$. In these simulations, we assume that a fixed fraction (9.23×10^{-3} by mass) of the metals are in the form of dust.

The effect of varying metallicity on the physical and thermodynamic evolution of the gas is shown in Figure D.10 for the high mass halo. The evolution of the low mass halo is visually similar, with the exception of the lower virial temperature. Increasing the amount of metals alters the cooling rate in three ways. First, metals directly cool the gas, allowing the temperature to reach the CMB floor more quickly and at lower densities. Second, increasing the metallicity increases the amount of dust present. As dust-mediated reactions become the dominant molecular formation channel, H_2 and HD are able to form efficiently at densities below $n_H = 10^8$ cm $^{-3}$, when 3-body reactions become effective. This leads to more cooling at lower densities. Thirdly, dust itself becomes an effective coolant at densities above $n_H = 10^9$ cm $^{-3}$.

The effects of metals on the physical state of the gas may be understood by looking at projections of gas density in the core of the halo. In Figure D.11, we show the final state of the high mass halo at a scale of 3 pc. Projections through the same regions of the low mass halo show similar behavior.

At high metallicities, the gas is able to cool rapidly, meaning that the densest region will be able to collapse before a large mass of gas has built up in the core. For low metallicity and metal-free gas, however, the gas must rely on H_2 and HD to cool. The collapse is delayed, which gives the core more time to grow, leading to a larger mass of dense gas in the central region. This is clearly seen in Figure D.11 (particularly in Panel A), where the densest regions in the low metallicity runs are surrounded by more gas than in the high metallicity runs. The accretion rate is lower in the low mass halo, and the trend is not as clear. From the collapse times given in Table D.1, it is evident that there is a trend of faster collapse with increasing metallicity.

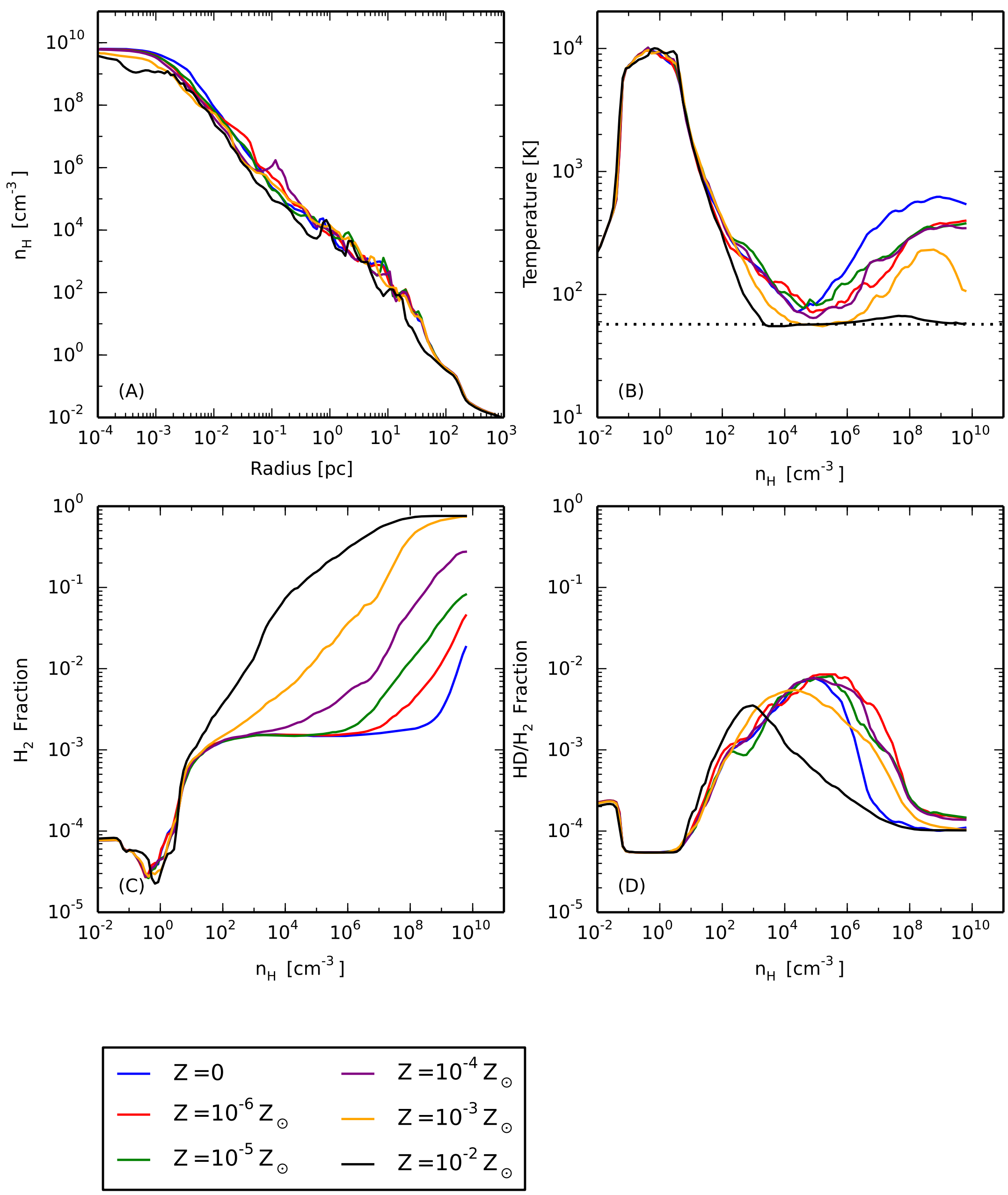

Figure D.10 **Gas Profiles for Simulations With Different Metallicities:** Comparison of the physical, thermal, and chemical state of our high mass halo as metallicity is varied, at the point when the simulation reaches a central density of $n_H = 10^{10}$ cm $^{-3}$. Panel A shows spherically averaged, mass weighted density as a function of radius. Runs with higher metallicity collapse faster, leading to lower densities in the regions surrounding the densest point. Panel B shows spherically averaged, mass weighted temperature as a function of density. As metallicity is increased, the gas is able to cool to lower temperatures. The CMB temperature is indicated by a dashed line. Panel C shows the molecular hydrogen mass fraction as a function of density. In the metal free case, molecular hydrogen is formed primarily through the three body process, which does not become effective until densities of $n_H \sim 10^8$ cm $^{-3}$. As metallicity is increased, dust catalyzed reactions become the dominant mode of H_2 formation. Panel D shows the ratio of the HD to H_2 mass fractions, which is enhanced over the atomic value through chemical fractionation.

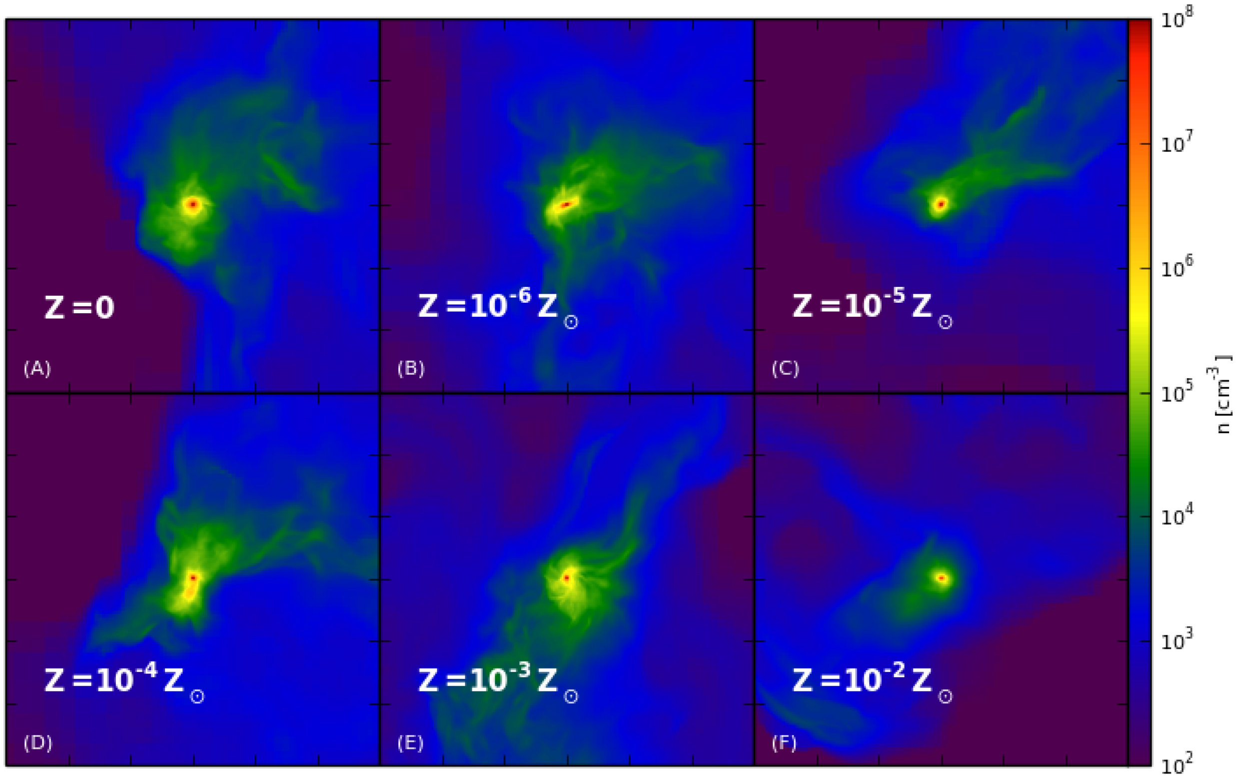

Figure D.11 **Projections of Gas Density for High Mass Halos:** Projections of average density through the densest point in the simulation for runs with different metallicity for our $10^7\,M_{\odot}$halo. Each projection has a width of 3 pc, and is taken when the central density has reached $n_H = 10^{10}$ cm $^{-3}$.

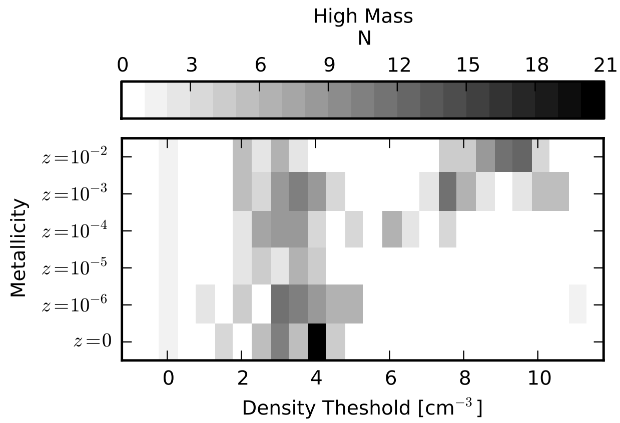

Figure D.12 **Bound Clumps for Simulations with Different Metallicity:** The number of bound or potentially bound clumps identified by our clump finding algorithm as partially bound for runs in which metallicity is varied.

We expect that as the cooling rate increases, the amount of fragmentation will increase. In Figure D.12, we show the distribution of clumps as a function of n_H for the high and low mass halos. In the density range $10^1 < n_H < 10^5$ cm $^{-3}$, all runs show evidence of fragmentation, with slightly more fragmentation at higher metallicities. Here, the gas is able to fragment because the temperature is decreasing with increasing density. After the gas reaches the CMB floor it is no longer able to cool as density increases, inhibiting further fragmentation. As H_2 is formed, thermal energy is injected into the gas. The halos with higher metallicity are able to effectively radiate away this energy, which allows for more fragmentation at higher densities. In our high mass halo, only the simulations with metallicities about $10^{-3}\,Z_{\odot}$show evidence of fragmentation at $n_H \gtrsim 10^7$ cm $^{-3}$. We note that cooling from dust may lead to further fragmentation in the lower metallicity runs at higher densities. As noted by Schneider et al. (2006) and Schneider & Omukai (2010), dust cooling may lead to fragmentation in haloes with metallicities above $10^{-6}\,Z_{\odot}$at densities above $n_H = 10^{12}$, where the gas and dust temperatures couple.

For those simulations where the clump finder indicates fragmentation at higher densities, it is interesting to see what effect cooling is having on the gas structure at the relevant scales. Figure D.13 shows projections through the core at a width of 0.05 pc, which encompasses the density range above $n_H \sim 10^6$ cm $^{-3}$, at the density regime the clump finder indicates that metallicity affects fragmentation. The projections indicate that the gas in the core does indeed form a whispy substructure for high metallicity gas. Although the density contrast is small, the clump finder indicates that some of these structures are marginally gravitationally bound, giving rise to the possibility that some of these structures could become protostars.

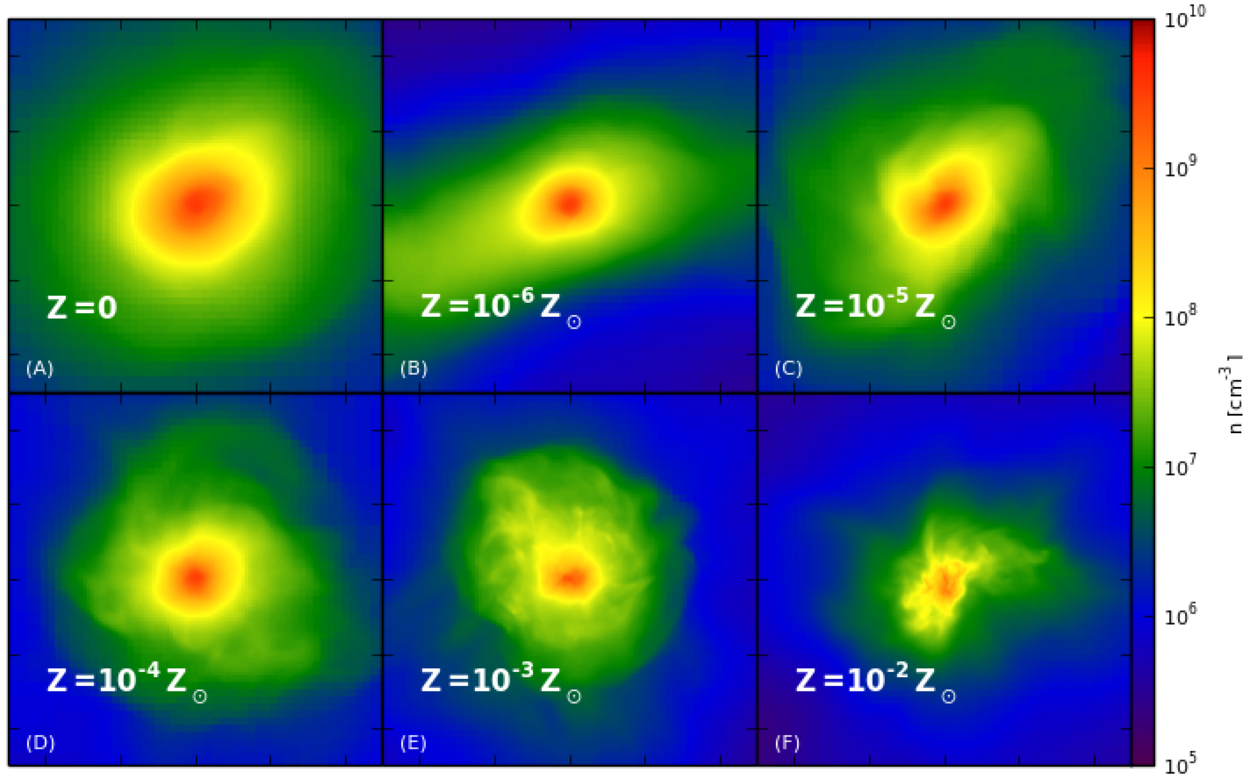

Figure D.13 **Fragmentation in High Metallicity Halos:** Projections of average density through the densest point in the simulation for runs with different metallicity for our $10^7\,\mathrm{M}_{\odot}$halo at the scales where the clump finder finds evidence of fragmentation in high mass halos. Each projection has a width of 0.05 pc, and is taken when the central density has reached 10^{10} cm^{-3}. Substructure is evident in the higher metallicity runs (shown in the bottom row), and the clump finder confirms that some of these structures may become gravitationally bound if cooling persists.

D.5.2 Spin

We have performed a series of runs where we vary the initial magnitude of angular momentum in our halos, as described by the spin parameter λ (Equation D.8 in Section D.2.2.4). For our high and low mass halos, we vary the spin parameter from $\lambda = 0.0$ to $\lambda = 0.1$, spanning the likely range of spin parameters for cosmological halos (e.g. Yoshida et al. (2003)). The turbulent component of the velocity also imparts some angular momentum to the gas, and is kept constant throughout these simulations. As the turbulent field is isotropic and the largest length scale is substantially smaller than the virial radius of the halo, the turbulent field should provide no net rotation, but will dominate the motion of the gas on local scales. The full list of spin parameter-related simulations can be found in Table D.3.

Projections of the cores of simulations with different spin parameters in the high mass halo are shown in Figure D.14 at a scale of 3 pc. While there are substantial differences between the different runs, no clear trend relating fragmentation or gas density profile to initial spin emerges. This result is easy to understand in the context of Figures D.15, in which we plot average angular momentum as a function of mass enclosed for the high and low mass halos respectively. The angular momentum distribution is similar in the low mass halo. Turbulence is able to efficiently transport angular momentum away from the inner regions of the halo and normalize the angular momentum distribution for all runs to roughly the same level, such that the dynamics of the core are dominated by the turbulent motion rather than by initial rotation. During the collapse, angular momentum is transported to larger radii by turbulence, though the total angular momentum of the sphere is conserved. The differences in fragmentation that we observe are more likely due to stochastic effects resulting from the perturbation of the initial conditions.

In order to confirm that the initial spin does not correlate with the amount of fragmentation in the halo, we identified clumps in each simulation using the mechanism as described in the previous sections. The number of clumps in each half-dex bin, shown in Figure D.16, show no identifiable relationship between fragmentation and spin parameter.

D.5.3 Turbulence

To study the effects of the level of turbulent motion on the evolution of our model, we simulated our high and low mass halos with varying levels of turbulence. In our simulations, the RMS velocity of the initial turbulent field is normalized to some fraction f_{cs} of the virial sound speed of the halo. Here, we show results for halos with values of f_{cs} from 0.0 (no turbulence) to 0.8 (trans-sonic turbulence). The full list of turbulence related simulations can be found in Table D.4. A projection through the core of the high mass halo for the different runs is shown in Figure D.17.

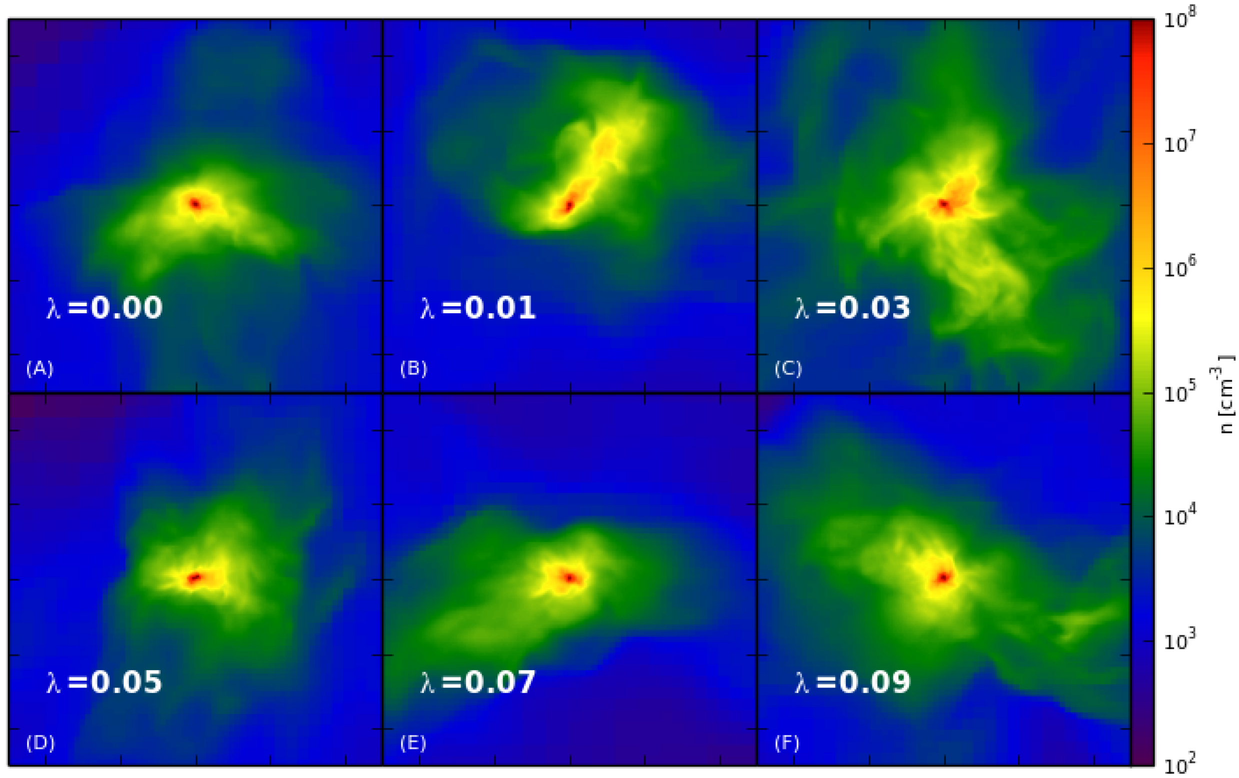

Figure D.14 **Effect of Spin Parameter on Gas Density:** Projections through the core of our simulations in which the spin parameter is varied. Although differences in structure are observed, there is no systematic trend in the fragmentation with increasing spin. The width of each image is 3.0 pc.

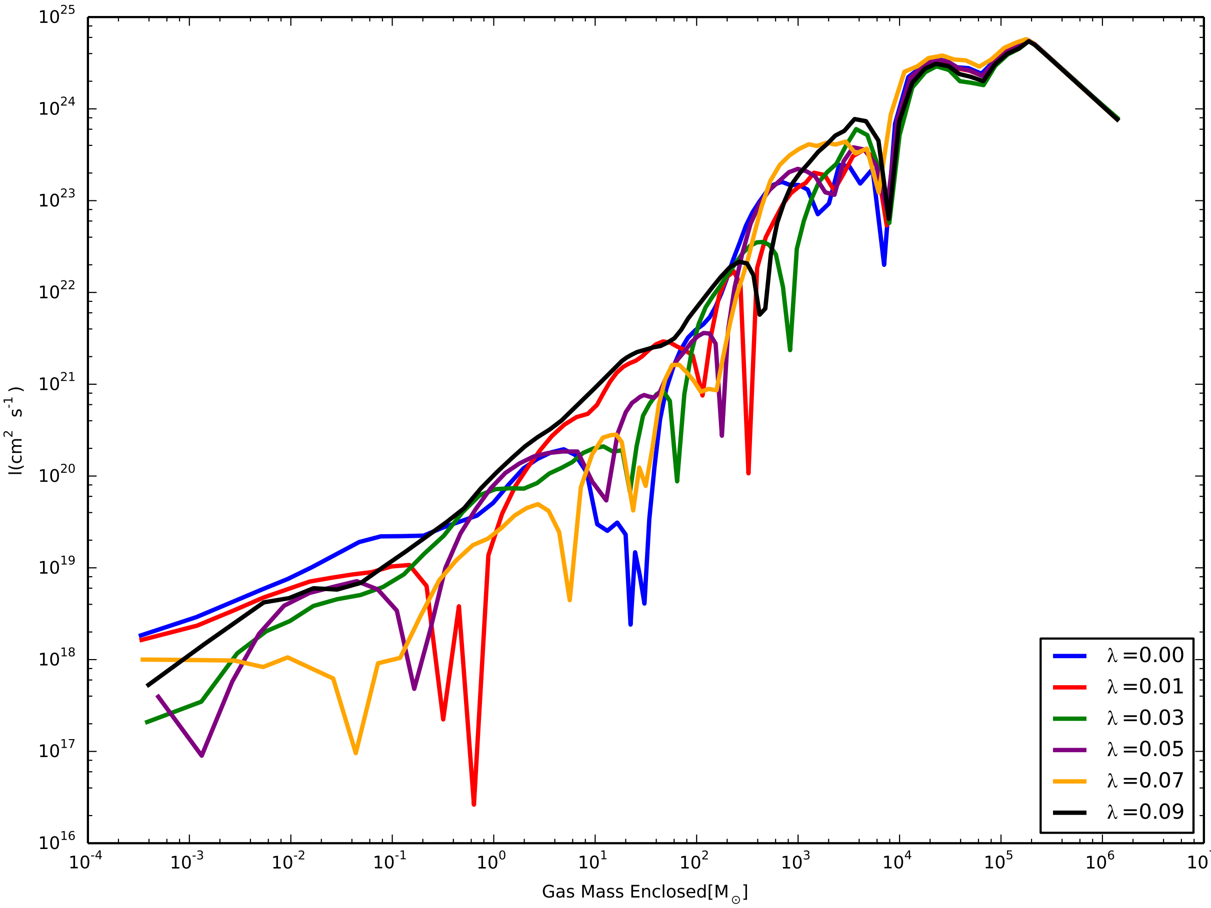

Figure D.15 **Effect of Spin Parameter on Angular Momentum Distribution**Average angular momentum vs. mass enclosed for runs with different initial spin parameters for our high mass halos when the central density of each simulation reaches $n_H = 10^{10}$ cm $^{-3}$. By this point, turbulence has randomized the distribution of angular momentum.

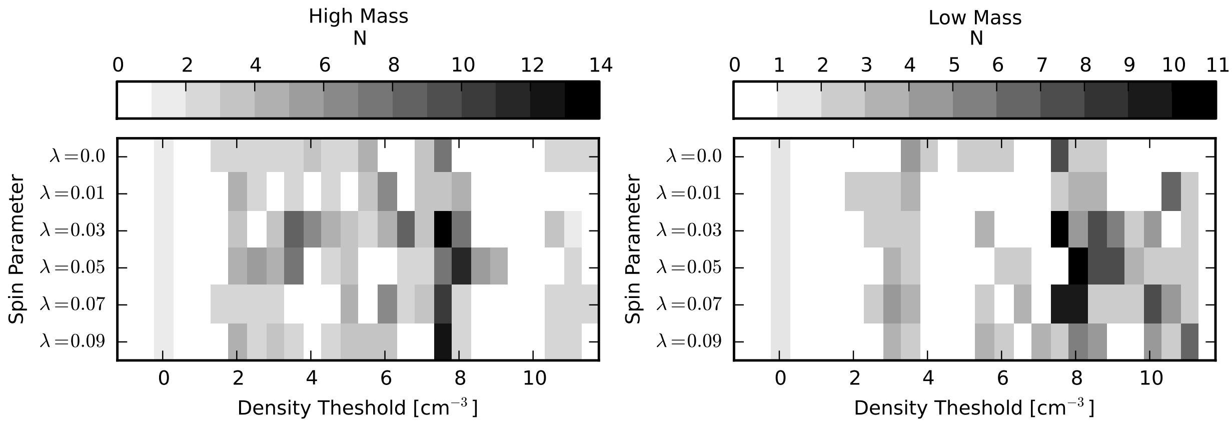

Figure D.16 **Effect of Spin Parameter on Fragmentation**The number of bound or nearly bound clumps is shown for runs with with different initial spin parameter as identified by our clump finder. The number of clumps in each half dex contour interval is shown above. Clump finding is performed when each run reaches a central density of $n_H = 10^{10}$ cm $^{-3}$. The fragmentation profile confirms that spin has no clear effect on fragmentation beyond perturbing the initial conditions.

It is clear that even a small amount of turbulence has a dramatic effect on the evolution of the halo. In the runs with no turbulence, the halo simply collapses radially and does not fragment. When even a small amount of turbulence is added, the core becomes asymmetric and forms considerably more substructure.

Once again, we attempt to quantify fragmentation by looking for potentially bound collapsing clumps within our simulation. In Figure D.18, we show the distribution of clumps as a function of density for different levels of turbulence. While the level of fragmentation differs with the initial level of turbulence, there is not a clear relationship between the two. In fact, the most fragmentation seems to occur for intermediate levels of turbulence. We speculate that higher levels of turbulence result in substantial shock heating of the gas as the turbulence decays away, which suppresses the formation of gravitationally bound clumps and also delays the collapse of gas in the halo. This is supported by the collapse times shown in Table D.4, when both low and high mass halos with the highest level of turbulence take longer to collapse than their intermediate-turbulence counterparts.

D.5.4 Dust

To better understand the effects of dust on halo evolution, we ran our fiducial model without dust chemistry – that is, assuming that all metals are in the gaseous phase. Comparisons of the physical and thermal evolution of the runs with and without dust are shown in Figure D.19. Without dust, H_2 is not able to form in significant quantities until the onset of 3-body reactions, which occurs around a density of $n_H \sim 10^8$ cm $^{-3}$. This inhibits the ability of the gas to cool at low densities. Additionally, the gas does not undergo a

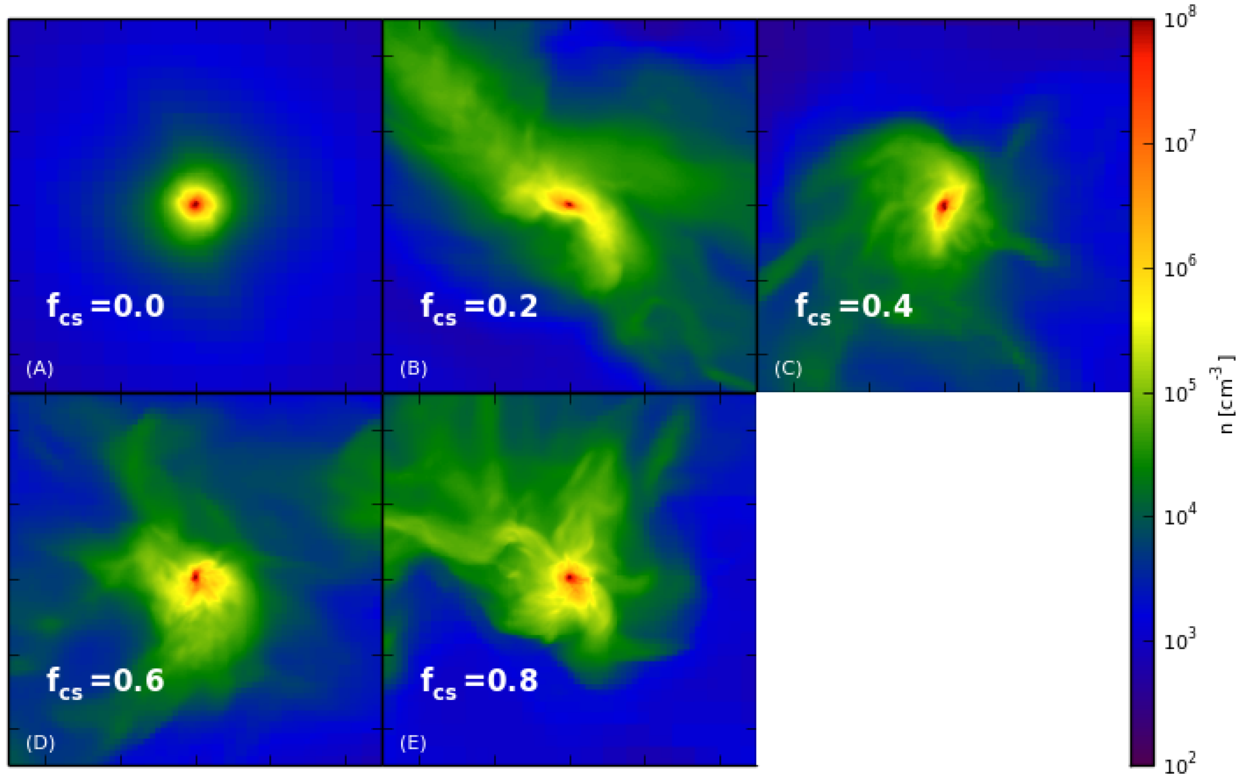

Figure D.17 **Effect of Turbulence on Gas Density:** Projections through the core of our simulations in which the amount of initial turbulence is varied. The scale of each image is 3.0 pc.

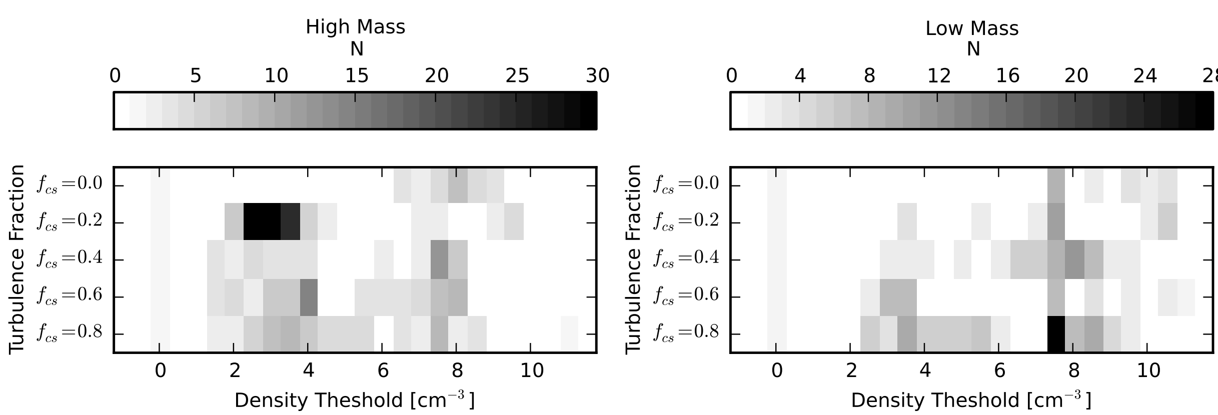

Figure D.18 **Effect of Turbulence on Fragmentation:** The number of bound or partially bound clumps is shown for runs with with different levels of turbulence. The RMS velocity of the initial turbulent field is normalized to the fraction of the sound speed that is plotted on the y-axis. The number of clumps in each half-dex contour interval is shown above. Clump finding is performed when each run reaches a central density of $n_H = 10^{10}$ cm $^{-3}$.

second period of dust-driven cooling at high densities.

D.6 Discussion

With the results of our model in hand, we return to the questions we set out to investigate: which physical properties of the star-forming halo affect fragmentation in low metallicity gas, and is there a true 'critical metallicity' that governs the transition from a high-mass Population III stellar IMF to one that is more like the galactic IMF? We find that metallicity does have an effect on gas fragmentation at densities above $n_H \sim 10^6$ cm $^{-3}$, corresponding to physical scales smaller than 0.1 pc. Our results lend tentative support to the idea of a critical metallicity found by Bromm et al. (2001) and Smith et al. (2009), among others. However, on density scales below $n_H \sim 10^6$ cm $^{-3}$, corresponding to a physical scale of greater than 0.1 pc, we do not find metallicity to have a strong impact on fragmentation. We also find that the effect of varying metallicity on the thermodynamic properties of the gas, as shown in Panel B of Figures D.10, is not as dramatic as is seen in other studies such as Omukai et al. (2005) and Smith et al. (2009). In particular, the gas in all of our simulations is able to cool below the 200 K floor set by molecular hydrogen cooling. We explain the differences between our results and previous work as reflecting our choice of initial conditions and the physics, in particular the inclusion of dust and deuterium chemistry, in our model.

D.6.1 The Role of HD Cooling

As discussed in Section D.3, HD is a powerful coolant that can lower the temperature of the gas substantially below the limit set by H_2 cooling. Because the formation of HD from H_2 is energetically favored (see Equations D.12 and D.13 and the discussion that follows), enough HD can form to have a significant impact on the thermodynamic evolution of the gas. Using 1D simulations,

In order to confirm that HD is responsible for cooling the gas below 200 K in the absence of metals, we have rerun our fiducial model with a reduced chemical model that does not include deuterium chemistry. The results, shown in Figure D.20, confirm that the inclusion of deuterium chemistry is able to lower the temperature of the gas well below the temperatures reached by H_2 cooling alone, even in the primordial runs. In the case of the $10^{-3}\,Z_{\odot}$run, the gas is able to cool all the way to the CMB floor. As the combined H_2 and HD cooling rates dominate the metal cooling rate for metallicities below $10^{-3}\,Z_{\odot}$, there is little variation in the cooling properties of the gas at low densities, leading to little change in fragmentation at those densities as metallicity is varied (see Figures D.10 and D.12). For higher metallicities, the metal cooling rate dominates, leading to increasing fragmentation with increasing metallicity.

The importance of HD cooling in our simulations is somewhat surprising, given that other works have

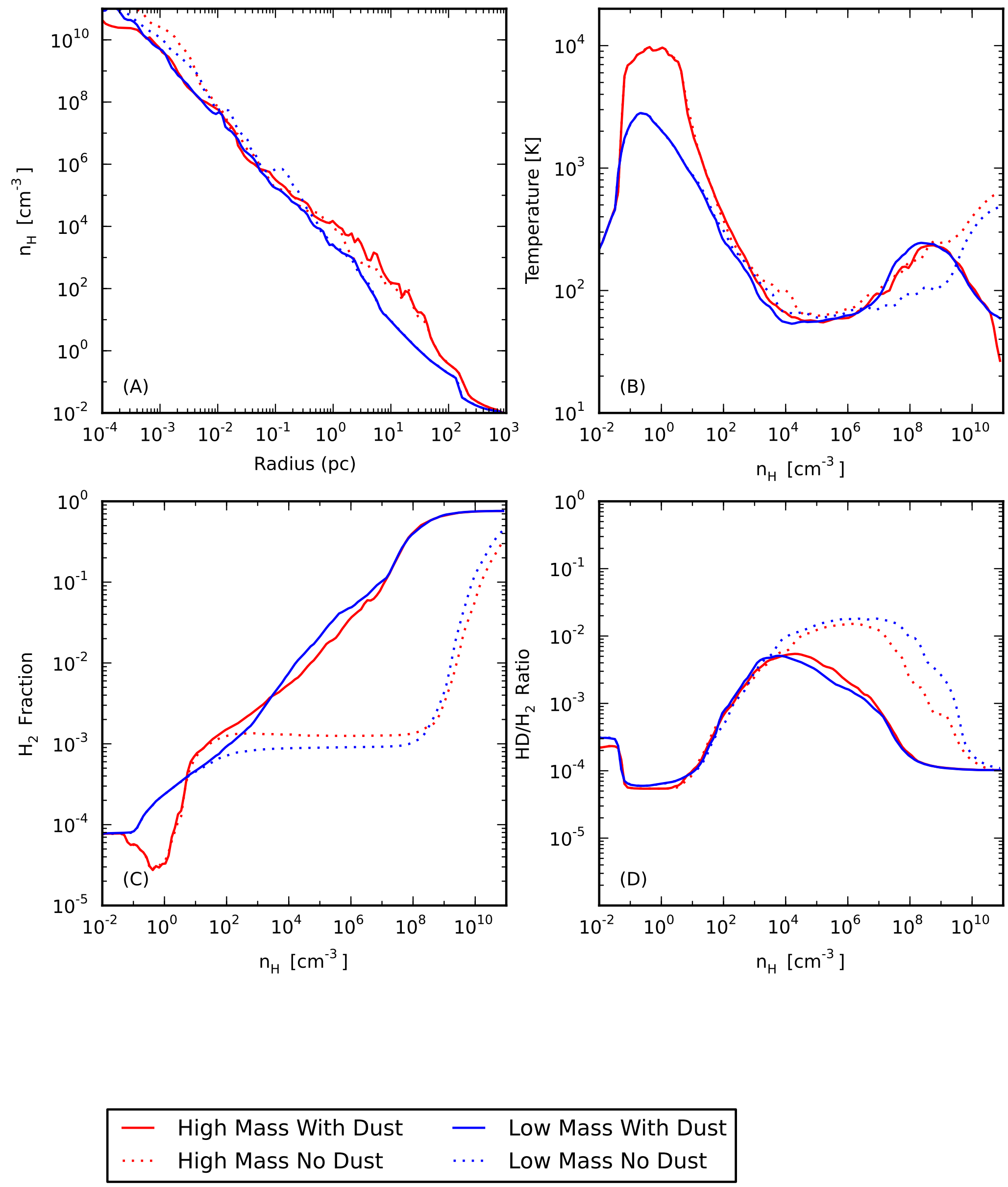

Figure D.19 **Effects of Dust Chemistry on Gas Profiles:** The effects of dust on the physical and thermal evolution of the halo are shown for the high and low mass halo. Panel A shows the physical evolution, which is not greatly affected, as dust cooling is only important at high densities, as shown in Panel B. The primary effect of dust is to serve as a catalyst for the formation of H_2 and HD at low densities. The H_2 mass fraction is shown in Panel C. Without dust, molecules are only formed once three body reactions become important at $n_H \sim 10^8$ cm $^{-3}$. The addition of dust allows the gas to cool at lower densities through molecular transitions, and at high densities where the dust itself is able to radiate energy from the gas. In Panel D, the HD/H_2 ratio is depressed by dust as more H_2 is formed at low densities, decreasing the denominator.

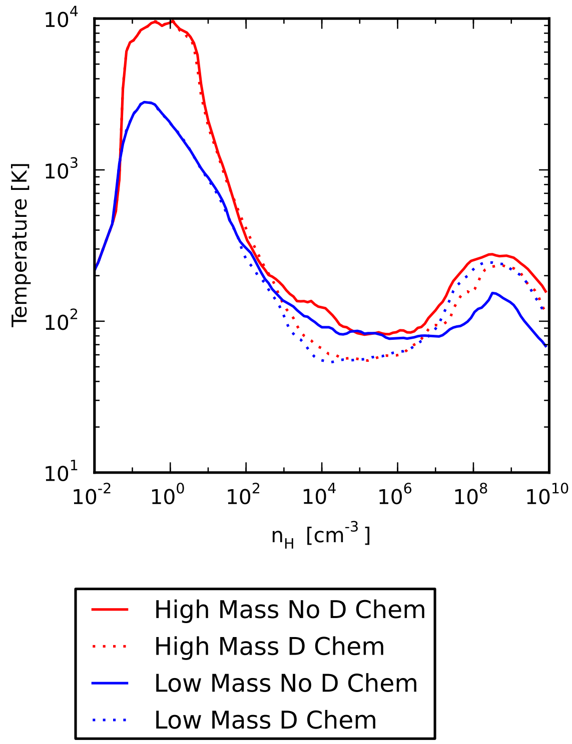

Figure D.20 **Effect of Deuterium Chemistry on Temperature Profiles:** The mass-weighted average temperature is shown as a function of density for simulations that include and neglect deuterium chemistry. The conditions are the same as in our high mass and low mass fiducial runs.

found HD cooling to be negligible (Omukai et al., 2005; Bromm et al., 2002) in gas with low initial ionization but is in agreement with the works of Ripamonti (2007) and Greif et al. (2011). Ripamonti (2007) concludes that HD cooling can affect the intermediate stages of the fragmentation if the HD fraction is given time to increase as the gas cools and collapses. In that work, HD cooling is found to be most important in low mass halos, where the gas collapses over a longer timespan. After investigating the factors affecting the HD cooling rate, we conclude that the amount of HD that forms is affected by the initial conditions of our simulation. Starting from a low central density, the halo is able to fully build up an accretion shock before collapsing. In our model, the high and low mass halos both form enough HD for the temperature to drop well below the temperature floor set by H_2 cooling, even in the runs with primordial gas. The collapse reaches higher temperatures, possibly ionizing the gas, and takes longer. In contrast, the one zone models used by Omukai et al. (2005) do not develop the accretion shock and assume a collapse which occurs on a dynamical timescale. Bromm et al. (2002) starts from a higher initial density and uses a top hat density profile, which again does not develop the accretion shock and allows for a faster collapse.

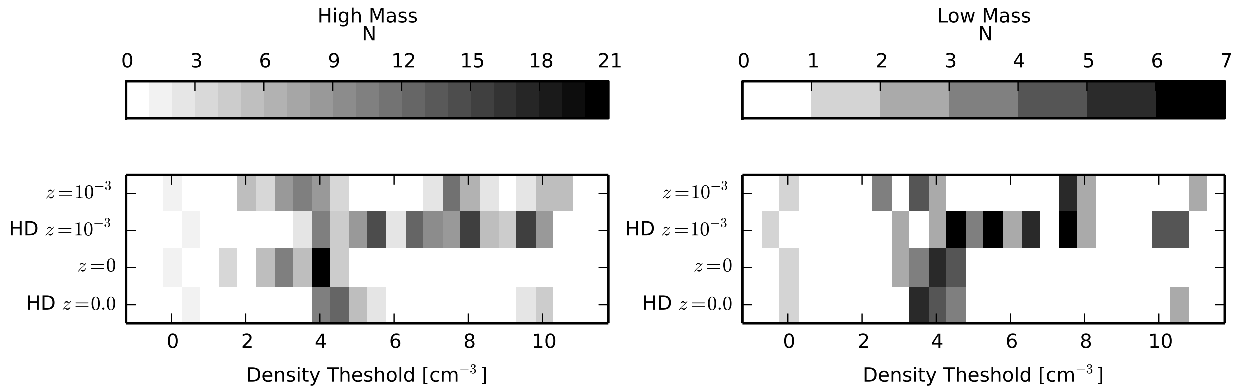

Figure D.21 **Bound Clumps in Simulations with High Density ICs:** The number of gravitationally bound or nearly bound clumps is shown for runs with different initial density profiles. The left hand panel shows results for the high mass setup with metallicities of $10^{-}3$ and primordial gas. The right hand plot shows the same runs for the low mass halo. Runs marked with HD start with an initial central baryon density 100x higher than in the fiducial model.

D.6.2 The Role of Dust Cooling

Recent studies (Schneider et al., 2006; Clark et al., 2008; Dopcke et al., 2011; Schneider et al., 2012, e.g.,) have found that radiation from dust grains can dominate the cooling of the gas at high ($n_H > 10^{12}$ cm $^{-3}$) densities for gas with metallicity above $10^{-6}\,Z_\odot$. These simulations find support for a second metallicity threshold around $10^{-5}\,Z_\odot$, above which dust cooling leads to a sudden drop in temperature, spurring additional fragmentation. The fragments which are formed predict a stellar IMF peaking around $1\,M_\odot$, consistent with modern-day star formation. As our simulations do not follow the evolution of the gas to densities above $n_H = 10^{10}$ cm $^{-3}$, we are not able to observe this fragmentation. However, in the simulations with metallicities high enough for dust cooling to occur at densities below $n_H \sim 10^{10}$ cm $^{-3}$, we observe that this dust cooling phase can lead to significant fragmentation. Therefore, we expect that we would have observed fragmentation in our lower metallicities runs had we carried them up to higher densities.

D.6.3 Initial Density Profile

When we start our model from a relatively high initial density ($n_H = 10^2$ cm $^{-3}$), the halo begins to collapse and fragment before the gas has been fully heated by the accretion shock. This speeds up the collapse and does not give the gas enough time to build up a significant amount of HD. This in turn inhibits the gas from cooling at low densities. This is shown in Figure D.22, which compares the physical, thermal, and chemical properties of our high and low mass fiducial models, as well as our high and low mass primordial models, with runs started from a higher central density. Divergence in the evolution of the gas is most evident in

Panel b at densities below $n_H \sim 10^2$ cm $^{-3}$. The gas collapses before the accretion shock has fully developed, and the temperature reaches a maximum value below 1,000 K, compared to over 10,000 K for the fiducial high mass halo.

Our clump finding method confirms that the shape of the initial density profile leads to a marked change in the fragmentation properties of the halo. The number of clumps, shown in Figure D.21, is much higher in runs where the initial baryon density is increased. In three of our four runs, we note several additional clumps being formed when the initial density is higher, and the gas collapses before it has evolved to an equilibrium state.

D.6.4 Choice of Redshift

As described in Section D.1, we assume a redshift of $z = 20$ in all of our simulations, which affects the properties of the NFW halo and the temperature of the CMB. Our assumption of $z = 20$ is based on several works, including Trenti & Stiavelli (2009), Norman (2010) and Crosby et al. (2013), which allow for the formation of both primordial and low metallicity stars in large numbers at a redshift of 20. As the collapse is dominated by the self gravity of the baryons at late times (see Figure D.2), variations in the NFW density profile due to small variations in redshift will not have a strong impact on our results. As the gas does cool to the CMB temperature in our high metallicity runs (see Figures D.10, it is likely that changes to T_{CMB} due to redshift could affect the fragmentation. Smith et al. (2009) has looked at the effects of a strong CMB on primordial and low metallicity star formation and has found that at high redshifts, a CMB temperature floor can inhibit fragmentation in high metallicity halos. Thus, we expect that if we carried out our simulations at a lower redshift, we would see more fragmentation in the runs with metallicities of 10^{-2} and $10^{-3}\,Z_{\odot}$, which cool to the CMB floor, but that we would see little change in the other runs, which do not reach the CMB temperature. This would strengthen the observed dichotomy in fragmentation properties and would lend further support to the idea of a critical metallicity.

D.6.5 Limitations of This Work

While our simulations attempt to accurately model the collapse and evolution of star forming halos of primordial composition and at low metallicities, our model is necessarily limited by our idealized initial setup and from the choice of physics included in our simulation. By modeling the collapse as spherically symmetric, we ignore the effects of gas accreting along filaments, which might modify the accretion shock we observe. Similarly, we model an isolated halo, which eliminates halo growth and heating due to mergers. This has been shown to affect the thermodynamic behavior of the gas (e.g., O'Shea & Norman, 2007), but

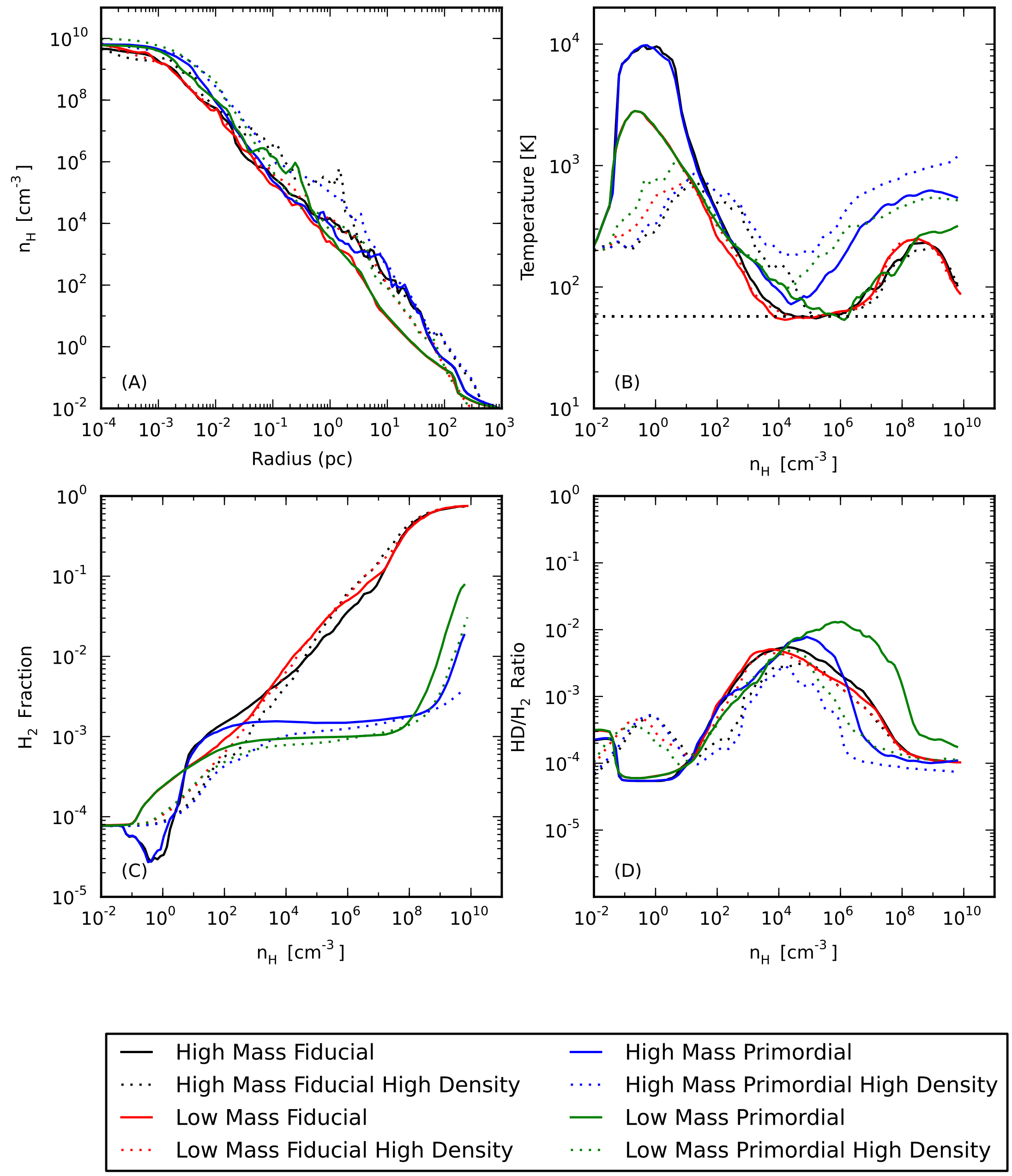

Figure D.22 **Gas Profiles for Simulations With High Density ICs:** The effects on the physical, thermal, and chemical evolution of the gas when the simulation is started from a higher initial gas density. Conditions are the same as in our fiducial run, except that the central gas density is $\rho_c = 100$ cm $^{-3}$instead of $\rho_c = 1$ in our fiducial model. When the central density is higher, the gas collapses before it has time to erase the imprint of the initial conditions. The accretion shock is not fully formed, resulting in no ionization and the formation of less HD at low densities. The lower HD fraction prevents the gas from cooling to the level seen in the fiducial model.

in somewhat unpredictable ways.

Our model makes several assumptions about the chemistry of the gas that may effect the evolution of the halo. While our assumption of uniform metallicty is likely not correct, violent relaxation in post-merger halos could efficiently mix the gas, making our approximation of uniformity appropriate. Throughout this work, we have assumed that the distribution of metals follows a scaled solar abundance. While it is quite possible that the heavy elements produced by the first generation of stars might not have had a solar abundance pattern (as has been implied by observations of metal poor stars – see Beers & Christlieb (2005)), what matters in our simulation is the overall cooling rate of the gas, not the details of the composition. If the composition of the gas were varied compared to solar, it would potentially change the metallicity where changes to the fragmentation become evident, but not the qualitative behavior shown in this work.

Throughout this work, we have assumed that the gas in the halo of interest is mostly neutral and has not been ionized by previous star formation. It is important to note that many low metallicity stars may form in halos that have hosted previous generations of star formation, meaning that our assumption of no previous ionization may not be valid in all cases. As discussed in Smith et al. (2009) and Glover & Abel (2008) among others, previous ionization and subsequent recombination could affect the molecular fraction, as free electrons serve as catalysts during the molecule formation process.

Another source of uncertainty comes in the assumed properties of dust in our dust model. Through out this work, we have assumed dust grains with a size distribution and composition similar to grains in the solar neighborhood. If the properties of dust grains in early universe or low metallicity environments were drastically different from those in our model, our assumptions of the H_2 formation rate on dust grains and the rate of cooling from dust would not necessarily be valid. Until dust properties can be further constrained, the effects of dust on the formation of the first stars can not be fully understood, and our assumption of solar neighborhood like dust properties is reasonable (see Omukai et al. (2005); Schneider et al. (2006); Schneider & Omukai (2010) for more discussion).

As discussed in the preceding section, the initial conditions of the simulation are important for determining the outcome of the fragmentation process. Perhaps the largest uncertainty in this study comes in the choice of initial conditions for our low metallicity halos. Although we have attempted to base our simulations on the results of cosmological simulations, the properties of 'typical' early universe star forming halos are still in the process of being constrained (e.g., see Crosby et al., 2013). Future generations of semi-analytic and cosmological hydrodynamic simulations will be able to better constrain the conditions under which the Population III to metal enriched star formation transition occurred.

D.7 Summary and Conclusions

In this work, we have explored the parameter space of fragmentation in low metallicity star forming halos with the goal of better understanding the transition between metal-free and metal-enriched star formation. We have done so using the adaptive mesh hydrodynamics code Enzo, **using an idealized spherical setup at** $z = 20$ with initial conditions modeled on the results of simulations that start from cosmological initial conditions. Our simulations utilize a chemical model that includes deuterium chemistry. We have also included a dust model that tracks the formation of H_2 on dust grains as well as heating and cooling by dust grains. In our study, we have systematically varied the metallicity, the initial spin rate, and the level of turbulence of halos with initial dark matter masses of $10^6\,\mathrm{M}_\odot$and $10^7\,\mathrm{M}_\odot$, with the aim of determining the effects of each parameter on gas evolution and fragmentation. Additionally, we have conducted simulations where we vary the physics that are included in our model and the form of our initial conditions in order to investigate how these properties affect our results.

We have carried out a number of simulations where N_J, the number of cells required to cover the local Jeans length, is varied. We find that a change in the qualitative properties of the fragmentation occurs after between $N_J = 32$ and $N_J = 64$. We use $N_J = 64$ in our studies, but caution that increasing N_J further might have non-negligible effects on the fragmentation.

We conclude that varying the metallicity of the cloud has the largest impact on fragmentation, although its influence **in our models** is less important than in previous works. As metallicity is increased, the gas is able to cool and collapse faster, which increases fragmentation. Above a metallicity of $10^{-4}\,\mathrm{Z}_\odot$, the gas is able to fragment at higher densities, leading to the formation of substructure on sub-parsec scales and a multitude of possible star formation sites. We would likely see dust induced fragmentation at lower metallicities if we carried our simulations up to higher densities. We find tentative support for the idea of a critical metallicity, but do not see as much of a variation in evolution as has been reported in previous works. **However, given that our assumed redshift of** $z = 20$ **results in a relatively high** $T_{\mathbf{CMB}}$**, and given that our two simulations above the critical metallicity cool to the CMB floor, we theorize that at lower redshifts varying metallicity would results in a greater variation in cooling and fragmentation than what we observe.** We find that the initial spin has negligible effect on fragmentation. The level of turbulence in the initial velocity field has been shown to alter the fragmentation of the cloud, but does not do so in a systematic way, with intermediate levels of turbulence typically resulting in more fragmentation than either high or low levels.

Our final results were found to be influenced by the initial conditions of our simulation as well as the physics included in our code, and are in generally good agreement with previous works. We found that the inclusion of deuterium chemistry alters the thermal evolution of the gas at all metallicities by allowing the gas to cool below the lower limit of H_2 at densities lower than the regime in which metal cooling dominates. The amount of HD that is formed and the densities where it forms is heavily dependent on the initial density profile and the subsequent evolution of the cloud. In this study we have purposely started from a low initial density so that the simulation will have time to evolve, and thus erase the details of the initial conditions. When we have started the simulation from a higher central density, the halo collapses before the gas has had time to fully form an accretion shock. The resulting collapse does not form a significant amount of HD, resulting in higher temperatures during the collapse.

The initial mass function of the first stars and the nature of the transition from metal free to low metallicity star formation remain open questions. As current observations cannot directly detect the first generation of stars, simulation has emerged as the main method for studying the evolution of baryons in the early universe. Semi-idealized simulations are a powerful tool for exploring the formation and evolution of the first stars, but their results can only be considered valid if the simulations include the relevant physics and initial conditions, which must be inferred from simulations based on cosmological initial conditions. Further, these calculations must be resolved numerically; inadequate spatial resolution suppresses fragmentation, thus fundamentally affecting results. These simulations in turn can benefit from semi-idealized models in order to determine what regions are most likely to host the sites of low metallicity star formation. It is our hope that with future increases in computing power and a better understanding of the conditions in the early universe, the transition from Population III to metal-enriched star formation and the history of the first stars in the universe can be fully understood.

D.8 Acknowledgments

This work used the Extreme Science and Engineering Discovery Environment (XSEDE), which is supported by National Science Foundation grant number OCI-1053575. All simulations were funded by XSEDE award TG-AST090040 and performed on the TACC Ranger and Stampede resources. This work was funded by the NASA ATFP program (NNX09AD80G and NNX12AC98G), the NSF AST program (AST-0908819), the LANL Institute for Geophysics and Planetary Physics, and MSU's Institute for Cyber-Enabled Research. The authors would like to thank Mike Norman, Matthew Turk, and Jeff Oishi for useful discussions. We would also like to thank Mark Voit of MSU for his support of this project. `Enzo` and `yt` are developed by a large number of independent research from numerous institutions around the world. Their committment to open science has helped make this work possible.

Table D.1 Varying Metallicity

Run	Halo Mass ($M_\odot$)	Metallicity ($Z_\odot$)	Collapse Time
lmzmi	10^6	0.0	95.156
lmzm6	10^6	10^{-6}	95.070
lmzm5	10^6	10^{-5}	94.677
lmzm4	10^6	10^{-4}	93.430
lmzm3	10^6	10^{-3}	91.196
lmzm2	10^6	10^{-2}	85.805
hmzmi	10^7	0.0	57.229
hmzm6	10^7	10^{-6}	57.506
hmzm5	10^7	10^{-5}	56.532
hmzm4	10^7	10^{-4}	56.472
hmzm3	10^7	10^{-3}	55.360
hmzm2	10^7	10^{-2}	51.314

Note. — **Varying Metallicity:** These are the runs performed in this work to test the effects of varying metallicity. Aside from the metallicity, all runs have the same parameters as the fiducial models. The last column gives the time in millions of years for the simulation to reach a maximum density of $n_H = 10^{10}$ cm^{-3}.

Table D.2 Varying Jeans Refinement

Run	Halo Mass ($M_\odot$)	Jeans Cells	Collapse Time (Myr)
lmj4	10^6	4	91.114
lmj8	10^6	8	91.150
lmj16	10^6	16	91.912
lmj32	10^6	32	91.531
lmj64	10^6	64	91.606
hmj4	10^7	4	54.381
hmj8	10^7	8	54.841
hmj16	10^7	16	52.673
hmj32	10^7	32	54.407
hmj64	10^7	64	54.257

Note. — **Varying Jeans Refinement:** These are the runs performed in this work to test the effects of varying the Jeans refinement criteria. Other than the number of cells required to cover the Jeans length, all runs have the same parameters as the fiducial models. The last column gives the time in millions of years for the simulation to reach a maximum density of $n_H = 10^{10}$ cm^{-3}.

Table D.3 Varying Spin

Run	Halo Mass ($M_\odot$)	Spin Parameter λ	Collapse Time (Myr)
lmsp00	10^6	0.00	91.614
lmsp01	10^6	0.01	91.572
lmsp03	10^6	0.03	91.519
lmsp05	10^6	0.05	91.603
lmsp07	10^6	0.07	91.582
lmsp09	10^6	0.09	91.533
hmsp00	10^7	0.00	53.731
hmsp01	10^7	0.01	54.054
hmsp03	10^7	0.03	54.427
hmsp05	10^7	0.05	54.051
hmsp07	10^7	0.07	53.023
hmsp09	10^7	0.09	54.302

Note. — **Varying Spin:** These are the runs performed in this work to test the effects of varying the rotation, as characterized by the dimensionless spin parameter λ. Other than the spin parameter, all runs have the same parameters as the fiducial models. The last column gives the time in millions of years for the simulation to reach a maximum density of $n_H = 10^{10}$ cm^{-3}.

Table D.4 Varying Turbulence

Run	Halo Mass ($M_\odot$)	Turbulence Factor λ	Collapse Time (Myr)
lmt00	10^6	0.0	70.278
lmt02	10^6	0.2	86.686
lmt04	10^6	0.4	91.599
lmt06	10^6	0.6	98.232
lmt08	10^6	0.8	108.922
hmt00	10^7	0.0	19.760
hmt02	10^7	0.2	55.234
hmt04	10^7	0.4	54.087
hmt06	10^7	0.6	61.464
hmt08	10^7	0.8	62.704

Note. — **Varying Turbulence:** These are the runs performed in this work to test the effects of varying the degree of turbulence. The RMS of the initial turbulent velocity field is normalized to some fraction of the halo sound speed. This is shown in the third column. Other than the degree of turbulence, all runs have the same parameters as the fiducial models. The last column gives the time in millions of years for the simulation to reach a maximum density of $n_H = 10^{10}$ cm^{-3}.

Table D.5 Other Runs

Run	Halo Mass ($M_\odot$)	Collapse Time (Myr)	Description
lmnd	10^6	92.711	No Dust
hmnd	10^7	55.270	No Dust
lmm2	10^6	93.013	Reduced Chemical Network
hmm2	10^7	55.571	Reduced Chemical Network
hmhd	10^7	4.651	Higher Initial Density
hmhdp	10^7	5.677	Higher Initial Density (Primordial)
lmhd	10^6	12.315	Higher Initial Density
lmhdp	10^6	16.300	Higher Initial Density (Primordial)

Note. — **Other Runs:** This table shows additional runs performed in this paper. In all cases, the parameters are the same as those of our fiducial model unless otherwise noted. In the first set of runs, we do not include dust chemistry. In the second set of runs, we use a reduced chemical model which does not include Deuterium chemistry. In the third set of runs, we start with an initial baryon density 100 times higher than in our fiducial model.

Appendix E Use of Copyrighted Material

This dissertation (specifically Chapters 3 and 4 and Appendix D make use of material that has been published in or submitted for publication in The Astrophysical Journal (ApJ). ApJ, the publisher IOP, and the American Astronomical Society (AAS) allow for this type of reuse. Further information about the IOP reuse policy may be found at http://iopscience.iop.org/page/copyright.

My correspondences with the IOP on this matter are included below.

From: Greg Meece <meecegre@msu.edu>

To: permissions@iop.org,

Date: 08/04/2016 21:01

Subject: Permission to Reuse Papers from ApJ

Dear IOP,

I am completing a doctoral dissertation Michigan State University entitled "AGN Feedback and Delivery Methods for Simulations of Cool-Core Galaxy Clusters". I would like your permission to reprint in my dissertation/thesis the following:

Meece, G. R., OShea, B. W., & Voit, G. M. Growth and Evolution of Thermal Instabilities in Idealized Galaxy Cluster Cores, 2015 ApJ, 808, 43 (http://iopscience.iop.org/article/10.1088/0004-637X/808/1/43/meta)

Meece, G. R., Smith, B. D., & OShea, B. W. Fragmentation in Dusty Low-metallicity Star-forming Halos. 2014, ApJ, 783, 75 (http://iopscience.iop.org/article/10.1088/0004-637X/783/2/75/meta)

Both of which are published in The Astrophysical Journal, and

"Triggering and Delivery Algorithms for AGN Feedback" by Gregory Meece, G. Voit, and Brian O'Shea

which was submitted to ApJ on March 15th, 2016 (manuscript # AAS00223)
(http://adsabs.harvard.edu/abs/2016arXiv160303674M)

The requested permission extends to any future revisions and editions of my dissertation, including non-exclusive world rights in all languages, and to the prospective publication of my dissertation/thesis by ProQuest Information and Learning (ProQuest) through its UMI Dissertation Publishing business. ProQuest may produce and sell copies of my dissertation/thesis on demand and may make my dissertation/thesis available for free internet download at my request. These rights will in no way restrict republication of the material in any other form by you or by others authorized by you. Your signing of this letter will also confirm that you own [or your company owns] the copyright to the above-described material.

If this is acceptable to you, please let me know,

Thank you,

--Gregory Meece

From: Permissions <permissions@iop.org>

To: Greg Meece <meecegre@msu.edu>

Date: Mon, Apr 11, 2016 at 5:26 AM

Subject: Re:Permission to Reuse Papers from ApJ

Dear Gregory Meece,

Thank you for your enquiry.

AAS grants back to authors the non-exclusive right of republication, subject only to giving appropriate credit to the journal in which the article was published. This non-exclusive right of republication gives authors the right to approve or deny reproduction of all or part of the article and to post the final published version online.

Therefore, please go ahead with the inclusion of this material in your new work no permission is required from AAS.

If you have any questions, please contact the Permissions team.

Kind regards,

Kathryn Shaw

Copyright & Permissions Team

Gemma Alaway Rights & Permissions Adviser

Kathryn Shaw - Editorial Assistant

Contact Details

E-mail: permissions@iop.org

For further information: http://iopscience.iop.org/page/copyright

Please note: We do not provide signed permission forms as a separate attachment.

Please print this email and provide it to your publisher as proof of permission.

BIBLIOGRAPHY

BIBLIOGRAPHY

Abazajian, K., Fuller, G. M., & Patel, M. 2001, Phys. Rev. D, 64, 023501

Abel, T., Anninos, P., Zhang, Y., & Norman, M. L. 1997, New A, 2, 181

Abel, T., Bryan, G. L., & Norman, M. L. 2002, Science, 295, 93

Abell, G. O. 1958, ApJS, 3, 211

Abell, G. O., Corwin, Jr., H. G., & Olowin, R. P. 1989, ApJS, 70, 1

Ackermann, M., et al. 2014, ApJ, 787, 18

Alpher, R. A., Bethe, H., & Gamow, G. 1948, Physical Review, 73, 803

Anderson, L., et al. 2012, MNRAS, 427, 3435

Anninos, P., Zhang, Y., Abel, T., & Norman, M. L. 1997, New A, 2, 209

Arieli, Y., Rephaeli, Y., & Norman, M. L. 2008, ApJ, 683, L111

Arieli, Y., Rephaeli, Y., & Norman, M. L. 2010, ApJ, 716, 918

Baade, W., & Minkowski, R. 1954, ApJ, 119, 206

Babul, A., Sharma, P., & Reynolds, C. S. 2013, ApJ, 768, 11

Balbus, S. A. 1988, ApJ, 328, 395

Balbus, S. A. 2000, ApJ, 534, 420

Balbus, S. A. 2001, ApJ, 562, 909

Balbus, S. A., & Soker, N. 1989, ApJ, 341, 611

Banerjee, N., & Sharma, P. 2014a, ArXiv e-prints

Banerjee, N., & Sharma, P. 2014b, MNRAS, 443, 687

Bardeen, J. M., Steinhardt, P. J., & Turner, M. S. 1983, Phys. Rev. D, 28, 679

Barkana, R., & Loeb, A. 2001, Phys. Rep., 349, 125

Bartelmann, M., & Schneider, P. 2001, Phys. Rep., 340, 291

Beers, T. C., & Christlieb, N. 2005, ARA&A, 43, 531

Begelman, M. C., & Rees, M. J. 1978, MNRAS, 185, 847

Begelman, M. C., Volonteri, M., & Rees, M. J. 2006, MNRAS, 370, 289

Bennett, A. S. 1962, MmRAS, 68, 163

Bennett, C. L., et al. 2003, ApJ, 583, 1

Best, P. N., von der Linden, A., Kauffmann, G., Heckman, T. M., & Kaiser, C. R. 2007, MNRAS, 379, 894

Binney, J., & Tabor, G. 1995, MNRAS, 276, 663

Bîrzan, L., Rafferty, D. A., McNamara, B. R., Wise, M. W., & Nulsen, P. E. J. 2004, ApJ, 607, 800

Blandford, R. D., & Payne, D. G. 1982, MNRAS, 199, 883

Blandford, R. D., & Znajek, R. L. 1977, MNRAS, 179, 433

Bode, P., Ostriker, J. P., & Turok, N. 2001, ApJ, 556, 93

Böhringer, H., Matsushita, K., Churazov, E., Ikebe, Y., & Chen, Y. 2002, A&A, 382, 804

Bondi, H. 1952, MNRAS, 112, 195

Bondi, H., & Hoyle, F. 1944, MNRAS, 104, 273

Booth, C. M., & Schaye, J. 2009, MNRAS, 398, 53

Brecher, K., & Burbidge, G. R. 1972, ApJ, 174, 253

Bregman, J. N., & David, L. P. 1988, ApJ, 326, 639

Bridle, A. H., & Feldman, P. A. 1972, Nature Physical Science, 235, 168

Broadhurst, T., et al. 2005, ApJ, 621, 53

Bromm, V., Coppi, P. S., & Larson, R. B. 2002, ApJ, 564, 23

Bromm, V., Ferrara, A., Coppi, P. S., & Larson, R. B. 2001, MNRAS, 328, 969

Bromm, V., & Larson, R. B. 2004, ARA&A, 42, 79

Bromm, V., & Loeb, A. 2003, ApJ, 596, 34

Bryan, G. 1996, PhD thesis, , Univ. Illinois, (1996)

Bryan, G. L., & Norman, M. L. 1998, ApJ, 495, 80

Bryan, G. L., et al. 2014, ApJS, 211, 19

Burns, J. O., Hallman, E. J., Gantner, B., Motl, P. M., & Norman, M. L. 2008, ApJ, 675, 1125

Byram, E. T., Chubb, T. A., & Friedman, H. 1966, Science, 152, 66

Caffau, E., et al. 2011, Nature, 477, 67

Caffau, E., et al. 2012, A&A, 542, A51

Carilli, C. L., & Taylor, G. B. 2002, ARA&A, 40, 319

Carlstrom, J. E., et al. 2011, PASP, 123, 568

Carr, B. J. 2003, in Lecture Notes in Physics, Berlin Springer Verlag, Vol. 631, Quantum Gravity: From Theory to Experimental Search, ed. D. Giulini, C. Kiefer, & C. Laemmerzahl, 301–321

Cavagnolo, K. W., Donahue, M., Voit, G. M., & Sun, M. 2008, ApJ, 683, L107

Cavagnolo, K. W., Donahue, M., Voit, G. M., & Sun, M. 2009, ApJS, 182, 12

Cavaliere, A., & Fusco-Femiano, R. 1976, A&A, 49, 137

Cavaliere, A. G., Gursky, H., & Tucker, W. H. 1971, Nature, 231, 437

Churazov, E., Brüggen, M., Kaiser, C. R., Böhringer, H., & Forman, W. 2001, ApJ, 554, 261

Churazov, E., Forman, W., Jones, C., & Böhringer, H. 2003, ApJ, 590, 225

Churazov, E., Sazonov, S., Sunyaev, R., Forman, W., Jones, C., & Böhringer, H. 2005, MNRAS, 363, L91

Churazov, E., Sunyaev, R., Forman, W., & Böhringer, H. 2002, MNRAS, 332, 729

Clark, P. C., Glover, S. C. O., & Klessen, R. S. 2008, ApJ, 672, 757

Clark, P. C., Glover, S. C. O., Klessen, R. S., & Bromm, V. 2011, ApJ, 727, 110

Colella, P., & Woodward, P. R. 1984, Journal of Computational Physics, 54, 174

Cowie, L. L., Fabian, A. C., & Nulsen, P. E. J. 1980, MNRAS, 191, 399

Cowie, L. L., & Songaila, A. 1998, Nature, 394, 44

Crawford, C. S., Allen, S. W., Ebeling, H., Edge, A. C., & Fabian, A. C. 1999, MNRAS, 306, 857

Crosby, B. D., O'Shea, B. W., Smith, B. D., Turk, M. J., & Hahn, O. 2013, ApJ, 773, 108

Curtis, H. D. 1918, Publications of Lick Observatory, 13, 9

Davis, A. J., & Natarajan, P. 2010, MNRAS, 407, 691

Defouw, R. J. 1970, ApJ, 160, 659

Di Matteo, T., Colberg, J., Springel, V., Hernquist, L., & Sijacki, D. 2008, ApJ, 676, 33

Dijkstra, M., Haiman, Z., Mesinger, A., & Wyithe, J. S. B. 2008, MNRAS, 391, 1961

Donahue, M., Mack, J., Voit, G. M., Sparks, W., Elston, R., & Maloney, P. R. 2000, ApJ, 545, 670

Donahue, M., et al. 2014, ApJ, 794, 136

Dopcke, G., Glover, S. C. O., Clark, P. C., & Klessen, R. S. 2011, ApJ, 729, L3

Doroshkevich, A. G., Zeldovich, Y. B., Syunyaev, R. A., & Khlopov, M. Y. 1980, Pisma v Astronomicheskii Zhurnal, 6, 457

Dubois, Y., Devriendt, J., Slyz, A., & Silk, J. 2009, MNRAS, 399, L49

Dubois, Y., Devriendt, J., Slyz, A., & Teyssier, R. 2010, MNRAS, 409, 985

Dubois, Y., Devriendt, J., Slyz, A., & Teyssier, R. 2012, MNRAS, 420, 2662

Dunn, R. J. H., & Fabian, A. C. 2006, MNRAS, 373, 959

Dunn, R. J. H., Fabian, A. C., & Sanders, J. S. 2006, MNRAS, 366, 758

Dursi, L. J., & Pfrommer, C. 2008, ApJ, 677, 993

Eddington, A. S. 1916, MNRAS, 77, 16

Edge, A. C. 2001, MNRAS, 328, 762

Edge, A. C., Stewart, G. C., & Fabian, A. C. 1992, MNRAS, 258, 177

Edge, D. O., Shakeshaft, J. R., McAdam, W. B., Baldwin, J. E., & Archer, S. 1959, MmRAS, 68, 37

Egan, H., O'Shea, B. W., Hallman, E., Burns, J., Xu, H., Collins, D., Li, H., & Norman, M. L. 2016, ArXiv e-prints

Einasto, J. 1965, Trudy Astrofizicheskogo Instituta Alma-Ata, 5, 87

Ensslin, T. A., Biermann, P. L., Klein, U., & Kohle, S. 1998, A&A, 332, 395

Fabian, A. C. 1994, Anual Reviews of Astronomy and Astrophysics, 32, 277

Fabian, A. C. 2012, ARA&A, 50, 455

Fabian, A. C., Allen, S. W., Crawford, C. S., Johnstone, R. M., Morris, R. G., Sanders, J. S., & Schmidt, R. W. 2002, MNRAS, 332, L50

Fabian, A. C., Pringle, J. E., & Rees, M. J. 1976, Nature, 263, 301

Fabian, A. C., Sanders, J. S., Allen, S. W., Crawford, C. S., Iwasawa, K., Johnstone, R. M., Schmidt, R. W., & Taylor, G. B. 2003, MNRAS, 344, L43

Fabian, A. C., Sanders, J. S., Taylor, G. B., Allen, S. W., Crawford, C. S., Johnstone, R. M., & Iwasawa, K. 2006, MNRAS, 366, 417

Fabian, A. C., et al. 2011, MNRAS, 418, 2154

Fabjan, D., Tornatore, L., Borgani, S., Saro, A., & Dolag, K. 2008, MNRAS, 386, 1265

Fanaroff, B. L., & Riley, J. M. 1974, MNRAS, 167, 31P

Fath, E. A. 1909, Lick Observatory Bulletin, 5, 71

Federrath, C., Sur, S., Schleicher, D. R. G., Banerjee, R., & Klessen, R. S. 2011, ApJ, 731, 62

Felten, J. E., Gould, R. J., Stein, W. A., & Woolf, N. J. 1966, ApJ, 146, 955

Feng, J. L. 2010, ARA&A, 48, 495

Feretti, L., Giovannini, G., Govoni, F., & Murgia, M. 2012, A&A Rev., 20, 54

Ferland, G. J., Korista, K. T., Verner, D. A., Ferguson, J. W., Kingdon, J. B., & Verner, E. M. 1998, PASP, 110, 761

Ferrarese, L., & Ford, H. 2005, Space Sci. Rev., 116, 523

Ferrarese, L., & Merritt, D. 2000, ApJ, 539, L9

Ferrarese, L., et al. 2006, ApJ, 644, L21

Ferrari, C., Govoni, F., Schindler, S., Bykov, A. M., & Rephaeli, Y. 2008, Space Sci. Rev., 134, 93

Field, G. B. 1965, ApJ, 142, 531

Fogarty, K., Postman, M., Connor, T., Donahue, M., & Moustakas, J. 2015, ApJ, 813, 117

Forman, W., Jones, C., Cominsky, L., Julien, P., Murray, S., Peters, G., Tananbaum, H., & Giacconi, R. 1978, ApJS, 38, 357

Fryxell, B., et al. 2000, ApJS, 131, 273

Fujita, Y., Kimura, S., & Ohira, Y. 2013, MNRAS, 432, 1434

Fujita, Y., & Ohira, Y. 2011, ApJ, 738, 182

Fujita, Y., & Ohira, Y. 2012, ApJ, 746, 53

Galli, D., & Palla, F. 1998, A&A, 335, 403

Galli, D., & Palla, F. 2002, Planet. Space Sci., 50, 1197

Gao, L., Navarro, J. F., Cole, S., Frenk, C. S., White, S. D. M., Springel, V., Jenkins, A., & Neto, A. F. 2008, MNRAS, 387, 536

Gaspari, M., Brighenti, F., D'Ercole, A., & Melioli, C. 2011a, MNRAS, 415, 1549

Gaspari, M., Brighenti, F., & Temi, P. 2012a, MNRAS, 424, 190

Gaspari, M., Melioli, C., Brighenti, F., & D'Ercole, A. 2011b, MNRAS, 411, 349

Gaspari, M., Ruszkowski, M., & Sharma, P. 2012b, ApJ, 746, 94

Gebhardt, K., et al. 2000, ApJ, 539, L13

Giacconi, R., Murray, S., Gursky, H., Kellogg, E., Schreier, E., Matilsky, T., Koch, D., & Tananbaum, H. 1974, ApJS, 27, 37

Giacconi, R., Murray, S., Gursky, H., Kellogg, E., Schreier, E., & Tananbaum, H. 1972, ApJ, 178, 281

Glover, S. 2005, Space Sci. Rev., 117, 445

Glover, S. C. O., & Abel, T. 2008, MNRAS, 388, 1627

Glover, S. C. O., & Jappsen, A.-K. 2007, ApJ, 666, 1

Gonzalez, A. H., Sivanandam, S., Zabludoff, A. I., & Zaritsky, D. 2013, ApJ, 778, 14

Gonzalez, A. H., Zaritsky, D., & Zabludoff, A. I. 2007, ApJ, 666, 147

Gott, III, J. R., Jurić, M., Schlegel, D., Hoyle, F., Vogeley, M., Tegmark, M., Bahcall, N., & Brinkmann, J. 2005, ApJ, 624, 463

Greif, T. H., Springel, V., White, S. D. M., Glover, S. C. O., Clark, P. C., Smith, R. J., Klessen, R. S., & Bromm, V. 2011, ApJ, 737, 75

Gürkan, M. A., Fregeau, J. M., & Rasio, F. A. 2006, ApJ, 640, L39

Guth, A. H. 1981, Phys. Rev. D, 23, 347

Hahn, O., Martizzi, D., Wu, H.-Y., Evrard, A. E., Teyssier, R., & Wechsler, R. H. 2015, ArXiv e-prints

Heger, A., & Woosley, S. E. 2010, ApJ, 724, 341

Hollenbach, D., & McKee, C. F. 1979, ApJS, 41, 555

Hollenbach, D., & McKee, C. F. 1989, ApJ, 342, 306

Hopkins, P. F., & Hernquist, L. 2006, ApJS, 166, 1

Hosokawa, T., Omukai, K., Yoshida, N., & Yorke, H. W. 2011, Science, 334, 1250

Hoyle, F., & Lyttleton, R. A. 1939, Proceedings of the Cambridge Philosophical Society, 35, 405

Inogamov, N. A., & Sunyaev, R. A. 2003, Astronomy Letters, 29, 791

Jansen, F., et al. 2001, A&A, 365, L1

Jappsen, A.-K., Klessen, R. S., Glover, S. C. O., & Mac Low, M.-M. 2009a, ApJ, 696, 1065

Jappsen, A.-K., Mac Low, M.-M., Glover, S. C. O., Klessen, R. S., & Kitsionas, S. 2009b, ApJ, 694, 1161

Jeltema, T., & Profumo, S. 2016, MNRAS

Johnstone, R. M., Fabian, A. C., Edge, A. C., & Thomas, P. A. 1992, MNRAS, 255, 431

Joung, M. R., Bryan, G. L., & Putman, M. E. 2012, ApJ, 745, 148

Kaastra, J. S., Ferrigno, C., Tamura, T., Paerels, F. B. S., Peterson, J. R., & Mittaz, J. P. D. 2001, A&A, 365, L99

Katz, J. I. 1976, ApJ, 207, 25

Kauffmann, G., et al. 2003, MNRAS, 346, 1055

Kelly, P. L., et al. 2015, Science, 347, 1123

Kerr, R. P. 1963, Physical Review Letters, 11, 237

Khalatyan, A., Cattaneo, A., Schramm, M., Gottlöber, S., Steinmetz, M., & Wisotzki, L. 2008, MNRAS, 387, 13

Khlopov, M. Y., Rubin, S. G., & Sakharov, A. S. 2005, Astroparticle Physics, 23, 265

Kim, J.-h., et al. 2014, ApJS, 210, 14

Kim, W.-T., El-Zant, A. A., & Kamionkowski, M. 2005, ApJ, 632, 157

King, A. 2003, ApJ, 596, L27

Kirkpatrick, C. C., & McNamara, B. R. 2015, MNRAS, 452, 4361

Kirkpatrick, C. C., McNamara, B. R., & Cavagnolo, K. W. 2011, ApJ, 731, L23

Klessen, R. S., Glover, S. C. O., & Clark, P. C. 2012, MNRAS, 421, 3217

Kravtsov, A. V., & Borgani, S. 2012, ARA&A, 50, 353

Latif, M. A., Schleicher, D. R. G., Schmidt, W., & Niemeyer, J. 2013, MNRAS, 432, 668

Lawrence, A. 1987, PASP, 99, 309

Lea, S. M., Silk, J., Kellogg, E., & Murray, S. 1973, ApJ, 184, L105

Leccardi, A., & Molendi, S. 2008, A&A, 487, 461

Li, Y., & Bryan, G. L. 2012, ApJ, 747, 26

Li, Y., & Bryan, G. L. 2014a, ApJ, 789, 54

Li, Y., & Bryan, G. L. 2014b, ApJ, 789, 153

Li, Y., Bryan, G. L., Ruszkowski, M., Voit, G. M., O'Shea, B. W., & Donahue, M. 2015, ApJ, 811, 73

Linde, A. D. 1982, Physics Letters B, 108, 389

Loewenstein, M. 1990, ApJ, 349, 471

Loubser, S. I., Babul, A., Hoekstra, H., Mahdavi, A., Donahue, M., Bildfell, C., & Voit, G. M. 2015, ArXiv e-prints

Loubser, S. I., Babul, A., Hoekstra, H., Mahdavi, A., Donahue, M., Bildfell, C., & Voit, G. M. 2016, MNRAS, 456, 1565

Lynden-Bell, D. 1969, Nature, 223, 690

Magorrian, J., et al. 1998, AJ, 115, 2285

Malagoli, A., Rosner, R., & Bodo, G. 1987, ApJ, 319, 632

Malagoli, A., Rosner, R., & Fryxell, B. 1990, MNRAS, 247, 367

Markevitch, M., & Vikhlinin, A. 2007, Phys. Rep., 443, 1

Mathews, W. G., Faltenbacher, A., & Brighenti, F. 2006, ApJ, 638, 659

Mathews, W. G., & Guo, F. 2012, ApJ, 754, 154

Matsushita, K. 2011, A&A, 527, A134

McCourt, M., Sharma, P., Quataert, E., & Parrish, I. J. 2012, MNRAS, 419, 3319

McDonald, M., Veilleux, S., Rupke, D. S. N., & Mushotzky, R. 2010, ApJ, 721, 1262

McDonald, M., Veilleux, S., Rupke, D. S. N., Mushotzky, R., & Reynolds, C. 2011, ApJ, 734, 95

McDonald, M., et al. 2015, ArXiv e-prints

McKee, C. F., & Tan, J. C. 2008, ApJ, 681, 771

McKinney, J. C., Tchekhovskoy, A., & Blandford, R. D. 2012, MNRAS, 423, 3083

McNamara, B. R., & Nulsen, P. E. J. 2007, ARA&A, 45, 117

McNamara, B. R., & Nulsen, P. E. J. 2012, New Journal of Physics, 14, 055023

McNamara, B. R., Nulsen, P. E. J., Wise, M. W., Rafferty, D. A., Carilli, C., Sarazin, C. L., & Blanton, E. L. 2005, Nature, 433, 45

Meece, G. R., O'Shea, B. W., & Voit, G. M. 2015, ApJ, 808, 43

Meece, G. R., Smith, B. D., & O'Shea, B. W. 2014, ApJ, 783, 75

Meece, G. R., Voit, G. M., & O'Shea, B. W. 2016, ArXiv e-prints

Menanteau, F., et al. 2012, ApJ, 748, 7

Merritt, D. 2000, in Astronomical Society of the Pacific Conference Series, Vol. 197, Dynamics of Galaxies: from the Early Universe to the Present, ed. F. Combes, G. A. Mamon, & V. Charmandaris, 221

Milgrom, M. 1983, ApJ, 270, 365

Million, E. T., Werner, N., Simionescu, A., Allen, S. W., Nulsen, P. E. J., Fabian, A. C., Böhringer, H., & Sanders, J. S. 2010, MNRAS, 407, 2046

Mitchell, R. J., Culhane, J. L., Davison, P. J. N., & Ives, J. C. 1976, MNRAS, 175, 29P

Momjian, E., Carilli, C. L., Walter, F., & Venemans, B. 2014, AJ, 147, 6

Nagai, D., Kravtsov, A. V., & Vikhlinin, A. 2007, ApJ, 668, 1

Nandra, K., et al. 2013, ArXiv e-prints

Navarro, J. F., Frenk, C. S., & White, S. D. M. 1997, ApJ, 490, 493

Navarro, J. F., et al. 2004, MNRAS, 349, 1039

Navarro, J. F., et al. 2010, MNRAS, 402, 21

Norman, M. L. 2010, in American Institute of Physics Conference Series, Vol. 1294, American Institute of Physics Conference Series, ed. D. J. Whalen, V. Bromm, & N. Yoshida, 17–27

Norman, M. L., Bryan, G. L., Harkness, R., Bordner, J., Reynolds, D., O'Shea, B., & Wagner, R. 2007, ArXiv e-prints

Nulsen, P. E. J. 1986, MNRAS, 221, 377

Nulsen, P. E. J., & McNamara, B. R. 2013, Astronomische Nachrichten, 334, 386

O'Dea, C. P., et al. 2008, ApJ, 681, 1035

O'Dea, K. P., et al. 2010, ApJ, 719, 1619

Oesch, P. A., et al. 2016, ApJ, 819, 129

Ohkubo, T., Nomoto, K., Umeda, H., Yoshida, N., & Tsuruta, S. 2009, ApJ, 706, 1184

Omma, H., Binney, J., Bryan, G., & Slyz, A. 2004, MNRAS, 348, 1105

Omukai, K. 2000, ApJ, 534, 809

Omukai, K., Tsuribe, T., Schneider, R., & Ferrara, A. 2005, ApJ, 626, 627

O'Shea, B. W., Bryan, G., Bordner, J., Norman, M. L., Abel, T., Harkness, R., & Kritsuk, A. 2004, ArXiv Astrophysics e-prints

O'Shea, B. W., & Norman, M. L. 2007, ApJ, 654, 66

Parker, E. N. 1953, ApJ, 117, 431

Parrish, I. J., Quataert, E., & Sharma, P. 2009, ApJ, 703, 96

Peebles, P. J. E. 1971, A&A, 11, 377

Penrose, R., & Floyd, R. M. 1971, Nature Physical Science, 229, 177

Peterson, J. R., & Fabian, A. C. 2006, Phys. Rep., 427, 1

Peterson, J. R., Kahn, S. M., Paerels, F. B. S., Kaastra, J. S., Tamura, T., Bleeker, J. A. M., Ferrigno, C., & Jernigan, J. G. 2003, ApJ, 590, 207

Peterson, J. R., et al. 2001, A&A, 365, L104

Pizzolato, F., & Soker, N. 2005, ApJ, 632, 821

Planck Collaboration et al. 2014a, A&A, 571, A20

Planck Collaboration et al. 2014b, A&A, 571, A24

Planck Collaboration et al. 2015a, ArXiv e-prints

Planck Collaboration et al. 2015b, ArXiv e-prints

Pollack, J. B., Hollenbach, D., Beckwith, S., Simonelli, D. P., Roush, T., & Fong, W. 1994, ApJ, 421, 615

Postman, M., et al. 2012, ApJS, 199, 25

Press, W. H., & Schechter, P. 1974, ApJ, 187, 425

Prestwich, A. H., Joy, M., Luginbuhl, C. B., Sulkanen, M., & Newberry, M. 1997, ApJ, 477, 144

Puchwein, E., Sijacki, D., & Springel, V. 2008, ApJ, 687, L53

Quataert, E. 2008, ApJ, 673, 758

Rafferty, D. A., McNamara, B. R., & Nulsen, P. E. J. 2008, ApJ, 687, 899

Rasia, E., et al. 2015, ApJ, 813, L17

Rayleigh. 1882, Proceedings of the London Mathematical Society, s1-14, 170

Reynolds, C. S., McKernan, B., Fabian, A. C., Stone, J. M., & Vernaleo, J. C. 2005, MNRAS, 357, 242

Ripamonti, E. 2007, MNRAS, 376, 709

Ripamonti, E., & Abel, T. 2004, MNRAS, 348, 1019

Rogallo, R. S. 1981, NASA STI/Recon Technical Report N, 81

Ruhl, J., et al. 2004, in Society of Photo-Optical Instrumentation Engineers (SPIE) Conference Series, Vol. 5498, Z-Spec: a broadband millimeter-wave grating spectrometer: design, construction, and first cryogenic measurements, ed. C. M. Bradford, P. A. R. Ade, J. E. Aguirre, J. J. Bock, M. Dragovan, L. Duband, L. Earle, J. Glenn, H. Matsuhara, B. J. Naylor, H. T. Nguyen, M. Yun, & J. Zmuidzinas, 11–29

Russell, H. R., et al. 2016, MNRAS, 458, 3134

Ruszkowski, M., Brüggen, M., & Begelman, M. C. 2004, ApJ, 611, 158

Ruszkowski, M., Enßlin, T. A., Brüggen, M., Heinz, S., & Pfrommer, C. 2007, MNRAS, 378, 662

Ruszkowski, M., Lee, D., Brüggen, M., Parrish, I., & Oh, S. P. 2011, ApJ, 740, 81

Ruszkowski, M., & Oh, S. P. 2010, ApJ, 713, 1332

Ruszkowski, M., & Oh, S. P. 2011, MNRAS, 414, 1493

Ryan, S. G., Norris, J. E., & Beers, T. C. 1996, ApJ, 471, 254

Salpeter, E. E. 1955, ApJ, 121, 161

Salpeter, E. E. 1964, ApJ, 140, 796

Sambruna, R. M., Eracleous, M., & Mushotzky, R. F. 1999, ApJ, 526, 60

Sarazin, C. L. 1988, X-ray emission from clusters of galaxies

Sarazin, C. L., & White, III, R. E. 1987, ApJ, 320, 32

Sądowski, A., & Narayan, R. 2015, MNRAS, 453, 3213

Scannapieco, E., Gray, W. J., & Pan, L. 2012, ApJ, 746, 57

Schekochihin, A. A., Cowley, S. C., Dorland, W., Hammett, G. W., Howes, G. G., Quataert, E., & Tatsuno, T. 2009, ApJS, 182, 310

Schmidt, M. 1963, Nature, 197, 1040

Schneider, R., & Omukai, K. 2010, MNRAS, 402, 429

Schneider, R., Omukai, K., Bianchi, S., & Valiante, R. 2012, MNRAS, 419, 1566

Schneider, R., Omukai, K., Inoue, A. K., & Ferrara, A. 2006, MNRAS, 369, 1437

Schure, K. M., Kosenko, D., Kaastra, J. S., Keppens, R., & Vink, J. 2009, A&A, 508, 751

Seager, S., Sasselov, D. D., & Scott, D. 1999, ApJ, 523, L1

Seager, S., Sasselov, D. D., & Scott, D. 2000, ApJS, 128, 407

Seyfert, C. K. 1943, ApJ, 97, 28

Sharma, P., Chandran, B. D. G., Quataert, E., & Parrish, I. J. 2009, ApJ, 699, 348

Sharma, P., McCourt, M., Parrish, I. J., & Quataert, E. 2012a, MNRAS, 427, 1219

Sharma, P., McCourt, M., Quataert, E., & Parrish, I. J. 2012b, MNRAS, 420, 3174

Sharma, P., Parrish, I. J., & Quataert, E. 2010, ApJ, 720, 652

Shlosman, I., Frank, J., & Begelman, M. C. 1989, Nature, 338, 45

Sievers, J. L., et al. 2013, J. Cosmology Astropart. Phys., 10, 060

Sijacki, D., Pfrommer, C., Springel, V., & Enßlin, T. A. 2008, MNRAS, 387, 1403

Sijacki, D., Springel, V., Di Matteo, T., & Hernquist, L. 2007, MNRAS, 380, 877

Silvia, D. W. 2013, PhD thesis, University of Colorado at Boulder

Silvia, D. W., O'Shea, B. W., Smith, B. D., Shull, J. M., Turk, M., & Reynolds, D. 2015, in American Astronomical Society Meeting Abstracts, Vol. 225, American Astronomical Society Meeting Abstracts, 253.07

Singh, A., & Sharma, P. 2015, MNRAS, 446, 1895

Skillman, S. W., Xu, H., Hallman, E. J., O'Shea, B. W., Burns, J. O., Li, H., Collins, D. C., & Norman, M. L. 2013, ApJ, 765, 21

Skory, S., Hallman, E., Burns, J. O., Skillman, S. W., O'Shea, B. W., & Smith, B. D. 2013, ApJ, 763, 38

Smith, B., O'Shea, B. W., Voit, G. M., Ventimiglia, D., & Skillman, S. W. 2013, ApJ, 778, 152

Smith, B., Sigurdsson, S., & Abel, T. 2008, MNRAS, 385, 1443

Smith, B. D., Turk, M. J., Sigurdsson, S., O'Shea, B. W., & Norman, M. L. 2009, ApJ, 691, 441

Smith, B. D., Wise, J. H., O'Shea, B. W., Norman, M. L., & Khochfar, S. 2015, MNRAS, 452, 2822

Smoot, G., et al. 1990, ApJ, 360, 685

Smoot, G. F., et al. 1992, ApJ, 396, L1

Sommer-Larsen, J., Götz, M., & Portinari, L. 2003, ApJ, 596, 47

Spergel, D. N., & Steinhardt, P. J. 2000, Physical Review Letters, 84, 3760

Spitzer, L. 1962, Physics of Fully Ionized Gases

Springel, V., Di Matteo, T., & Hernquist, L. 2005a, MNRAS, 361, 776

Springel, V., et al. 2005b, Nature, 435, 629

Stacy, A., Greif, T. H., & Bromm, V. 2012, MNRAS, 422, 290

Steigman, G. 2007, Annual Review of Nuclear and Particle Science, 57, 463

Steinborn, L. K., Dolag, K., Hirschmann, M., Prieto, M. A., & Remus, R.-S. 2015, MNRAS, 448, 1504

Stone, J. M., & Norman, M. L. 1992, ApJS, 80, 753

Storm, E., Jeltema, T. E., Profumo, S., & Rudnick, L. 2013, ApJ, 768, 106

Sunyaev, R. A., & Zeldovich, Y. B. 1970, Ap&SS, 7, 3

Sutherland, R. S., & Dopita, M. A. 1993, ApJS, 88, 253

Sutter, P. M., Yang, H.-Y. K., Ricker, P. M., Foreman, G., & Pugmire, D. 2012, MNRAS, 419, 2293

Tamura, T., Bleeker, J. A. M., Kaastra, J. S., Ferrigno, C., & Molendi, S. 2001a, A&A, 379, 107

Tamura, T., et al. 2001b, A&A, 365, L87

Tan, J. C., & McKee, C. F. 2004, ApJ, 603, 383

Tanaka, T., & Haiman, Z. 2009, ApJ, 696, 1798

Tchekhovskoy, A., Narayan, R., & McKinney, J. C. 2011, MNRAS, 418, L79

Thomson, W. 1871, The London, Edinburgh, and Dublin Philosophical Magazine and Journal of Science, 42, 362

Tielens, A. G. G. M., & Hollenbach, D. 1985, ApJ, 291, 722

Trenti, M., & Stiavelli, M. 2009, ApJ, 694, 879

Truelove, J. K., Klein, R. I., McKee, C. F., Holliman, II, J. H., Howell, L. H., Greenough, J. A., & Woods, D. T. 1998, ApJ, 495, 821

Turk, M. J., Abel, T., & O'Shea, B. 2009, Science, 325, 601

Turk, M. J., Oishi, J. S., Abel, T., & Bryan, G. L. 2012, ApJ, 745, 154

Turk, M. J., Smith, B. D., Oishi, J. S., Skory, S., Skillman, S. W., Abel, T., & Norman, M. L. 2011, ApJS, 192, 9

Urry, C. M., & Padovani, P. 1995, PASP, 107, 803

Valdarnini, R. 2006, New A, 12, 71

Vernaleo, J. C., & Reynolds, C. S. 2006, ApJ, 645, 83

Viel, M., Becker, G. D., Bolton, J. S., & Haehnelt, M. G. 2013, Phys. Rev. D, 88, 043502

Vogelsberger, M., Genel, S., Sijacki, D., Torrey, P., Springel, V., & Hernquist, L. 2013, MNRAS, 436, 3031

Vogelsberger, M., et al. 2014, MNRAS, 444, 1518

Voigt, L. M., & Fabian, A. C. 2004, MNRAS, 347, 1130

Voigt, L. M., Schmidt, R. W., Fabian, A. C., Allen, S. W., & Johnstone, R. M. 2002, MNRAS, 335, L7

Voit, G. M. 2005, Reviews of Modern Physics, 77, 207

Voit, G. M. 2011, ApJ, 740, 28

Voit, G. M., & Bryan, G. L. 2001, Nature, 414, 425

Voit, G. M., Bryan, G. L., Balogh, M. L., & Bower, R. G. 2002, ApJ, 576, 601

Voit, G. M., Bryan, G. L., O'Shea, B. W., & Donahue, M. 2015a, ApJ, 808, L30

Voit, G. M., Cavagnolo, K. W., Donahue, M., Rafferty, D. A., McNamara, B. R., & Nulsen, P. E. J. 2008, ApJ, 681, L5

Voit, G. M., & Donahue, M. 2015, ApJ, 799, L1

Voit, G. M., Donahue, M., Bryan, G. L., & McDonald, M. 2014, ArXiv e-prints

Voit, G. M., Donahue, M., Bryan, G. L., & McDonald, M. 2015b, Nature, 519, 203

Voit, G. M., Donahue, M., O'Shea, B. W., Bryan, G. L., Sun, M., & Werner, N. 2015c, ApJ, 803, L21

Volonteri, M. 2010, A&A Rev., 18, 279

von der Linden, A., et al. 2014, MNRAS, 439, 2

Wagh, B., Sharma, P., & McCourt, M. 2014, MNRAS, 439, 2822

Wagoner, R. V. 1973, ApJ, 179, 343

Walg, S., Achterberg, A., Markoff, S., Keppens, R., & Meliani, Z. 2013, MNRAS, 433, 1453

Weisskopf, M. C., Tananbaum, H. D., Van Speybroeck, L. P., & O'Dell, S. L. 2000, in Proc. SPIE, Vol. 4012, X-Ray Optics, Instruments, and Missions III, ed. J. E. Truemper & B. Aschenbach, 2–16

Werner, N., et al. 2010, MNRAS, 407, 2063

Werner, N., et al. 2014, MNRAS, 439, 2291

Weymann, R. 1960, ApJ, 132, 452

Whalen, D. J., et al. 2013, ApJ, 777, 110

Willott, C. J., Bergeron, J., & Omont, A. 2015, ApJ, 801, 123

Willott, C. J., McLure, R. J., & Jarvis, M. J. 2003, ApJ, 587, L15

Wilman, R. J., Edge, A. C., & Johnstone, R. M. 2005, MNRAS, 359, 755

Wilson, A. S., & Colbert, E. J. M. 1995, ApJ, 438, 62

Wise, J. H., Demchenko, V. G., Halicek, M. T., Norman, M. L., Turk, M. J., Abel, T., & Smith, B. D. 2014, MNRAS, 442, 2560

Wurster, J., & Thacker, R. J. 2013, MNRAS, 431, 2513

Xu, H., Ahn, K., Wise, J. H., Norman, M. L., & O'Shea, B. W. 2014, ApJ, 791, 110

Yang, H.-Y. K., & Reynolds, C. S. 2015, ArXiv e-prints

Yang, H.-Y. K., Sutter, P. M., & Ricker, P. M. 2012, MNRAS, 427, 1614

Yong, D., et al. 2013, ApJ, 762, 27

Yoshida, N., Abel, T., Hernquist, L., & Sugiyama, N. 2003, ApJ, 592, 645

Zakamska, N. L., & Narayan, R. 2003, ApJ, 582, 162

Zandanel, F., Pfrommer, C., & Prada, F. 2014, MNRAS, 438, 124

Zanstra, H. 1955a, Vistas in Astronomy, 1, 256

Zanstra, H. 1955b, in IAU Symposium, Vol. 2, Gas Dynamics of Cosmic Clouds, 70

Zel'dovich, Y. B. 1970, A&A, 5, 84

Zel'dovich, Y. B., & Novikov, I. D. 1965, Soviet Physics Doklady, 9, 834

Zhuravleva, I., et al. 2014, Nature, 515, 85

Zhuravleva, I., et al. 2015, MNRAS, 450, 4184

Zhuravleva, I., et al. 2016, MNRAS

ZuHone, J. A., Markevitch, M., & Johnson, R. E. 2010, ApJ, 717, 908

Zwicky, F. 1933, Helvetica Physica Acta, 6, 110